TNO TU Delft

SENSITIVITIES AND PREREQUISITES OF THE APPLICATION OF THE ENERGY FLUX ANALYSIS TO HIGH-RISE STRUCTURES EXCITED BY WIND USING IN SITU MEASUREMENTS

CASE: NEW ORLEANS TOWER, ROTTERDAM

M. Sonneveld

Sensitivities and prerequisites of the application of the Energy Flux Analysis to high-rise structures excited by wind using in situ measurements

Case: New Orleans tower, Rotterdam

by

M. Sonneveld

to obtain the degree of Master of Science
in Civil Engineering, specialisation Structural Mechanics
at the Delft University of Technology,

to be defended publicly on Monday June 29, 2020 at 1:45 PM.

Student number:	4296974	
Project duration:	September 1, 2019 - June 29, 2020	
Thesis committee:	Prof. dr. A.V. Metrikine,	TU Delft, chair
	Dr. ir. S. Sánchez Gómez,	TU Delft, supervisor
	Dr. E. Lourens,	TU Delft, supervisor
	Ir. A.J. Bronkhorst,	TNO, daily supervisor

An electronic version of this thesis is available at `http://repository.tudelft.nl/`.

TNO TU Delft

Preface

This thesis was written to fulfil the graduation requirements for the Civil Engineering master track Structural Engineering, with a specialisation in Structural Mechanics, at the Delft University of Technology. The research has been conducted from September 2019 till June 2020 in collaboration with TNO, a Dutch organisation for applied scientific research. It combines two of my great interests. Like most structural engineers, I am intrigued by the challenges involved with designing high-rise structures. My first experience with high-rise structures was during a year of full time work as a structural engineer, where I was involved in the design of some fascinating high-rise structures to be built in the Netherlands. I discovered my second great interest at the end of my studies, when I followed the course Structural Dynamics given by Prof. dr. A. V. Metrikine. After this, I was determined I wanted structural dynamics to be part of my graduation topic. When I discovered TNO was researching an energy based approach to identify damping in high-rise structures, I knew I wanted to be involved.

I have experienced writing this thesis as one of the most challenging tasks I have had so far, and I enjoyed the learning curve it involved. Where throughout your studies it is exactly dictated what is expected of you, during the thesis you have to formulate your own assignment. An assignment that should not only meet your personal interests, but also that of all parties involved. My goal was to present a thesis result that shows my full intellectual potential, but I soon discovered that there is much more to research than understanding and producing positive, ground-breaking results. As colleagues have told me, the result will rarely ever feel this satisfying. In the end, I am happy with what I will present to you in this thesis. It highlights the importance of issues and components for the application of the Energy Flux Analysis that had not been addressed before. Personally, I am convinced that performing this research has made me a more educated person.

Due to the current COVID-19 crisis, we all had to work from home for the past few months. The distance did not stop my daily supervisor Okke Bronkhorst from being involved in my work, and from showing much interest in my results. I sincerely want to thank Okke for always taking the time, and for providing new challenges and questions to consider. I am also very grateful with the help of Liesette la Gasse from TNO. Besides helping me content wise, and correcting my report, Liesette was a mentor to me guiding me through the process that is called the thesis. Besides, I am very happy I had Prof. dr. A. V. Metrikine and Sergio Sánchez Gómez in my assessment committee, as they are both extremely knowledgeable and showed the simplicity of issues that seemed so complex at first.

Working from home can be challenging, especially when you are living with nine other students. I would like to express my appreciation for my roommates being very considerate and for creating a pleasant working environment. The same holds for my parents, as I have also spent a few months working from my family home. I am privileged with my parents. They have always unconditionally supported me, giving me the freedom to make my own decisions, and having full trust in them. My sister was the first to read my thesis. Although she is an extremely fast reader, I am very thankful for the energy she has put into correcting my report. Besides, my sister has always been a role model and a source of inspiration for me. Last, but most definitely not least, I would like to thank Jan for always having an ear for anything that goes on in my mind, for giving me advice, and for always being so incredibly patient.

M. Sonneveld
Delft, 21 June 2020

Abstract

As buildings get taller and lighter, structural engineers are increasingly faced with the consequences of the dynamic response of high-rise buildings to wind. Damping is an important property for the dynamic response of high-rise structures, but is a combination of many mechanisms, which makes it a complex phenomenon to account for in the structural design. Empirical damping predictors currently exist, but a large scatter is found among predictors, as well as between predictors and identified damping from measurements. Damping values are prescribed in codes, but are not consistently conservative. Therefore, there is a strong desire from both structural engineers and researchers to obtain further understanding of damping behaviour in high-rise structures.

Damping identification techniques, such as the Half-power Bandwidth method and the Random Decrement technique are commonly used. However, these are not applicable to buildings with closely spaced modes, and require extensive measurements. Besides, they only provide a damping value, and cannot find damping of separate components of a system. A novel technique, the Energy Flux Analysis, approaches damping from an energy point of view, making it more widely applicable, and allowing for damping identification in components of a structure. The Energy Flux Analysis has been verified to lab structures, but its performance when applied to a high-rise structures using in situ measurements is still unknown.

The aim of this research is to investigate the sensitivities of and prerequisites for the application of the Energy Flux Analysis to high-rise buildings excited by wind using spatially limited measurements. The sensitivities were sought for in the uncertainty of required input for the Energy Flux Analysis: structure motion, which includes internal forces, wind load, data acquisition, and structural properties. The research was performed through application of the Energy Flux Analysis to the New Orleans tower in Rotterdam.

While the sensitivity to structural properties and the magnitude of measurements is limited, the Energy Flux Analysis demonstrated to be highly sensitive to the phase of structural motion, internal forces, and wind load. The first two points are relevant for computing the energy flux at the boundary of a system, when one is interested in damping in the superstructure and due to soil-structure interaction separately. The last point is relevant when one is interested in the total or superstructure damping.

The phase differences occurring between structure motion and internal forces are a direct result of damping. Material damping resulted in a phase difference between stress and strain in the numerical model, while a local damper resulted in a phase difference between structure motion at different locations. The many damping mechanisms occurring in a high-rise structure may each affect the phase of structure motion and internal forces differently. When these phase differences are not taken into account in the Energy Flux Analysis, for instance due to extrapolation of measurements, an erroneous result will be obtained. A brief investigation was performed as to whether these effects can be expected in true structures, but additional research is required.

The fluctuating wind load at the natural frequency of the structure is dominant for the flux of energy from wind to the structure, which is obtained by multiplication of the wind load with the structure velocity. Again, the phase of this wind load is highly important. When measured at one location, little is known about the phase of the wind load at other heights. Different approaches of extrapolating the measured wind load demonstrated a large scatter in the Energy Flux Analysis results. In this research, the Energy Flux Analysis found not to be repeatable, which was proven to be a direct result of the phase difference between the measured wind load and structure velocity. Possible causes for this varying phase difference were formulated.

It is essential, but due to the major advantages of the Energy Flux Analysis also profitable, to perform further research into its application to high-rise structures. Therefore, this study provides extensive recommendations mostly focused on simple numerical and lab experiments.

Keywords: damping, high-rise, wind, Energy Flux Analysis, mode coupling, Half-power Bandwidth, Random Decrement, spatial incompleteness, measurement accuracy, measurement uncertainty, pressure tap, foundation stiffness, soil-structure interaction, phase difference

Contents

List of Tables

List of Figures

List of Abbreviations

CPT	Cone Penetration Test
DE	Differential Equation
E	East
EFA	Energy Flux Analysis
EoM	Equation of Motion
FEM	Finite Element Method
FFT	Fast Fourier Transform
FRF	Frequency Response Function
HPBW	Half-Power Bandwidth
MDOF	Multi-Degree-of-Freedom
MRD	Multi-mode Random Decrement
MS	Mode Shape
N	North
PSD	Power Spectral Density
RD	Random Decrement
RDS	Random Decrement Signature
SDOF	Single-Degree-of-Freedom
S	South
SLS	Serviceability Limit State
SOS	Second Order Sections
SS	Superstructure
SSI	Soil-Structure Interaction
TNO	Dutch Organisation for Applied Scientific Research
ULS	Ultimate Limit State
W	West

List of Symbols

Variable	Unit	Name
A	m^2	Area
b	m	Width
C		Damping coefficient
C_p		Pressure coefficient
D	m	Foundation dimension
E	Nm	Total energy
E^*	N/m^2	Kelvin-Voight factor for material damping
E_{diss}	Nm	Dissipated energy
EI	Nm^2	Bending stiffness
F	N	Concentrated load
f	Hz	Linear frequency
f_n	Hz	Natural frequency
f_s	Hz	Sampling frequency
g	m/s^2	Gravitational acceleration
H	m	Height
I		Turbulence intensity
J	Ns	Impulse
K	Nm	Kinetic energy
K_t	N/m	Translational stiffness
K_θ	Nm	Rotational stiffness
k	N/m	Spring stiffness
m	kg	Mass
N		Number
P	Nm	Potential energy
p	Pa	Wind pressure
p_0	Pa	Static wind pressure
$\bar{p}$	Pa	Mean wind pressure
p'	Pa	Fluctuating wind pressure
S	Nm/s	Energy flux at system boundary
S_{xx}		Spectral density function
T	s	Period length
t	s	Time
U	m/s	Total wind velocity
$\bar{U}$	m/s	Mean wind velocity
u'	m/s	Fluctuating wind velocity
u_*	m/s	Friction velocity
V	m^3	Volume
W_{diss}	Nm/s	Energy dissipation
W_{ext}	Nm/s	External energy flux
x_s	Hzs	Monin coordinate
q	N/m	Distributed load
z_0	m	Roughness length

Variable	Unit	Name
γ		Shear strain
ϵ		Axial strain
Δ	m	Separation of two points
δ		Logarithmic decrement
ζ		Damping ratio
θ		Rotation
λ	Nm/m	Lagrangian density
ρ_a	kg/m^3	Mass density of air
ρ_b	kg/m^3	Building mass density
σ	N/m^2	Stress
σ_u	m/s	Standard deviation wind velocity
σ_x	m	Root mean square top displacement
$\chi_{p,u}$	Ns/m	Aerodynamic admittance
ω	rad/s	Circular frequency
$\phi(x)$		Unit mode shape
ϕ	rad	Phase
ω_n	rad/s	Angular natural frequency

I

INTRODUCTION

1 Introduction

This chapter provides an introduction to this thesis. First, a general introduction of the state of the art is presented together with a brief problem statement. This is followed by the objective of this thesis, the methodology used, and the scope. Finally, an overview of the outline of this document is presented, which may be used as a reading guide.

1.1. Introduction

Technological and economical developments at the end of the 19^{th} century led to the start of the construction of high-rise buildings in North American cities. Two major contributions are the advancement of steel structures and the development of vertical transportation. Another aspect leading to the worldwide trend of high-rise construction is the increasing rate of urbanisation, leading to scarcity of land in densely populated urban areas. Besides, the desire to build the tallest building drives the development of high-rise buildings at present day (Kayvani, 2014). In the Netherlands, multiple buildings of over 150 m tall are planned to be constructed within the next few years. Contrary to 19^{th} and 20^{th} century high-rise buildings, high-rise buildings nowadays have a mixed-use including a residential purpose, instead of offices only.

Structural engineers face several challenges when designing high-rise buildings; fire safety, optimisation of floor systems for vertical load reduction, design of vertical load bearing systems, condensed pile foundations and the stability system. Besides, the structural engineer should limit the impact of the structure on the total floor area, and should consider costs, constructability, durability, and sustainability. Not only the Ultimate Limit State (ULS), which guarantees safety, should be considered. Additionally, the design should agree with Serviceability Limit State (SLS) demands, which consider comfort. This often refers the maximum allowable deflections. In a wind-excited high-rise structure, the aspect of wind-induced vibrations should additionally be considered. Vibrations should be limited from an SLS point of view. However, in case of large amplitude vibrations or fatigue, it may also affect the ULS design (Smith and Willford, 2008). Due to the use of lightweight materials and buildings becoming more slender, high-rise buildings nowadays are more vulnerable to wind-induced vibrations. Figure 1.2 visualises this dynamic response of a high-rise structure. Codes prescribe limit values for the vibrations expressed in maximum accelerations depending on the natural frequency of the building and its use. Figure 1.1 presents these limit values prescribed in NEN-EN 1991-1-4 depending on the function of the structure.

Important factors affecting the dynamic behaviour of high-rise buildings are its natural frequency and damping. The former mainly depends on the building mass and stiffness, while the latter is a combination of many complex damping mechanisms that occur in different parts of the structure. Knowledge of these properties is essential in the design of a high-rise structure. However, the damping ratios found using empirical predictors such as the Jeary (Jeary, 1996), Tamura (Yoshida and Tamura, 2003), and Lagomarsino (Lagomarsino, 1993) predictors show a large scatter as is visualised in fig. 1.3. The measured damping rarely ever agrees with predicted damping. Where codes should provide a conservative estimate for damping, which means that it should underestimate it, fig. 1.3 shows that this is not generally the case.

The fact that codes do not consistently provide conservative estimates, and the fact that damping predictors are based on empirical relations that show large differences, indicates that the understanding of damping behaviour in high-rise structures is limited. Additionally, commonly used damping identification techniques

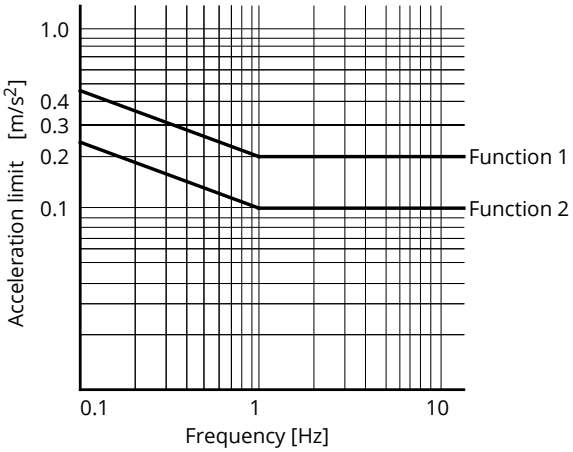

Figure 1.1: Limit values acceleration based on natural frequency (NEN, 2011)

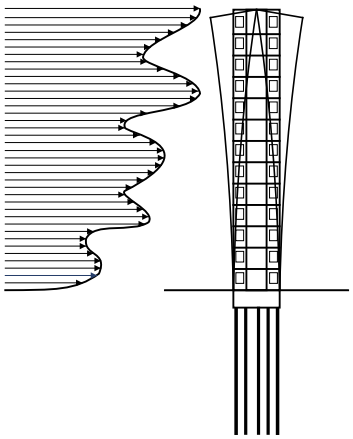

Figure 1.2: Dynamic behaviour high-rise structure

are only suitable for high-rise structures with well separated modes, and the results are only reliable when extensive measurements are available.

There is a strong desire from both structural engineers and researchers to improve the understanding of damping behaviour in high-rise structures. A novel technique, called the Energy Flux Analysis, approaches the problem from an energy point of view, making it more widely applicable. This technique provides insight into the behaviour of the structure using both loading and response information. The result of the Energy Flux Analysis is dissipated energy, which can then be translated to the frequently used damping ratios. Where commonly used damping identification techniques used in ambient conditions can only identify the total damping of a structure, the Energy Flux Analysis allows for identification of damping contributions of components of a structure. Previous research has already found evidence that the contribution of soil-structure interaction may be significant for soft soils in the Netherlands (Gómez, 2019).

The application of the Energy Flux Analysis in the field of structural mechanics for the identification of damping has been proposed by Gómez (Gómez, 2019). In this work, the principles of the Energy Flux Analysis were discussed and it was applied to two lab structures, and to a high-rise structure to identify total damping, and superstructure and soil-structure interaction damping separately. For the lab structures, the method was successfully verified. However, where for the lab structures the structural properties can be measured or experimentally identified, and the applied force is known, this does not hold for the high-rise structure. Assumptions have to be made with respect to the extrapolation of structure motion measurements over the structure height, the wind load acting on the structure, and the model and structural properties used to describe the high-rise building. The Energy Flux Analysis was later used to identify the damping mechanisms prescribed to the Finite Element Method (FEM) model of an Euler-Bernoulli beam by Talib (Talib, 2019). Damping was successfully recovered when considering only one damping mechanism, but discrepancies were found when trying to find the contribution of two separate damping mechanisms. Further effort is required to find the explanation for these discrepancies, and to find the effect of the required assumptions as a result of limited measurements, measurement uncertainty, and uncertainty in structural properties on the result of the Energy Flux Analysis when applied to a high-rise structure.

1.2. Objective

The benefits of the Energy Flux Analysis are clear; it is an advanced damping identification technique that is more generally applicable than current techniques and allows for investigating the damping behaviour in a structure and its separate components. This section will elaborate on the contribution of this thesis to the development of the Energy Flux Analysis. First, the objective of this thesis is presented together with the research questions. This is followed by a definition of the scope of this thesis.

1.2.1. Objective

Before the Energy Flux Analysis is applied for in situ damping identification in high-rise structures, the Energy Flux Analysis requires further investigation. Previous research has focused on developing the Energy Flux Analysis and validation of the method compared to specific lab structures and a FEM model. The effect

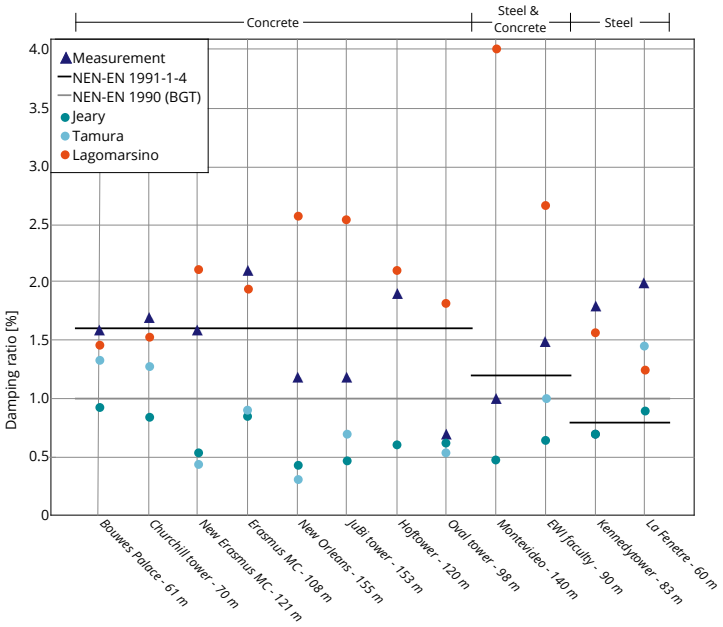

Figure 1.3: Comparison damping from Eurocode, damping predictors and measured damping for high-rise buildings in the Netherlands. Adapted from Bronkhorst (Bronkhorst et al., 2018)

of uncertainties in spatial incompleteness of measurements, measurement uncertainty and uncertainty in structural properties should yet be investigated. Aditionally, means to cope with these complications should be formulated. Besides, it is useful to have an overview of the assumptions and requirements for commonly used damping identification techniques, and what distinguishes the novel approach from these techniques. The main research question of this thesis is:

What are the sensitivities of, and prerequisites for the application of the Energy Flux Analysis to a high-rise structure excited by wind using spatially limited in situ measurements to identify the total, superstructure, and soil-structure interaction dissipated energy?

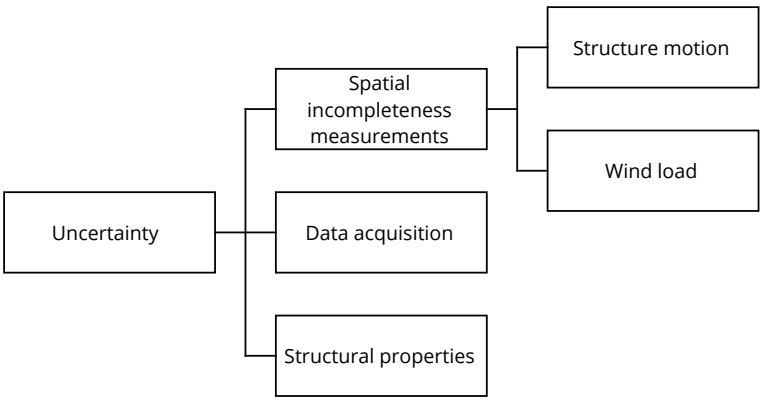

Figure 1.4: Uncertainties introduced to the Energy Flux Analysis when applied to high-rise structures excited by wind using in situ measurements

The answer to this main question is investigated with the use of six sub-questions. These sub-questions cover all aspects that may introduce prerequisites and sensitivities of the application of the Energy Flux Analysis to a wind-induced high-rise structure as presented in fig. 1.4; structure motion, wind load, data acquisition, and structural properties. The answer to the final sub-question should provide the reader with a comparison between commonly used damping identification techniques and the Energy Flux Analysis. Each sub-question is now briefly covered.

1. *Which structure motion measurements are required to identify the total, superstructure, and soil-structure interaction dissipated energy?*

2. *Considering spatial incompleteness caused by limited measurements, what is the sensitivity of the Energy Flux Analysis to the model used to extrapolate structure motion?*

These two questions are covered together, since they are closely related. Theoretically, knowledge of the structure motion along the complete building height is required. However, due to practical and economical reasons this will not be available and therefore spatial incompleteness of motion measurements should be considered. Prerequisites of applying the Energy Flux Analysis, and the sensitivity of the result should be investigated based on the model of extrapolation used. The answer to these questions should provide the reader with an advice on how to measure structure motion to obtain reliable results, and it should provide knowledge on the effect of the chosen extrapolation model on the results of the Energy Flux Analysis. By investigating different extrapolation models, the sensitivity of the Energy Flux Analysis to these models is investigated.

3. *What is the sensitivity of the Energy Flux Analysis to the modelling of wind load?*

Similar to the structural motion, ideally the wind load is known along the complete building height, but in practice this will not be the case. Therefore, the wind load has to be defined differently. By answering this question, the means of modelling wind load will be explored, and its effect on the Energy Flux Analysis results will be investigated.

4. *What is the sensitivity of the Energy Flux Analysis to uncertainties introduced by data acquisition?*

Uncertainties in data acquisition refers to uncertainties due to measurement instruments and set-up, data collection, and data processing. Previous research has not considered the effects of these uncertainties; this thesis will investigate whether it plays a significant role.

5. *What is the sensitivity of the Energy Flux Analysis to the required input of structural properties?*

The Energy Flux Analysis requires input of the structural properties building mass, building stiffness, and foundation stiffness. However, accurate estimation of these structural properties is not straightforward and it is therefore essential to know the sensitivity of the Energy Flux Analysis result to this user-defined input.

6. *What distinguishes the Energy Flux Analysis from commonly used damping identification techniques?*

It is important to know how the Energy Flux Analysis distinguishes itself from commonly used damping identification techniques. This question should answer whether application of the the Energy Flux Analysis can circumvent the shortcomings of the other techniques, but also whether it introduces new difficulties.

1.2.2. Methodology

Answering the questions presented in § 1.2.1 requires a variety of methods of data collection and data analysis. The four different methods will be described in the below sections, which will each provide a brief overview on the method selection and its use. Throughout the thesis, a case high-rise structure is used; the New Orleans tower at the Kop van Zuid in Rotterdam, the Netherlands.

Literature review

The aim of the literature review is, firstly, to get acquainted with the state of the art in wind engineering, structural dynamics with its specific application to high-rise structures, the phenomenon of damping and its identification in high-rise structures, and the Energy Flux Analysis. Secondly, a literature review is performed in order to understand the application and assumptions of commonly used damping identification techniques. Thirdly, possible uncertainties in measurements are discovered by exploring literature on this topic. Finally, a short literature review provides additional understanding of performing a sensitivity study.

Technical reports

Besides literature, technical reports are studied to define the structural properties of the New Orleans tower and the uncertainty in these properties.

Numerical research

For the investigation of the structure motion and its spatial incompleteness, numerical research is performed. The structure is modelled in the Finite Element Method software Abaqus. The modelling of wind load is performed in both Python and Matlab programming languages. The commonly used damping identification techniques and the Energy Flux Analysis are executed using the programming language Python.

Experimental research

In order to investigate the prerequisites and sensitivities of in situ application of the Energy Flux Analysis, it is advantageous to use in situ measurements. Measurements of both structure motion and wind pressures are acquired from the New Orleans tower. The measurement set-up has been designed and installed by TNO, a Dutch organisation for applied scientific research. The measurements are processed for application of the Energy Flux Analysis. The measurement campaign on the New Orleans tower is continuously measuring, which allows for investigation of the repeatability of the Energy Flux Analysis.

1.2.3. Scope

It is not possible to address all simplifications and assumptions in the Energy Flux Analysis within the time frame of a master thesis. This section provides an overview of the assumptions of the research presented in this report. Investigation of these assumptions is outside the scope of this thesis.

- An Euler-Bernoulli beam with rigid floors is assumed to model the high-rise structure. Naturally, the translation of the structure to a beam model is a major simplification. However, for tall structures with dominant bending deformation the Euler-Bernoulli beam is thought to be most suitable.
- The building mass and stiffness are assumed to be continuous over the structure height. For the structure considered in this thesis, this is thought to be a valid assumption. However, the influence of any discontinuities is not investigated.
- The foundation stiffness is assumed to be the same in two orthogonal directions. This is thought to be an important assumption in this thesis, because soil properties are highly uncertain and an-isotropic.
- The deformations due to wind load are assumed to be in the elastic range. This assumption is justified as the wind load under consideration in this thesis is much smaller than the ULS wind load used in the design of the structure.
- For the translation of dissipated energy to damping ratios, viscous damping is assumed. This damping model is mathematically most convenient and commonly used in engineering. The combined effect of many damping mechanisms present in the structure is said to resemble viscous damping (Tamura, 2013).
- Aerodynamic damping will be neglected in this research. This assumption was based on the findings by Gómez (Gómez, 2019).
- It is assumed that the wind load will only cause structure motion in lateral and rotational directions. Axial deformation and torsion will not be considered, as they are thought to be marginal compared to the lateral and rotational directions for the structure under consideration.
- The perception of structural motion is outside the scope of this research, it is assumed that accelerations are a good measure for human perception.

1.3. Outline

Figure 1.5 presents the outline of this thesis. The coloured dots show the relation between the introductory chapters and the main chapters in parts 2, 3, and 4.

I Introduction	Chapter 1 **Introduction**	Chapter 2 **Modelling wind**	Chapter 3 **High-rise dynamic response**	Chapter 4 **Damping**	Chapter 5 **Energy Flux Analysis**
II Case: New Orleans tower			Chapter 6 **Case: New Orleans tower**	Chapter 7 **Measurement Analysis**	Chapter 8 **EFA model**
III Sensitivity		Chapter 9 **Structure motion**	Chapter 10 **Wind load**	Chapter 11 **Data acquisition**	Chapter 12 **Structural properties**
IV Comparison techniques			Chapter 13 **Half-power Bandwidth method**	Chapter 14 **Random Decrement technique**	Chapter 15 **Comparison**
V Conclusions and recommendations				Chapter 16 **Conclusions**	Chapter 17 **Recomm-endations**

Figure 1.5: Thesis outline

2

Modelling wind

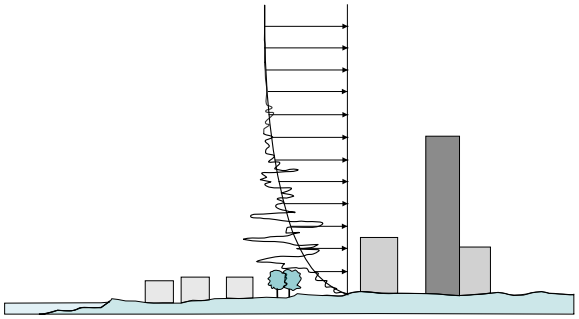

Figure 2.1: Mean wind profile and wind fluctuations

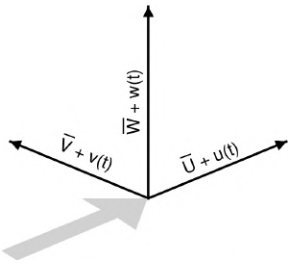

Figure 2.2: Mean wind direction and its components

This chapter will focus on the characteristics of wind, both of upstream wind approaching the structure and the interaction of wind with the structure. This interactions leads, as is described by the aerodynamic admittance, to pressures on the structure's facade resulting in a global wind load on the structure. Chapter 3 will focus on the translation from this wind load on the structure to the structural response.

2.1. Wind velocity

In its simplest form the approaching flow of air is smooth. This means that there is little turbulence present in the approaching air flow and the wind flow is characterised by a mean wind velocity, which does not vary rapidly in time. However, in reality the wind flow is neither uniformly distributed in time nor space. The magnitude of the mean wind velocity generally increases with height, whereas fluctuations in the wind velocity are usually larger for smaller height. The latter is often referred to as turbulence intensity and is due to friction with the Earth's surface and interaction with obstacles in the wind flow such as trees or structures, as is shown in fig. 2.1. Because of the non-uniformity of wind velocity in time, a mean wind velocity usually given as the 10 minute mean value of the wind velocity, and the fluctuations of the wind velocity around this mean value are expressed through its standard deviation. This description applies to all wind components in three orthogonal directions: the longitudinal wind velocity, $\bar{U} + u(t)$, the lateral wind velocity, $\bar{V} + v(t)$, and a vertical component, $\bar{W} + w(t)$. The horizontal component is the most important for wind loading on high-rise structures. In fig. 2.2 the mean wind direction is shown with the grey arrow; the black arrows indicate the wind components.

$$\sigma_u = \sqrt{\frac{1}{T}\int_0^T \left(U(t) - \bar{U}\right)^2 \, \mathrm{d}t} \tag{2.1}$$

In the expression of the standard deviation in eq. (2.1), $U(t)$ is the total velocity component in the direction under investigation and $\bar{U}$ is the mean wind velocity component. The mean and fluctuating part of the wind velocity will be discussed in § 2.1.1 and § 2.1.2 separately.

2.1.1. Mean wind velocity

The mean wind velocity is described over the building height using a vertical mean wind profile. This mean wind profile is not the same for any location; it is dependent on the upstream terrain characteristics. These characteristics are usually described through the roughness length z_0. There are several methods available to find this roughness length (Counehan, 1971, Lettau, 1969, Macdonald et al., 1998). Some simplified values are available based on terrain categories, which specify the presence of vegetation, buildings or other obstacles (Holmes, 2001). Another important factor is the so called 'zero-plane displacement', z_h. In urban areas and forests it may be taken as $\frac{3}{4}$ of the general surrounding obstacle height, for other areas is 0 (Holmes, 2001).

Several descriptions for the mean wind profile exist, of which the logarithmic wind profile and the power law profile are most commonly used. The logarithmic profile is shown in fig. 2.1, where the fluctuating wind velocity moves around this mean wind profile.

Logarithmic profile

Equation (2.2) provides the description of the logarithmic mean wind profile, which is also used in the Eurocode.

$$\bar{U}(z) = \frac{u_*}{\kappa} \ln\left(\frac{z - z_h}{z_0}\right) \tag{2.2}$$

In this expression $\bar{U}(z)$ is the mean wind speed dependent on the height z. The nonphysical friction velocity, u_*, is dependent on the surface shear stress and the air density. It can be found using eq. (2.2) when the mean wind velocity is known at one specified height. Experiments shows that for the Von Kárman's constant, κ, a value of 0.4 may be used (Holmes, 2001).

Power law profile

Although the logarithmic profile is based on theory, due to the fact that it may arise some mathematical difficulties, the power law wind profile has been developed (Panofsky and Dutton, 1984). It is easier to apply and most useful when one is interested in calculating bending moments at the base of a structure.

$$\bar{U}(z) = \bar{U}(z_A)\left(\frac{z}{z_A}\right)^{\alpha} \tag{2.3}$$

In this profile, expressed using eq. (2.3), the mean wind speed is related to a reference wind speed $\bar{U}(z_A)$ at reference height z_A. The exponent α depends on the roughness length and can be found by matching the power law profile with the logarithmic profile at a reference height.

Some more advanced vertical wind profiles were developed by Deaves and Harris (Harris and Deaves, 1981) and Gryning (Gryning et al., 2012). The logarithmic wind profile is based on interaction of the wind flow with the surface. This is valid up to a height of approximately 80 m, after which the wind speed increases more rapidly than the logarithmic profile predicts (Kent et al., 2018). The Gryning profile (Gryning et al., 2012) subdivides the atmospheric boundary layer into three different parts. Additionally, the friction velocity, u_*, is assumed to decrease linearly with height instead of being constant as assumed in the logarithmic profile. The Deaves and Harris 'equilibrium model' (Harris and Deaves, 1981) is based on the assumption of a uniform upstream terrain, similarly to the logarithmic profile, while the Deaves and Harris the 'non-equilibrium model' (Harris and Deaves, 1981) includes the option of upwind terrain variability. Both models are designed for strong wind conditions and wind speeds of over 10 m/s measured at a height of 10 m.

Kent (Kent et al., 2018) has investigated the difference between aforementioned wind profiles using surface observations in a city centre during strong winds. It was concluded that in general the Gryning profile and the 'equilibrium model' of Deaves and Harris show most similarities with the observations. The 'non-equilibrium model' of Deaves and Harris is more accurate than the logarithmic and power law profiles. However, in case of more homogeneous fetch and a gradual reduction of upwind roughness, the logarithmic and power law profiles turned out to be most suitable (Kent et al., 2018).

2.1.2. Fluctuating wind velocity

On top of the mean wind velocity, fluctuations of the wind velocity in time occur. The magnitude of these fluctuations may be expressed through the turbulence intensity, which decreases with height. For a smaller height the mean wind velocity might be lower, the relative magnitude of the fluctuations around this mean value are larger compared to other heights. The turbulence intensity is a function of the standard deviation of the wind velocity and the mean wind velocity only:

$$I(z) = \frac{\sigma_u(z)}{\bar{U}(z)} \tag{2.4}$$

It is alternatively described using the roughness length of the upwind terrain for each point along the height z (Simiu and Scanlan, 1996):

$$I(z) = \frac{1}{\ln\left(\frac{z}{z_0}\right)} \tag{2.5}$$

The variations of the turbulence components are of random nature and it will never exactly repeat in time. Therefore, these components cannot be predicted and are commonly described using statistical methods. Measurements have shown that wind velocity components in the atmospheric boundary layer Normal or Gaussian distribution (Holmes, 2001).

When the mean value and the standard deviation are known, the magnitude of the fluctuating wind velocity and its probability of occurring may be obtained. However, this does not predict the rate at which this wind velocity magnitude varies in time. With the so called the spectral density function, $S_{uu}(n)$, it is possible to see how the magnitude of the turbulence relates to the frequency. The variance, the square of the standard deviation, can be found by integrating over the spectral density function.

$$\sigma_u^2 = \int_0^\infty S_{uu}(f)\,\mathrm{d}f \tag{2.6}$$

Many forms of the spectral density function have been derived empirically. The spectrum developed by Simiu and Scanlan (Simiu and Scanlan, 1996) is written as:

$$\frac{fS_{uu}(f)}{u_*^2} = \frac{200x_s}{(1+50x_s)^{5/3}} \tag{2.7}$$

In this case the frequency is indicated by f and x_s is the Monin coordinate, found using $x_s = fz/\bar{U}(z)$. A slightly different spectrum is derived by Kaimal (Kaimal and Finnigan, 1994, Kaimal et al., 1972) and by Högström (Högström et al., 1982). These wind spectra all have a shape shown in fig. 3.1 with maximum values below 1 Hz.

Through these spectra it is possible to obtain knowledge on the magnitude of the wind velocity, its fluctuations and its distribution over different frequencies, thus the way it varies in time. However, as previously mentioned, wind fluctuations do not only vary in time but also in space. The intensity over the height is described by the turbulence intensity and is accounted for in the spectra.

However, when the wind velocity is known at z_1, previous relations do not provide information about the fluctuations at a different height z_2 in time. There exists a relation between the fluctuations at two points, which is given by the coherence. The coherence is an exponential function:

$$coh_{u1u2}(f) = e^{-F} \tag{2.8}$$

Equation (2.8) by Davenport (Davenport, 1961) is widely accepted. It is a function of the distance between the two points, the mean wind velocity of these two points and the frequency:

$$F = f\frac{\sqrt{((z_1-z_2)c_z)^2 + ((y_1-y_2)c_y)^2}}{\frac{1}{2}\left(\bar{U}(z_1)+\bar{U}(z_2)\right)} \tag{2.9}$$

The factors c_z and c_y are commonly called exponential decay factors and are derived experimentally. In this case z refers to the vertical distance and y refers to the horizontal distance. Solari (Solari, 1987) gives a wide range of possible values for c_z and c_y, but Simiu (Simiu and Scanlan, 1996) suggests $c_z = 10$ and $c_y = 16$.

2.2. Wind pressure

Once the wind velocity is known, it is of interest to translate it to wind pressure. Aerodynamics refers to the study of moving air and the interaction of it with bodies present in this flow of air. As explained in previous section, the approaching flow of air is hardly ever smooth. However, not only upstream wind conditions described in § 2.1 lead to fluctuations in wind. The body present in the wind flow can influence it, which may also lead to a change of wind characteristics. Figure 2.3 visualised that this effect is limited for a streamlined body, but structures are usually bluff bodies.

Figure 2.3 shows that instead of a thin boundary layer, a larger separation layer is formed around bluff bodies depending on its shape. The flow of air in this shear layer is highly unstable, layers of air will roll up

and move towards the wake of the body. These rotating air layers are called vortices and are visible around the bluff body in fig. 2.3. The formation of these vortices alternates between sides, leading to varying positive and negative pressures at the sides of the body. This is commonly referred to as vortex shedding. It is an harmonic motion and in rare cases the frequency of this alternation coincides with the natural frequency of the building, referred to as lock-in. In case of a long body, with a large dimension in the wind direction, these shear layers might reattach to the surface of the sides of the body leading to a limited effect. However, for some bodies these vortices significantly contribute to the wind load at the sides of body. They also influence the pressure at leeward side. Generally, negative pressures are observed here and the pressures are usually of a magnitude lower than the fluctuations at the sides of the body (Holmes, 2001). The pressures at windward side are dependent on the upstream wind, pressures are positive and smaller fluctuations occur.

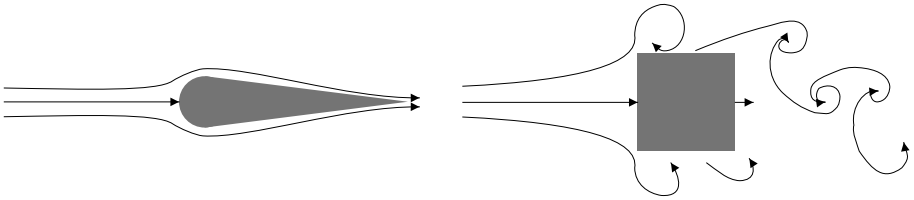

Figure 2.3: Aerodynamics of a streamlined body (left) and a bluff body with vortices (right)

As opposed to the fluctuations of wind velocity and windward pressure fluctuations, the pressure fluctuations at the sides of the body are not well fitted by the Gaussian or Normal distribution (Holmes, 2001). The measured statistical properties of pressure in a certain period of time can vary from the measured properties in the next period of time. Therefore, it is not possible to predict these cross wind pressures using standard deviations and mean values (Holmes, 2001).

Interference of wind with buildings of similar size in the surroundings will have an influence on the wind pressures. For velocities representative of design conditions and for a suburban upwind terrain, a square cross-section building may be affected by a similar upwind building with an aspect (height/width) ratio of 6. It may produce an increase of the peak along wind response of 30% and an increase of the peak cross wind response of 70% (Holmes, 2001). This is maximal when the upwind building is two to three building widths to the side of a straight line taken from the upstream building, and about nine buildings widths upstream from the building under consideration. A downwind building can also increase the cross wind loads on a structure if it is located in a critical position. For a building with an aspect ratio of 4, this critical position would be 1 building width to the side and 2 building widths downwind (Holmes, 2001). A detailed overview of interference effects is given in the work of Kwok (Kwok, 1995) and Khanduri (Khanduri et al., 1998).

The pressure on a body as a result of a smooth approaching flow may be described by Bernoulli's equation (as cited in Holmes, 2001):

$$p - p_0 = \frac{1}{2}\rho_a(U_0^2 - U^2) \tag{2.10}$$

This equation is not valid in the separated regions at the sides of a body, in cross wind direction or in case of unsteady approaching wind. However, using this equation, reasonably good predictions can be made of the pressure coefficients when the wind velocity U is taken just outside the shear layer around the body (Holmes, 2001).

Similar to wind velocity, wind pressure can be described by a mean and a fluctuating part. Mean pressure coefficients and fluctuating pressure coefficients exist to describe the relation between pressure and approaching velocity. As mentioned before, the fluctuations in the wind velocity are not the only reason for fluctuations in the wind pressure. In total there are three main causes for the fluctuations in the pressures or forces:

1. The fluctuations in approaching wind flow. If the dimensions of the body are small compared to the length scales of the wind velocity turbulence, the pressure fluctuations tend to follow the fluctuations in the wind velocity;
2. Unsteady flow generated by the body itself through phenomena such as vortex shedding;
3. Additional fluctuating forces due to movement of the body itself, also called aerodynamic damping. This is only relevant for very flexible, vibration prone aeroelastic bodies (Holmes, 2001). Dutch high-rise buildings investigated by Gómez (Gómez, 2019) indicated that aerodynamic damping was of minor importance compared to structural and soil damping.

In § 2.2.1, only pressure fluctuations as a result of the first point will be considered. After this, in § 2.2.2, the second point will be included.

2.2.1. Quasi-steady pressure fluctuations

Neglecting the second and third point discussed in previous section, the pressure fluctuations are assumed to follow the fluctuations in wind velocity. The pressure at any time of interest can then be described by:

$$p(t) = \frac{1}{2}\rho_a C_{po}\left(\bar{U} + u'(t)\right)^2 \tag{2.11}$$

In case of small turbulence intensities, the mean value for the pressure can simply be described by the mean value of the wind velocity. The quasi-steady pressure coefficient C_{po} is then approximately equal to the mean pressure coefficient C_{pm}:

$$\bar{p} \approx \frac{1}{2}\rho_a C_{po}\bar{U}^2 \approx \frac{1}{2}\rho_a C_{pm}\bar{U}^2 \tag{2.12}$$

Subtracting the mean value in eq. (2.12) from eq. (2.11), the fluctuating wind pressure is obtained:

$$p'(t) = C_{po}\frac{1}{2}\rho_a\left(2\bar{U}u'(t) + u'(t)^2\right) \tag{2.13}$$

In case of low turbulence intensities $u'(t)^2$ may be neglected. A fluctuating pressure coefficient may be found using the following expression:

$$C_{p'} = \frac{\overline{p'}}{\frac{1}{2}\rho_a\bar{U}^2} \tag{2.14}$$

Square cross-sections have larger pressure fluctuations in cross wind direction due to the vortices than rectangular sections. The risk of vortex shedding is larger for slender structures with a distance of no more than approximately 10-15 times the width of these structures (Dyrbye and Hansen, 1997).

2.2.2. Body-induced pressure fluctuations

Separating shear layers and vortex shedding occurs whether or not the upwind flow is turbulent. The pressure as a result of these phenomena can be distinguished from those generated by the wind flow. Vortex shedding appears on bodies of all shapes, alternating the side of the body and leaving behind a decaying row of vortices, also known as the Kárman vortex street (Holmes, 2001). Vibration of the body may enhance the vortex strength, and the frequency of vortex shedding can change to the building natural frequency, referred to as lock-in. Depending on the body shape, the frequency of vortex shedding, f_{vs}, is proportional to the approaching flow velocity, and inversely proportional to the width of the body. It is expressed in non-dimensional form, called the Strouhal number:

$$St = \frac{f_{vs}b}{\bar{U}} \tag{2.15}$$

If the body shape is circular, the Strouhal number also depends on the Reynolds number. As long as the wind velocity frequency is not close to the region that produces lock-in and the wind loading does not lead to large response amplitude, wind pressure can be assumed to be independent of building motion (Chen and Kareem, 2005).

2.2.3. Pressure spectra

The windward pressure distribution over the frequencies is derived from the wind velocity spectrum using the aerodynamic admittance, $\chi_{p,u}$. No pressure spectrum for leeward sides or cross wind sides can be derived. The pressure spectrum for windward side is expressed as follows:

$$S_{pp}(f) = \left|\chi_{p,u}(f)\right|^2\left(C_{pm}\rho_a\bar{U}\right)^2 S_{uu}(f) \tag{2.16}$$

The following relation for the aerodynamic admittance is proposed based on wind tunnel measurements (Kawai et al., 1980):

$$\left|\chi(f)_{p,u}\right|^2 = \left|1 + 20\left(\frac{fb}{\bar{U}}\right)^2\right|^{-\alpha} \tag{2.17}$$

The exponent is defined as $\alpha = \frac{2}{3}(1-(2y_{mid}/b)^2)$ in which y_{mid} is the distance between the vertical symmetry line of the structure and the pressure tap, and b is the structure width.

Usually it is the area-averaged pressure that is desired. Adapted expressions for the pressure spectrum and the aerodynamic admittance exist for the area-averaged pressures:

$$S_{pp,A}(f) = \left|\chi_{p,A}(f)\right|^2 \left(C_{p,Am}\rho_a \bar{U}\right)^2 S_{uu}(f) \tag{2.18}$$

An equation for the area-averaged pressure admittance was given by Sharma (Sharma, 1996):

$$\left|\chi_{p,A}(f)\right|^2 = \left(\left(1+80x_s^2\right)\left(1+20\left(\frac{f\sqrt{A}}{\bar{U}}\right)^2\right)\right)^{-\frac{5}{12}} \tag{2.19}$$

The expression was originally used to predict internal pressures in a building, but it may also be useful to determine wind loads concentrated in nodes or line elements (Geurts, 1997).

2.2.4. Coherence pressure fluctuations

Many researchers attempted to describe the coherence, a description of the correlation between two fluctuating pressures along a body in the frequency domain. The coherence between wind velocity fluctuations was described in § 2.1.2. It is often assumed that the lateral and vertical coherence of pressures on the windward and leeward face of a body is the same as the coherence for wind velocity. However, the coherence between pressures is higher (Geurts, 1997). Using the wind velocity coherence would lead to an underestimation of overall loads on a body. Besides, it is often assumed that the coherence between pressures on the windward face and the leeward face is 1. Geurts (Geurts, 1997) demonstrated that this results in an overestimation of the total wind load spectrum. Therefore, descriptions for the coherence of the pressures are defined separately. These are separated in coherence for two pressures at windward side, two pressures at leeward side, and a pressure at windward side and a pressure at leeward side.

Windward side
The coherence for two pressures at windward side is expressed as:

$$\sqrt{coh_{p_w p_w}(f)} = e^{-\left(\frac{Kf\Delta}{\frac{1}{2}(\bar{U}_1+\bar{U}_2)}\right)} \tag{2.20}$$

The separation of the two points both horizontally and vertically is given by Δ. A relation with the coherence found for the wind velocity at two points can be represented by $F = 2Kf/(\frac{1}{2}(\bar{U}_1 + \bar{U}_2)$. Full scale tests and wind tunnel tests have been used to find values for K, but a range of values was found (Geurts, 1997).

Leeward side
Multiple wind tunnel tests resulted in the leeward coherence proposed by Breeze (Breeze, 1992):

$$\sqrt{coh_{p_l p_l}(f)} = e^{-\alpha\left(\frac{f\Delta}{\frac{1}{2}(\bar{U}_1+\bar{U}_2)}\right)^{\beta}} \tag{2.21}$$

The proposed values for α and β respectively are 68 and 1.3. The coherence of the pressures at leeward side were found to be higher than the coherence of the pressures at windward side (Geurts, 1997).

Windward and leeward side
The coherence of the pressures at windward and at leeward side was described by Vellozzi (Vellozzi and Cohen, 1968) through modifying the cross spectra of these pressures:

$$S_{pw1pl2}(f) = S_{p_{w_1}p_{w_2}}(f)N(f) \tag{2.22}$$

The pressure p_{w_2} is found at a point at windward side as a projection of the leeward side pressure of interest p_{l_2}. $N(f)$ is found through:

$$N(f) = \frac{1}{\xi}\frac{1-e^{-2\xi}}{2\xi^2} \tag{2.23}$$

$$\xi = \frac{15.4fD}{\bar{U}^{\frac{2}{3}}H} \tag{2.24}$$

This gives an expression for the coherence of a wind pressure at windward side and a pressure at leeward side:

$$\sqrt{coh_{p_w p_l}(f)} = \sqrt{coh_{p_w p_w}(f)}\frac{\sqrt{S_{p_w p_w}(f)}}{\sqrt{S_{p_l p_l}(f)}}N(f) \tag{2.25}$$

3

High-rise dynamic response

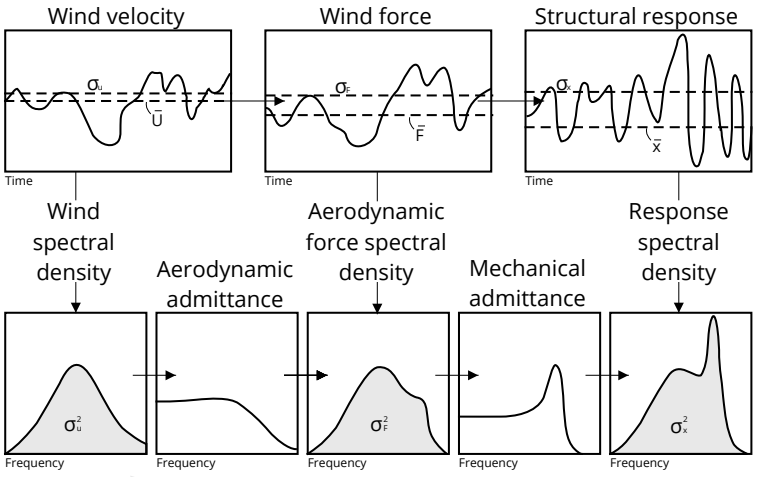

Figure 3.1: Spectral approach. Adapted from Davenport (Davenport, 1961)

In this chapter, the response of high-rise buildings subject to wind loading is discussed. The characteristics of wind and wind loading were discussed in chapter 2. Basic dynamics are assumed to be known, but for further explanation appendix A provides an extensive overview of the basic principles of structural dynamics, which will be referred to often in this thesis. Damping is one of the most relevant features for the dynamic response of high-rise structures, therefore it will be discussed separately in chapter 4.

3.1. Spectral approach

As was shown in chapter 2, it is not possible to describe or predict wind load in time domain and therefore the concept of stationary random processes is used. A stationary random process is a process in which the statistical properties such as standard deviation, correlation and spectral density do not change with time, and as a result it is possible to describe the process using these quantities. This approach is shown in fig. 3.1; the dynamic response of a structure is presented in frequency domain rather than time domain and calculations are often performed in frequency domain. The translation from wind velocity to wind force described by the building dimensions and shape dependent aerodynamic admittance was already discussed in chapter 2. This chapter discusses the translation from wind load to structural response through the mechanical admittance. This mechanical admittance depends on structural properties such as stiffness, mass, natural frequency and damping ratio.

The bottom middle figure in fig. 3.1 shows that the wind force spectrum has a somewhat broad spectrum, while the mechanical admittance shows a large peak for a specific frequency. The frequency at which this resonance response occurs is the natural frequency of the structure. Since wind loads contain mostly frequencies below 1 Hz, this resonance response will generally only occur for structures with a natural frequency

below 1 Hz provided damping is sufficiently low. This is the case for high-rise structures. This resonant response can be distinguished from the background response, a much smaller response of the structure for frequencies other than the natural frequency of the structure.

The dynamic response of a high-rise structure in along wind direction is primarily produced by the turbulent velocity fluctuations in the approaching wind, whereas in the cross wind direction loading and dynamic response are generated by random vortex shedding. The root-mean-square fluctuating deflection of the top of a high-rise building is approximated for the along wind response by Davenport (Davenport, 1966, 1971, as cited in Holmes, 2001) using:

$$\frac{\sigma_x}{H} = A_x \left(\frac{\rho_a}{\rho_b}\right)\left(\frac{\bar{U}_h}{f_n b}\right)^{k_x} \frac{1}{\sqrt{\zeta}} \tag{3.1}$$

and for the cross wind response by:

$$\frac{\sigma_y}{H} = A_y \left(\frac{\rho_a}{\rho_b}\right)\left(\frac{\bar{U}_h}{f_n b}\right)^{k_y} \frac{1}{\sqrt{\zeta}} \tag{3.2}$$

In these formulae A_x and A_y are specific factors for the building shape, ρ_a is the air density, ρ_b is the building mass density, $\bar{U}_h$ is the mean wind speed at the top of the building. The term $\bar{U}_h/(f_n b)$ is known as the reduced velocity. The width of the building is given by b. The natural frequency is given by f_n and ζ is the critical damping ratio in the first mode of vibration. The factors k_x and k_y are exponents. The k_x factor is greater than 2, because the spectral density of the wind velocity near the natural frequency increases with more than a power of 2. The k_y factor for cross wind is generally 3, or even 4. These formulae are based on the assumption that the response is dominated by the resonant response, which is valid for tall buildings with the first natural frequency below 0.5 Hz and a damping ratio of less than 2% (Holmes, 2001). This generally applies to structures of over 20 storeys (Kareem and Gurley, 1996).

When designing for wind-induced motion, it is assumed that the building experiences linear elastic behaviour and non-linear effects are disregarded. However, the resonant response of a structure results in a complex time history effect. The response at a given time does not only depend on the wind velocity or force acting on the structure at that given time, but also on the previous time history of the wind (Holmes, 2001). This makes it impossible to predict the time domain response of wind-induced high-rise buildings.

In short, determining the dynamic response of a high-rise structure is a complex matter. Kareem categorised the important and uncertain parameters for dynamic response in high-rise buildings under three categories (Kareem, 1988):

1. Wind environment and meteorological data: for example the mean wind speed discussed in chapter 2;
2. Parameters related to the random pressure field around the structure. This is an uncertainty related to the aerodynamic admittance to translate the wind spectral density to the wind force spectral density, which was briefly discussed in chapter 2;
3. Structural properties: mass, stiffness, natural frequency and damping. These properties are related to the mechanical admittance to translate the wind force spectrum to the response spectral density and are discussed in this chapter.

The uncertainties in each category can result from uncertainties originating from physical sources, uncertainties of measurements devices, statistical uncertainties caused by a lack of measured data, a lack of knowledge about a process itself, or as a result of simplifications in the model used, whether deliberately or not.

3.2. Natural frequency

In order to describe the dynamic response of a structure, it is important to know the frequencies at which the resonant response will occur. For most buildings, resonance response in the range below 1 Hz can be observed for three natural frequencies; two for lateral motion and one torsional natural frequency. As the modes corresponding to these frequencies account for 90% of the overall dynamic behaviour of buildings under wind-excitation, it is thought to be reasonable to neglect any higher modes (Ellis, 1980).

There are multiple approaches of determining the natural frequency of a system. The most simple way is through the single degree of freedom relation between mass and stiffness:

$$\omega_n = \sqrt{\frac{k}{m}} \tag{3.3}$$

In this equation k is the spring stiffness and m is the mass. In order to apply this to a high-rise building, the equivalent mass and equivalent spring stiffness have to be found, as is explained in appendix A. A better approach for high-rise structures is to model the high-rise building as an Euler-Bernoulli beam, either free-fixed or free-flexible. The roots of the characteristic equations in appendix A then have to be used to find the natural frequencies of the system. In a later stage of the design, the natural frequencies of a structure are obtained from the FEM model used for the structural design. In case of a finalised structure, it is possible to quite accurately determine the natural frequency from the response measurements.

However, discrepancies are usually found between the estimated natural frequency from the FEM models and the measurements (Kim and Kim, 2014). The measured natural frequencies are usually significantly larger (Kwok et al., 2011) and errors of up to 50% are not uncommon (Ellis et al., 1980). From the simple formula in eq. (3.3) it is clear that the natural frequency depends on mass and stiffness. The estimation of both building mass and stiffness is uncertain. As the building mass is thought to be relatively more straightforward to compute than the building stiffness, errors found in the natural frequency are mostly expected to be a result of erroneous predictions or description of the stiffness of the building. Interestingly, the natural frequency is usually better estimated by the empirical approximation by Tamura (Tamura, 2013) which only depends on building height H:

$$f_{n,l_1} = \frac{67}{H} \tag{3.4}$$

Jeary and Ellis (Ellis, 1980) provide empirical formulae for both lateral modes and the torsional mode:

$$f_{n,l_1} = \frac{46}{H},\ f_{n,l_2} = \frac{58}{H},\ f_{n,t} = \frac{72}{H} \tag{3.5}$$

It is good to mention that the natural frequency reduces with amplitude of vibration, which is most likely due to a decreasing stiffness for larger amplitudes. Amplitude dependence of both natural frequency and damping is discussed in more detail in chapter 4.

3.3. Structural properties

Structural properties such as mass and stiffness affect the dynamic characteristics and response of a structure. As previously explained, these properties also determine the natural frequency of a structure. Looking at a simple mass-spring system excited by a sinusoidal force with a frequency below the natural frequency of the system, the response is determined by the stiffness of the structure. On the other hand, if the excitation force has a frequency above the natural frequency of the structure, the response is determined by its mass (Ungar, 1973). This means that low frequency response, below the natural frequency of the system, depends on the potential energy storage characteristics of the system, while high frequency response depends on the kinetic energy storage properties of a structure (Ungar, 1973). It is therefore expected that the building mass is of dominant importance for the dynamic building response, while both mass and stiffness determine the magnitude of the natural frequency.

Many studies have focused on the uncertainties associated with wind loading, assuming the system to have deterministic structural properties or assuming the uncertainty in these properties is much smaller (Kareem, 1988). Fewer studies focused on the uncertainty in structural properties. However, discrepancies between estimated and measured natural frequency show that also the structural properties are uncertain. This section will briefly discuss relevant considerations, which undoubtedly affect the structural properties.

Material properties

Mass and stiffness properties are directly linked to the properties of the materials used. The most important material property for building mass is the material mass density, while the most important property for building stiffness is the elastic modulus. Different values are available for the elastic modulus, depending on considering the Ultimate Limit State (ULS) or the Serviceability Limit State (SLS). Which value best represents the true building stiffness depends on whether, for instance, the concrete is cracked or not. It may occur that a certain level of cracking is expected in the service life of the building, but that this cracking has not occurred yet. This would result in assuming a lower stiffness than the true stiffness. Besides, uncertainties in spatial random variation in the material leads to uncertainties in the material properties. A study on several high-rise buildings mentions that the in situ elastic modulus was found to be around 10% larger than the design value, because the compressive strength is generally underestimated (Kim and Kim, 2014). This in turn resulted in an increase in the assumed natural frequency of 7-12% for the buildings under consideration.

Structure configuration
The configuration of structural elements and the connection between these elements is of major importance for the stiffness property. One study demonstrated the importance of considering the floor system for the building stiffness (Erwin et al., 2007). Although this does not hold for systems made of tall slender shear walls (Erwin et al., 2007). Besides, an increase of 1-6% of the natural frequency was found as a result of the use of beam-end offset (Kim and Kim, 2014). An extensive study of the development of structural properties through the construction of a tall building may be found in (Tamura et al., 2002). Besides configuration, the fabrication of structural elements and their connections is of importance. Another source of uncertainty is the fact that the structural configuration is assumed to be constant over the building height, while in reality this is rarely ever the case. A lack of knowledge in the idealisation of the system may lead to additional uncertainties.

Non-structural elements
Even if the structural engineer has accurate knowledge of all structural information, still the engineer would not be able to assess the influence of non-structural elements, such as partition walls and cladding, on the behaviour of the structure. These elements are conservatively taken into account in the design loads, they are not for the building stiffness. However, they are found to contribute (Ellis and Bougard, 2001, Ellis et al., 1980). In one study, the natural frequencies increased with 5-12% due to non-structural elements, while for one building this was even 26% (Kim and Kim, 2014).

Soil conditions
Many foreign buildings are constructed on rock soils which may be modelled using a very large stiffness. However, when the structure is constructed on any other soil than rock, the foundation type and soil properties do affect the structure's dynamic response. Most relevant for the response of high-rise structures to wind load is the horizontal motion and rocking motion of the foundation, each may be modelled using a separate foundation stiffness. In case of a shallow foundation, the foundation can be evaluated using a viscoelastic semi-finite medium (Novak and El Hifnawy, 1988). This model describes soil properties with known constants such as shear modulus, material damping ratio and Poisson's ratio, which should be obtained from separate experiments (Novak and El Hifnawy, 1983). In case of pile groups with piles that are far apart, group stiffness can be found as a sum of the contribution of all individual piles with their relative constants (Novak, 1974b). In case of closely spaced piles, so called pile-soil-pile interaction occurs which affects the stiffness constants of the pile group. Based on full-scale measurements, Japanese researchers found that the rocking motion of a high-rise building becomes dominant over the bending or lateral motion as the stiffness of the structure increases relative to the soil stiffness (Ishizaki and Hatakeyama, 1960).

Soil properties are highly uncertain. They may be experimentally obtained at limited locations, there is large spatial variability of soil properties (Baker and Calle, 2006). Besides, soil investigation methods may have its own inaccuracy and the investigation results may be erroneously interpreted (Baker and Calle, 2006). Even when the soil properties are known, it is difficult to describe the interaction of the soil with the structure and to translate this to the model quantities such as stiffness and damping.

3.4. Mode coupling

The modes of vibration may be coupled either aerodynamically or structurally. Aerodynamic coupling refers to the cross-correlation between different wind components, which is larger in case of, for instance, lock-in. High-rise buildings or long-span bridges may also be structurally coupled. For high-rise buildings, this occurs in case of complex geometrical shapes for which the centre of mass and centre of resistance are not coinciding. For structures with closely spaced modes even the slightest asymmetry in structural system (structural coupling), or a slight cross-correlation in the wind components (aerodynamic coupling) can already cause mode coupling to occur (Kareem and Chen, 2005). Modal properties can no longer be obtained through modal identification techniques assuming a single degree of freedom system, and the structural response cannot be considered separately.

To demonstrate the effect of structural mode coupling, the Wilberforce pendulum offers a simple example. It consists of a mass hanging from a flexible spring that can rotate and move vertically. When the mass is lifted and starts vibrating vertically, it slowly transfers its energy to the rotational mode. Provided the system is installed such that the frequencies for both modes are the same, the pendulum will alternate between motion in the vertical mode and in the torsional mode (Berg and Marshall, 1991). When plotting the response for both modes, it is clearly visible that the response in one mode will nearly cease to exists when the other mode is experiencing large vibrations and vice versa. This phenomenon is often referred to as beating.

Kareem (Kareem and Chen, 2005) investigated a building with a square cross-section that may experience slight mode coupling due to non-coinciding mass and resistance centre at the upper floors and closely spaced modes; the ratio of the first two natural frequencies is 1.023. Modal correlation coefficients were used to quantify mode coupling, and it was found that these varied with wind direction. Only certain wind directions resulted in coupled modes, which could additionally be observed through a large bandwidth of the response spectral peak. These results demonstrated that in this case not the slight structural coupling was responsible for the mode coupling, but rather the aerodynamic coupling.

4

Damping

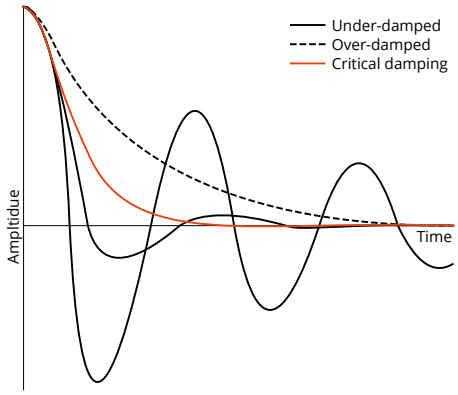

Figure 4.1: Under-damped, over-damped and critically damped response of harmonic vibrating system.

Damping is a very important property for the response of a structure. Think of a pendulum that is put in motion by an initial displacement. Without damping it would continue its motion endlessly, due to damping the motion is restrained and eventually the pendulum will come to a full stop. This also applies to systems with a continuously applied force; the system may not stop vibrating but damping will restrain the magnitude of its motion and thus the spectral peak in fig. 3.1. Figure 4.1 shows the response of three types of systems; an under-damped system, an over-damping system, and a critically damped system. An under-damped system will show harmonic motion around its equilibrium before coming to a full stop. Increasing the amount of damping, the first instance where harmonic motion no longer occurs is called critical damping. Critical damping allows the system to return to its equilibrium position in the least amount of time. When damping is increased even more, it is called an over-damped system. Usually, damping is expressed as a ratio ζ of critical damping and civil engineering structures are most often under-damped systems.

Damping is the dissipation of energy from a system, it is a result of many different mechanisms that contribute to the total damping of a system. Many researchers tried modelling damping, the first of which was Poisson, who investigated friction of a compressible fluid in 1831 (Poisson, 1831, as cited in Prandina, 2010). Later, Stokes writes the equation of motion for a pendulum considering damping due to internal friction in fluids (Stokes, 1951). The linear viscous damping model, which is often used today, was developed by Lord Rayleigh in 1978. Rayleigh also grouped the coefficients of a quadratic energy dissipation function into a symmetric matrix called the damping matrix (Baron Rayleigh Strutt, 1896). Rayleigh developed proportional damping, in which the damping matrix is proportional to the mass and stiffness of a system. Whether a damping model is suitable for a certain application depends on its dominant damping mechanism and how this mechanism can be described. Therefore, this chapter starts with a brief description of damping mechanisms occurring in a high-rise structure. After this, it will discuss the influence of damping on structural response, and the influence of structural characteristics on damping. After this, damping prediction and damping identification techniques are discussed, to conclude with a brief overview of damping models.

4.1. Damping mechanisms

It is not possible to distinguish and evaluate all damping sources in a structure separately, but it is possible for them to be classified into categories. In structures, one or two damping mechanisms usually dominate such that the other damping mechanisms are neglected (Ungar, 1973). This is beneficial, since modelling all damping mechanisms would make a damping model too complex and too computationally expensive (Prandina, 2010). Two main categories are distinguished: material and non-material damping (Prandina, 2010). These categories in turn consist of many subcategories, of which the relevant subcategories for building structures are discussed in this section and visualised in fig. 4.2.

	Material damping			Non-material damping		
	S	L	G	S-S	S-L	S-G
Friction	Internal friction damping			External friction damping		
Viscosity		Internal viscous damping			External viscous damping	
Radiation				Radiation damping		
Interaction					Hydrodynamic damping	Aerodynamic damping
Plasticity	Hysteretic damping					

Figure 4.2: Damping mechanisms relevant for buildings (S = Solid, L = Liquid, G = Gas). Adapted from Tamura (Tamura, 2008)

4.1.1. Material damping

Material damping is commonly called internal damping or hysteresis damping, although this refers to one of its mechanisms. Material damping occurs due to deformation. Internal friction damping refers to the dissipation of energy due to internal friction of solid materials. Relative displacements occur between molecules and slip of micro-cracks. Even tough the relative displacements are elastic, energy loss does occur. This energy loss is different from energy loss due to plastic hysteresis, in which case the microscopic structure of the material changes. The energy dissipation due to plastic hysteresis damping, or hysteretic damping, is significantly larger (Tamura, 2008). Another material damping mechanism is internal viscous damping, which in turn can be subdivided into molecular viscosity and turbulence viscosity. Molecular viscosity relates to the collision of molecules due to which kinetic energy is converted into thermal energy. Turbulence viscosity involves fluctuating velocity of the components of fluids, which creates a mixture and diffusion of kinetic energy (Tamura, 2008). In this thesis, damping will not be considered on this detailed level, but it does indicate the complexity of damping. What is usually investigated through experiments is the contribution of these material damping mechanisms combined by measuring dissipated energy per unit volume per cycle of motion for material samples (Prandina, 2010). The amount of material damping depends on the type of material, methods of manufacturing and finishing processes. In structures, material damping occurs to some extent in any structural material that is under dynamic loading, including the soil.

4.1.2. Non-material damping

Where material damping involved the damping mechanisms at micro interface level of a material, non-material damping involves damping occurring at the interface of separated and recognisable parts of a structure or an interface of the structure with the surroundings of the structure.

External friction damping

External friction damping occurs mainly due to sliding of two interfaces and the friction that occurs to prevent relative motion of these two solid interfaces. The friction happens due to attachment of molecules to the contact surface, and kinetic energy is converted to thermal energy. This external friction damping in buildings occurs mainly in the joints between different structural elements, but also between the interface of structural and non-structural elements such as partition walls, the facade or architectural cladding. The amount of damping in joints depends on, for instance, the use of welds or bolts.

Radiation damping
Radiation damping is the energy transfer between two solids or between a solid and a fluid. The energy radiates to the solid or fluid outside the body due to energy excited by the body onto this solid or fluid. Radiation damping occurs, for instance, due to wave generation of a floating structure. More specifically for building structures it occurs due to soil-structure interaction.

External viscous damping
External viscous damping refers to the dissipation of energy due to viscosity of liquid or a solid in contact with the body. For structures, external viscous damping would be exerted by water surrounding the structure. This external viscous damping is a function of the relative velocity of the body and the liquid or gas surrounding it.

Aerodynamic damping
Aerodynamic damping is a function of the relative velocity of the body and the air surrounding it. Usually, aerodynamic damping is quite small compared to material and joint damping in a structure (Kareem and Gurley, 1996), this is in agreement with the findings of Gómez (Gómez, 2019). For some rare cases the aerodynamic damping can be negative. These are special cases that should be considered with care, as it has led to collapse of structures in the past. The Tacoma Narrows Bridge is the most famous example (Billah and Scanlan, 1991).

Additional damping devices
As of today, damping cannot be estimated accurately in the design stage. Therefore, if damping is expected to be critical additional damping devices can be applied. Although this is quite commonly used in earthquake engineering, it is not as commonly used for wind engineering (Tamura, 1998). The tuned mass damper uses the inertia effect of the additional mass to absorb energy of the building and is visualised in fig. 4.3. Active damping devices are based on the idea of exerting an opposing force to the vibrating structure. Additional damping devices are mainly used for service level applications (Smith and Willford, 2008). This is because the device can become de-tuned or it may fail. Failure of an additional damping device is not unsafe when it is used for service applications, but it is when it is used for safety. In case it is used for safety, it has to be designed with high redundancy.

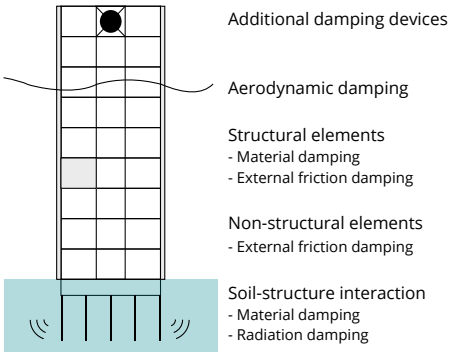

Figure 4.3: Damping mechanisms occuring in a building

4.2. Damping in high-rise structures

Damping affects the response of a high-rise structure in two ways. First, it changes the natural frequency of the system. This is further explained in appendix A, but can be neglected for structures with a damping ratio below 20% (Chopra, 2007), as is the case for high-rise structures. The second way damping influences the response is by limiting the magnitude of the response, a reduction of the magnitude of the spectral density in fig. 3.1. Mainly this resonant response depends strongly on the energy dissipation characteristics. It was found that for the design of structures under wind load, of all parameters that can be adjusted, increasing the damping is the only one that has consistently proven to reduce accelerations (Ellis, 1980).

Chapter 3 discussed that finding the stiffness of a building is not straightforward, but finding the damping of a building is far more elusive. Discrepancies found for the building stiffness are not due to a lack of correlation of this property to geometric and material properties but rather due to uncertain information about the

in situ material characteristics or about the most appropriate means to model specific elements of the lateral system. Damping, on the contrary, is hard to estimate precisely due to its lack of correlation to geometric and material properties which makes it a complex phenomenon. The complexity of damping has been shown in previous section by discussing all mechanisms that contribute to damping. Due to the lack of understanding of the damping in the design phase it happens that the acceleration levels measured in structures are larger than anticipated (Gómez and Metrikine, 2019, Kijewski-Correa and Pirnia, 2007).

Structural system and joint friction

While it is acknowledged that damping does depend on the structural material, guidelines have given little attention to the structural system, while there is evidence this also significantly defines the amount of damping occurring in a structure (Kijewski-Correa and Pirnia, 2007). For instance, it was found that the more efficient a system becomes for lateral loading, the less energy it dissipates (Pirnia, 2009). Also, it is likely that monolithic concrete structures or steel welded structures experience less damping in the joints than bolted connections (Smith and Willford, 2008). Other studies found a similar conclusion; buildings that are characterised by frame action have larger damping values than clamped buildings, since rigid connections do not allow for the external friction damping mechanism (Erwin et al., 2007, Kijewski-Correa and Pirnia, 2007, Kijewski-Correa et al., 2006). Through experiments (Beards, 1983) showed that damping in structures due to bolted, welded or riveted connections is often much larger than material damping.

Friction non-structural elements

Not only material type, structural system and friction in structural joints are expected to significantly contribution to the total damping; in addition, friction between structural and non-structural elements contributes to damping. The contribution of these elements to damping will be even larger in case of damage to the non-structural walls. However, usually this damage is not permitted in the allowable stress level design. The increased contribution can therefore not be expected near the elastic limit (Tamura, 2013). Tamura (Tamura, 2013) mentions that for buildings without damping devices, a large part of the energy dissipation is caused by external friction between surface of structural and non-structural elements, and by damping due to soil-structure interaction.

Soil-structure interaction

The contribution to damping due to soil-structure interaction was briefly mentioned in the damping mechanisms. It includes the contribution to damping due to soil material damping and radiation damping. Although much attention has been paid to damping due to soil-structure interaction in earthquake engineering, some studies have focused on this for structures under wind loading. Novak has investigated it and found that for lightly damped structures, having a flexible foundation results in a loss of structural damping (Novak and El Hifnawy, 1988). However, this loss of structural damping is compensated for by soil damping and usually results in an increase in the total damping (Novak, 1974a). Ellis (Ellis, 1986) also investigated the significance of dynamic soil-structure interaction through forced vibration tests on buildings. For one building, Ellis found that the soil-structure interaction accounted for 60% of the dissipated energy (Ellis, 1986). The influence of soil-structure interaction was further studied by Gómez (Gómez, 2019), and the conclusion was drawn that the soil-structure interaction plays an important role for high-rise buildings constructed on soft soils. For these buildings, the building material, which is an important characteristic in current damping predictors, was of inferior importance compared to the soil conditions in case of soft soil (Gómez et al., 2018).

A study of TNO (Bronkhorst et al., 2018) found that increasing the building stiffness increases the foundation damping. Besides, the study found that decreasing the building mass increases the superstructure damping. Two methods to obtain soil characteristics were compared. The first is the cone model (Wolf and Deeks, 2004), which does not account for the influence of piles on the overall damping. This used model focuses on soil radiation damping only, not on soil material damping. The second method, Dynapile, does consider the influence of piles explicitly. The damping obtained through Dynapile resulted in smaller damping results than those obtained using the cone model. The study also found that changing the stiffness of the soil has a large influence on the damping results obtained with the cone model. The conclusion is drawn that the pile plan layout has a small direct influence on the overall damping and can be considered negligible from a design point of view (Bronkhorst et al., 2018).

4.3. Damping prediction

Currently, no theoretical method exists to predict damping. The methods that are available are based on studies that have investigated damping behaviour based on measurements, and have empirically written expressions to predict damping. Some of the methods will be briefly discussed here in order to get an understanding of the behaviour and dependency of damping. The models discussed here are based on the research of Davenport and Hill-Carroll (Davenport and Hill-Carroll, 1986), Jeary and Ellis (Jeary, 1986, Jeary and Ellis, 1979), Tamura (Tamura et al., 1994), Lagomarsino (Lagomarsino, 1993) and Gómez (Gómez, 2019).

Davenport and Hill-Carroll damping predictor
The damping predictor by Davenport and Hill-Carroll (Davenport, 1986, as cited in Bronkhorst et al., 2018) depends on the building material and the amount of storeys of a building; contrary to the other damping predictors it does not depend on frequency.

$$\begin{aligned}
\zeta_{Davenport} &= 3.0\left(\frac{\sigma_x}{H}\right)^{0.075} \text{ (5-20 storeys, steel)} \\
\zeta_{Davenport} &= 3.0\left(\frac{\sigma_x}{H}\right)^{0.110} \text{ (5-20 storeys, concrete)} \\
\zeta_{Davenport} &= 2.0\left(\frac{\sigma_x}{H}\right)^{0.110} \text{ (>20 storeys, steel)} \\
\zeta_{Davenport} &= 2.5\left(\frac{\sigma_x}{H}\right)^{0.110} \text{ (>20 storeys, concrete)}
\end{aligned} \tag{4.1}$$

Jeary damping predictor
Figure 4.4 shows the three regions used by Jeary when describing damping. The first is the low-amplitude plateau (ζ_0), describing damping of vibrations with very low amplitudes. For the low-amplitude region, damping is not dependent on the amplitude of vibration. The second region is called the non-linear region (ζ_1), where non-linearity is caused by the formation and rapid elongation of micro-cracks in the material for larger amplitudes and therefore making damping amplitude dependent (Jeary, 1996). After this follows the high-amplitude plateau where damping is not expected to increase any further as was explained in the previous section. The following formula was found empirically (Jeary, 1998):

$$\zeta_{Jeary} = \zeta_0 + \zeta_1 = 0.01 f_n + 10^{\frac{\sqrt{D}}{2}} \frac{x}{H} \leq \frac{0.6}{H} + 0.013 \tag{4.2}$$

In this equation x represents the horizontal vibration amplitude and D is the dimension of the foundation in the direction of motion.

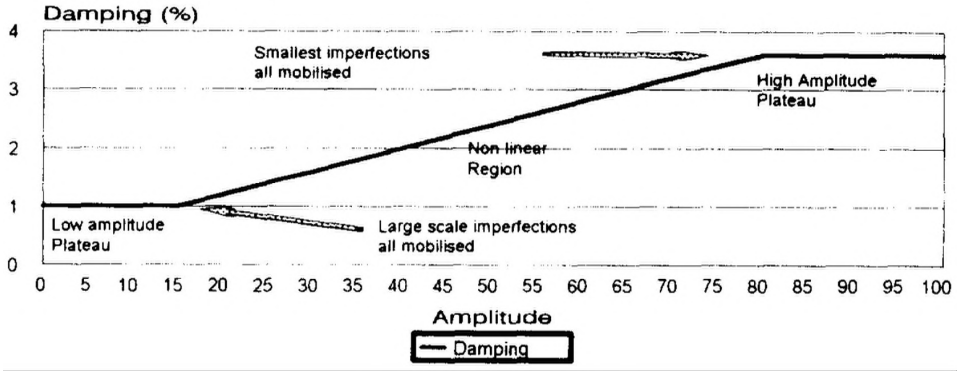

Figure 4.4: Damping as described by Jeary (Jeary, 1996)

The increase of damping with amplitude can be explained by the increasing friction between structural elements, and non-structural elements and the occurrence of hysteretic damping rather than internal friction damping. Besides, a decrease in natural frequency with increasing amplitude is found, which can be accounted for by the decrease in building stiffness due to, for instance, cracks. However, there is an amplitude for which the increasing tendency of damping stops. This amplitude is called the critical tip acceleration

amplitude and this phenomenon is visible in the damping prediction by Jeary in fig. 4.4. After this critical tip acceleration the damping might even decrease (Tamura, 2013). The fact that damping can decrease for an increasing amplitude is due to the increased number of slipping surfaces in the "stick-slip" model (Davenport and Hill-Carroll, 1986). As previously mentioned, natural frequency decreases for increasing amplitude. This decreasing tendency does not stop at the critical tip acceleration for an observed structure and may also be explained by the even further reduced stiffness due to an increasing number of slipping surfaces (Tamura, 2013).

Tamura damping predictor
Tamura provides an empirical damping predictor and distinguishes between reinforced concrete and steel buildings. The predictor is based on data of existing buildings available in the Japanese Damping Database (Tamura, 2013):

$$\begin{aligned} \zeta_{Tamura} &= 0.014 f_n + 470 \frac{x}{H} - 0.0018 \text{ for reinforced concrete buildings} \\ \zeta_{Tamura} &= 0.013 f_n + 400 \frac{x}{H} + 0.0029 \text{ for steel buildings} \end{aligned} \tag{4.3}$$

Lagomarsino damping predictor
The damping predictor of Lagomarsino (Lagomarsino, 1993), like the previous methods, is based on frequency and amplitude, but has a more extensive description of the building parameters which are incorporated in the coefficients.

$$\begin{aligned} \zeta_{Lagomarsino} &= 0.72 f_n + \frac{0.70}{f_n} \text{ for reinforced concrete buildings} \\ \zeta_{Lagomarsino} &= 0.32 f_n + \frac{0.78}{f_n} \text{ for steel buildings} \\ \zeta_{Lagomarsino} &= 0.29 f_n + \frac{1.29}{f_n} \text{ for mixed buildings} \end{aligned} \tag{4.4}$$

Gómez damping predictor
After evaluating the aforementioned damping predictors, Gómez proposed a damping predictor (Gómez, 2019). The predictor is based on the two regimes by Jeary, the natural frequency, building height, vibration amplitude and foundation dimension:

$$\begin{aligned} &\zeta = \zeta_0 + \zeta_I = 0.0035 f_n + \frac{0.0075}{f_n^p} + 10^{\frac{\sqrt{D}}{2}} \frac{x}{H} \\ &p = 1 \text{ for } H \leq 120m \\ &p = 0.8 \text{ for } 120m \leq H \leq 150m \\ &p = 0.3 \text{ for } 150m \leq H \end{aligned} \tag{4.5}$$

The trend of the Davenport and Hill-Carroll, Jeary, Tamura, and Gómez damping models demonstrates a reduction of damping values with increasing building height. Where usually the damping ratio has a value of under 3%, for buildings of over 250 m the damping ratio is rarely larger than 1% (Smith and Willford, 2008).

Eurocode
Although the aim of the Eurocode is not to predict damping, but rather to provide a conservative estimate, it is still discussed in this section to address current design practice. The Eurocode (NEN, 2005) divides damping in structural damping, aerodynamic damping and additional damping measures. The structural damping values are based on measurements of foreign buildings (Bronkhorst et al., 2018), but are purely prescribed based on the construction material used. It prescribes the values in terms of a logarithmic decrement, but for comparison reasons these are translated to a damping ratio (Bronkhorst et al., 2018).

$$\begin{aligned} &\zeta = 0.8\% \text{ for steel buildings} \\ &\zeta = 1.6\% \text{ for concrete buildings} \\ &\zeta = 1.2\% \text{ for mixed concrete and steel buildings} \end{aligned} \tag{4.6}$$

This section demonstrated the simplicity of the current design practice and damping predictors compared to the complexity of damping occurring in high-rise structures discussed in § 4.1 and § 4.2. Due to the lack of theoretical understanding and prediction methods, it is usually not possible to estimate the damping closer than approximately 30% until the building is completed (Kareem and Gurley, 1996). Also Ungar (Ungar, 1973) mentions that damping properties of structures are hard to predict, and that their experimental determination requires complex dynamic measurements. A similar statement is made by Novak (Novak, 1974b), saying that even after completion it is difficult to apply damping identification techniques due to the non-linear character of damping.

Therefore in § 4.4, some commonly used techniques for the identification of damping in structures based on measurements are briefly discussed and chapter 5 describes the newly developed technique. The comparison between this new technique and two of the other techniques will be discussed in chapter 15.

4.4. Damping identification

A large variety of damping identification techniques are available; what these techniques have in common is that they all require measurements. There are two approaches in terms of measurements to identify damping (Ellis, 1996). The first is by using exciters on a structure after which an analysis is done of the subsequent vibration. Alternatively, damping can be identified through measurements of the ambient response, which is most relevant for high-rise structures. The techniques are divided based on their application; in time domain, in frequency domain, or based on energy. The latter does not use ambient vibration, but since the Energy Flux Analysis is also energy-based it is still relevant to discuss.

Time domain

A time domain technique that is very commonly used is the Random Decrement technique. In this technique, a set of segments from the time domain is created based on a certain triggering value as is visualised in chapter 14 in chapter 14. The response of all these segments is then averaged and the resulting signature is called the Random Decrement Signature (RDS). This signature resembles a free decay response as is shown in fig. 4.1, and dynamic properties can be identified from this signature using various approaches. A more thorough explanation of this technique, its assumptions and its prerequisites is given in chapter 14. Other time domain damping identification techniques are summarised by Tamura (Tamura, 2013).

Frequency domain

A frequency domain technique that is very commonly used is the half-power bandwidth method. As described in chapter 3, the relation between the wind force input and the structural response is described through the mechanical admittance. This transfer function, or frequency response function as discussed in appendix A, depends on the dynamic properties of the system such as mass, stiffness, natural frequency and damping. The half-power bandwidth method uses this dependency to identify dynamic parameters when the mechanical admittance function is known. It uses the peak value of the power spectral density, its natural frequency, and the values at half the peak height. In reality, the mechanical admittance function is often not available since the input spectrum is unknown. What is available is the response function, which is a result of this transfer function and the input. Assuming the input is a white-noise spectrum, the response function may be used directly. For a more detailed explanation of this technique, refer to chapter 13. Tamura summarises more frequency domain techniques (Tamura, 2013).

Modal analysis to identify damping for high-rise buildings is not possible due to the fact that extensive information of the structural behaviour is required for this approach. Modal properties of buildings can be studied through modal analysis and when sufficient number of modes are involved in the measurement (Prandina, 2010). However, ambient vibrations only excite lower modes of the building.

Energy based method

The work of Prandina (Prandina, 2010) discusses many damping identification techniques, and more specifically an energy based approach in order to identify the damping but also its location. This section will discuss the findings by Prandina (Prandina, 2010).

The dissipated energy in the system is defined as the energy input minus the energy contribution of the system. In case the input is such that the motion of the system is retained, the dissipated energy per cycle will be the same as the energy input by the external force. This is true, because integration over a cycle of periodic motion or an integer amount of cycles, for a constant periodic excitation, is equal to zero. To achieve this requirement, for which the mass and stiffness matrices can be eliminated, the excitation and the response

should have a common frequency. If the damping is expected to be small and the system is excited by a single harmonic force close to the natural frequency of the system, then the spatial response of the system may be written using the mode shape of the relevant frequency of an undamped structure. This mode shape can be derived from an analytical model, but in that case it is still required to have information on the mass and stiffness.

When applying this energy-based technique, it is very important to wait for the transient response of the system to end upon measuring the system motion. When this transient response is still present, the energy balance equation used is wrong since the response is not periodic and therefore the system energy term will not vanish.

Since the result of the method is dissipated energy, the decision has to be made on how to present this dissipated energy as damping. Although the viscous damping model is most common, various other models are available. However, the error found in the damping estimation from a simulation was much smaller in case viscous damping was modelled than for other forms of damping (Prandina, 2010).

4.5. Modelling damping

As mentioned in previous section, different models exist to account for damping. Most commonly used is the viscous model, which relates damping to velocity. In the Coulomb model, damping is related to the sign of velocity, while the quadratic model relates damping to the velocity-squared. It was found that the total effect of different damping mechanisms may cause a structure to respond as if it has a linear viscous damping system. Therefore, in structural dynamics for engineering purposes it is thought to be appropriate to model the overall damped behaviour of a structure as being viscous (Tamura, 2013). This is mathematically convenient since it results in a linear second order differential equation (Tamura, 2013). However, since force in the equation of motion for viscous damping is inherently independent of amplitude, any source of non linearity is hidden in this approach (Kijewski-Correa, 2003).

5

Energy Flux Analysis

This chapter will explain the Energy Flux Analysis, a method applied in this thesis to find the damping in a high-rise structure. First, the general idea behind the Energy Flux Analysis is explained in § 5.1. In order to apply it to a high-rise building, the building has to be modelled. The application of the Energy Flux Analysis to a high-rise building modelled as an Euler-Bernoulli beam is discussed in § 5.2. The result of the Energy Flux Analysis is dissipated energy, while usually the energy dissipation characteristic of a structure is expressed in a damping ratio. Therefore, § 5.3 will draw attention to the translation from energy dissipation to damping value and damping ratio. Finally, the previous research of this method applied to a high-rise building will be discussed in § 5.4.

5.1. General model

5.1.1. Energy balance

The Energy Flux Analysis is based on an energy balance or energy flux balance. The concept of an energy balance stems from thermodynamics, which essentially deals with the transfer of energy from one place to another and the transformation of energy from one form to the other. The Law of Conservation of Energy states that energy can neither be created nor destroyed (Campbell et al., 2020). This means that the total energy of a system plus its surroundings remains constant, but energy can flow over the system boundaries. The Law of Conservation of Energy was used to write the energy flux balance (Gómez, 2019):

$$\frac{\mathrm{d}}{\mathrm{d}t}E(t) + S(x,t)\Big|_{\partial\Omega} = W_{ext}(t) - W_{diss}(t) \tag{5.1}$$

In this equation $E(t)$ is the energy in the system given as the summation of the kinetic and the potential energy. These are responsible for the motion of the structure, and its derivative is the change of energy over time. This term can only change if there is energy flowing in or out of the system. The total energy flowing in and out of the structure at a system boundary is given by $S(x,t)$, a positive value represents energy flowing out of the system. The external energy is defined separately in this equation since it refers to the load on the structure and is given as $W_{ext}(t)$. Whether the dissipated energy remains in the system boundaries is not relevant, it is transformed to another type of energy which is not kinetic or potential and will not be recovered by the structure. This dissipated energy is given by $W_{diss}(t)$ and is the desired damping. An overview of the system described by eq. (5.1) can be found in fig. 5.1. Important to note is that eq. (5.1) is an energy flux balance with units Nm/s rather than Nm. Taking its integral over time yields the energy balance.

The energy balance is very established, has many applications and can be applied to any system. Depending on the system chosen, the terms to fill in the energy balance change. In this research the focus is on a high-rise structure. Both the total structure, and the separation between superstructure (SS) and soil-structure interaction (SSI) are considered.

5.1.2. Hamiltonian mechanics

The aim of this section is finding a description for the dynamic motion of the structure. The energy change and the energy flux terms will be obtained using Hamiltonian mechanics. Its advantage compared to classical mechanics is the fact that once an expression is found for the Lagrangian density λ, finding the equation of

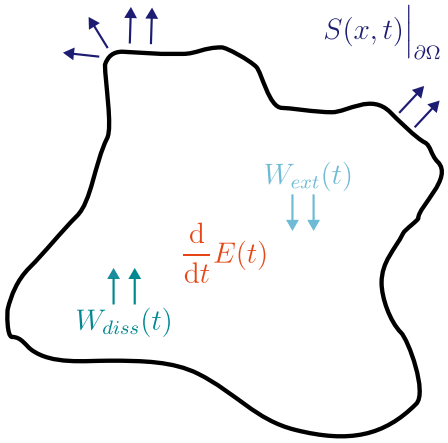

Figure 5.1: Energy balance inspired by equation 5.1

motion (EoM), the boundary conditions, the energy change and the energy flux is a matter of filling in the expressions. This makes it generally applicable. This chapter was written with the help of the Lecture Notes on Classical and Quantum Mechanics (Thijssen, 2008) and chapter 3 of the PhD report of Gómez (Gómez, 2019).

Using the Lagrangian density λ, which is defined as the difference between kinetic and potential energy, the equation of motion can be obtained through:

$$\frac{\partial\lambda}{\partial\mathbf{u}} - \frac{\partial}{\partial x}\frac{\partial\lambda}{\partial\mathbf{u}'} + \frac{\partial^2}{\partial x^2}\frac{\partial\lambda}{\partial\mathbf{u}''} - \frac{\partial}{\partial t}\frac{\partial\lambda}{\partial\dot{\mathbf{u}}} + \frac{\partial}{\partial t}\left(\frac{\partial}{\partial x}\left(\frac{\partial^2\lambda}{\partial\dot{\mathbf{u}}\partial\mathbf{u}'}\right)\right) + \frac{\partial\mathscr{D}}{\partial\dot{\mathbf{u}}} + \mathbf{q} - \frac{\partial\mathbf{m}}{\partial x} = 0 \tag{5.2}$$

The term $\mathscr{D}$ accounts for the energy dissipation and $\mathbf{m}$ is a distributed mass. The natural, or Neumann, boundary conditions, are defined through:

$$\mathbf{m} + \tfrac{\partial\lambda}{\partial\mathbf{u}'} - \tfrac{\partial}{\partial x}\tfrac{\partial\lambda}{\partial\mathbf{u}''} - \tfrac{\partial}{\partial t}\left(\tfrac{\partial^2\lambda}{\partial\dot{\mathbf{u}}\partial\mathbf{u}'}\right) = T \quad \text{at } x = 0, L \tag{5.3}$$

$$\tfrac{\partial\lambda}{\partial\mathbf{u}''} = M \quad \text{at } x = 0, L \tag{5.4}$$

The Hamiltonian density, as given in eq. (5.5), which is also dependent on the Lagrangian density, can be used to find the energy term by taking its integral over the system length. The energy change term can simply be found taking the first derivative to time of the term in eq. (5.6).

$$e = \left(\frac{\partial\mathbf{u}}{\partial t}, \frac{\partial\lambda}{\partial t}\right) + \left(\frac{\partial^2\mathbf{u}}{\partial x\partial t}, \frac{\partial^2\lambda}{\partial x\partial t}\right) - \lambda \tag{5.5}$$

$$E(t) = \int_L e\,\mathrm{d}x \tag{5.6}$$

The energy flux at any specific boundary found in equation eq. (5.1) is defined as:

$$\mathbf{S} = \left(\frac{\partial\mathbf{u}}{\partial t}, \frac{\partial\lambda}{\partial\mathbf{u}'} - \frac{\partial}{\partial x}\frac{\partial\lambda}{\partial\mathbf{u}''} - \frac{\partial}{\partial t}\frac{\partial\lambda}{\partial\mathbf{u}'\partial\dot{\mathbf{u}}}\right) + \left(\frac{\partial^2\mathbf{u}}{\partial x\partial t}, \frac{\partial\lambda}{\partial\mathbf{u}''}\right) \tag{5.7}$$

Almost all necessary terms of the energy balance in eq. (5.1) can be obtained using Hamiltonian mechanics. What remains is the external energy term. Assuming external energy is introduced due to a general distributed load, q, on the system, the external load can be expressed as follows:

$$W_{ext}(t) = \int_L \mathbf{q}(x,t)\dot{\mathbf{u}}\,\mathrm{d}x \tag{5.8}$$

5.2. Euler-Bernoulli beam model

In this section the general model for the Energy Flux Analysis is translated for its application to a high-rise building and its subsystems; the superstructure (SS) and soil-structure interaction (SSI). A model needs to be

chosen in order to describe, for instance, the displacements, rotations, curvatures, and strains in the system. The high-rise building is modelled using an Euler-Bernoulli beam. This means that bending deformation is taken into account while excluding shear distortion and rotary inertia. This is assumed to be valid for slender structures, which have much smaller cross-sectional dimensions than their axial length. Of course, this is a simplification and following the limit of slenderness given by Blevins (Blevins, 1979) not every tall building can be considered slender. Besides, the structural system of a high-rise building has an impact on the behaviour in terms of bending and shear. However, in this research is assumed to be a valid model. Another simplification is the fact that the beam is modelled with continuous distribution of stiffness and mass over its height. In reality, this is usually not the case due to for instance different entrance levels and optimisation of the structural system over the building height.

In this section, the Euler-Bernoulli beam model will be briefly described and used to obtain an expression of the Lagrangian density. Finally, this Lagrangian density is used to fill in the expressions of § 5.1.1 and § 5.1.2.

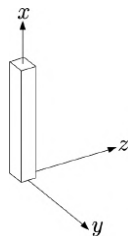

Figure 5.2: Coordinate system

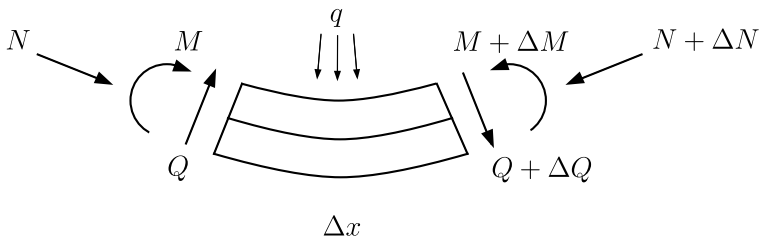

Figure 5.3: Sign convention

The sign convention and coordinate system used for the Energy Flux Analysis are presented fig. 5.2 and fig. 5.3. Additionally, small displacements are assumed resulting in $\sin\theta \approx \tan\theta \approx \theta$.

5.2.1. Kinematic relations

The total displacement u of any material point in the beam will be described in terms of the translational displacement w and the displacement due to rotation θ. Using the Euler-Bernoulli kinematic assumptions, implying that plane sections remain plane and orthogonal to the deformed beam axis, the following expressions for u in all coordinate directions can be found:

$$\begin{aligned} u_x(x,y,z,t) &= w_x(x,t) + z\theta_y(x,t) - y\theta_z(x,t) \\ u_y(x,z,t) &= w_y(x,t) - z\theta_x(x,t) \\ u_z(x,y,t) &= w_z(x,t) + y\theta_x(x,t) \end{aligned} \tag{5.9}$$

The kinematic equations give the relation between the displacements found in eq. (5.9) and the strains:

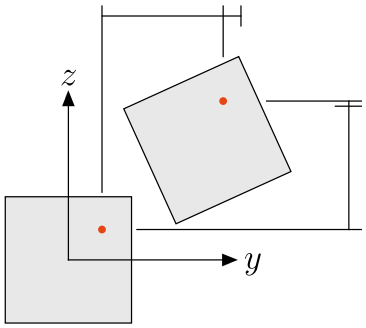

Figure 5.4: Rigid floor rotation to derive equation 5.9

$$
\begin{aligned}
\epsilon_{xx}(x,y,z,t) &= \frac{\partial u_x(x,y,z,t)}{\partial x} = \frac{\partial w_x(x,t)}{\partial x} + z\frac{\partial \theta_y(x,t)}{\partial x} - y\frac{\partial \theta_z(x,t)}{\partial x} \\
\epsilon_{yy}(x,z,t) &= \frac{\partial u_y(x,z,t)}{\partial y} = 0 \\
\epsilon_{zz}(x,y,t) &= \frac{\partial u_z(x,y,t)}{\partial z} = 0 \\
\gamma_{xy}(x,z,t) &= \frac{\partial u_x(x,y,z,t)}{\partial y} + \frac{\partial u_y(x,z,t)}{\partial x} = \frac{\partial w_y(x,t)}{\partial x} - z\frac{\partial \theta_x(x,t)}{\partial x} - \theta_z(x,t) \\
\gamma_{xz}(x,y,t) &= \frac{\partial u_x(x,y,z,t)}{\partial z} + \frac{\partial u_z(x,y,t)}{\partial x} = \frac{\partial w_z(x,t)}{\partial x} + y\frac{\partial \theta_x(x,t)}{\partial x} + \theta_y(x,t) \\
\gamma_{yz}(x,t) &= \frac{\partial u_y(x,z,t)}{\partial z} + \frac{\partial u_z(x,y,t)}{\partial y} = 0
\end{aligned}
\tag{5.10}
$$

The fact that ϵ_{yy}, ϵ_{zz} and γ_{yz} are zero follows from the Euler-Bernoulli kinematic assumptions. Since plane sections remain orthogonal to the deformed beam axis, the rotation of the beam can be described as follows, using positive rotation in the given coordinate system:

$$
\begin{aligned}
\theta_y(x,t) &= -\frac{\partial w_z(x,t)}{\partial x} \\
\theta_z(x,t) &= \frac{\partial w_y(x,t)}{\partial x}
\end{aligned}
\tag{5.11}
$$

5.2.2. Energy Flux Analysis

For clarity reasons, from now on the dependency on x, y, z, and t is discarded, the time derivative will be marked with a dot, and the derivative to x will be marked with a prime.

It is now time to find λ for the specific application of the Hamiltonian principle to an Euler-Bernoulli beam. As was mentioned in § 5.1.2, it is found using the difference between the kinetic and the potential energy for any point in the beam.

$$\lambda = K(x,t) - P(x,t) \tag{5.12}$$

The kinetic energy density, K, is given by the motion of the building in both x-, y- and z-direction and the mass density of the building ρ_b.

$$K(x,t) = \frac{1}{2}\rho_b \int_A \left(\dot{u}_x^2 + \dot{u}_y^2 + \dot{u}_z^2\right) \mathrm{d}A \tag{5.13}$$

Assuming the cross-section is continuous over the building height, and filling in the expressions of eq. (5.9) and eq. (5.11) the kinetic energy is given as:

$$K(x,t) = \frac{1}{2}\rho_b \int_A \left(\left(\dot{w}_x - z\dot{w}'_z - y\dot{w}'_y\right)^2 + \left(\dot{w}_y - z\dot{w}'_x\right)^2 + \left(\dot{w}_z + y\dot{w}'_x\right)^2\right) \mathrm{d}A \tag{5.14}$$

The potential energy is given by the strain energy in the beam, and therefore depends on ϵ_{xx}, γ_{xy} and γ_{xz},the Young's modulus E, and shear modulus G.

$$P(x,t) = \frac{1}{2}E\int_A \epsilon_{xx}^2 \mathrm{d}A + \frac{1}{2}\int_L G\int_A \gamma_{xy}^2 + \gamma_{xz}^2 \,\mathrm{d}A \tag{5.15}$$

Filling in the equation using eq. (5.10), eq. (5.9), and eq. (5.11), the potential energy can be rewritten as follows:

$$P(x,t) = \frac{1}{2}E\int_A \left(w'_x - zw''_z - yw''_y\right)^2 \,\mathrm{d}A + \frac{1}{2}G\int_A \left(-zw''_x\right)^2 + \left(yw''_x\right)^2 \,\mathrm{d}A \tag{5.16}$$

Finally, subtracting the potential energy from the kinetic energy, an expression is found for the Lagrangian density λ:

$$
\begin{aligned}
\lambda(x,y,z,t) = \frac{1}{2}\rho_b \int_A &\left(\left(\dot{w}_x - z\dot{w}'_z - y\dot{w}'_y\right)^2 + \left(\dot{w}_y - z\dot{w}'_x\right)^2 + \left(\dot{w}_z + y\dot{w}'_x\right)^2\right) \mathrm{d}A \\
-\frac{1}{2}E\int_A &\left(w'_x - zw''_z - yw''_y\right)^2 \,\mathrm{d}A - \frac{1}{2}G\int_A \left(-zw''_x\right)^2 + \left(yw''_x\right)^2 \,\mathrm{d}A
\end{aligned}
\tag{5.17}
$$

The external energy flux term in the energy balance can be found using eq. (5.18).

$$W_{ext}(t) = \int_L q(x,t)\left(-z\dot{w}'_z - y\dot{w}'_y + \dot{w}_y + \dot{w}_z\right) \mathrm{d}x \tag{5.18}$$

5.3. Dissipated energy to damping

Once the Energy Flux Analysis has been applied, the result is the dissipated energy. However, for comparison reasons and for application in models it is useful to express the dissipated energy as a damping value or damping ratio. Many approaches for this translation exist. As mentioned in chapter 4, damping is a result of many damping mechanisms and is usually modelled to describe the collective damping occurring due to all these mechanisms. This thesis assumes viscous damping.

5.3.1. Total structure

When the energy dissipation has been obtained for the total structure, a total damping ratio should be calculated and is not possible to use separate models for the superstructure or SSI damping to find a damping ratio. Therefore, in order to create a damping ratio for the entire structure, this structure is translated to a single degree of freedom (SDOF) system through an equivalent mass and stiffness description. For this SDOF system it is possible to find the critical damping, and to find a damping value assuming a single viscous damper. The equivalent mass of the beam is obtained through:

$$M_e = \int_0^H \rho_b A \phi(x)^2 \, \mathrm{d}x \tag{5.19}$$

In this formula $\phi(x)$ is the unit mode shape. The critical damping from the SDOF system can be found using:

$$c_{crit} = 2 M_e \omega_n \tag{5.20}$$

The angular natural frequency is given by ω_n. The damping ratio is defined as the ratio of the damping value over the critical damping:

$$\zeta = \frac{C}{c_{crit}} \tag{5.21}$$

It is assumed here that the SDOF equivalent mass is located at the top of the beam, it is the motion of this location that defines the damping value:

$$E_{diss}(t) = \int_0^t C \dot{u}(H,t)^2 \, \mathrm{d}t \tag{5.22}$$

The damping value C is found by matching this dissipated energy with the dissipated energy found through the Energy Flux Analysis. A different approach was used by Gómez (Gómez, 2019) and is discussed in § 5.4.

5.3.2. Superstructure

To describe model damping in the superstructure, again, many models exist. First of all, damping in the superstructure can be described through the material properties. The Kelvin-Voigt material damping model does this as follows:

$$\sigma = \left(E + E^* \frac{\partial}{\partial t} \right) \epsilon \tag{5.23}$$

The energy dissipation computed through this model is given as follows (Gómez, 2019):

$$W_{diss}(t) = E^* \int_0^L \frac{\partial^5 w(x,t)}{\partial z^4 \partial t} \frac{\partial w(x,t)}{\partial t} \, \mathrm{d}x \tag{5.24}$$

This energy dissipation should match the energy dissipation computed with the Energy Flux Analysis to obtain the constant for Kelvin-Voigt material damping E^*.

5.3.3. Damping SSI

For the SSI, the damping can be expressed in terms of dampers at foundation level. Considering viscous dampers in translational and rotational direction for both directions, the computed energy dissipation becomes:

$$W_{diss}(t) = C_{t,SSI,y} \dot{u}_y^2(0,t) + C_{t,SSI,z} \dot{u}_z^2(0,t) + C_{\theta,SSI,y} \dot{u}_y'^2(0,t) + C_{\theta,SSI,z} \dot{u}_z'^2(0,t) \tag{5.25}$$

5.4. Previous research

The Energy Flux Analysis approach for finding damping in high-rise buildings was first proposed by Gómez (Gómez, 2019). In this research it was successfully applied and verified using a cantilever beam, and a frame lab structure. After this, it is applied to the Jubi tower in The Hague, The Netherlands. Motion measurements were performed under strong wind conditions for a period of 2 hours. The Jubi tower is a 146 m tall tower with a concrete tube-in-tube structure, and is asymmetric. The main focus was to identify the dissipative properties of a full-scale high-rise building and additionally an attempt was made to identify the energy dissipation in the superstructure separately from the SSI. It will now be discussed how the required information for the Energy Flux Analysis was obtained in this research.

Motion data
The following motion measurements were performed:

- At the 9$^{\text{th}}$ floor: 2 accelerometers, positioned perpendicular to measure in the weak and stiff direction, and 24 strain gauges on various components, such as the cores, columns, and outer walls.
- At the 22$^{\text{nd}}$ floor: 2 accelerometers, positioned perpendicular to measure in the weak and stiff direction.
- At the 37$^{\text{th}}$ floor: 4 accelerometers, 3 in the weak direction and 1 in the stiff direction.

To find the energy in the structure, the motion of the structure along the building height should be known. This was approximated through linear interpolation of the measurements on the 37$^{\text{th}}$ floor and on the 9$^{\text{th}}$ floor. The potential energy and the energy flux were assumed negligible compared to the kinetic energy at the top of the building. At the bottom, both kinetic and potential energy could be computed using the accelerometers and strain gauges respectively.

Energy flux
With the strain information, the energy flux crossing the bottom level could also be computed. However, since the lowest measurements are on the 9$^{\text{th}}$ floor, the dissipated energy in the lower floors is included in the SSI dissipated energy. Due to the very high rigidity of the bottom floors compared to the soil stiffness, the energy dissipated in the bottom part of the building was assumed to be significantly smaller than due to SSI. Therefore, the result is assumed to be representative for the SSI energy dissipation and the bottom part of the building is assumed to move as a rigid body.

Soil conditions
Prior to construction, a Cone Penetration Test (CPT) was performed at several locations at the building site. Based on these tests, the shear-wave speed was calculated by means of the Robertson's correlation. This procedure is further described in appendix N. The complex interaction between the soil and the building is modelled by means of springs representing the dynamic stiffness of the soil. The stiffness of the soil is computed with Dynapile by inserting the soil profile, the pile plan and the pile characteristics.

External energy flux
During the measurement campaign, no wind pressure sensors were installed on the building. The wind peak velocity and 1-hour average velocity was obtained through the KNMI database.

$$W_{ext}(t) = \frac{1}{2}\rho_a C_f B \int_L \dot{u}_y(x,t)\left(\bar{U}(x) + u'(x,t)\right)^2 \,\mathrm{d}x \tag{5.26}$$

However, a linearised version was used under the assumption that the fluctuating component, $u'(x,t)$, and the building velocity are much smaller than the mean velocity, $\bar{U}(x)$.

$$W_{ext}(t) = \frac{1}{2}\rho_a C_f B \int_L \dot{u}_y(x,t)\bar{U}^2(x) \,\mathrm{d}x \tag{5.27}$$

Whether this assumption is valid requires further investigation. In order to describe the mean wind velocity over the complete building height, the commonly used logarithmic wind profile was applied. The building velocity for this equation was, equally to the energy, found by linear interpolation of the measurements on the top measurement floor and lower measurement floor.

Damping
Before solving the energy flux balance, all terms were translated to the frequency domain. Once this was done, the energy dissipation for the total structure, the superstructure and the SSI could be separately determined. For translation to a damping ratio, three dependencies were evaluated by Gómez (Gómez, 2019): viscous damping, quadratic damping and hysteretic damping.

The theoretical energy dissipation is related to the dissipated energy found with the Energy Flux Analysis using the Fourier transform through:

$$\mathscr{F}\left(W_{diss_i}(t)\right) = A\tilde{W}_{diss,EFA}(\omega) \tag{5.28}$$

where

$$A = \frac{2\pi\omega i}{e^{i\omega T} - 1} \tag{5.29}$$

The factor A is a frequency multiplier accounting for the finite duration of the measurement. The damping operator constants, C_i, can be estimated through minimisation of the mismatch:

$$\min_{C_i} \sum_{\omega_n} \left| \tilde{W}_{diss}(\omega) - \mathscr{F}\left(W_{diss_i}(t)\right) \right| \tag{5.30}$$

Since the damping operators are assumed to be constant, the focus is on minimisation at the maxima of the spectra, which are the natural frequencies of the building. For other frequencies different damping operators could be found. The non-linearity is said to not be highly influential, since the velocities in this application are not large. The quadratic damping mechanism turns out to be most sensitive to changes in the constant and the linear viscous model gives the best match. Therefore, in this research linear viscous damping is used.

In order to obtain a damping ratio from these damping operators, the equations of motion are used. The damping operators are used to describe the equations of motion and the boundary conditions. These are used to compute the frequency equations, a procedure that has been applied in appendix A. The roots of these frequency equations are the complex-valued natural frequencies of the system.

$$\det|\mathbf{A}(\omega_n)| = 0 \tag{5.31}$$

$$\det|\mathbf{B}(\omega_n)| = 0 \tag{5.32}$$

The complex-valued roots of eq. (5.31) describe the translational modes, while the complex roots of eq. (5.32) describe the torsional modes. The complex-valued natural frequencies are used to compute the damping ratio of the respective mode using SDOF dynamics:

$$\zeta_n = \frac{\Im(\omega_n)}{\sqrt{\Re(\omega_n)^2 + \Im(\omega_n)^2}} \tag{5.33}$$

This is a different, alternative approach from what has been demonstrated in § 5.3.1.

Building stiffness
The bending EI and shear GJ stiffness used was obtained through technical information of the building. The mass per unit length, $\rho_b A$, of the building is calculated using the density of reinforced concrete and the area of the cores and outer walls. The mass of the floors is quantified using the technical information of the floors. Whether or not these properties were updated based on the measured natural frequency not known.

Comparison EFA and HPBW method
A comparison of the results of the Energy Flux Analysis was made with the results of applying the HPBW method. After transforming the measurements to the frequency domain, it was observed that the sensors were not measuring in the principal directions, in which case it is not possible to directly identify the modal damping for the HPBW method. Therefore, the signals had to be manipulated using rigid-body kinematics. After this, the SDOF HPBW method as briefly described in § 4.4, could be applied to the signals providing comparison for the identified damping through the Energy Flux Analysis. However, applying the HPBW method was not straightforward, since the Jubi tower has two relatively closely spaced frequencies. An equivalent viscous damping ratio was identified over the two closely spaced peaks and was averaged. The torsional peak was well-separated and could be considered separately. It is mentioned that these identified damping

ratios are not true damping values due to the fact that the modes are coupled. It is therefore questionable whether or not these values provide good comparison. It does show the limitations of techniques such as the HPBW method. The values found with the EFA and the HPBW method are compared and are given in table 5.1.

Table 5.1: Damping ratios for EFA and HPBW (Gómez, 2019)

	HPBW	EFA
ζ_y	1.0%	1.1%
ζ_z	1.2%	2.0%
ζ_{θ_x}	0.73%	1.2%

The damping values with the HPBW method are lower than identified through the EFA, but the differences are said to be acceptable due to the complexity of the structure. It is noted that the ratios found using the EFA are real damping ratios, while the HPBW identified damping ratios are indicative of the presence of closely spaced modes. However, it was concluded that for low-damped systems, these damping ratios are close enough to the modal damping values.

After the research by Gómez, Talib (Talib, 2019) continued with the investigation of the Energy Flux Analysis. This research was mainly focused on verification of the technique and had a reverse engineering approach. A FEM Euler-Bernoulli beam model was created of which the damping values were prescribed and known. The soil conditions were modelled here in terms of a rotational spring, no translation was considered and the problem was considered in one direction. The beam was set in motion using an initial displacement. The aim was to find the error found when obtaining these damping values through the energy approach. In case only SSI damping is present in the model, the Energy Flux Analysis could find the damping value with high accuracy. As there was only one damping mechanism, there was no need to compute the energy flux at the boundary. However, if material damping was introduced to the beam, the distinctive energies were found with a 13% error. This research also focused on finding the error made when only spatially limited measurements are used. However, this was done for a model with SSI damping only, where measurements at the bottom were used. As computation of SSI damping does not require knowledge on the building motion, it is not surprising that again a small error was found. After this, the initial displacement was replaced with a wind load based on wind tunnel measurements. Using all wind load information, the results found were the same as for the initial displacement. A study into the results of having limited measurements was also performed, but instead of application of the original load on the FEM model, and application of an extrapolated load in the EFA model, the load in the FEM model was changed to that of the EFA model. Therefore, this study did not provide insight into the sensitivity of the method to having limited wind load or structure motion information.

Although the benefits of the Energy Flux Analysis are clear, the method requires further attention. The method has been verified using simple lab specimen by Gómez (Gómez, 2019), but when applied to a high-rise structure no comparison for verification could be made. Talbi (Talib, 2019) focussed on verification using a FEM model. This section briefly discusses the assumptions that were made in previous and in this research when applying the Energy Flux Analysis to a high-rise structure, and what distinguishes this research from previous work. Similar to the work of Gómez and Talib, this research uses an Euler-Bernoulli beam to derive the formulae for the EFA, assuming rigid floors. Gómez used linear extrapolation for motion measurements, while Talib used the fundamental mode shape of the Euler-Bernoulli beam. The impact of this assumption has not been addressed before, and will be investigated in this research. Additionally, this research will focus on the impact of different approaches to model the wind load on the result of the EFA. This has not been investigated before. Gómez did not have wind measurements available and used KNMI data and theory to describe the wind load, Talib had all required wind information available in the model. Both Gómez and Talib used technical information to find the building stiffness and building mass, and used Dynapile to compute the soil stiffness. No attention has been paid yet to the uncertainty in these properties, something that will be treated in this thesis. Besides, this thesis will discuss uncertainties introduced by measurements themselves.

II

CASE: NEW ORLEANS TOWER

6

New Orleans tower

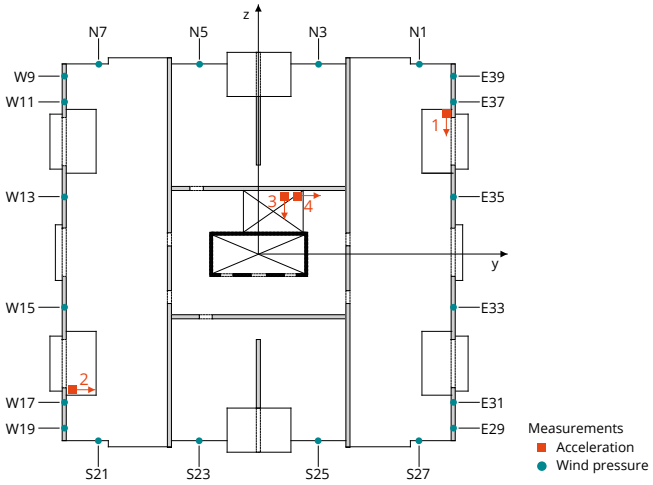

Figure 6.1: Floor plan of the New Orleans tower including accelerometers and pressure taps

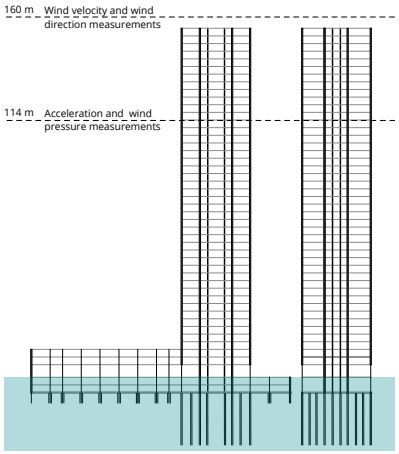

Figure 6.2: Cross-sections New Orleans tower and measurement locations

The New Orleans tower will be used as a case for this research. It is a 44-storey building and its structural height is 155 m. The building is located at the Kop van Zuid in Rotterdam, the Netherlands, and was constructed in 2010. This chapter will provide a brief overview of the structural system and the location of the building. Chapter 7 presents the measurements performed on this building. These measurements will be applied in the Energy Flux Analysis later on in this research. The Energy Flux Analysis model derived from chapter 5 to apply to the New Orleans tower will be discussed in chapter 8

6.1. Structural system

The New Orleans tower is part of a bigger building, shown schematically in fig. 6.2. It has a basement of two storeys with on top of it a lower plinth building. The plinth building consists of three floors and has a rectangular floor plan of approximately 112 by 29 m. At the east end of this lower building rises the New Orleans tower. The entire structure of the tower is made of reinforced concrete and the floor plan is roughly 29 by 29 m.

The load bearing system is shown in fig. 6.1 and consists of a rectangular core and walls oriented in one direction only. All walls have a thickness of 300 mm. Naturally, the core starts at the foundation and rises to the top of the building, but the walls start at the 2nd and 3rd storey. Below these walls 14 steel columns of HD 400x1086 with steel grade S460 are present to enable the presence of glass walls at the entrance. A transitional steel construction allows for the large forces from the tower walls to be introduced into these steel columns. During construction, the columns and the transition structure were not directly connected. Only after the

19th floor was finished, this connection was realised to make sure the foundation of the core would settle first to avoid large settlement differences.

The stability of the structure is guaranteed by three stability systems; the stability core, the walls acting as outriggers in z-direction, and frame action through walls and floors in y-direction. The design calculations mention that in y-direction, the contribution to the stability by this frame action is approximately 32 to 34 %. This y-direction is the stiffer direction of the tower. With the exception of several floors, the structural system over the complete building height is identical. Except for the openings in the core, the structure is double symmetric.

The floors of the New Orleans tower are made of 300 mm thick concrete. The foundation of the New Orleans tower consists of a 350 mm thick concrete foundation slabs with 2500 mm and 600 mm thick foundation blocks to introduce the column and core forces to the foundation piles. These foundation piles are 450 x 450 mm prefab piles which are 20 m long and reach a depth of approximately 29 m. This means that these piles are founded on the first sand layer, which is above the well-known Kedichem layer in Rotterdam. This layer is mainly made of clay with some silt and sand, and will introduce settlements. Most piles are concentrated directly beneath the stability core due to the 350 mm thin connection foundation slab between the foundation blocks underneath the core and the columns, the bending moments in the core due to wind are received to a large extent by the piles directly underneath the core. This limits the bending moments present in the remaining part of the foundation, limiting its reinforcement. Besides, in the tower forces as a result of wind loading have already been transferred to the columns through the structural walls. To account for horizontal forces from the tower due to wind, a large number of strut piles is applied. Due to this strut orientation of the piles, the pile plan at the top of the piles looks significantly different from the pile plan at the bottom of the piles. At the south side of the building a quay wall is present, which is protected by permanent sheet piling at the south side of the foundation. This steel sheet pile has a depth of approximately 23 m.

Due to the presence of soft soils, which is general practice in the Netherlands, the soil stiffness has to be accounted for in the design. The design assumes that approximately 20% of the horizontal deflection at the top of the tower is a result of foundation rotation. For this thesis, the soil properties are assumed to be the same in any direction, it is assumed isotropic.

A more quantitative overview of the building structure is discussed in chapter 12. No values are mentioned in this chapter, since structure properties are uncertain. Chapter 12 also discusses the soil stiffness obtained from the design directly, from the design properties, through a model called Dynapile by TNO (Bronkhorst et al., 2018), and from the cone model (Wolf and Deeks, 2004). Chapter 12 is aided by a more extensive overview of the property background and calculations in appendix K, appendix L, appendix O, appendix M, and appendix N.

The SSI damping values obtained with the Dynapile and the cone model by TNO are presented in table 6.1. Like the other structure properties, these values contain a high degree of uncertainty.

	C_t [Ns/m]	C_θ [Nms/rad]
Wolf model	4.59×10^8	6.34×10^{10}
Dynapile 0%	8.41×10^5	2.59×10^{10}
Dynapile 3%	2.07×10^8	1.77×10^{11}

Table 6.1: SSI damping values New Orleans (Bronkhorst et al., 2018)

6.2. Surroundings

The surrounding environment highly influences the wind flow approaching a structure. The New Orleans tower is located at the Kop van Zuid, a location where many high-rise structure are built such as the Montevideo tower and De Rotterdam. Figure 6.3 shows that the Montevideo tower is located at around 160 m to the southwest of the New Orleans tower. De Rotterdam is located to the north and was just finished at the time of the measurements used in this research. These structures are relevant, because as mentioned in chapter 2, surrounding structures will influence the wind environment around the building. This also holds for structures downstream.

Figure 6.3 also shows that to the south of the tower the Rijnhaven is located, providing 300 meters of terrain without obstacles for the approaching wind flow when considering wind from this direction.

When considering the wind load on the New Orleans tower, the plinth building is neglected since the

wind load on this building will be transferred to the tower as the tower functions as a stability system for this lower building in the longitudinal direction. Any additional load due to friction on the longitudinal facades has been neglected in the design of the tower.

Figure 6.3: New Orleans tower and its surroundings, angle is indicated relative to the north.

7

Measurement Analysis

7.1. Sensor set-up

TNO has continuously performed measurements on the New Orleans tower since the construction of the tower in 2010, and has once updated the sensors present since. The measurements are divided into 10-minute segments of measurements. In this measurement campaign, accelerations and wind pressures are measured at approximately 114 m height. Figure 6.1 shows the accelerometers in orange and pressure taps in green at this height. In total, 40 pressure taps are present along the circumference of the building. Half of these pressure taps measure the pressure in the facade cavities, which are irrelevant for this research, and the other half measure the external pressure around the facade of the building. Combining the measurements of the different accelerometers, the acceleration in y- and in z-direction of the coordinate system shown in fig. 6.1 and the torsional acceleration can be derived. A more detailed explanation of this projection of the measured accelerations to the principal axes of the building can be found in appendix B. Besides the measurements at 114 meter height, wind velocity and wind direction have been continuously measured at 160 m height. This is around 5 meters above the top floor of the tower at the centre of the floor plan. The measurement techniques and further data acquisition specifics will be discussed in more detail in chapter 11. The sensors were initially installed by TNO for another purpose.

7.2. Measurements

This section will present and discuss the measurements obtained from the New Orleans tower. These measurements will be used in the Energy Flux Analysis and the measurement analysis functions as a check as to whether the measurements show any irregularities compared to the theoretical expectations from chapter 2 and chapter 3.

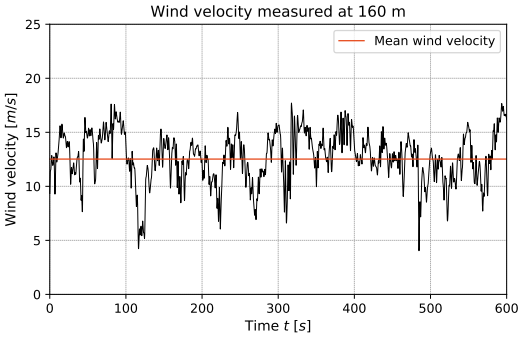

Figure 7.1: Wind velocity measured at 160 m

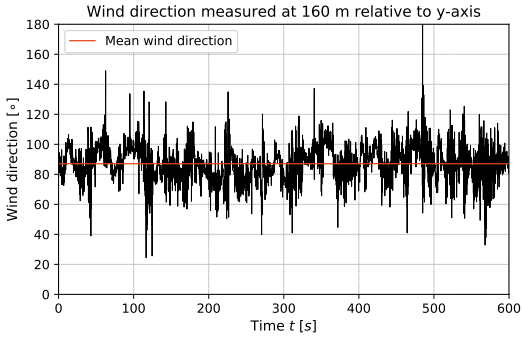

Figure 7.2: Wind direction measured at 160 m

Figure 7.1 and fig. 7.2 show the mean wind velocity of the considered 10-minute signal. The mean wind velocity is around 13 m/s and the mean wind direction is at an angle of around 90° with the y-axis, which means that the wind is flowing in the positive z-direction. The coordinates are visualised in fig. 6.1. From this

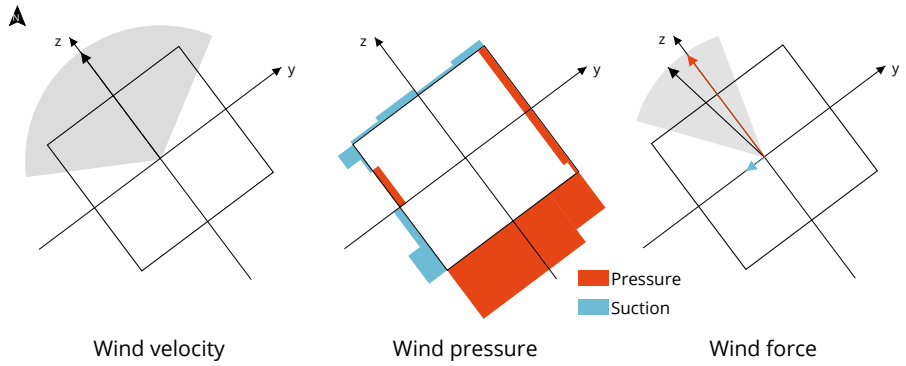

Figure 7.3: Visualisation of wind velocity, wind pressures and wind force signal 7

direction, little obstacles are present upstream of the wind flow due to the Rijnhaven. The closest obstacle is 300 m away from the New Orleans tower as is presented in fig. 6.3.

The wind direction measured in time related to the floor plan is visualised in the left figure of fig. 7.3. The middle figure visualises the wind pressures measured on the building facade. Orange represents positive pressure and blue represents suction. It shows that on the windward, south facade, pressure is always positive and has a relatively large magnitude. Although not presented in the figure, the pressure fluctuations are relatively low on this facade. The pressure on the leeward side, the north facade, is negative of sign and has a much smaller magnitude, but larger relative fluctuations. This is according to aerodynamic theory as was discussed in § 2.2; pressure at windward side and suction at leeward side.

Large fluctuating suction forces are expected at the sides of the building, especially near the windward corner. This is only observed for the west facade, at the east facade small positive pressures are observed. There are several possible explanations for this observation. First, it may indicate that the mean wind direction is not exactly perpendicular to the south facade as was concluded from fig. 7.2. This could be true since the wind direction and velocity measurements are performed at only a few meters above the building roof. The roof edge may affect the wind velocity and direction measurements. Besides, as a result of neighbouring obstacles the wind climate on the east and the west facade may differ. Figure 6.3 showed that at approximately 160 m to the southwest of the structure, which is directly next to the so called west facade, the Montevideo tower is present which has a similar height. Diagonally behind the east facade, De Rotterdam is present. As discussed before, these structures can have a major effect on the wind environment around the building.

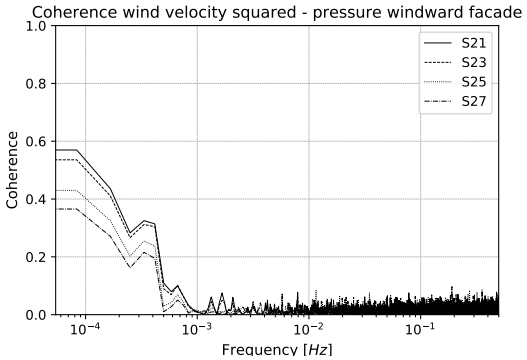

Figure 7.4: Coherence wind velocity squared - wind pressure for the sensors on windward facade

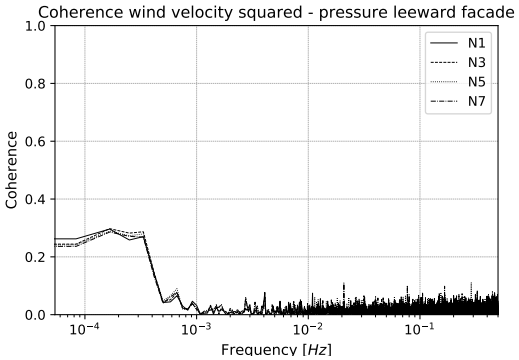

Figure 7.5: Coherence wind velocity squared - wind pressure for the sensors on leeward facade

Theoretically a linear relation should exist between the wind velocity squared and the wind pressure. The squared wind velocity should be considered due to the squared term in eq. (2.11). The coherence between the measured wind velocity squared and the measured pressure on windward facade are shown in fig. 7.4, while the coherence for pressures on leeward facade are shown in fig. 7.5. These coherence plots were created with 117 10-minute signals in this wind direction, since using this 10-minute signal alone would be too

little. Unsurprisingly, the coherence for leeward side is much smaller than for windward side. However, the coherence on windward side is quite small and the largest coherence occurs for frequencies well below the natural frequency of the structure. This could indicate once again that the wind velocity measurements are affected by the building itself.

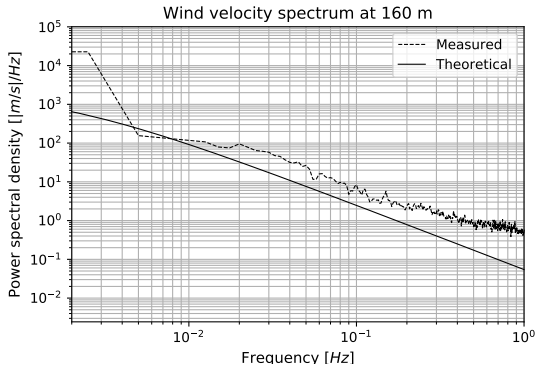

Figure 7.6: Wind velocity power spectra at 160 m

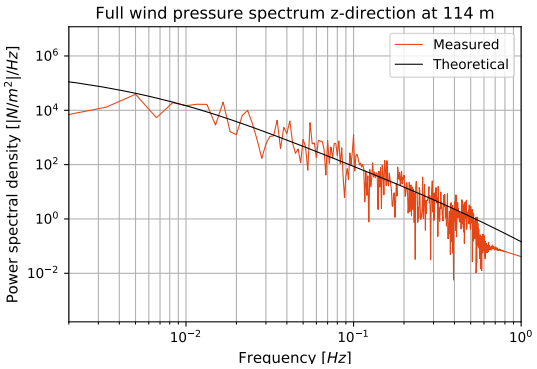

Figure 7.7: Wind pressure power spectra at 114 m in z-direction

The measured wind velocity spectrum of the measurements is shown in fig. 7.6 together with the theoretical wind velocity spectrum discussed in chapter 2. For most frequencies, the measured wind velocity spectrum is much larger than the theoretical spectrum. This again suggests that the wind velocity measurements are not representative. Alternatively, the theoretical spectrum is not suitable. The wind pressure spectrum, which is related to the wind force spectrum in fig. 7.12, is visualised in fig. 7.7 together with the theoretical spectrum from chapter 2. This measured spectrum shows much better agreement with the theory. It is concluded that the pressure measurements may be used for application of the Energy Flux Analysis in this thesis.

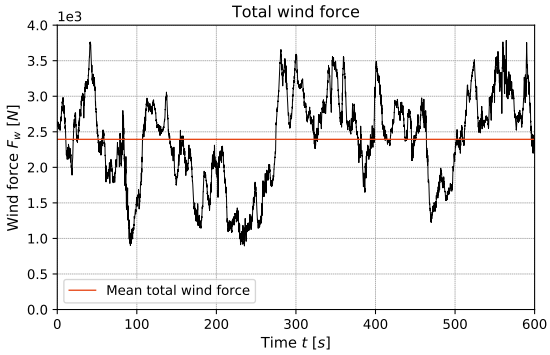

Figure 7.8: Total wind force at 114 m

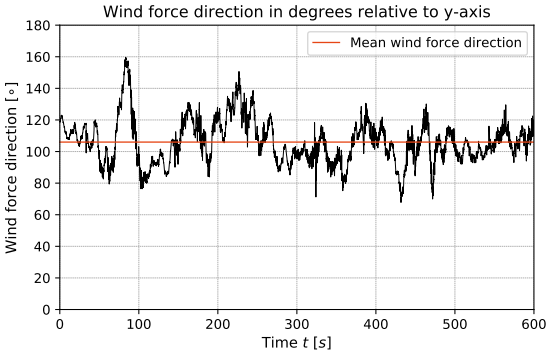

Figure 7.9: Wind force direction at 114 m

From the measured wind pressures around the facade, a resulting wind force in the z-direction, the y-direction, and a total resulting force can be computed and are presented in fig. 7.3. The total resulting force is presented in fig. 7.8 and its direction is presented in fig. 7.9. The average direction of this wind force is slightly different from what was measured for the average wind velocity. The average direction of the wind force is almost 110° rather than 90°. The resulting force was obtained as a combination of the forces on each facade and are presented in fig. 7.10. The total wind force in the along wind direction is presented in orange and results in a positive force. The blue signal shows the total wind force in the cross wind direction. This force vibrates closer to zero as would be expected from vortex shedding, although it has a mean wind force in negative y-direction.

The spectral representation of the wind force may be found in fig. 7.12. For the cross wind direction no specific peak is observed at the natural frequency of the building, indicating that vortex lock-in does not occur. The wind force has a larger contribution of high frequency components, while the along wind force has a larger mean and low frequency contribution. The spectrum at the natural frequency of the building is slightly

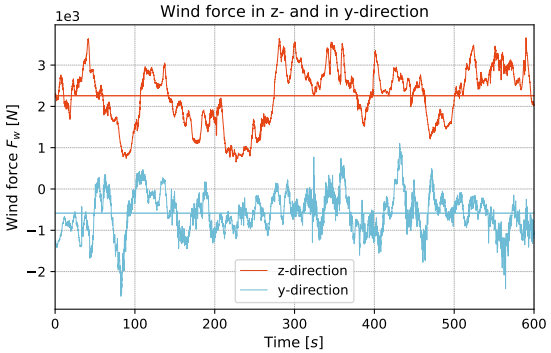

Figure 7.10: Wind force measured in z- and y-direction

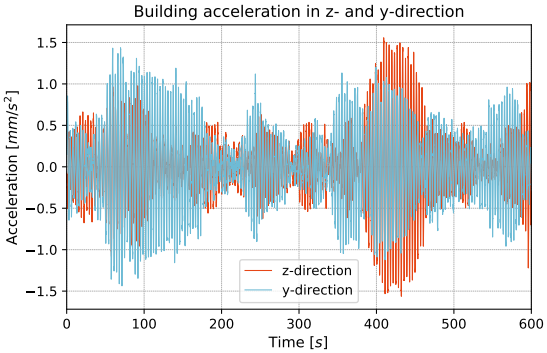

Figure 7.11: Building acceleration measured in z- and y-direction

larger for the cross wind force. The acceleration spectrum also shows slightly larger values for the natural frequency of the building in cross wind direction as is visualised in fig. 7.12. The mechanical admittance function presented in fig. 7.12 relates the force with the structure response as was discussed in chapter 3. The mechanical admittance function depends on the structure properties such as mass and stiffness.

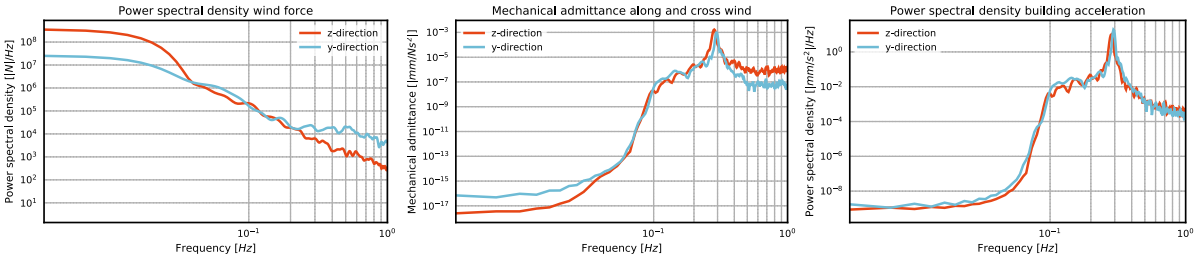

Figure 7.12: Force spectrum, mechanical admittance, and acceleration spectrum

From fig. 7.12 it is directly visible that the acceleration measurements do not contain a mean component. This is because the mean wind force results in a static deflection and therefore is not retrievable from the building accelerations. The building accelerations show clear peaks at the first natural frequency of the building in both translation modes. A slight peak for the torsional motion occurs at a frequency larger than 1 Hz and is not considered in this research. The peak of the response in cross wind direction is slightly larger than the response in along wind direction. This is a result of the wind force being larger in cross wind direction. The natural frequency in along wind direction (z-direction) is approximately 0.283 Hz. The natural frequency in cross wind direction is slightly larger, it is 0.293 Hz. This is a result of the larger building stiffness in y-direction.

Figure 7.11 shows the measured acceleration in time domain. The magnitude of the acceleration in both directions is similar, which is in agreement with the response shown in fig. 7.12. Although not as obvious for this measurement, some measurements show alternating maximum amplitudes for z- and y-direction. Since the natural frequencies for both lateral directions are close, this could mean that coupling occurs in the building. The alternating motion between the two directions, when this is not a direct result of the force, could imply energy is being transferred between the two directions. As explained in chapter 3, coupling occurs in asymmetric systems or in systems that only have a small asymmetry but have closely spaced modes in terms of their frequency. The small asymmetry might occur in the New Orleans tower as a result of some deviating floor plans and the orientation of the openings in the stability core. Besides, the foundation contains very slight asymmetries.

The sudden increase in structural response could also be a result of a shift in wind direction, where the wind aligns with the corner of the building (Kijewski-Correa and Pirnia, 2007). This means that the wind direction would be at an angle of 45° or 135°. Comparing fig. 7.2 and fig. 7.12, it is possible to spot such a pattern for some instances, but this is definitely not a proof that this is occurring.

A similar measurement analysis has been performed for other wind directions. These measurements showed similar results. However, since this thesis will only use the measurements with the wind direction perpendicular to the south facade, the other measurements are not discussed here.

8

Energy Flux Analysis model

Chapter 5 explained the Energy Flux Analysis for general application, provided a structure can be modelled using an Euler-Bernoulli beam. This chapter will derive the EFA equations to be used for the application to the New Orleans tower, or any high-rise building where the following assumptions can be made:

- Twist or torsion will not be considered. Due to the square cross-section of the New Orleans tower, twist is not expected to be of major importance and is not significantly present in the measurements. This assumption will cancel out all the $w'_x(x,t)$ terms.
- Axial deformation is assumed to be very small compared to deformations in y- and z-direction. Most of the building's axial deformation will take place during construction or in the beginning of its service life, pure axial deformation due to wind load is not expected. As a result γ_{xy} and γ_{xz} are 0.

Using these two assumptions, λ can be reduced to:

$$\begin{aligned}\lambda &= \frac{1}{2}\rho A\left(\left(-z\dot{w}'_z - y\dot{w}'_y\right)^2 + \dot{w}_y^2 + \dot{w}_z^2\right) - \frac{1}{2}E\int_A\left(-zw''_z - yw''_y\right)^2 \,\mathrm{d}A \\ &= \frac{1}{2}\rho A\left(z^2\dot{w}'^2_z + y^2\dot{w}'^2_y + 2yz\dot{w}'_z\dot{w}'_y + \dot{w}_y^2 + \dot{w}_z^2\right) - \frac{1}{2}EI_{yy}w''^2_z - \frac{1}{2}EI_{zz}w''^2_y - EI_{yz}w''_z w''_y\end{aligned} \tag{8.1}$$

The expression for λ is used to find the equations of motion with the free and flexible boundary conditions for the beam, and to find the energy change in the beam and the energy-flux at any specified boundary. This is done with the help of eq. (5.2) and § 5.1.2. The equations of motion are as follows:

$$\rho A\ddot{w}_y + EI_{zz}w''''_y + EI_{yz}w''''_z = 0 \quad \text{in y-direction} \tag{8.2}$$
$$\rho A\ddot{w}_z + EI_{yy}w''''_z + EI_{yz}w''''_y = 0 \quad \text{in z-direction} \tag{8.3}$$

The boundary conditions for a beam with a flexible end at $x = 0$, and a free end at $x = L$ are the following:

$$EI_{zz}w'''_y + EI_{yz}w'''_z = -K_t w_y \quad \text{for } x = 0 \text{ in y-direction} \tag{8.4}$$
$$EI_{yy}w'''_z + EI_{yz}w'''_y = -K_t w_z \quad \text{for } x = 0 \text{ in z-direction} \tag{8.5}$$
$$EI_{zz}w'''_y + EI_{yz}w'''_z = 0 \quad \text{for } x = L \text{ in y-direction} \tag{8.6}$$
$$EI_{yy}w'''_z + EI_{yz}w'''_y = 0 \quad \text{for } x = L \text{ in z-direction} \tag{8.7}$$

These boundary conditions represent the forces at the flexible and the free end. The boundary conditions for the bending moments at these ends are given by:

$$-EI_{zz}w''_y - EI_{yz}w''_z = -K_\theta w'_y \quad \text{for } x = 0 \text{ in y-direction} \tag{8.8}$$
$$-EI_{yy}w''_z - EI_{yz}w''_y = -K_\theta w'_z \quad \text{for } x = 0 \text{ in z-direction} \tag{8.9}$$
$$-EI_{zz}w''_y - EI_{yz}w''_z = 0 \quad \text{for } x = L \text{ in y-direction} \tag{8.10}$$
$$-EI_{yy}w''_z - EI_{yz}w''_y = 0 \quad \text{for } x = L \text{ in z-direction} \tag{8.11}$$

It is assumed that the translational stiffness K_t and the rotational stiffness K_θ of the springs, representing the soil, are the same in both directions.

The total energy flux at a system boundary, considering both directions, gives the following result:

$$\begin{aligned} S(x,t) &= \dot{w}_z\left(EI_{yy}w_z''' + EI_{yz}w_y'''\right) + \dot{w}_y\left(EIzzw_y''' + EI_{yz}w_z'''\right) \\ &+ \dot{w}_z'\left(-EI_{yy}w_z'' - EI_{yz}w_y''\right) + \dot{w}_y'\left(-EI_{zz}w_y'' - EI_{yz}w_z''\right) \\ &= \dot{w}_z'M_y + \dot{w}_y'M_z - \dot{w}_zQ_y - \dot{w}_yQ_z \end{aligned} \tag{8.12}$$

The Hamiltonian density is given as follows:

$$e = \frac{1}{2}\rho A\left(z^2\dot{w}_z'^2 + y^2\dot{w}_y'^2 + 2yz\dot{w}_z'\dot{w}_y' + \dot{w}_y^2 + \dot{w}_z^2\right) + \frac{1}{2}EI_{yy}w_z''^2 + \frac{1}{2}EI_{zz}w_y''^2 + EI_{yz}w_z''w_y'' \tag{8.13}$$

This results in the energy term for the beam, of which the first derivative is the energy change as given in the energy flux balance in eq. (5.1).

$$\begin{aligned} E_{SS}(t) &= K_{SS} + P_{SS} \\ &= \int_L \frac{1}{2}\rho A\left(z^2\dot{w}_z'^2 + y^2\dot{w}_y'^2 + 2yz\dot{w}_z'\dot{w}_y' + \dot{w}_y^2 + \dot{w}_z^2\right) + \frac{1}{2}EI_{yy}w_z''^2 + \frac{1}{2}EI_{zz}w_y''^2 + EI_{yz}w_z''w_y''\mathrm{d}x \end{aligned} \tag{8.14}$$

This equations gives the total energy in the Euler-Bernoulli beam. The potential energy due to the SSI stiffness should be added to this and is shown in eq. (8.15). The SSI does not have kinetic energy, since no additional mass is assumed here.

$$E_{SSI}(t) = P_{SSI} = \frac{1}{2}K_t(w_y^2 + w_z^2) + \frac{1}{2}K_\theta(w_y'^2 + w_z'^2) \tag{8.15}$$

Together, E_{SS} and E_{SSI} give the total system energy.

The total energy flux for a specific system is given by the difference between the flux at the upper and the flux at the lower bound value of the system. For the superstructure, the upper bound is at the top of the building at $x = L$ and the lower bound is at the foundation at $x = 0$. Since the energy flux is dependent on the bending moment and shear force in the beam, it is plausible to assume that the energy-flux at the top of the beam is zero.

$$\begin{aligned} S_{SS}(t) &= 0 - S(0,t) \\ &= -\dot{w}_z'\left(-EI_{yy}w_z'' - EI_{yz}w_y''\right) - \dot{w}_y'\left(-EI_{zz}w_y'' - EI_{yz}w_z''\right) \\ &+ \dot{w}_z\left(-EI_{yy}w_z''' - EI_{yz}w_y'''\right) + \dot{w}_y\left(-EIzzw_y''' - EI_{yz}w_z'''\right) \end{aligned} \tag{8.16}$$

The energy flux at the bottom of the SSI system is zero, any flux here is taken care of by the springs in the total energy. The energy flux of the SSI at the boundary of the superstructure is exactly opposite to that of the superstructure:

$$\begin{aligned} S_{SSI} &= S(0,t) - 0 \\ &= \dot{w}_z'\left(-EI_{yy}w_z'' - EI_{yz}w_y''\right) + \dot{w}_y'\left(-EI_{zz}w_y'' - EI_{yz}w_z''\right) \\ &- \dot{w}_z\left(-EI_{yy}w_z''' - EI_{yz}w_y'''\right) - \dot{w}_y\left(-EIzzw_y''' - EI_{yz}w_z'''\right) \end{aligned} \tag{8.17}$$

Finally the external energy flux with eq. (5.18) and assuming the external force is only acting horizontally:

$$W_{ext}(t)_= \int_L q(x,t)\left(\dot{w}_y + \dot{w}_z\right)\,\mathrm{d}x \tag{8.18}$$

Since this is the change of external energy introduced to the system, it is the derivative of the external energy. In this equation $q(x,t)$ is the distributed force over the system height.

The energy dissipation flux is obtained through the energy flux balance:

$$W_{diss}(t) = -\frac{\mathrm{d}E(t)}{\mathrm{d}t} - S(t) + W_{ext}(t) \tag{8.19}$$

Finally, the dissipated energy is simply found from the energy dissipation flux through integration over running time:

$$E_{diss} = \int_0^t W_{diss}(t)\mathrm{d}t \tag{8.20}$$

III

SENSITIVITY

9

Structure motion

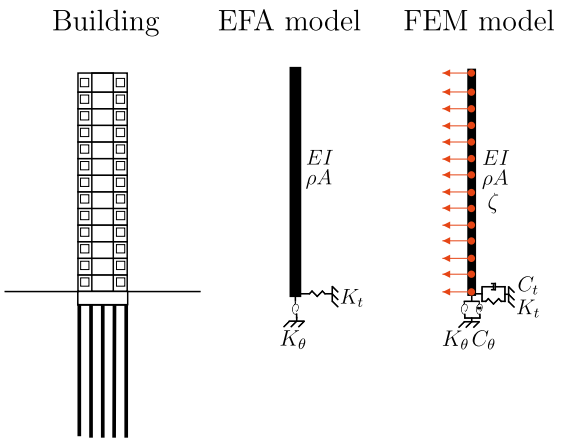

Figure 9.1: Models and extracting nodal information from FEM model

This chapter focuses on the sensitivity of the Energy Flux Analysis (EFA) to the inevitable spatial incompleteness of structure motion information. First, the model built to perform the EFA presented in chapter 8 is verified by comparison with the results of a Finite Element Method (FEM) model. The verification is part of this chapter, as the FEM model is excited by an initial displacement rather than an external load, and because the structure properties are the same for both models. It verifies the model based on structure motion only. After this, the actual sensitivity of the EFA to spatial incompleteness is investigated using the same FEM model. The sensitivity study is performed by applying several measurement set-ups and extrapolation models, and comparison of their results with the FEM results.

9.1. Model verification

The EFA is performed through a Python script. Upon applying this script to the actual measurements, there was a desire to verify it. Besides, a convergence study was performed in terms of sampling frequency and mesh of the FEM model. For the verification study, all nodal information of this FEM model is used.

The FEM model is made in Abaqus. Identical to the EFA model, the high-rise structure in the FEM model is represented by an Euler-Bernoulli beam model. The beam is free at one end and has flexible translational and rotational supports at the other end. The beam model motion is considered in one direction only. The structure properties building mass, building stiffness, and foundation rotational and translational stiffnes used for the EFA and FEM model are the same, and the rotational and translational viscous damper values were taken from the Dynapile calculations performed by TNO (Bronkhorst et al., 2018). Damping in the superstructure is modelled using Rayleigh damping with a stiffness proportional value β of 0.023. This value

was found using the damping values for two natural frequencies obtained using Jeary's damping predictor (Jeary, 1986). The FEM model was made of 862 elements, a mesh size of 0.18 m. A mesh study showed that this mesh size does not affect the results.

Rather than modelling the wind load, the model was brought to motion through an initial displacement followed by a free decay of motion. This is justified arguing that the structure under wind loading vibrates in its lower natural frequencies only. This is also the case for the free decay motion, especially after several cycles. According to previous studies discussed in chapter 3 the deformed shape of a high-rise building under wind excitation resembles either this first mode shape or vibrates more linearly. The deformation shape depends on the structure itself, such as its height or structural system.

The FEM model directly provides the energy and energy dissipation in time for different parts of the model. The systems under investigation in this chapter are the total structure, the superstructure (SS) and soil-structure interaction (SSI) as is visualised in fig. 9.2. These energies are compared to the energies computed through the EFA. In order to compute these energies, all nodal building motion information is extracted; displacement, rotation, velocity, rotational velocity, foundation shear force and foundation bending moment. This is visualised in fig. 9.1.

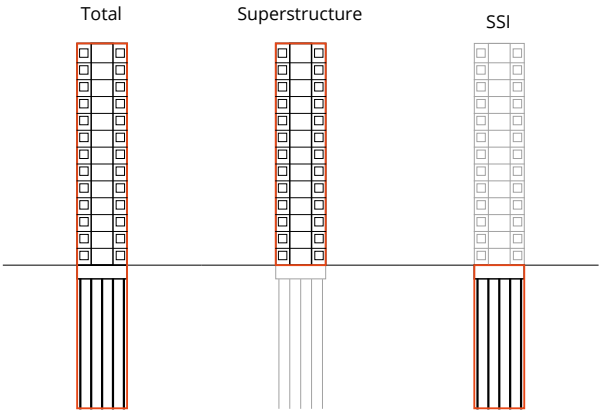

Figure 9.2: Systems under investigation for damping identification using limited motion measurements

The beam kinetic energy, K_{SS}, the beam potential energy, P_{SS}, and the spring potential energy, P_{SSI}, calculated in the EFA are shown in fig. 9.3. The dissipated energy in the total system obtained through the EFA and obtained from FEM are shown in fig. 9.4. This total dissipated energy, which is the sum of the superstructure dissipated energy in eq. (8.14) and the soil-structure interaction dissipated energy in eq. (8.15), has an error of no more than 0.2% compared to the FEM energy. This error was calculated as an average of the error between the two signals at any point in time. The error is small and could be a result of numerical differences.

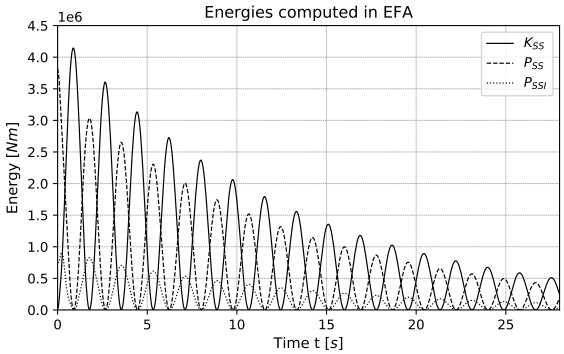

Figure 9.3: Energies in the total system computed using the EFA

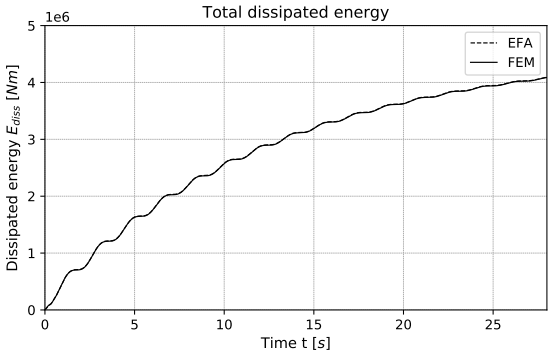

Figure 9.4: Total dissipated energy from the EFA and FEM

An interesting feature of the EFA is its ability to make a distinction between the contribution of the superstructure and the SSI separately to this dissipated energy using eq. (8.14) and eq. (8.15). In these equations the energy flux at the system boundary has to be computed. The equation was solved using the shear force,

translation velocity, bending moment, and rotational velocity at foundation level of the FEM model directly. Again, the dissipated energy found in time resembles that obtained from the FEM model directly. This means that the EFA has been verified when all required information is available.

As previously mentioned, in practice there will always be spatial incompleteness of measurements. Therefore, next section will compare the results of several measurement set-ups in terms of measurement location and information, and the extrapolation model used.

9.2. Measurement sensitivity

Accurate results for the dissipated energy using the EFA can be obtained when all nodal information is available. Since in practice limited measurements can be performed, a decision always has be to made on what to measure, where to measure, and how to extrapolate the measurements to the remaining of the structure. The sensitivity of the EFA results to spatial incompleteness and the decisions on measurement set-up and extrapolation model is investigated by comparing the computed dissipated energy with the dissipated energy obtained directly from the FEM model. The sensitivity study is performed using the same FEM model as used for the verification in § 9.1.

9.2.1. Measurement models

When applying the Energy Flux Analysis to the Jubi tower, Gómez (Gómez, 2019) used linear interpolation of the measurements on the 9^{th} and 37^{th} floor. The approach of Gómez is described in more detail in § 5.4. However, an alternative approach would be using the fundamental mode shape as extrapolation model. It is yet to be investigated what the effect is of this extrapolation model chosen. The two extrapolation models that will be compared in this chapter are the linear model and the model based on the Euler-Bernoulli beam mode shape. The latter model is applied using different measurement set-ups. A short description of the models used is provided:

- Linear model (Linear): For this model acceleration measurements at 0 and 114 m are used and at 0 m the translation and rotational velocity, shear force and bending moment information are used. The measurements at foundation level are included because a linear model does not allow for predicting the motion at the foundation through the deformed shape. The measured deformation at 114 m height is linearly extrapolated to the measured value at foundation level, and the measured bending moment at foundation level is linearly extrapolated to 0 at the free end of the beam.
- Mode shape (MS): The mode shape, the deformed shape of the free-flexible beam model for the first fundamental mode of vibration described in chapter 3, is used for extrapolation. The structure properties used to find this mode shape are the same as those used as input for the FEM model, and the mode shape is normalised to the measurement location at 114 m. This approach is divided in three cases with an increasing amount of information used:
  - Mode shape 1 (MS1): Only acceleration measurements at 114 m are used.
  - Mode shape 2 (MS2): Acceleration measurements at 0 and at 114 m are used.
  - Mode shape 3 (MS3): Acceleration measurements at 0 and at 114 m are used and additionally the rotational velocity at 0 m is used.

The measurement location of 114 m height was chosen as this is the measurement location of the New Orleans tower. To make sure the mesh size of the mode shape does not affect the EFA results, a short mesh convergence study has been performed and is presented in appendix C.

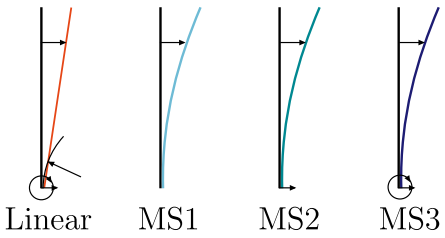

Figure 9.5: Measurement models compared

9.2.2. Results

This section will present the energies obtained with the measurement models compared to the energy output of the FEM model. Figure 9.6 presents the kinetic energy of the superstructure found with the measurement models. It visualises the substantial overestimation of the kinetic energy in the beam when using the linear extrapolation model. This is due to the fact that the linear model overestimates the beam deformation. Similar results were found for the beam potential energy, as the linear model overestimates the beam curvature for any point along the beam height. Although not directly visible from fig. 9.6, the kinetic energy found using the other extrapolation models is in very good agreement with the energy from the FEM model. In fig. 9.7

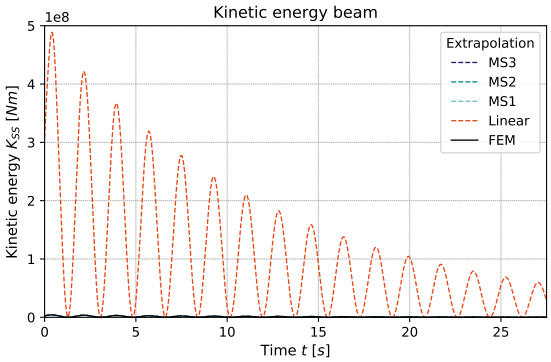

Figure 9.6: Kinetic energy in beam

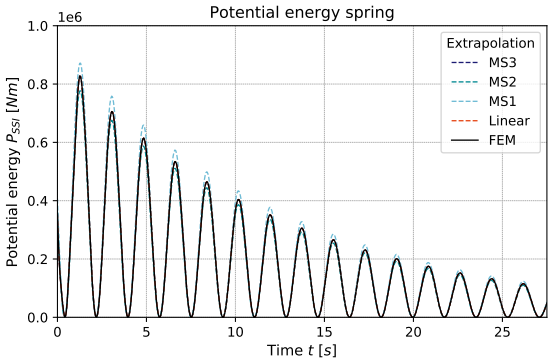

Figure 9.7: Potential energy in spring

the potential energy in the springs representing the SSI for each extrapolation model is shown. The linear and MS3 model provide the exact energies, because all required information is measured at foundation level. The MS1 model slightly overestimates the potential spring energy, whereas the MS2 model slightly underestimates it. This is a result of the MS1 model overestimating the foundation translation deformation, and both MS1 and MS2 underestimating the foundation rotation.

Total structure

The total dissipated energy computed with the different extrapolation models is visualised in fig. 9.8. It demonstrates the substantial overestimation of the energy using the linear extrapolation model. This overestimation is a direct result of the overestimation of the total energy in the system, resulting in more energy being dissipated per cycle. A zoomed in figure of the graph in fig. 9.9 demonstrates that the dissipated energies found with the mode shape models show improved results. Although not the differences are extremely small, the MS3 model provides the best approximation of the FEM dissipated energy. The difference between the MS1 and MS2 results is even smaller.

The conclusion is drawn that the EFA is very sensitive to the extrapolation model used. If linear extrapolation is performed for a building with vibrates in its fundamental mode shape, overestimation of damping is expected. It is advised to investigate the deformed shape of a structure upon applying an extrapolation model. Measuring at multiple locations along the building height will reveal the deformation shape of the structure. Once this shape is known, a suitable extrapolation model can be chosen and results can be considered sufficiently accurate. For very tall structures it is often argued that the deformed shape is in the first mode of vibration, as was discussed in chapter 3. In this case measurement at one location only and using the mode shape extrapolation should yield sufficiently accurate results. Possible discontinuities in terms of structural properties which may further alter the deformation shape have not been considered.

Contribution superstructure (SS) and soil-structure interaction (SSI)

The dissipated energy for the superstructure is shown in fig. 9.10. This is again a zoomed in figure, the linear extrapolation model largely overestimates the superstructure dissipated energy. This time the mode shape models also overestimate the superstructure dissipated energy. However, fig. 9.11 shows that all mode shape models underestimate the soil-structure interaction dissipated energy. In fact, the overestimation for the superstructure and the underestimation for the soil-structure interaction are of equal magnitude. This means that the error is a direct result of the energy flux term computed at the boundary of the superstructure and the foundation presented in eq. (8.16) and eq. (8.17). Another conclusion drawn from these graphs is the fact

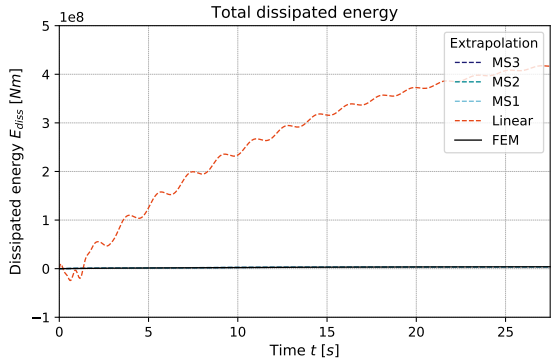

Figure 9.8: Total dissipated energy extrapolation models

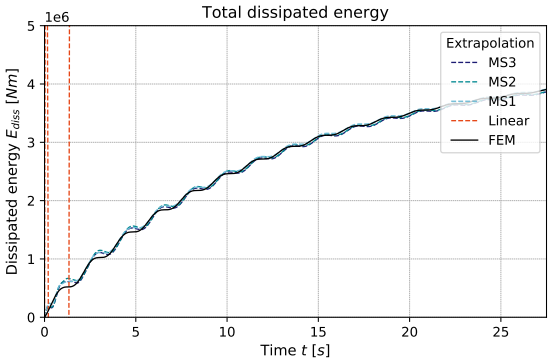

Figure 9.9: Zoom total dissipated energy extrapolation models

that measurement of the translation deformation at foundation level does not result in an improvement of the dissipated energy estimate. This is because the translation dashpot has a relatively small damping value.

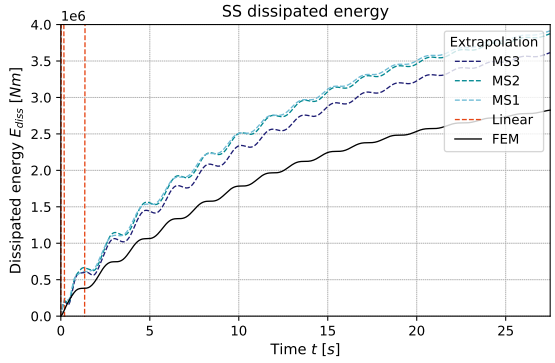

Figure 9.10: Zoom SS dissipated energy extrapolation models

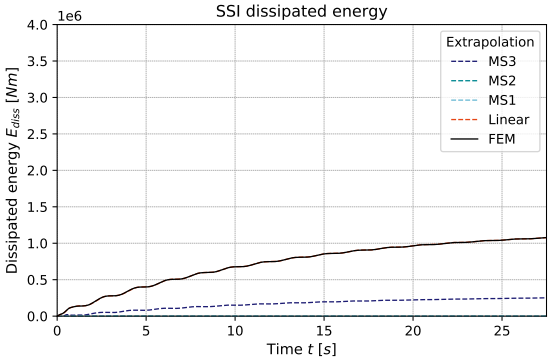

Figure 9.11: SSI dissipated energy extrapolation models

9.2.3. Phase difference

It is of importance to find the cause for the erroneous description of the energy flux at the superstructure and soil-structure interaction boundary. Two causes were found. Both are a direct result of the modelling of damping which results in a phase difference. Both causes and their consequences will be discussed separately in this section.

Dashpot damping

First of all, measurement of the rotation at foundation level improves the results as the MS3 model better approaches the FEM dissipated energy than the MS1 and MS2 models. Clearly, the approximation of the rotation at foundation level through the mode shape introduces an error. To visualise this, the rotation obtained from the FEM model and the rotation computed using the measurement at 114 m and the mode shape are compared in fig. 9.12. This figure shows a slight difference in amplitude, and a slight difference in phase. The phase difference between the captured motion at 114 m height and foundation level is approximately 0.0065 s and is constant in time. It is this phase difference that it most relevant to capture to better approximate the dissipated energy in the separate structural components. This phase difference is a result of the dashpot located at the bottom of the beam to account for SSI damping. Due to the small damping value prescribed to the translation dashpot, this effect mainly occurs in terms of rotation through the rotational dashpot. The phase difference between the rotation at foundation level and a location along the beam height increases with beam height as is shown in fig. 9.14. This means that measuring at a larger height does not allow for capturing this phase difference and therefore does not allow for computing the separate contributions to the total damping.

This effect is a direct result of the method of modelling SSI damping in this FEM model using a dashpot.

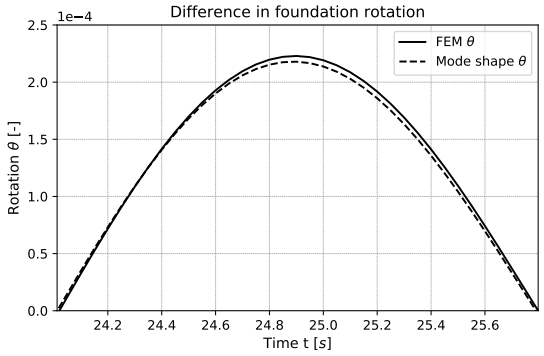

Figure 9.12: Difference rotation directly from FEM and calculated using the mode shape

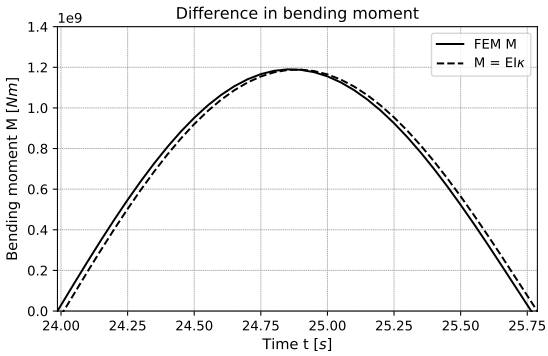

Figure 9.13: Difference bending moment directly from FEM and calculated using the curvature

It is important to consider whether this effect will occur in a true structure. As damping affects the time response of a system, it is not unlikely that localised damping will result in a phase difference in terms of motion compared to the structure motion away from this damping location. The effect of correcting for this phase difference is shown in fig. 9.10 and fig. 9.11 as the difference between the dissipated energy of MS1 and MS2 on the one hand and MS3 on the other. However, these figures also show that this is not the only cause for the erroneous results. The second cause is found in the phase difference as a result of material damping.

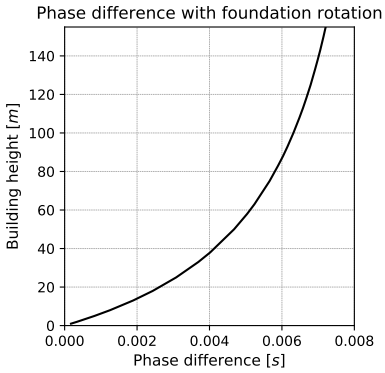

Figure 9.14: Phase difference between foundation rotation and motion along the structure height

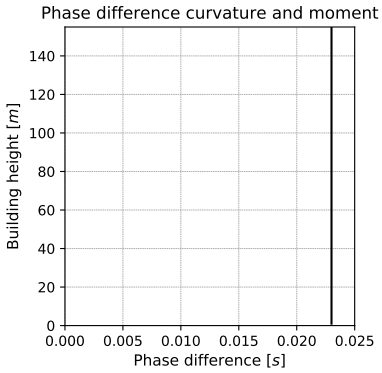

Figure 9.15: Phase difference between bending moment and curvature

Material damping

Another phase difference was observed. This phase difference occurs between stress and strain, or rather between the FEM curvature and the FEM bending moment. The curvature obtained from the mode shape is very similar to the curvature obtained directly from the FEM model at foundation level. Only a slight difference occurs in terms of amplitude. However, when either of these curvatures is used to compute the bending moment through $M = EI\kappa$, both show a difference in terms of phase with the bending moment directly obtained from the FEM model. This difference is visualised in fig. 9.13.

When the bending moment directly obtained from FEM is used to compute the dissipated energy, the results presented in fig. 9.16 and fig. 9.17 are obtained. The results obtained with the MS3 model are sufficiently accurate. This means that either the difference in amplitude, the difference in phase, or both, caused the error in the dissipated energy previously presented.

The sensitivity of the dissipated energy result to the bending moment amplitude and the bending moment phase was investigated separately for the SSI dissipated energy, and the results are visualised in fig. 9.18 and fig. 9.19. From these figures it is clear that the sensitivity of the dissipated energy to the amplitude of the bending moment is relatively small. An error in the amplitude of 50% results in an error in the dissipated energy of approximately 75%. Looking at fig. 9.13 one can see that the difference in amplitude is very small, a small error in the dissipated energy can be expected as a result of the amplitude error.

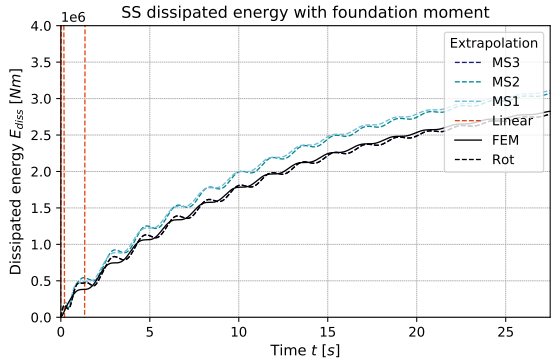

Figure 9.16: Dissipated energy superstructure extrapolation models using foundation moment

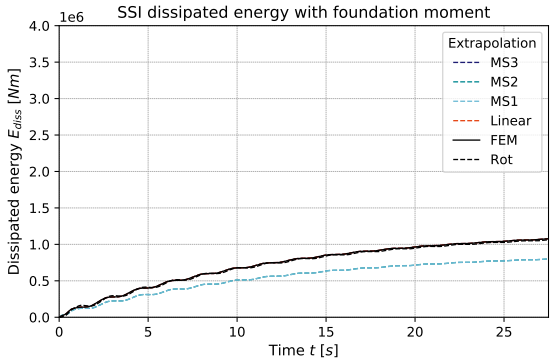

Figure 9.17: Dissipated energy SSI extrapolation models using foundation moment

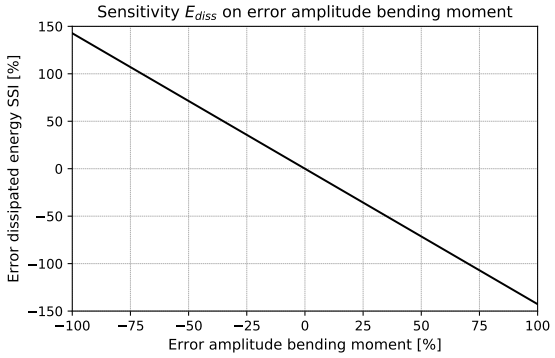

Figure 9.18: Error E_{diss} SSI due to amplitude error

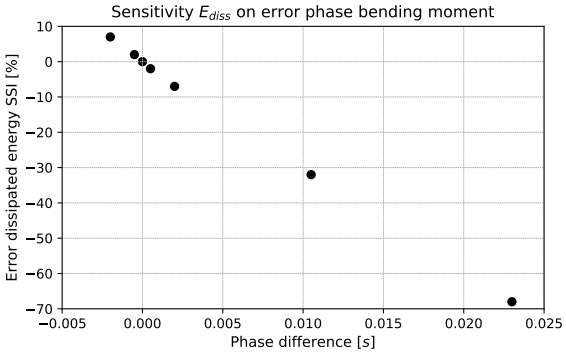

Figure 9.19: Error E_{diss} SSI due to phase difference

However, a very small phase difference of only 0.023 s results in an error in the dissipated energy of almost 70%. Clearly, the phase difference between the bending moment and the curvature has to be captured to obtain accurate results for the dissipated energy. The cause of this phase difference was found in the description of material damping in the FEM model and fig. 9.15 shows that this phase difference is constant over the beam height. The material damping in the FEM model is further discussed in appendix D.

The question remains whether this phase difference between bending moment and curvature, or between stress and strain, will occur when measurements are performed on a real structure. In case of an ideal elastic material, the stress and the strain are in phase. For an ideal viscous material, the stress and strain are 90° out of phase (Meyers and Chawla, 2008). For viscoelastic materials, the behaviour is a combination of an ideal elastic response and an ideal viscous response and for these materials a phase shift occurs between 0 and 90° (Meyers and Chawla, 2008). It is important to know whether the building materials of high-rise buildings behave visco-elastically under wind loading. The behaviour of concrete under dynamic loading is viscoelastic (Fan et al., 2013), whereas steel is an elastic material for the small amplitudes of vibration occurring in high-rise buildings and therefore no phase shift is expected. Wood is used more often for high-rise buildings nowadays and is also viscoelastic. Therefore, for high-rise buildings containing concrete or wood, a phase shift between the stress and strain should be expected.

Assuming the phase difference in the relation between stress and strain occurs in a true structure, it is important to calculate the energy flux using the building internal force directly rather than through building motion. Rather than from the curvature, the bending moment should be computed from the stress directly using $M = \sigma I / y$. In this equation y is the distance from the centre to the fibre and σ is the measured stress at this fibre. This is challenging as stress measurements are usually performed using strain gauges.

It is important to mention that the phase differences discussed in this section occur as a result of an applied dashpot and material damping. The influence of damping of non-structural elements or damping in joints on the measurements is unknown. Whether the phase difference due to dashpot or material damping is relevant depends on the contribution of different damping mechanisms occurring in the structure.

9.3. Conclusions

This chapter focused on the sensitivity of the Energy Flux Analysis to the inevitable spatial incompleteness of building motion information. Upon performing the sensitivity study, the Energy Flux Analysis model was verified using a FEM model. Both model the high-rise building as an Euler-Bernoulli beam with the same structural properties, and the model was brought in motion by an initial displacement rather than an external load. From this verification study it followed that the total dissipated energy of the structure, as well as the superstructure and soil-structure interaction dissipated energy was accurately retrieved using the Energy Flux Analysis.

After this verification study, the influence of the measurement set-up and extrapolation model of the measured building motion on the results of the Energy Flux Analysis was investigated. This study showed that the linear extrapolation model largely overestimates the total energy in the structure, and it subsequently overestimates the total dissipated energy and superstructure dissipated energy. This means that the Energy Flux Analysis is highly sensitive to the extrapolation model used, and that the aim should be to resemble the true structure deformation. This true structure deformation could be investigated by measuring acceleration at several points along the structure height. For very tall structures it is often argued that bending is the dominant deformation, the mode shape should be the most suitable extrapolation model for these structures. However, the effect of discontinuities in structural properties over the structure height on the structure deformation will also affect the deformed shape.

When using limited measurements, and applying the measurement set-up and extrapolation models using acceleration measurements along the building height only, it is possible to accurately describe total structure dissipated energy. However, when a distinction needed to be made between the superstructure and soil-structure interaction dissipated energy, large differences were found. These differences were a direct result of an erroneous description of the energy flux at the superstructure and foundation boundary. The modelling of damping by means of a dashpot at foundation level resulted in a phase difference between rotation at foundation level and structure motion along the beam height. This phase difference increases with height, and has to be captured to accurately describe the component dissipated energy. A similar effect was found for the material damping modelled. This resulted in a phase difference between curvature, either obtained from FEM or computed through the mode shape, and the bending moment. The classical relation of $M = EI\kappa$ is no longer valid and the phase of the bending moment has to be captured to obtain reliable dissipated energy results. Whether these phase differences may occur in a true structure is to be investigated. Besides, a true structure will contain many more damping mechanisms which may result in similar effects. To be able to describe the energy flux at the boundary using the right phase information, it is advised to measure all required terms, structure motion and internal forces, at the boundary directly rather than through extrapolation. This is challenging as stress is commonly measured through strain gauges, while a phase difference is expected between stress and strain. It is good to remember that this energy flux at the boundary does not have to be calculated when one is interested in the total dissipated energy of the structure.

10

Wind load

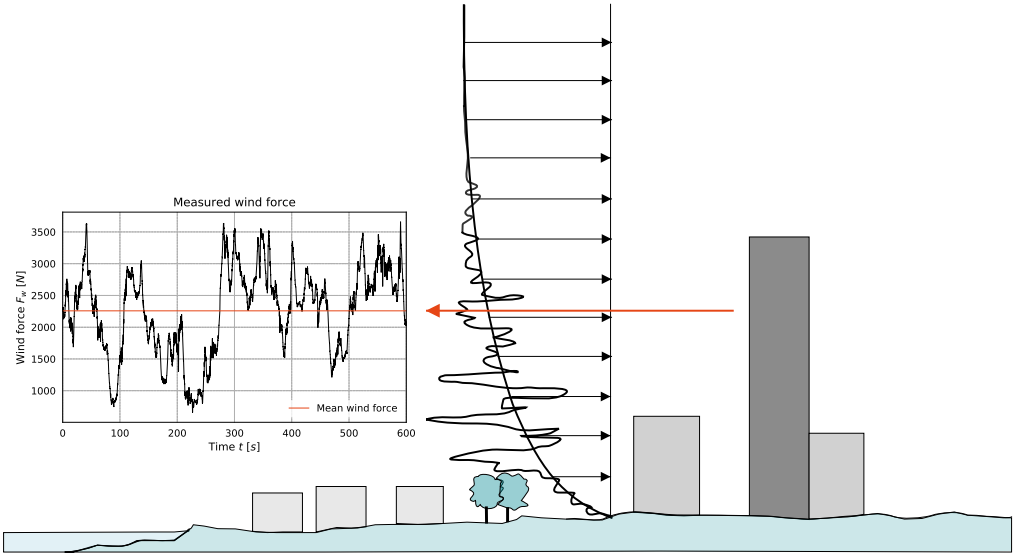

Figure 10.1: Mean and fluctuating wind load and measurement at 114 m height

10.1. Introduction

Previous section focused on the sensitivity of the Energy Flux Analysis (EFA) to the structure motion and the inevitable spatial incompleteness of structure motion information. This chapter will focus on the sensitivity of the EFA to the wind load input. Spatial incompleteness of wind load information is also inevitable, and due to the random nature of wind load it is not straightforward to extrapolate measured wind load to other locations. As the focus of this thesis is the sensitivity of the EFA rather than an accurate description of the wind load, the wind load will be modelled using a reference approach. Sensitivity is then investigated through alternative approaches to model wind load and the result of the EFA using these approaches will be compared.

In this chapter, the FEM model from previous chapter is no longer used. The EFA is now performed using 10-minute wind pressure and acceleration measurements on the New Orleans tower. In all measurements, the wind is approaching in the positive z-direction. The axes are shown in fig. 6.1 and this wind angle is visualised in fig. 6.3 indicated with a 144 degree angle with the north. The average wind velocity in these measurements is 13 m/s. A further analysis of the measurements was discussed in chapter 7. The structural properties used for the EFA in this chapter remain the same and are presented in table 10.1. Variation of these properties is studied in chapter 12. These structural properties meet the measured natural frequency in z-direction of 0.283 Hz and in y-direction of 0.293 Hz using the natural frequency of an Euler Bernoulli beam presented in appendix A.

The dissipated energy computed in this chapter is based on the structural motion measurements at 114 m height only, which were discussed in chapter 7. This means that based on the findings in chapter 9, it is only possible to accurately find the total dissipated energy of the structure. Therefore, this chapter will only present the total dissipated energy of the building and structure motion extrapolation is done using the fundamental mode shape of the Euler Bernoulli beam with the properties presented in table 10.1.

ρ_b [kg/m^3]	EI_{yy} [N/m^2]	EI_{zz} [N/m^2]	EI_{yz} [N/m^2]	$K_{\theta_y} = K_{\theta_z}$ [Nm/rad]	$K_y = K_z$ [N/m]
555	9.24×10^{13}	1.02×10^{14}	5.32×10^{10}	1.13×10^{13}	1.62×10^{9}

Table 10.1: Structural properties used for the wind sensitivity study

10.2. Reference wind load

10.2.1. Reference wind modelling

Chapter 2 described the wind load as the combination of a mean wind load and a fluctuating wind load. In this case, the mean wind load refers to the 10-minute mean of the measurements. This chapter also showed that a common profile to describe wind velocity over height is the logarithmic profile. The relation between wind velocity and wind pressure is squared, as is presented in eq. (2.10). Therefore, the reference approach uses the logarithmic squared vertical wind profile to extrapolate the wind load. Usually this profile is used to extrapolate the mean only, but the reference also uses it to extrapolate the measured wind fluctuations as is presented in fig. 10.2. The resulting wind load fluctuations vary over the building height in terms of magnitude, but they do not vary in terms of phase. The fact that through this modelling the wind fluctuations are larger at the top of the structure rather than at the bottom as is expected from the turbulence intensity is considered acceptable as the aim of this study is a sensitivity study.

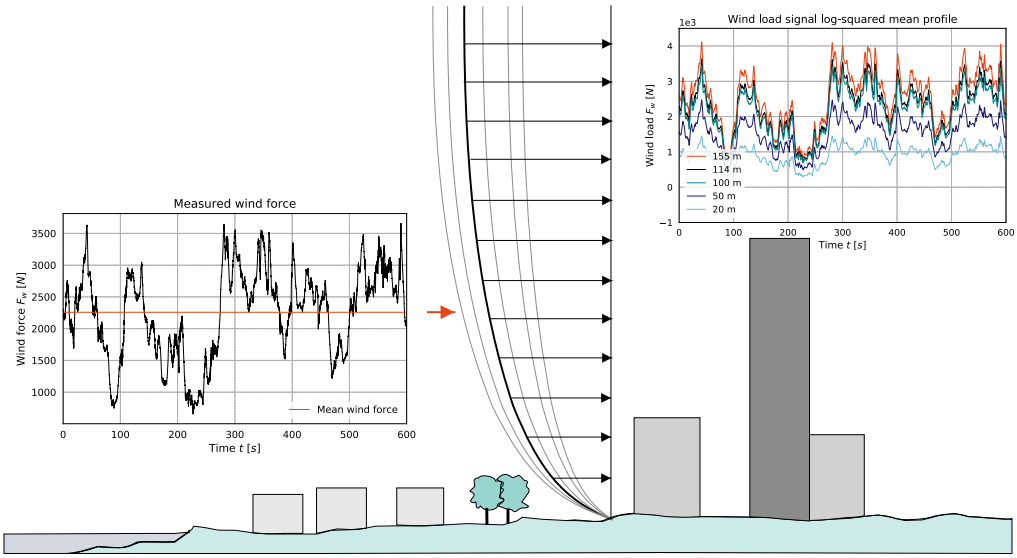

Figure 10.2: Reference wind modelling using measurement and logarithmic squared wind profile

The description of the vertical logarithmic profile was discussed in § 2.1.1 in eq. (2.2). The roughness length z_0 is taken to be 1.0 m, and no zero-displacement height is found for wind approaching from the direction shown in fig. 6.3. Using the wind velocity measurements at the top of the building, the friction velocity u_* was determined.

10.2.2. Reference results

First, the reference wind load is used to perform the Energy Flux Analysis for the 16 measurements described in § 10.1. The dissipated energy in time and the computed damping ratios computed using § 5.3 corresponding to z- and y-direction are presented in fig. 10.3.

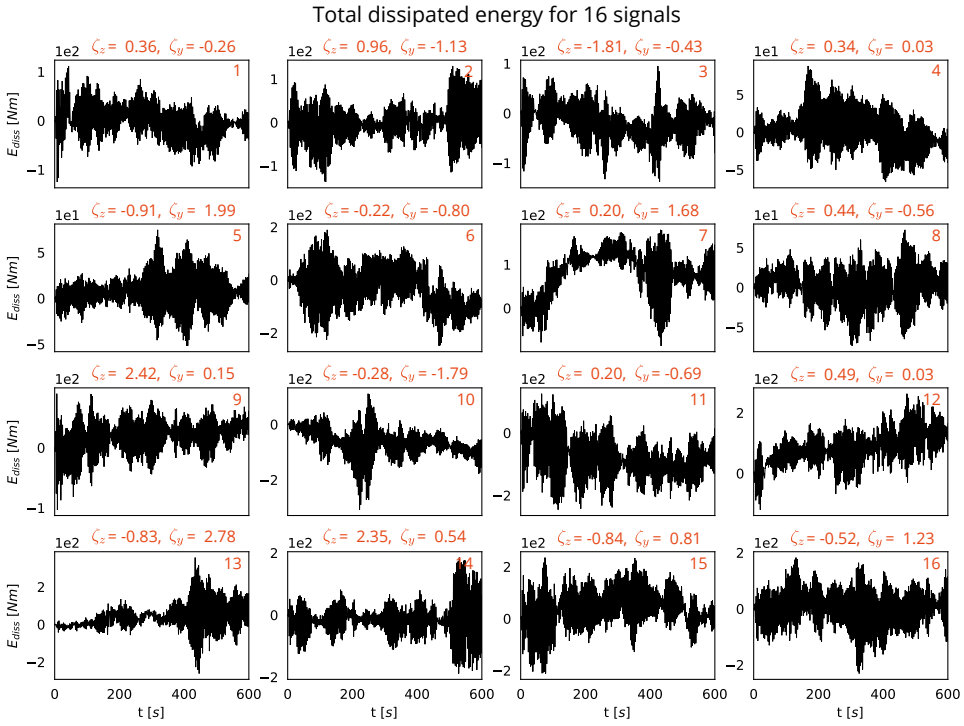

Figure 10.3: Total dissipated energy for 16 different signals with wind velocity of 13 m/s and wind in z-direction

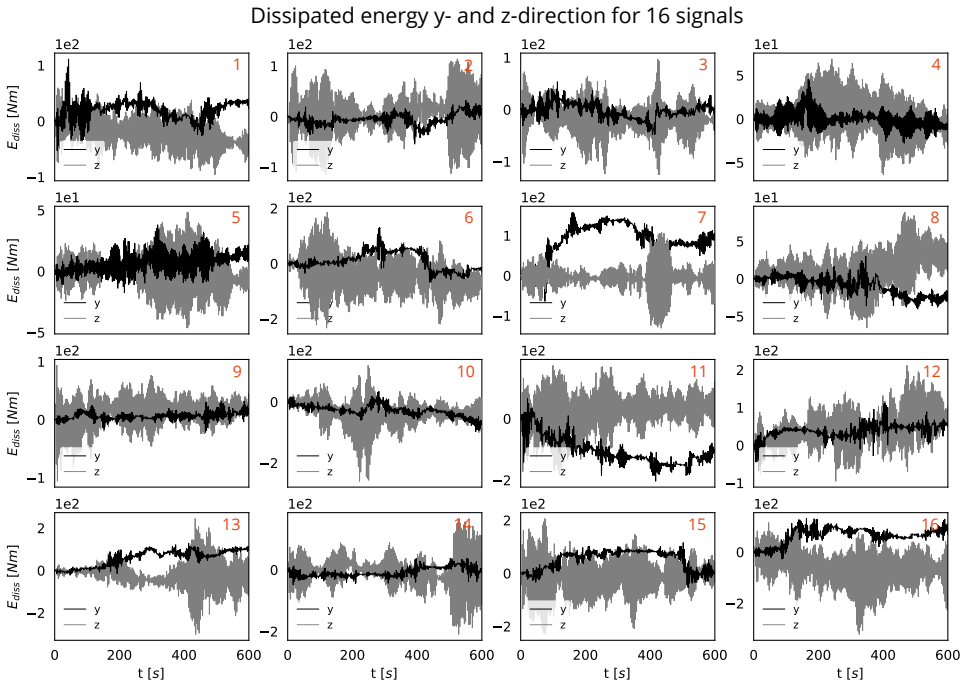

Figure 10.4: Dissipation in y- and in z-direction for the same 16 signals as shown in fig. 10.3

Since the wind continuously supplies energy to the structure, while the structure motion does not infinitely increase, one would expect the dissipated energy to increase in time. However, this is definitely not the case for every measurement. Even within 10-minute measurements, the trend trend of the dissipated energy may vary from increasing, to decreasing to remaining constant. This inconsistency directly translates to the damping ratios computed, which vary largely per signal and even show negative values.

The dissipated energy presented here is the total of the dissipated energy in along wind direction (z-

direction) and cross wind direction (y-direction). The previous statement of expecting the dissipated energy to increase holds for the along wind direction, and the summation of the along wind and cross wind energies. However, due to vortex shedding, for the cross wind direction the dissipated energy signal does not necessarily have to be an increasing signal. In vortex shedding the interaction between wind and the building motion might cause the wind to extract energy from the building. Therefore, fig. 10.4 presents the dissipated energy when computed for y- and z-direction separately. These graphs show that the varying trend in dissipated energy occur for both along wind and cross wind direction, while it is only physically possible for cross wind direction. These figures also showed that calculating the dissipated energy for z- and y-direction separately and summation of these results, yields the dissipated energy shown in fig. 10.3. This indicates that the cross term EI_{yz} applied in the Energy Flux Analysis in table 10.1 is negligible.

The dissipated energy signals in fig. 10.4 show large fluctuations of the signals in z-direction and smaller fluctuations of the signals in y-direction. This is a result of the mean wind load being much larger in z-direction. The dissipated energy is obtained from the energy flux balance, in which the external energy is obtained as the multiplication of the wind load with the building velocity. Integration of the obtained flux yields the dissipated energy. When the constant mean wind load is multiplied with the building velocity which has a zero mean, integration will result in a fluctuating signal with a net zero result. Therefore, the magnitude of the mean wind load itself is not relevant, it is the fluctuating wind load that results in structure motion and energy dissipation.

This analysis showed that it is the fluctuating wind load that is relevant for the Energy Flux Analysis. By means of alternative approaches to model wind load, the next sections will focus on the sensitivity of the Energy Flux Analysis result to the modelling of the fluctuating wind load. First, only the magnitude of the fluctuations will be altered in § 10.3. After this, both the magnitude and the phase of the modelled wind load over the building height is altered in § 10.4.

10.3. Magnitude wind fluctuations

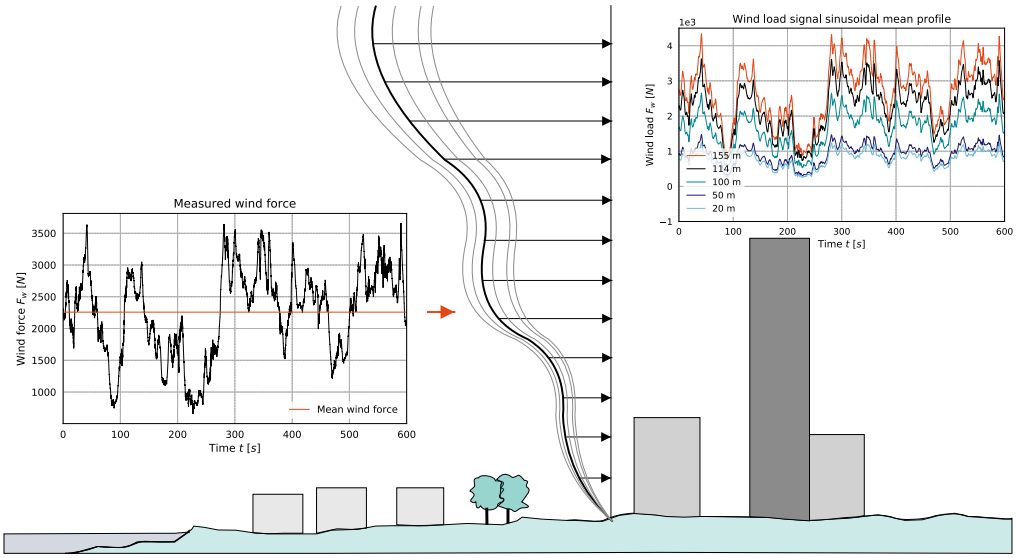

Figure 10.5: Alternative wind modelling using measurement and sinusoidal wind profile to alter fluctuation magnitude

This section focuses on the sensitivity of the EFA result to the magnitude of the wind fluctuations. This is investigated by modelling the wind load using alternative mean wind profiles visualised in fig. 10.6, and again relating the magnitude of the fluctuations to this mean wind profile. Previous section showed that the mean wind load itself does not affect the dissipated energy obtained. It should be noted that these wind profiles are not necessarily realistic, but serve to investigate sensitivity.

The profiles considered are visualised in fig. 10.6 and are a logarithmic profile (LOG), a constant wind force (C), an increasing linear profile (L1), a decreasing linear profile (L2), a parabolic profile with the maximum value halfway the building height (P1), a parabolic profile with the maximum values at top and bottom of the building height (P2), and an increasing and decreasing combined linear and sinusoidal profile which are called LS1 and LS2 respectively. The procedure of applying the LS1 profile is visualised in fig. 10.5. Similar to

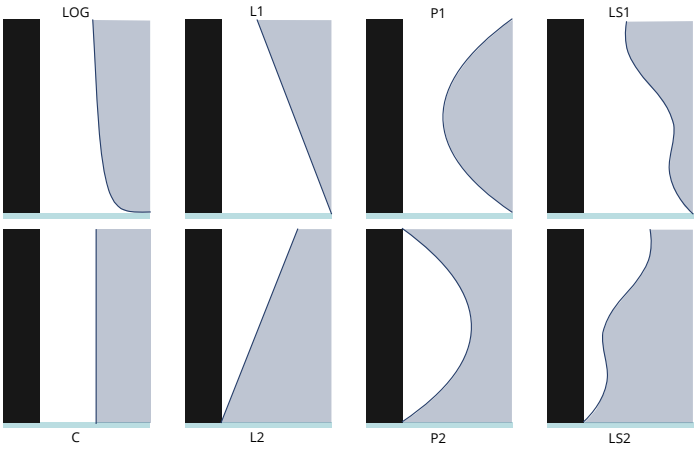

Figure 10.6: Magnitude of wind profiles used for sensitivity study, mathematical description provided in appendix E

	Difference F_w [%]	Difference E_{diss} [%]
LOG	+9.8	+1.4
C	+23.7	+3.8
L1	-15.9	-0.4
L2	+63.4	+8.1
P1	+5.3	-10.7
P2	+42.1	+18.4
LS1	-20.8	-5.8
LS2	+68.3	+13.5

Table 10.2: Difference wind force and dissipated energy relative to the logarithmic-squared profile

the application of the logarithmic-squared profile, the vertical wind profiles are used for both the along wind and cross wind direction and the mathematical description is given in appendix E.

The results of the different profiles are compared to the result of the reference logarithmic-squared profile discussed in § 10.2 in table 10.2. The first column shows the difference in the total force applied to the structure for each profile, this difference is the same at every time instant. The second column shows the difference in the dissipated energy, defined as the difference in the area under the dissipated energy plot. In terms of force applied to the building, the P1 vertical profile is closest to the logarithmic-squared profile. However, the force does not have the same distribution over the building height resulting in a different dissipated energy. The profiles P2 and LS2 largely overestimate the wind force on the building, while LS1 underestimates it. While the differences in the wind force are quite large for these profiles, the difference in dissipated energy is much smaller. This is again caused by the distribution of the wind force over the structure height. The dissipated energy is obtained using the external energy, which is the multiplication of the wind force with the building velocity for every point over the building height. The building velocity is much larger at the top of the building, and thus the wind force at the top of the structure is more relevant.

This sensitivity study shows that the overestimation or underestimation of the dissipated energy depends mainly on the wind load description at the top of the structure. Looking at the error in the wind force and the error in the dissipated energy suggests that the EFA is not very sensitive to the wind force magnitude. Naturally, this is also because the mean wind force does not contribute but even the largely varying fluctuation magnitude does not result in extreme differences. This result also shows that it is not worth investing too much in an accurate description of the logarithmic-squared profile.

Finally, this study will investigate whether the EFA is sensitive to the phase of the fluctuating wind load over the building height. So far, the phase of the fluctuations over the building height was kept the same. Next section will generate a wind load that also adapts the phase of the fluctuating wind.

10.4. Phase wind fluctuations

The aim of this section is to generate a wind load that satisfies the logarithmic-squared mean wind profile, varies the magnitude of the fluctuating wind load over the structure height, and additionally varies the phase of the fluctuating wind load over the structure height.

The magnitude of the fluctuating wind load is generated using the theoretical pressure spectrum for every location along the structure height. The theoretical pressure spectrum for 114 m height is compared to the measured pressure spectrum at this height in fig. 10.7 and is in good agreement. The magnitude of the fluctuations at any specific height is taken from this pressure spectrum and translated to a wind force. The phase of the fluctuations is related to the phase of the fluctuations at any other height using the coherence between the locations under consideration. This means that there is also a random component in the phase of the fluctuations, although it is in agreement with the prescribed coherence. Obtaining the theoretical pressure spectrum and coherence was discussed in § 2.2.4. It should be noted that the pressure spectrum is used to describe the total wind pressure, adding windward and leeward pressures, while the theoretical description is

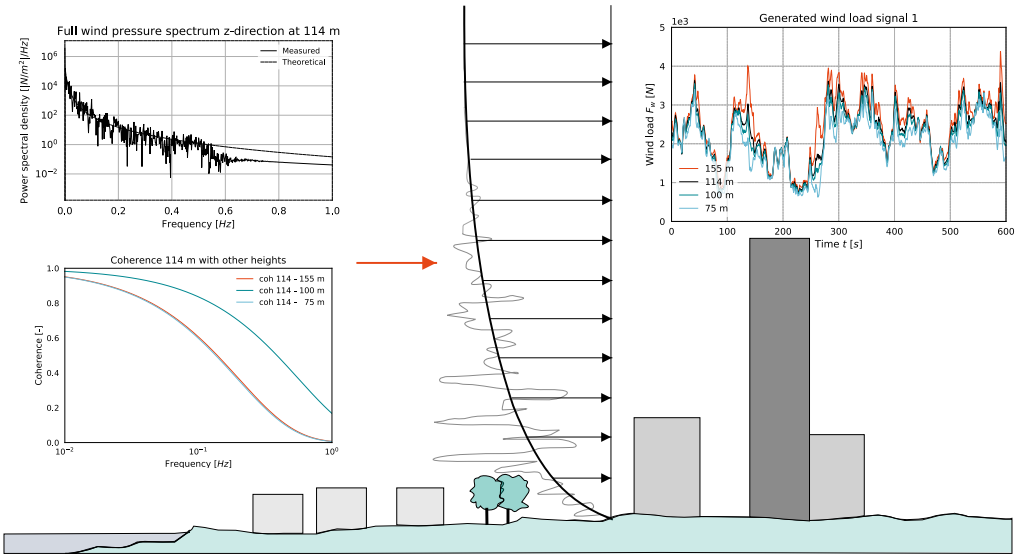

Figure 10.7: Alternative wind modelling using measurement and generating wind using wind profile, wind spectrum and coherence

intended for the windward facade. Besides, the coherence used is the coherence of the wind velocity at different heights. The coherence of the pressure at different heights is generally larger than the velocity coherence (Geurts, 1997). A more detailed explanation of this approach is presented in appendix F.

As the generated wind load in this approach has no relation to the measured wind load at 114 m height in time, the generated loads are related to the generated load at 114 m height. This relation is used to extrapolate the measured wind load. However, this approach does affect the coherence between wind loads at various heights. The final wind loads have larger coherence than the coherence that was specified based on wind velocity.

Figure 10.7 demonstrates the generated wind loads in z-direction for various locations along the building height. The mean wind load corresponds to the mean wind load according to the logarithmic-squared profile, and the turbulence intensity is increasing with decreasing building height. As this generated wind load contains a random component, it has been generated multiple times of which two more are shown in fig. 10.8 and fig. 10.9.

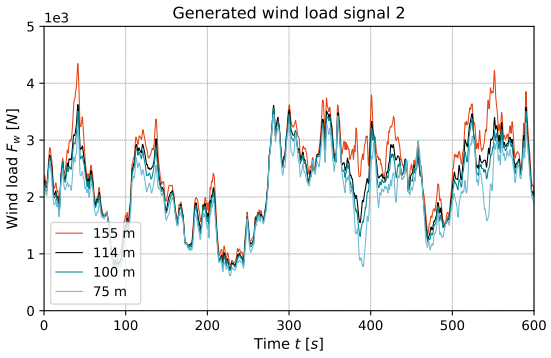

Figure 10.8: Generated wind signal 2

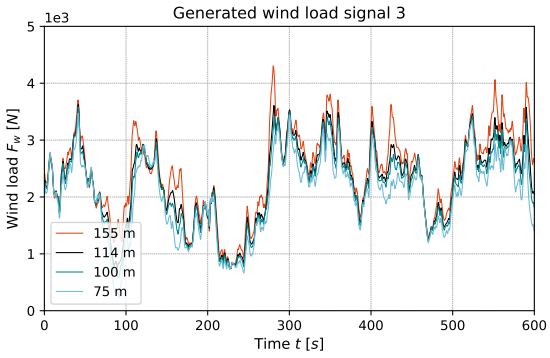

Figure 10.9: Generated wind signal 3

The magnitude of the fluctuating wind load is quite similar for all generated wind loads. However, the difference of the dissipated energy with the generated with the reference dissipated energy is 93.1, 67.5 and 33.0% respectively. These differences are much larger than the differences found in § 10.3, indicating that the EFA is very sensitive to the phase of the wind fluctuations, more than the magnitude of the wind fluctuations.

10.5. Phase difference structure velocity and wind load

Previous sections discussed the influence of the magnitude and phase of the modelled wind load over the structure height on the dissipated energy obtained with the Energy Flux Analysis. Where the sensitivity to the magnitude of the wind load is limited, its sensitivity to the phase of the fluctuating wind load is relevant. However, none of the approaches used in previous sections to model the wind load provided a solution for the nonphysical result of the dissipated energy.

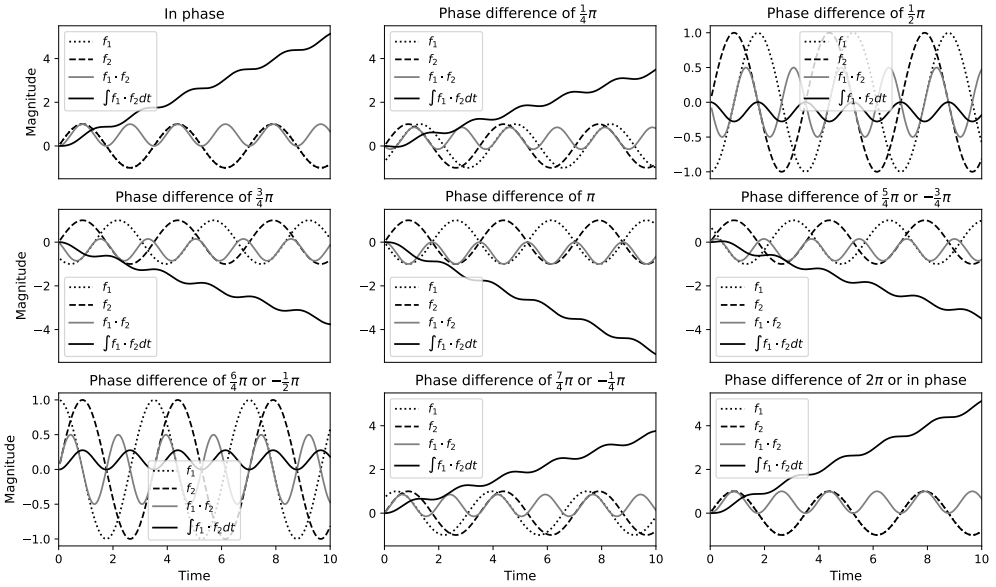

Figure 10.10: Effect of phase difference on multiplication and integration of function 1 and function 2

The trend of the dissipated energy signal was found to be a direct result of the phase difference between the structure velocity and the fluctuating wind load at this same velocity. The effect of a phase difference between two signals is elucidated using a simple mathematical example shown in fig. 10.10. In this example two functions f_1 and f_2 are first multiplied and then integrated over the running time. This is the same as what is done with the building velocity and wind force to obtain the external energy. The figure shows that as long as the phase difference between the two functions is less than $\pm\frac{1}{2}\pi$, the result will be an increasing signal. When the phase difference is larger, the resulting signal will be decreasing.

Based on this knowledge, a first check was done as to whether the results could be improved by applying a constant phase shift to all measurements. This constant phase shift could have been a result of the measurement technique or processing. However, no single shift could improve all results. The required phase shift to obtain an overall positive trend is presented in appendix G for each of the 16 signals. This investigation drew attention to the fact that the phase difference between the structure velocity and wind load is not constant in the measured time.

The measured structure velocity in the along wind direction and the cross wind direction are presented in fig. 10.11. The wind force component at the building natural frequency is also presented in fig. 10.11. Naturally, the total wind force contains more frequency components, but this component is dominant in the contribution to the external energy. The external energy as a result of these signals is presented in fig. 10.11. Only the external energy is presented here, but it directly influenced the trend in the dissipated energy signal. This can be easily confirmed by comparing the external energy in fig. 10.11 with the dissipated energy in z- and y-direction presented in fig. 10.4. It should be noted that the magnitude is not the same, as this section only focuses on the external energy at 114 m height.

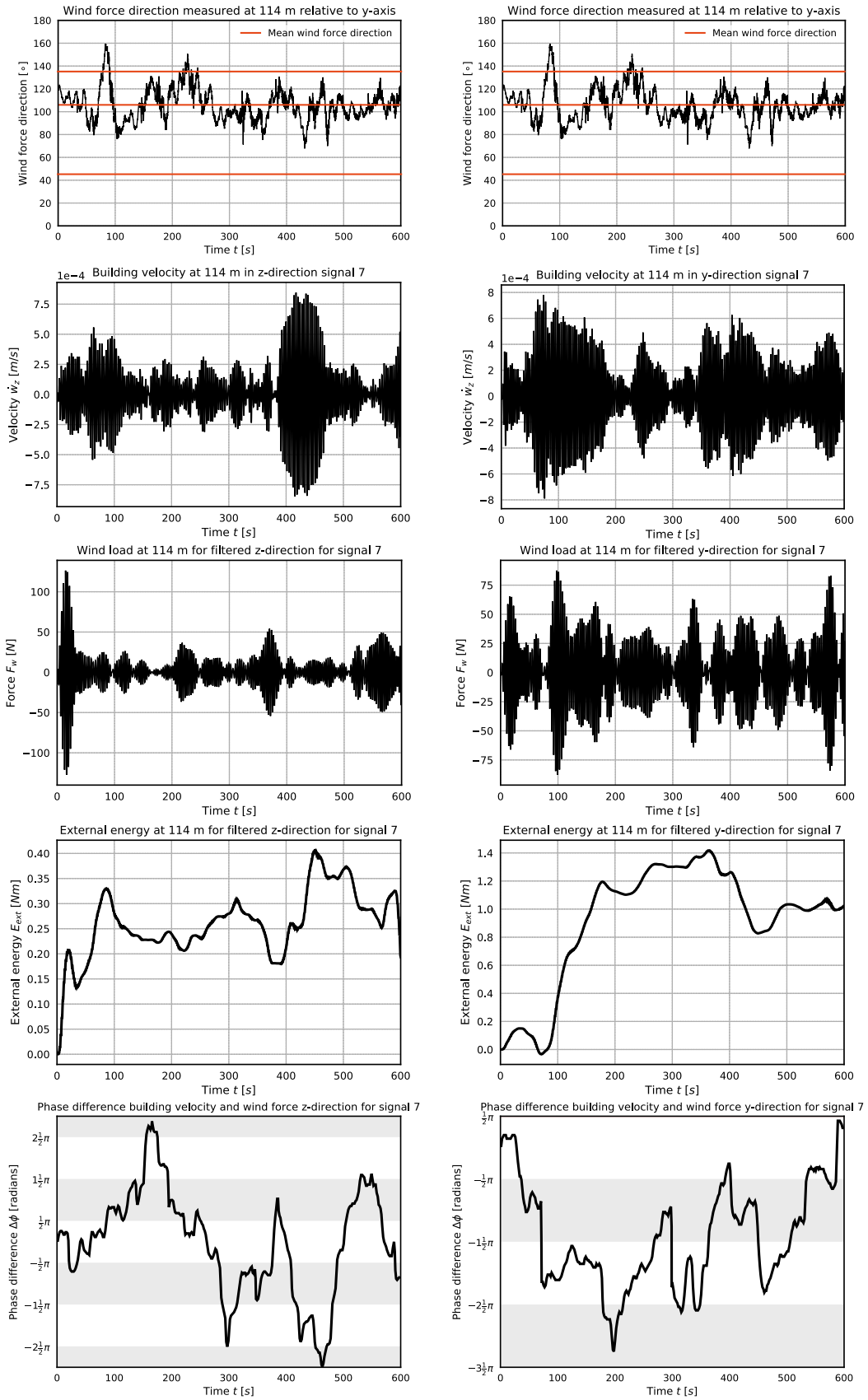

Figure 10.11: Comparing the wind force direction, building velocity, wind force magnitude, and external energy with the phase difference between building velocity and wind force

The phase differences between the building velocity and wind force are also demonstrated in fig. 10.11 for signal 7. The observations for signal 11 are provided in appendix H and show similar behaviour. The phase difference is shown over the measurement time and is presented in radians. It is common to present the phase getting disposing any complete cycles, which means that a phase larger than π can be expressed between 0 and -π. However, the decision was made to present the phase difference while using entire cycles, since it is also of interest to see this phase difference develop in time. In these two figures, a phase difference in a grey area indicates that the phase difference should result in a decreasing signal according to fig. 10.10, with the decreasing trend being largest in the middle of this area. A white area indicates an increasing trend and a phase difference exactly at the boundary results in a constant signal for the external energy.

The source for the nonphysical results has been found. However, the cause for the varying phase difference is yet unknown. An attempt was made to find a relation between a steep drop or rise in the phase difference and the amplitude of, for instance, the structure velocity or the wind force. However, any such relation could not be visually detected. Similarly a relation between wind direction and a steep drop or rise in the phase difference was sought for. It has been previously mentioned in chapter 7 that a sudden increase in structural response may be observed when a shift of wind direction occurs where the wind direction aligns with the corner of the building (Kijewski-Correa and Pirnia, 2007). For the New Orleans this would mean a wind direction of 45° or 135° rather than 90°. The visual comparison for another signal can be found in appendix H, but again, such a relation could not be detected. Another cause for the phase difference developing in time could be related to the coupling of modes, but is not further investigated in this thesis. Finally, data processing and acquisition may affect the phase of measurements. This will be discussed in chapter 11.

10.6. Conclusions

This chapter focused on the sensitivity of the Energy Flux Analysis to the wind load input. Wind pressures are measured at one location along the building height for this thesis, and due to practical and economical reasons this may also be expected for future applications. Therefore, it is crucial to model the wind load at other heights, which is not straightforward due to the random nature of wind.

The sensitivity was investigated by comparing different approaches of modelling the wind load to a reference approach. In this reference approach, the wind load is modelled using the theoretical logarithmic-squared mean wind profile to extrapolate both mean and fluctuating wind load. This was applied to 16 signals of 10-minutes under similar wind conditions. The conclusion was drawn that the mean wind load does not contribute and that in this application the cross term EI_{yz} had negligible influence on the Energy Flux Analysis results. This means that the total dissipated energy found is the same as the sum of the dissipated energy considering along wind direction only, and the dissipated energy considering cross wind direction only. The results of the 16 signals were surprising. Where it is expected that the dissipated energy signal increases in time, at least for the along wind direction and the total dissipated energy, this did not happen for every signal. In fact, even within the 10-minute measurements the trend of the dissipated energy may change from increasing to decreasing and vice versa. The cause for this nonphysical result was found in the phase difference between the structure velocity and the wind load at the structure natural frequency. Based on this phase difference, the dissipated energy signal will increase or decrease. Physical causes for rapid changes in the phase difference were sought for in terms of signal amplitude, and wind direction, but could not be visually detected. Mode coupling was proposed as another cause, together with data processing and acquisition. The latter will be discussed in next section.

The sensitivity to the magnitude and phase of the fluctuating wind load was investigated by comparing the results of approaches varying the fluctuating magnitude only, and approaches varying both magnitude and phase with the reference wind load previously discussed. Where the Energy Flux Analysis showed limited sensitivity to the fluctuating magnitude, it did show significant sensitivity to the fluctuating phase. This goes hand in hand with the discovery of the phase difference between structure motion and wind load being decisive for the trend of the dissipated energy signal.

11

Data acquisition

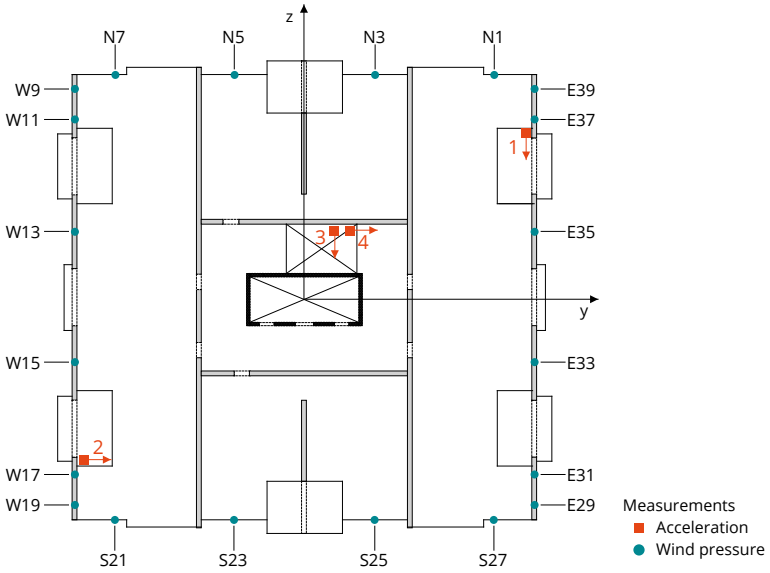

Figure 11.1: Acceleration (orange) and pressure measurements (green) at 114 m height of the New Orleans

Chapter 6 discussed the measurements on the New Orleans tower. These measurements are used in chapter 10 and chapter 12 to perform the Energy Flux Analysis. In these chapters, the effect of measurement and processing errors were assumed to be insignificant. However, the results found in chapter 10 were unexpected. Where the expectation is that the total dissipated energy and the dissipated energy in along wind direction increases in time, the dissipated energy found did not always increase and the trend of the dissipated energy signal even varied within each 10-minute signal. The trend in the dissipated energy was found to be a result of the phase difference between the wind force and structure velocity signals. This phase difference also varied largely in time, and possible explanations for this observation were given. One of the explanations given is data acquisition and data processing. This chapter will briefly discuss all aspects of data acquisition and processing that may affect the signal phase.

11.1. Data collection

Upon performing measurements, the measurement set-up has to be carefully designed as this will affect the measurements. For instance, the sampling frequency should be sufficiently large. If this sampling frequency is too low, a problem called aliasing will arise. This is visualised in fig. 11.2 and means that the highest frequencies of interest are not observable.

The required sampling frequency may be computed using the Nyquist criterion, stating that the sampling frequency should at least be twice the highest frequency of interest in the measured signal. Since the fre-

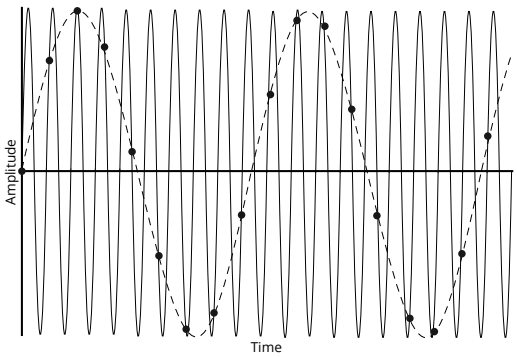

Figure 11.2: Effect of aliasing. The solid line = input signal, dashed line = measured signal, black dots = measurements

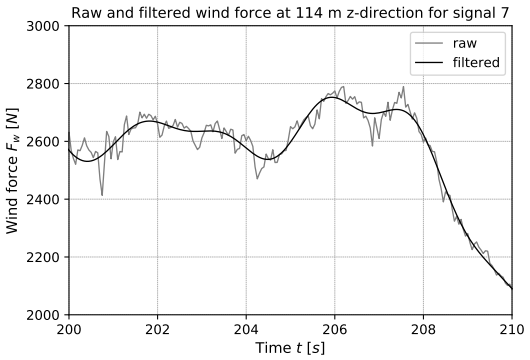

Figure 11.3: Close-up of filtered and raw wind force containing high-frequency components

quencies of interest in this research are below 1 Hz, the applied sampling frequency of 20 Hz is though to be sufficient. However, this means that the sampling interval is 0.05 s. Chapter 10 demonstrated that phase differences in the order of 0.0001 s already significantly affect the Energy Flux Analysis results. Therefore, a sampling interval of 0.05 s seems too large to capture the phase with such an accuracy. For future application, it is advised to consider the significance of the sampling frequency.

As the sampling rate is 0.05 s, this means that every sensor performs a measurement every 0.05 s. This measurement then has to be written, and all measurements are assigned to the same time column. It appears that measurements are performed time synchronous, but in fact one measurement is performed after the other has been written. This may take up to 1 ms, or 0.001 s. This means that measurement 1 will be performed at t_1, and the second will be performed at $t_1 + \Delta t$, where Δt can be up to 0.001 s. Since 46 measurements are performed in total in the measurement set-up, the 46^{th} measurement is performed at t_1 + 0.045 s. Due to the high sensitivity of the Energy Flux Analysis to the phase of the measured signals, it is very important to consider this writing time. It is advisable to correct for this delay, the delay can be quantified by assigning a new time axis to each signal.

It is important to note that, although the phase effects are relevant, none of the data collection aspects discussed here result in the magnitude of the phase difference between wind force and structure velocity observed in chapter 10. Most likely, there is another source affecting the phase of the signals.

11.2. Data processing

Data processing is required to make the acceleration and the pressure measurements signals useful. This section will inspect whether this processing affects the signal phase. This will be done by analysing the phase difference between the raw and the processed signal, and using the cross correlation between them to identify a possible time delay. This only works to identify a constant time delay, and is further explained in appendix I.

11.2.1. Accelerations

Velocity and displacement rather than acceleration as used as input for the Energy Flux Analysis, and are obtained through integration. In this thesis integration is done through trapezoidal integration. When the acceleration measurements are not processed upon integration, the resulting velocity and displacement will be as presented in fig. 11.4. The measured acceleration may contain a small offset from zero, which can be either constant, increasing or decreasing. This offset is not realistic as the building will vibrate around an equilibrium position, and the sum of accelerations should be zero. Integration of the signal with an offset results in an increasing velocity. Therefore, the first step is to remove the offset from the acceleration signal.

However, even after removing the offset in the acceleration data, integrating the signal introduces unrealistic results for the velocity and displacement. Noise in terms of low frequency fluctuations are present in the measured accelerations, causing the integrated signal to vibrate around a low frequency motion. This is visible from the low frequency harmonic shape of the velocity and displacement signals in fig. 11.4. This is called data drifting and can be resolved with the use of filters. The commonly used Butterworth high-pass filter (Butterworth, 1930) is applied. This filter removes frequencies below a certain cut-off frequency. Ideally this cut-off would be vertically, omitting every frequency below the limit and completely including all fre-

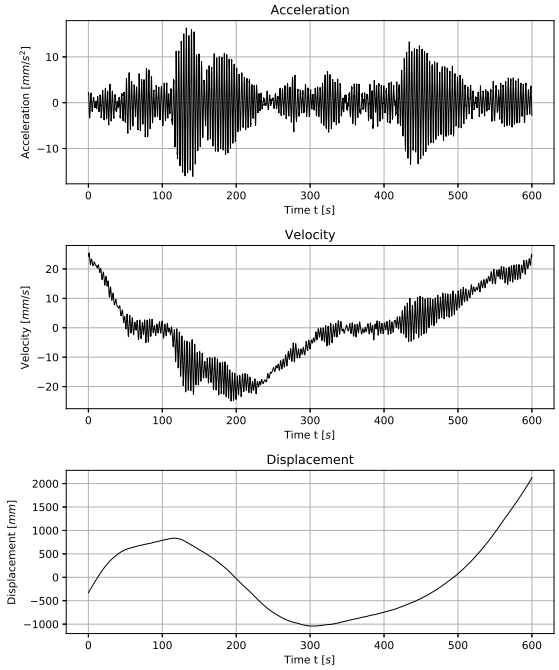

Figure 11.4: Acceleration, velocity and displacement before application of a highpass filter

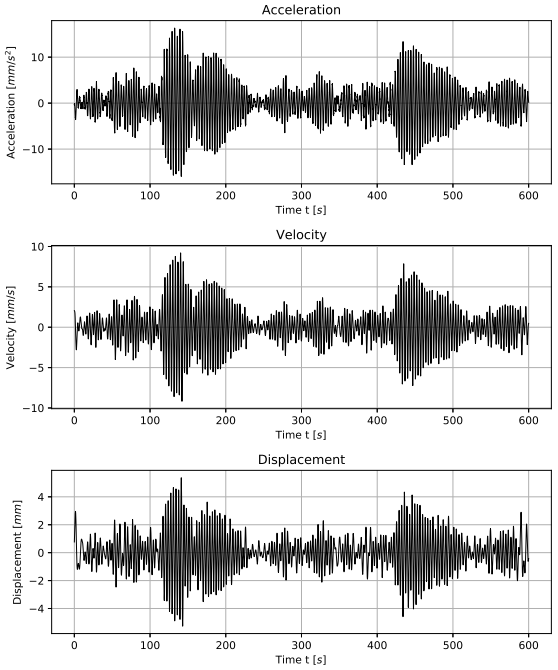

Figure 11.5: Acceleration, velocity and displacement after application of a highpass filter

quencies above it. In reality, filters have a slope, making it important to specify the filter with care. A filter of a higher order has a steeper slope, but a higher order filter might lose stability and therefore a method called SOS, meaning second order sections, is applied in the Butterworth filter. The order of the filter used is 8 and the frequency limit below which should be filtered is 0.10 Hz. Figure 11.5 shows that this filter gives satisfactory and realistic results for the velocity and displacement signal. Filters may affect the phase of a signal. The phase response of a Butterworth filter is near-linear, meaning that all frequency components are equally shifted in time (Butterworth, 1930). However, it does contain a slight dependence on frequency in terms of the phase shift. Investigation showed that for the frequencies of interest, no phase shift was introduced by the filtering procedure.

Integration of a harmonic function should result in a phase difference. For a simple harmonic function, integration will result in a delay of $-\frac{1}{2}\pi$. The definition of a simple harmonic function is an oscillatory motion where the net force on the system is a restoring force and makes sure the oscillator moves repeatedly over the same path back and forth. The building vibration is an oscillatory motion where the building vibrates back and forth, although with varying amplitude, over roughly the same path. The restoring force is the combination of the kinetic and potential energy in the system. Looking at the building vibration as a simple harmonic motion, the delay compared to the acceleration signal for the velocity should be $-\frac{1}{2}\pi$ and the delay for the displacement signal compared to the acceleration signal should be $-\pi$. When analysing the phase difference, a constant phase difference is indeed found. For all 16 signals under investigation the velocity is delayed with $\frac{1}{2}\pi$ from the acceleration signal and the displacement with π for both y-direction and z-direction measurements. To conclude, no phase differences were introduced by data processing of motion signals.

11.2.2. Wind pressures

The wind pressure measurements have also been processed before use in the Energy Flux Analysis. The green dots in fig. 6.1 show that at the north and south facade 4 wind pressure measurement points are present along the 29 m wide facade, and for the west and east facade 6 measurement points are present along the facade of equal length. The wind force on the facade is found by associating the measured wind pressure with the facade width it represents, considering 1 m in height. This means that one measurement point is used to express the force on a piece of facade of approximately 5 to 7 m wide. The measurement will contain local peak pressure that are not representative for the total area. Simply using the single point measurement would lead to an erroneous estimation of the wind load. The peak pressures may be filtered out by a procedure called

equivalent time averaging proposed by (Lawson, 1976), which filters point pressures by means of a moving average filter. This filter uses the following averaging time:

$$\tau \approx 4.5 \frac{L}{\bar{p}} \tag{11.1}$$

In this equation L is the diameter of the area covered by the point measurement and $\bar{p}$ is the average pressure. This procedure filters out high frequencies, and therefore alternatively a low-pass filter may be applied. The result of the Energy Flux Analysis of using the moving average filter, the Butterworth filter or not filtering at all was compared and this resulted in marginal differences in terms of magnitude. The procedure used in this research is a low pass Butterworth filter of order 8 with a cut-off frequency of 0.55 Hz. Figure 11.3 shows a close-up of the effect of filtering on the wind load, clearly higher frequencies have been omitted in the filtered wind load. The filtering did not have an effect on the phase of the signal and only had a marginal effect on the result of the Energy Flux Analysis.

11.2.3. Integration by parts

Another way of checking the influence of the signal processing of acceleration and wind pressures and the integration of the acceleration in time is by applying integration by parts rather than direct integration. Throughout this thesis, the external energy for one location along the building height is computed by:

$$E_{ext}(t) = \int_0^t F_w(t)\,\dot{w}(t)\mathrm{d}t \tag{11.2}$$

This expression can be rewritten using integration by parts. Theoretically this should yield the same result. However, with partial integration the acceleration is used additionally and the wind load is integrated prior to any multiplication with the building motion. Due to slight differences caused by signal processing, in practice integration by parts could yield a different result compared to direct integration. Using integration by parts, eq. (11.2) is rewritten to:

$$E_{ext}(t) = \dot{w}(t)J(t)\Big|_0^t - \int_0^t \ddot{w}(t)J(t)\mathrm{d}t \tag{11.3}$$

with $J(t)$ indicating the impulse of the wind force F_w:

$$J(t) = \int_0^t F_w(t)\mathrm{d}t \tag{11.4}$$

The external energy at 114 m height for the full wind load was performed once using direct integration in eq. (11.2) and once through integration by parts in eq. (11.3). The resulting external energy was the same.

11.3. Measurement technique

This section will briefly discuss the effect the measurement set-up and measurement instruments may have on the measured signal.

11.3.1. Accelerations

The accelerations have been measured using accelerometers. Sensor y_2 and y_4 are combined to obtain the acceleration in y-direction, and sensor z_1 and z_3 to find the acceleration in z-direction. A detailed explanation of combining the measurements to obtain accelerations in the principal directions is given in appendix B. Using the cross correlation approach, and additionally checking the phase characteristics through spectral plots and visually in time domain, no phase difference was found between y_2 and y_4 and between z_1 and z_3. Most likely it is smaller than 1 ms as was explained in § 11.1, and could not be observed.

Accelerometers consist roughly of a case and a mass. The case is mounted onto the system of which the translation acceleration is desired, and the mass is attached to this case through a suspension represented by a spring and a dashpot as is visualised in fig. 11.6. When the case is at rest, the characteristics of the spring and dashpot are chosen such that the displacement of the mass is at the equilibrium point (Collette et al., 2012). When the case accelerates, the mass does not directly do so due to inertia. The measured relative displacement between the mass and the case is translated to acceleration through a transfer function.

Besides translation acceleration, inertial devices are also sensitive to tilt. The sensor cannot distinguish between a displacement of the case or a displacement of the mass due to inclination of the case with respect

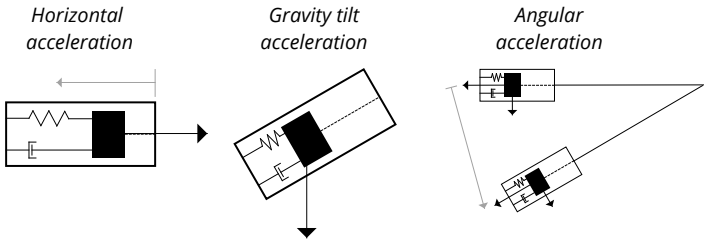

Figure 11.6: Tilt gravity and geometrical coupling. Black arrows indicate force on the mass, and grey arrows indication motion of the case.

to the gravitational field (Collette et al., 2012). This is represented in the middle figure in fig. 11.6, the left figure represents the translation acceleration measurement. The lower the natural frequency of the input motion, the more tilt seems to dominate the measurement (Matichard and Evans, 2015). At a very low frequency, an accelerometers tends to act as a tilt sensor and at high frequencies as an acceleration sensor (Matichard and Evans, 2015). Generally, tilt contribution becomes relevant below 0.1 Hz (Matichard and Evans, 2015). This is slightly lower than the frequency of interest in this application of 0.28 Hz, which indicates that gravity tilt does not affect the measurements used in this thesis.

It is important not to confuse tilt induced by gravity with tilt induced by geometrical coupling, or angular acceleration. Where gravity tilt acceleration depends on the inclination of the instrument and gravity, geometrical tilt coupling would occur even in the absence of gravity. The right figure in fig. 11.6 shows the angular acceleration due to geometrical tilt. This occurs when the sensing point additionally experiences rotation.

11.3.2. Wind pressures

Due to the writing of data, as explained in § 11.1, a phase difference of less than 1 ms may be expected between subsequent pressure measurements. A constant phase difference between all 40 measurements was sought for, but no such phase difference was found.

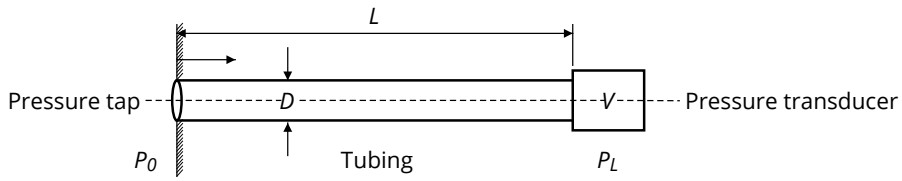

Figure 11.7: Measurement set-up wind pressures

Wind pressures are measured at the facade of the building, as is visualised in fig. 11.1. The pressure measured at these pressure taps has to be measured with respect to a reference pressure. In order to transfer the pressure at the measurement location P_0 to the pressure transducer, a tubing system is required. This measurement set-up is schematically shown in fig. 11.7. The tubes in the New Orleans tower have an inner and an outer diameter of 6 and 9 mm respectively. Since measurements are performed around the entire circumference of the building, the length of the tubing system can become substantial.

Using a pressure measurement system with tubes introduces complications. These complications may arise in the frequency response of the transducer, the frequency response of the signal processing electronics, and they may arise due to fluid coupling between the pressure tap and the pressure transducer (Whitmore and Fox, 2009). The latter of these is most important (Whitmore and Fox, 2009). The measured signal at the pressure transducer might deviate from the pressure at the pressure tap due to friction, pneumatic resonance, and wave reflections in the different components of the measurement system. The pressure impulses P_0 will propagate as longitudinal waves through the tubing system, and a pressure P_L is measured at the pressure transducer, which deviates in both magnitude and phase. The relation between the incoming pressure P_0 and the resulting pressure P_L is described through a factor depending on the frequency of the measured signal as demonstrated in fig. 11.8 for both the magnitude and the phase lag.

The peak in the magnitude plot of fig. 11.8 represents the resonance frequency of the tubing system. Up to this frequency, the measured pressure magnitude is generally larger than the pressure at the pressure tap. After this resonant frequency, the attenuation factor decreases again and may result a lower measured pressure.

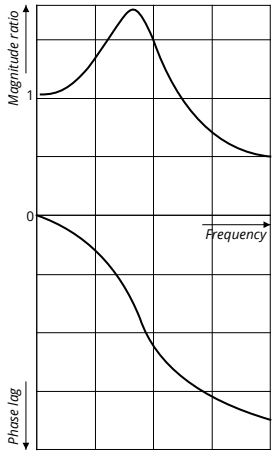

Figure 11.8: Magnitude and phase dependency P_L

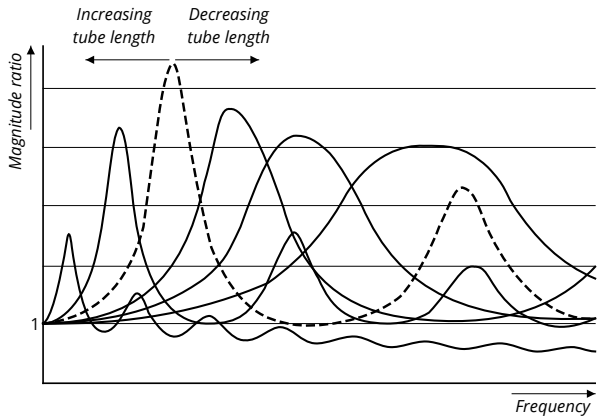

Figure 11.9: Dependency magnitude ratio on tube length

Although not shown in fig. 11.8 but shown in fig. 11.9, the attenuation factor will rise again when approaching the second resonance frequency of the tubing system. The tubing system will not only alter the pressure magnitude, it will also introduce a phase lag, or time lag. Like the attenuation factor, this latency of the pressure is also described depending on the pressure frequency. For higher frequencies the phase lag will become larger. Figure 11.8 shows the general observation of the dependence of the magnitude and phase difference on the pressure frequency. However, the exact shapes of these figures change for different configurations of the tubing system. A response test has been performed on the measurement system used by TNO. The most important characteristic of the measurement system is the tube length (Whitmore and Fox, 2009). Figure 11.9 shows the magnitude-frequency plot for different tube lengths. The shorter the tube length, the higher the natural frequency of the tubing system. The response test demonstrated that the magnitude of the resonance peak first increases for increasing tube length, up to a tube length of 3 m. After this, the resonance peak will decrease. For long and narrow tubes, the resonance peaks are eliminated due to viscosity and conductivity effects (Irwin et al., 1979). Berg and Tijdeman (Berg and Tijdeman, 1965) introduced a method to correct for the deviating pressure measurements, which is very commonly used and is further discussed in appendix J. Most parameters in the expression for the time lag are independent of time, but dependent on frequency. However, P_0 appears in the expression indicating that it does not only depend on the incoming frequency, but also on the magnitude.

TNO has performed corrections to account for the tubing system on the measurements. In terms of magnitude these corrections are observable, and details are available. In terms of phase the difference between the raw and corrected signal was found to be no more than 0.002 s. This suggests that either the required correction due to the tubing system is extremely small, or this difference originates from the altered magnitude, or a digital or numerical difference. As mentioned before, the measurement set-up was originally designed for another purpose. This purpose might not be as sensitive to any deviations in the phase of a signal as the Energy Flux Analysis. It is therefore recommended to study the corrections applied, and to discover whether the applied accuracy is sufficient for the specific application for the Energy Flux Analysis .

11.3.3. Noise

Sensor noise is contamination for measurements in general as it puts a limit on the sensor resolution. The source of noise can be either from environmental disturbances, such as pressure, temperature and magnetic fields, or the source can be stochastic (Collette et al., 2012). Noise will always be present and results in a change of amplitude and phase of the original signal to be measured. Therefore, a substantial amount of noise could be the explanation for the changing phase difference in time.

11.4. Measurement set-up

Besides signal processing, the measurement technique, and instruments used, the specific measurement set-up, the location of the sensors, will also affect the reliability of the measurements. This was already briefly discussed in chapter 7, which showed that there are strong suggestions that the wind velocity measurements are not reliable. A possible explanation given was the position of the anemometer, which is just above the

roof, at the centre of the floor plan. Fortunately, these wind velocity measurements are not used as input for the Energy Flux Analysis. However, this does not rule out that a similar effect occurs for the wind pressure measurements. Figure 11.1 shows the location of the pressure measurements at south and north facade. The facade is not a flat surface but contains set-backs and balconies. Interaction of these elements with the wind could result in local pressures that differ from the pressures that would be expected from a smooth approaching flow only. Basing the global wind load on these measurements will then lead to erroneous results.

Besides, the measurements show that there is a phase difference in the wind load and the structure velocity which results in a largely varying dissipated energy signal. This is what has been measured at 114 m height. The question arises whether it is physically possible that this is true for the measurement height, while at other locations the wind load is in fact in phase with the structure velocity, resulting in a significant external energy. This would mean that globally speaking the dissipated energy does increase, but that the measured wind load is just not representative for the total building height.

11.5. Conclusions

Up to this chapter, the effect of measurement uncertainty was assumed to be insignificant. However, chapter 10 showed that the unexpected results in the dissipated energy signal are a result of the phase difference between the measured building motion and wind load. Data acquisition and processing was pointed out as a possible influence, as this can affect the phase of a signal. This chapter went through all steps taken before using the obtained wind load, structure velocity, and structure displacement in the Energy Flux Analysis.

The first thing that was pointed out was the significance of data collection, through the sampling frequency and the writing of the measurements. After this, the effect of filtering and integration on the signal phase were investigated. None resulted in an undesirable phase shift.

Then the effect of the measurement devices used on the measured phase was explored. An accelerometer may affect the signal phase due to the presence of gravity tilt. However, this effect is relevant for signals below 0.1 Hz, while the frequency of interest in this thesis is 0.28 Hz.

Similarly, the pressure measurements could result in a phase error. The pressures of interest are at the facade of the building and therefore the pressure taps are placed here. A tubing system with a fluid is required to transfer the pressure at the pressure tap to the location of the reference pressure. Depending on the length of the tubing system and the natural frequency of the tubing system relative to the frequency components of the pressure, this tubing will affect the magnitude and the phase. Most interestingly, the time lag is not only affected by the tubing system and the frequencies, but also by the magnitude of the incoming pressure. Corrections for the tubing system have been done by TNO, but because the measurements originally had a different purpose, it is unsure whether the correction was performed as required for the Energy Flux Analysis.

Two other sources of uncertainty in the measurements were formulated. The first being inevitable measurements noise. The second may be introduced by the location of the pressure taps. Measurements are translated to a global wind load over the full building height, which is results in large flaws in the global wind load used for the Energy Flux Analysis.

12

Structural properties

12.1. Introduction

The calculation of the damping through the Energy Flux Analysis depends on the measurements and extrapolation of the building motion and wind load. Another input of the Energy Flux Analysis are the structure properties. In the application in this thesis, the structure properties are the building mass, the building stiffness and the foundation translational and rotational stiffness. However, as discussed in chapter 3 and chapter 6, the accuracy of the estimates of these properties is limited.

This chapter will focus on the effect of the structural properties on the damping found through the Energy Flux Analysis. The damping is therefore computed for many different combinations of the structural properties using the same 10-minute measurements. It should be noted that what is investigated is the effect of these properties on the Energy Flux Analysis result, and not what the effect is on the physical damping of the structure. The measurements used for this sensitivity study belong to the New Orleans tower. This structure has 'true' mass and stiffness properties, and a 'true' occurring energy dissipation. Changing the properties affects the results of the Energy Flux Analysis and its ability to approach this 'true' damping. Changing the input properties does not change the 'true' properties of the structure.

The sensitivity study is performed for one direction, which is the along wind direction. This is justified, because chapter 10 showed that the effect of considering two directions including coupling is almost identical to performing the EFA for the two directions separately and summing the results.

Upon performing the sensitivity study, a range of possible values for the properties has to be defined. Maximum and minimum values are found based on the structural and non-structural material and system, and the uncertainty in its behaviour. The motivation for the ranges is presented in § 12.2. After defining the range of possible solutions for the building mass, building stiffness and, foundation translational and rotational stiffness, only those combinations of these properties resulting in the measured natural frequency are deemed possible. This means that the system used in this thesis, where the structure is modelled by an Euler-Bernoulli beam with a fixed and a flexible end and continuous stiffness and mass properties, is assumed appropriate. The calculation of the frequency of this model, depending on the structural properties, is done through the frequency equation given in appendix A. The results are compared by translating the dissipated energy signal to a damping ratio using the approach explained in § 5.3 for the total structure.

A more detailed explanation of the methodology is given in § 12.3. The main focus is on the selection of combinations of the properties chosen to perform the Energy Flux Analysis. The results of the sensitivity study are presented in § 12.4. Finally, § 12.5 will provide the conclusions.

12.2. Parameter ranges

This section will present and motivate the ranges used for the structural properties. The ranges are defined through a lower bound and an upper bound and are presented in table 12.1. The bounds were found using the uncertainty in the characteristics and behaviour of the structural material and system, and the contribution of non-structural elements. Besides, design estimates are provided. These refer to the quantity of the property used in the dynamic design calculations of the New Orleans tower and are also included in table 12.1. Based on the measured frequency of 0.283 Hz and the estimated frequency using the design properties of

0.16 Hz, the assumed properties in the design are most likely erroneous. Chapter 3 and chapter 6 have already discussed the fact that specifically the building stiffness is usually underestimated in the design stage.

	ρ_b [kg/m^3]	EI_{yy} [N/m^2]	EI_{zz} [N/m^2]	$K_{\theta_y} = K_{\theta_z}$ [Nm/rad]	$K_y = K_z$ [N/m]
Lower bound	365	4.22×10^{12}	6.4×10^{12}	4.23×10^{11}	1.62×10^{9}
Design estimate	444	1.89×10^{13}		1.88×10^{12}	
Upper bound	723	1.38×10^{14}	2.21×10^{14}	2.99×10^{13}	7.85×10^{10}

Table 12.1: Structural property ranges

Before motivating the property ranges, it is interesting to visualise the frequency sensitivity to the structural properties. The red line in fig. 12.1 shows the measured frequency of 0.283 Hz. The frequency found in the design can be recognised as the value where all properties are at a 0% deviation from their design estimate as given in table 12.1. The black lines show the effect of allowing one of the properties to deviate 50 % above and under their design estimate.

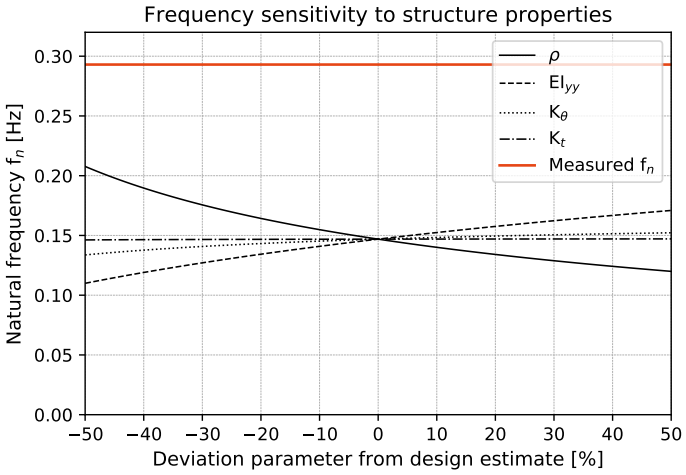

Figure 12.1: Frequency sensitivity to the building parameters

Figure 12.1 clearly shows that the building mass is a very important parameter for the natural frequency. A deviation of this mass of from its design estimate of +20% results in a decrease of the natural frequency of 9% and a deviation of -20% results in an increase of the natural frequency of 12%. Obviously, the natural frequency decreases with increasing mass. Second most important is the building stiffness, for this parameter the natural frequency increases with increasing stiffness. A deviation of the building stiffness of +20% results in an increase of the natural frequency of 7%, while a -20% deviation results in a natural frequency that is 9% smaller. Of inferior importance, is the building rotational stiffness showing a moderate version of the trend seen in the building stiffness. A difference in the rotational stiffness of ± 20% leads to a deviation in the natural frequency of approximately ± 2%. Deviating the translational stiffness with +20% leads to an increase in the natural frequency of +0.1% and when the translational stiffness is 20% smaller, the natural frequency is 0.1% smaller. It is possible to draw the conclusion that the foundation rotational and translational stiffness are less important for the natural frequency.

The error found in frequency resulting from the design estimates compared to the measured frequency, is most likely a result of either significantly overestimating the building mass, significantly underestimating the building stiffness, or both. According to literature, discrepancies found in the natural frequency measured in situ are mostly due to uncertainties in the estimated building and foundation stiffness (Kwok, 1995). The motivation is that relative to these stiffness properties, the building mass can be estimated reasonably accurate. However, one should be reminded that its influence is slightly larger.

12.2.1. Building mass

In this research, the building mass is assumed constant over the building height. The building mass can be subdivided in the mass of the structural system, the mass as a result of non-structural elements and the mass

resulting from variable load. The assumed loads in the building design are summarised in appendix K. The floor loads take into account the contribution of the structural system, the non-structural elements indicated as permanent load, and the variable load to the total load. The concrete walls are a structural load, whereas the facades are categorised as a permanent load.

In the design, it is always required to use safety factors. The design should provide a conservative estimate of the loads and therefore the use safety factors should result in a load with a very small probability of exceeding. For each floor a variable load is given, but it is not expected for these loads to take their maximum value on each floor at the same time. Therefore, combination factors ψ_0 are introduced. The variable load on each floor should be multiplied with this combination factor, except for the floor with the largest variable load. Considering the safety and combination factors, the following load combinations are used in the design:

$$\begin{aligned} F_d &= 1.20G_k + 1.50Q_k \\ F_d &= 1.35G_k + 1.50Q_k\psi_0 \end{aligned} \tag{12.1}$$

In this equation G_k is the characteristic permanent load, which is the structural and permanent load combined, and Q_k is the characteristic variable load. The second load combination reduces the variable load as explained before using the combination factor ψ_0. For the sensitivity study it is important to find a lower bound and an upper bound of the building mass. The safety and combination factors play an important role in the determination of the bounds.

Lower bound

The lower bound is defined as the mass of the structural system only, without any safety factors. This would be the building mass upon completion of the building, and this was chosen as a lower bound since it is not known how the non-structural elements participate in the dynamic behaviour. This lower bound is provided in table 12.2. The floor area used to calculate the total load is 29 x 29 m so 841 m^2.

	Structural load [kN/m^2]	N	Total load [kN]	Distributed mass [kg/m]
Floor 4 to 45	7.5	42	264,915	174,223
Floor 3	7.5	1	6,508	4,148
Floor 2	8.8	1	7,401	4,867
Floor 1	3.8	1	3,196	2,102
Floor 0	11.25	1	9,461	6,222
Floor -1 to -2	7.75	2	13,036	8,573
Walls				107,642
Total				307,777

Table 12.2: Ultimate lower bound mass building floors

The lower bound building distributed mass of 307,777 kg/m is equal to a building mass density of 365 kg/m^3.

Upper bound

For the upper bound, all loads are considered and both the design load combinations of eq. (12.1) are computed. The dynamic behaviour under consideration is a serviceability matter rather than the ultimate limit state, but since use of the load combinations with safety factors should, by definition, provide an upper bound, they is still applied here. The largest of the load combinations in eq. (12.1) will be used as upper bound. These two load combinations lead to the loads given in table 12.3 and table 12.4 respectively.

It is clear that the upper bound is provided by the second load combination, which was applied in table 12.4. This corresponds to a mass density of 723 kg/m^3. This is almost double the mass density provided by the lower bound.

Design estimate

The technical reports provide a building mass used to calculate the natural frequency of the structure. This load is smaller than the load used for the safety calculations of the load-bearing structure. This is because no safety factors are used and a lower load provides a more conservative, higher natural frequency. The design estimate of the building mass is 444 kg/m^3.

		Structural load [kN/m^2]	Permanent load [kN/m^2]		ψ	Variable load [kN/m^2]	N	Total load [kN]	Distributed mass [kg/m]
Floor 4 to 45	1.2	7.5	2.4	1.5	1.0	1.75	42	512,346	336,948
Floor 3	1.2	7.5	2.9	1.5	1.0	5.0	1	16,803	11,051
Floor 2	1.2	8.8	1.2	1.5	1.0	5.0	1	16,400	10,785
Floor 1	1.2	3.8	3.45	1.5	1.0	5.0	1	13,624	8,960
Floor 0	1.2	11.25	5.94	1.5	1.0	10.0	1	29,963	19,705
Floor -1 to -2	1.2	7.75	0.5	1.5	1.0	2.0	2	21,698	14,270
Walls	1.2								129,170
Facade	1.2								58,177
Total									589,066

Table 12.3: Upper bound mass building floors combination 1

		Structural load [kN/m^2]	Permanent load [kN/m^2]		ψ	Variable load [kN/m^2]	N	Total load [kN]	Distributed mass [kg/m]
Floor 4 to 45	1.35	7.5	2.4	1.5	0.4	1.75	42	509,167	334,857
Floor 3	1.35	7.5	2.9	1.5	0.25	5.0	1	13,385	8,802
Floor 2	1.35	8.8	1.2	1.5	1.0	5.0	1	17,661	11,615
Floor 1	1.35	3.8	3.45	1.5	0.25	5.0	1	9,808	6,450
Floor 0	1.35	11.25	5.94	1.5	1.0	10.0	1	32,132	21,132
Floor -1 to -2	1.35	7.75	0.5	1.5	0.7	2.0	2	22,265	14,643
Walls	1.35								145,317
Facade	1.35								65449
Total									608,265

Table 12.4: Upper bound mass building floors combination 2

12.2.2. Building stiffness

The second property considered is the building stiffness. In order to find a range for the building stiffness, not only the design estimate is considered, but the stiffness is computed separately considering the configuration of the structural elements and the elastic modulus. The calculation of these properties and the elastic moduli used in the design are presented in appendix L.

Lower bound

The lower bound for the building stiffness is found considering contribution of the stability core only. On top of this, the elastic modulus of cracked concrete, rather than that of uncracked concrete is used. This will lead to an even lower building stiffness and may occur if cracks in the core have developed during service life. The stiffness is found as a multiplication of the elastic modulus E and the second moment of area I of the core cross-section. The cracked elastic modulus for the core is 2.1×10^{10} N/m^2. The second moment of area in the weak direction, which is the z-direction, is indicated as I_{yy} and has a value of 200.881 m^4. Together this results in a lower bound building stiffness in the z-direction of 4.22×10^{12} Nm^2. The second moment of area in the stronger y-direction is indicated as I_{zz} and has a value of 304.935 m^4. This results in a building stiffness of 6.40×10^{12} Nm^2.

Upper bound

For the upper bound of the building stiffness not only the core, but also the structural walls are considered. The elastic modulus of uncracked concrete, which is 3.7×10^{10} N/m^2, will be used. The second moment of area in the weak direction I_{yy} considering all walls is 2661.534 m^4. This results in a building stiffness EI_{yy} of 9.85×10^{13} Nm^2. The building stiffness in y-direction is 1.58×10^{14} Nm^2. This provides an upper bound of the structural stiffness, since by considering the second moment of area of the structure cross-section, any connections present are assumed to be rigid. However, for this concrete building made of solid concrete walls the assumption is not unlikely. As explained in chapter 3, the in situ elastic modulus can be 10% higher than the assumed value in the design. Also, non-structural elements may cause the in situ stiffness to be 17-46%

larger (Kim and Kim, 2014). These two aspects have to be considered for the upper bound. To take this into account, the upper bound values of 9.85×10^{13} and 1.58×10^{14} Nm^2 are increased with 40% to a building stiffness in the weak direction. This results in a value for EI_{yy} of 1.38×10^{14} Nm^2 and a building stiffness in the strong direction, EI_{zz}, of 2.21×10^{14}.

Design estimate
In the design, the stiffness of the building was found using the deformations of the FEM model and knowledge of the load acting on the model. The dynamic stiffness was estimated to be 1.89×10^{13} Nm^2 in the weak direction, but no dynamic stiffness was given for the strong direction. In this stiffness, a 15% reduction due to openings in the core is applied. The design already acknowledges that due to frame action, the building stiffness is expected to be 23% larger. Additionally, an increase due to the larger in situ elastic modulus and the contribution of non-structural elements can already be expected (Kim and Kim, 2014).

12.2.3. Foundation stiffness

The foundation stiffness refers to the stiffness of the soil-structure interaction at the foundation. It is used in the Energy Flux Analysis to compute the potential energy stored in the soil and is an important property for the boundary conditions at the foundation. The foundation stiffness can be computed through several models, of which three are presented in appendix O. Both Dynapile and the calculation using the design pile plan configuration and the support stiffness consider the foundation configuration, while the cone model does not. The stiffness computed through the design pile plan configuration resulted in a rotational stiffness of 5.24×10^{12} Nm/rad on average, and a translational stiffness of 1.62×10^{9} N/m. The rotational stiffness found from Dynapile is 5.33×10^{12} Nm/rad and the translational stiffness was found to be 3.65×10^{9} N/m. These values are quite similar, most probably because the same assumptions were made for the soil properties.

The more simple model is the cone model discussed in appendix M and appendix O. This model does not consider the foundation geometry and its piles, but assumes it to be a rigid disk on an elastic half-space which is the soil. Due to the simplicity of the model it is an interesting tool to investigate the influence of the uncertainty in the soil properties on the foundation stiffness. The model depends on the soil mass density, Poisson's ratio and shear wave velocity. The Poisson's ratio of sand can take any value between 0.3 and 0.4 (Sharma et al., 1990) and the density of dense, saturated sand is expected to be between 19.5 and 24 kN/m^3 according to JCSS (Baker and Calle, 2006) and between 17 and 23 kN/m^3 according to Bowles (Bowles, 1996). This results in an expectation of the density to be between 17 and 24 kN/m^3, which corresponds to a mass density between 1733 kg/m^3 and 2446 kg/m^3. The measured mass density of the soil layer was 1955 kg/m^3. The ranges of the shear wave velocity were found using the results of Cone Penetration Tests (CPTs) and the theory in appendix N. Based on these ranges, the foundation stiffness was calculated with the cone model, divided in a minimum value, a best estimate value, and a maximum value shown in table O.7. This was also done for the soil layer above the load-bearing sand layer in table O.8. Interestingly, the cone model generally provides larger values than the other models, which is most likely due to the assumptions of this model itself.

Based on these models and values, a lower bound and an upper bound are defined in this section. For the building mass and building stiffness the upper and lower bound were well-founded based on structural considerations. However, due to the large uncertainty in these properties, it not ruled out that the true stiffness lies between the upper and lower bound. However, the range considered is large.

Lower bound
The lower bound used is the lowest of stiffness values found with either of the three models. The lower bound rotational stiffness is found using the cone model, assuming that the foundation stiffness is provided by the first soil layer rather than the second soil layer. This is realistic if the layout of the soil varies a lot within the building plot. In that case the CPTs may not be representative. The lower bound rotational stiffness is 4.23×10^{11} Nm/rad. The lower bound translational stiffness was found using the design pile plan configuration and is 1.62×10^{9} N/m.

Upper bound
The upper bound is also provided by the cone model, since this generally provides larger values. For the upper bound is a result of the second soil layer considering the largest measured mass density and shear wave velocity. The upper bound rotational stiffness is 2.99×10^{13} Nm/rad and the upper bound translational stiffness is 7.85×10^{10} N/m.

Design estimate

The design calculations also provide a soil stiffness, based on the third party point support stiffness values. The stiffness is found as a result of the FEM model, but is only given for the rotational direction. The design foundation rotational stiffness is 1.88×10^{12} Nm/rad. This design estimate is between the lower and the upper bound.

12.3. Methodology

In this sensitivity study the effect of the chosen structural properties on the EFA result will be investigated. For the same 10-minute measurements, the EFA is performed repeatedly using different combinations of the structural properties. This is done for the z-direction, the along wind direction only. The combinations of the structural properties have to match the measured natural frequency. The natural frequency as a result of these properties is found through the frequency equation in appendix A. The results of the EFA are compared by translating the dissipated energy to a damping ratio through the procedure explained in § 5.3. Finally, the combinations providing the maximum and minimum value will also be performed for other 10-minute signals to investigate the sensitivity of the results of this chapter to the measurements.

From the property ranges in table 12.1 all possible combinations matching the measured frequency of 0.283 Hz should be found. Depending on the amount of accuracy used many combinations can be found. In order to limit the amount of combinations, but to represent the entire parameter range, all ranges are subdivided in 50 bins of equal width. When multiple combinations are possible, of which all parameters fall within the same bin respectively, only one of these combinations is kept. Eventually, this approach leads to 203,773 possible combinations.

An interesting observation is the fact that not the entire property range is covered in the solutions. The lowest part of the range of the building stiffness cannot provide the required frequency in combination with the other properties. The lowest appearing building stiffness in the solutions is 4.72×10^{13} Nm^2. This value is even larger than the design estimate of 4.22×10^{12} Nm^2. Based on the idea that the building mass range is sufficiently large, this could indicate that the lower bound estimates for the building stiffness and even the design estimate were too low. Alternatively, it could indicate that the beam model used is not representing the building appropriately. The same happens for the foundation rotational stiffness. Instead of the lower bound of 4.23×10^{11} Nm/rad, the smallest value observed in the solutions is 1.78×10^{12} Nm/rad.

As mentioned in § 12.2, the influence of the foundation translation stiffness on the natural frequency is very limited. This is also observable from the solutions of combinations found. For the same building stiffness, building mass and foundation rotational stiffness, different values for the translational stiffness satisfy the natural frequency. This provides the possibility of investigating the isolated effect of this translational stiffness on the damping estimate. Since there is a slight influence, it was not possible to find a set of solutions where all properties are the same, and the entire range for the foundation translational stiffness is covered. The largest range of values for the foundation translational stiffness where all other properties are the same was found to contain 37 values ranging from 2.20×10^{10} N/m up to the upper bound of 7.85×10^{10} N/m. However, this set covers 74% of the range given in table 12.1. Naturally, the natural frequency found for these combinations cannot exactly the same. However, the maximum difference found in natural frequency is of an order of less than 0.2% while the difference in the natural frequency found for separate measurements under the same wind conditions is of an order of 0.8%.

All combinations produced the same damping ratio. This indicates that the translational stiffness for these properties does not affect the damping ratio. To exclude the possibility that it is just not relevant for the chosen building stiffness, mass and foundation rotational stiffness, the same has been done for another set with largely different parameter values. Both results are shown in table 12.5. This different set again resulted in the same damping ratio for all combinations in the set. Therefore, the translational stiffness is considered trivial for the damping ratio and will from now on be excluded. Leaving out the foundation translational stiffness resulted in 46,377 possible combinations to satisfy the natural frequency.

	N	ρ_b [kg/m^3]	EI_{yy} [Nm^2]	K_θ [Nm/rad]	K_t [N/m]	ζ [%]
1	37	365	5.06×10^{13}	1.19×10^{13}	2.20×10^{10} - 7.85×10^{10}	0.34
2	26	710	1.38×10^{14}	6.44×10^{12}	3.93×10^{10} - 7.85×10^{10}	0.15

Table 12.5: Varying the foundation translational stiffness only

Performing the EFA for all 46,377 combinations is too computationally expensive. Therefore, it is necessary to find less combinations that do represent the entire solution space. In an attempt to find these combinations, the central composite method is used. In the central composite method, the solution space for the variables is represented as good as possible with the least amount of combinations (Heckert et al., 2002).

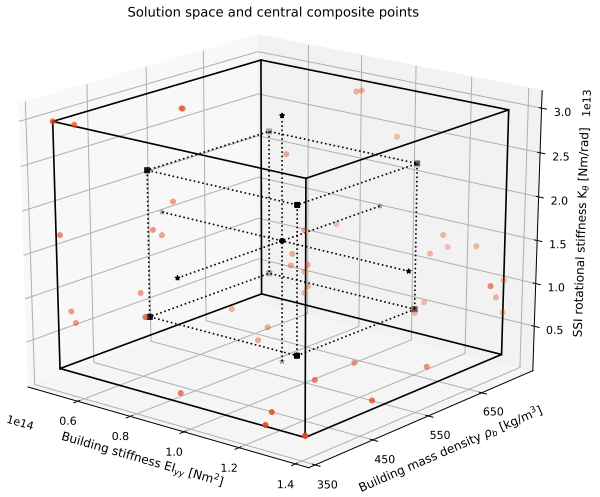

Figure 12.2: Central composite representation with centre point, corner points and star points

In order to represent the solution space as good as possible, some key points are defined. Figure 12.2 visualises the solution space with the black solid lines. The key points within this space are the centre point, indicated as a black sphere, the corner points, indicated with black cubes, and the start points indicated with black stars. In this case, the star points represent points on the solution boundaries. The location of the corner points is defined through a ratio $1/\alpha$ compared to the star points. This α is given as (Heckert et al., 2002):

$$\alpha = \left(2^k\right)^{1/4} \tag{12.2}$$

In this equation, k represents the amount of variables and α takes the value of 1.68. The number of points required is found through (Heckert et al., 2002):

$$N = 2^k + 2k + 1 \tag{12.3}$$

The first term represents the number of corner points, the second the number of star points and the last the centre point. This means that for 3 variables 15 runs should at least be performed. This approach is very useful in case of independent variables, but since the variables connected through the natural frequency, it is not possible to obtain the exact combinations for all the specified points. In fact, most could not be found in the solutions. Therefore, the combinations as close as possible were looked for and 32 additional intermediate points were added. These points are shown in fig. 12.2 in red. Clearly, the solution space is far from covered. However, this is a result of the restriction of combinations through the natural frequency.

In order to find more combinations, combinations were sought for where one property, or variable, is kept fixed while the other vary. This was done 9 times; each variable was fixed 3 times, once at the lower bound, once at the mid value, and once at the upper bound. The combinations found from this approach are added to fig. 12.2 and are shown in fig. 12.3 and fig. 12.4 from two different angles. It is clear that, for instance, for a smaller building mass, the entire property range of the building stiffness and foundation rotational stiffness are covered, although with limited combinations. For a large building stiffness, the smallest stiffness values are not covered. Also, for a large building stiffness all possible building mass values are present in the solutions, while this is not the case for a low building stiffness.

The shape of all possible combinations is clearly visible from these figures. The combinations investigated are considered an appropriate representation of all combinations possible. In total 1,675 runs were executed instead of the initial 46,377.

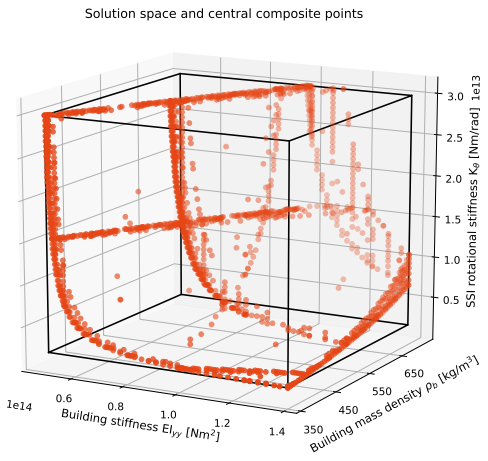

Figure 12.3: All possible combinations investigated, from angle 1

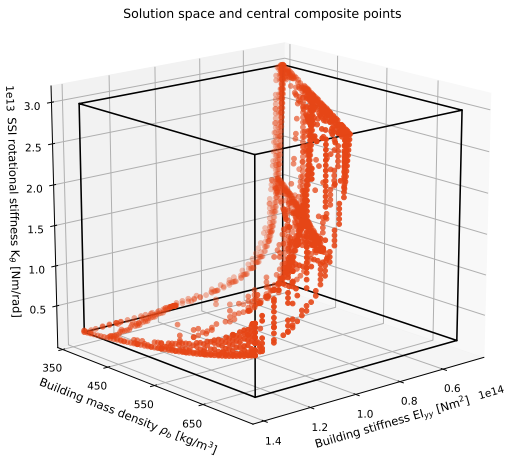

Figure 12.4: All possible combinations investigated, from angle 2

12.4. Results

The results of the structural property sensitivity study are shown in fig. 12.5. The resents are presented with the building mass density ρ_b on the horizontal axis, and the ratio of the foundation rotational stiffness over the building stiffness K_θ/EI_{yy} on the vertical axis. The damping ratio is shown in as a colour plot, with the lighter colours indicating a lower damping ratio. This figure directly shows that the building mass is the most important property influencing the damping ratio obtained through the EFA. This damping ratio is smaller for a larger assumed building mass, and larger for a smaller building mass. From this figure, it also seems like the stiffness ratio does not affect the damping ratio.

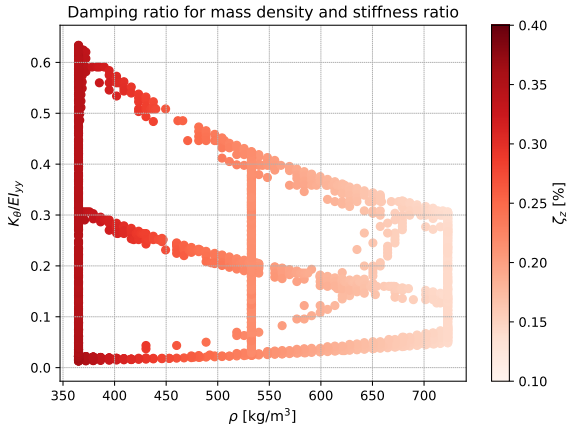

Figure 12.5: Damping ratio ζ_z based on the building mass density and the ratio of K_θ/EI_{yy}

To find out if there is a separate contribution of the assumed building stiffness or foundation rotational stiffness to the obtained damping ratio, an alternative visualisation of the results is presented in fig. 12.6. In this figure three plots are shown, and in each of these plots the building mass is fixed to either its lower bound, its mid value or its upper bound. The damping ratio is again presented as a colour plot with the same scale as in fig. 12.5, the horizontal axis shows the building stiffness EI_{yy}, and the vertical axis shows the foundation rotational stiffness K_θ. For a fixed building mass, all possible values for the stiffness result in the same damping ratio. This again indicates that the building mass is defining the damping ratio obtained, under the assumption that the combination of properties matches the measured natural frequency.

In order to allow for smaller differences to be visible, fig. 12.7 shows the same figure as the rightmost figure in fig. 12.6, but allowing a different scale for the damping ratio. Small differences can in fact be observed.

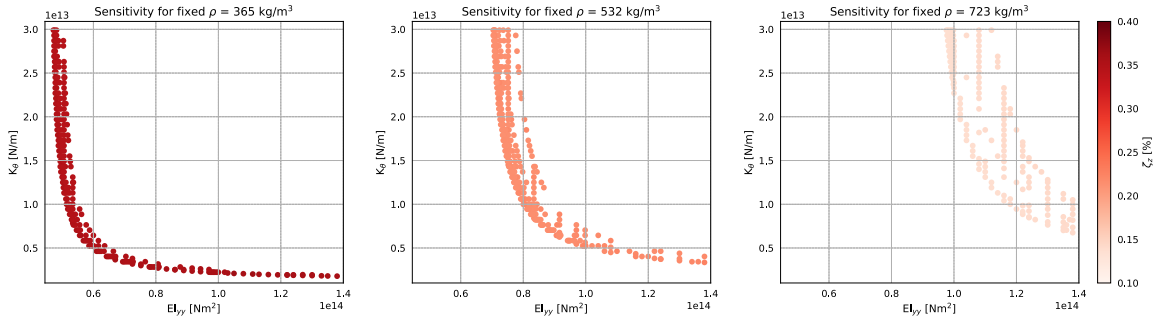

Figure 12.6: Damping ratio for fixed mass density depending on building and foundation stiffness

However, the difference between the largest and the smallest damping ratio is only 0.006 %. From this figure one could conclude that the combination of a larger building stiffness and a smaller foundation rotational stiffness results in a slightly lower damping ratio. However, since the differences in damping ratio are very small, one could also argue that this is a result of the slightly deviating natural frequency.

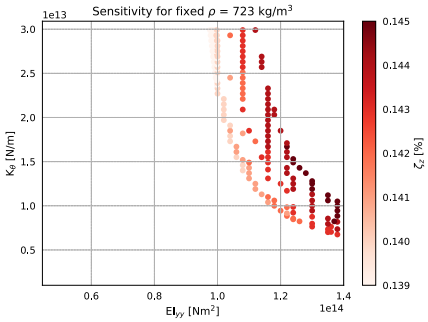

Figure 12.7: Damping ratio for fixed mass density with scaled damping ratio axis

	ρ_b [kg/m^2]	EI_{yy} [Nm^2]	K_θ [Nm/rad]	ζ_z [%]
1	365	1.05×10^{14}	2.09×10^{12}	0.37
2	555	9.24×10^{13}	1.13×10^{13}	0.20
3	723	9.98×10^{13}	2.37×10^{13}	0.14

Table 12.6: Combinations resulting in maximum and minimum damping ratio, and a combination with mid-range property values

Table 12.6 shows the resulting damping ratios obtained from three combinations of the structural properties. The first combination is the combination that results in the largest damping ratio of 0.37% found in this sensitivity study. The third combination uses the structural properties that result in the lowest damping ratio observed in this sensitivity study of 0.14%. The damping ratio of 0.20% was obtained with a combination such that all structural properties are closest the their mid range. The difference in damping ratio, expressed at the difference between the average and the maximum and minimum, is ± 45%. The sensitivity study showed that this depends on the building mass, which has a difference of ± 33 % from its mean value. This means the spread in damping ratios is diverging from the spread in the input building mass.

The results presented here are all based on the measurements in signal 11. Chapter 10 and chapter 11 showed that the current measurements do not provide results that are reliable. Therefore, the absolute values of the damping ratios obtained are not of interest. It is the variability in the EFA results that is of interest. To find out whether the presented results only apply to the measurement used, the damping ratios for the combinations in table 12.6 are also computed for the other 15 signals discussed in chapter 10. Again, it is not the absolute values of the damping ratios that one should focus on, it is the variability in these ratios. The damping ratios for all signals are presented in table 12.7. The last row shows the variability by means of the difference from its mean value.

A deviation in the damping ratios, all based on the ± 33% deviation in the building mass, vary between ± 19 % and ± 45%. This means that the results presented in this sensitivity study show the largest spread. Based on these measurements only, the conclusion is drawn that when the building mass input for the EFA has an error in the order of 30%, an error in the damping ratio of an order of 20-45% can be expected. When the stiffness values are matched based on the measured natural frequency, these will not significantly result in a damping ratio error.

For the comparison in this chapter, the calculation from dissipated energy to damping ratio was per-

	1	2	3	4	5	6	7	8
1	0.53	1.52	-2.89	0.57	-1.38	-0.30	0.29	0.69
2	0.36	0.96	-1.81	0.34	-0.91	-0.22	0.20	0.44
3	0.29	0.70	-1.31	0.23	-0.70	-0.19	0.16	0.32
$\Delta\zeta_z$ [%]	29	37	38	43	33	22	29	37
	9	10	11	12	13	14	15	16
1	3.28	-0.41	0.37	0.64	-1.19	3.01	-1.37	-0.75
2	2.42	-0.28	0.20	0.49	-0.83	2.35	-0.84	-0.52
3	2.02	-0.23	0.14	0.43	-0.67	2.06	-0.60	-0.42
$\Delta\zeta_z$ [%]	24	28	45	20	28	19	39	28

Table 12.7: Damping ratios obtained for 16 different signals for the 3 combinations of table 12.6

formed through the procedure explained in § 5.3 for the total structure. The influence of this means of comparison on the result was investigated by also performing a comparison based on the dissipated energy magnitude for one signal for all different structural property combinations. This again showed a strong relation between the dissipated energy obtained and the building mass, with increasing dissipated energy for a lower building mass. The variation in the results was of an order of 20% from its mean value rather than 33%. This difference is a result of the damping ratio calculation where the critical damping also depends on the structural properties. The influence of the stiffness properties was similar to what is presented in fig. 12.7. It indicates that a larger building stiffness and smaller foundation rotational stiffness results in larger damping values, but again the differences are extremely small and could also be a result of the slight difference in natural frequency.

12.5. Conclusions

The main purpose of this chapter is to investigate the sensitivity of the EFA to its structural property input. In order to perform this sensitivity study, a range of possible values for the structural properties building mass, building stiffness and foundation rotational and translational stiffness were defined. Defining these ranges highlighted the uncertainty in the structural properties.

Only combinations of the properties that match the measured natural frequency are allowed as input for the EFA. Therefore, the sensitivity of the natural frequency to these properties was first investigated. The most important property for the natural frequency is the building mass. For a decreasing building mass, the natural frequency increases. For the stiffness properties this is the other way around, the natural frequency increases for an increasing stiffness. The building stiffness influences the natural frequency with roughly the same order as the building mass. However, the foundation rotational stiffness and especially the translational stiffness values are of inferior importance for the natural frequency.

This means that in the combinations found, different values for the translational stiffness would result in a matching natural frequency while other properties are the same. This allowed for isolating the influence of the foundation translational stiffness on the damping ratio result of the EFA. This showed that this stiffness does not affect the EFA results.

Another conclusion drawn from the combinations, was the fact that the lowest building and foundation rotational stiffness were most likely a large underestimation. These values were not represented in the combinations based on the measured natural frequency.

The sensitivity study showed that a varying building mass input results in a variation in the EFA damping ratio output. However, the influence of the stiffness properties was not observable since large variations in the stiffness properties resulted in the slightest variations in the EFA results. The conclusion is drawn that this may also be a result of the slight variation in the natural frequency since a variation of up to 0.2% was allowed. This allowance was based on a similar difference in natural frequency for different measurements under the same wind conditions.

Based on the results of 16 measurements, it is concluded that a deviation in the building mass of the order of 30 % can result in a deviation in the damping ratio of an order of 20-45%. However, when comparing the dissipated energy rather than the damping ratio, the deviation in the dissipated energy is of an order of 20%. This is most likely due to the translation from dissipated energy to damping ratio using the critical damping. Performing this sensitivity study based on dissipated energy rather than damping ratio resulted in the same observations in terms of the influence of the properties.

IV

COMPARISON CLASSICAL TECHNIQUES

13

Half-power Bandwidth method

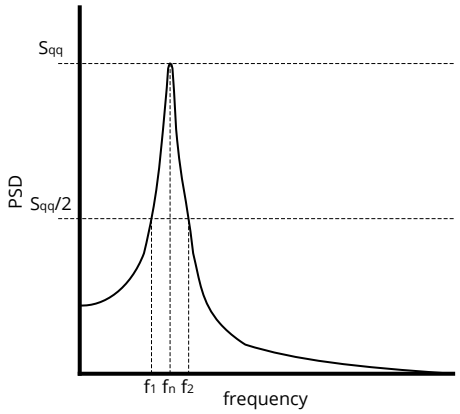

Figure 13.1: Half-power Bandwidth method

13.1. Introduction

The half-power bandwidth (HPBW) method is a frequency domain method to identify dynamic properties for SDOF systems. As described in chapter 3, the relation between the wind force input and the structural response is described through the mechanical admittance. This transfer function, or frequency response function as discussed in appendix A, depends on the dynamic properties of the system such as mass, stiffness, natural frequency and damping, and these can therefore be identified when the mechanical admittance function is known.

Looking at the Power Spectral Density (PSD) of the mechanical admittance as is visualised in fig. 13.1, the peak can be found at the natural frequency f_n. At half the height of the peak, two frequencies can be identified as f_1 and f_2. The frequency distance between these two frequencies is called the half-power bandwidth. Using this relation, the damping ratio is found through:

$$\zeta = \frac{f_2 - f_1}{2 f_n} \tag{13.1}$$

13.1.1. System prerequisites

There are several prerequisites to apply the HPBW method. First of all, as mentioned in previous chapter, it is assumed that the width at half-power is equal to $2\zeta f_n$. This is only valid for lightly damped structures, structures with a damping ratio ζ below 10%. For these structures, the resonant frequency may be taken as the natural frequency of the system. High-rise structures are lightly damped, and thus this method can be applied.

Secondly, the method is based on an SDOF system. It can identify the damping ratio corresponding to the peak of a single mode. In case of closely spaced modes, these peaks are not well separated and may have

a widened spectrum. This will affect the damping ratio, and therefore the method is not suitable for such systems. Depending on the structure, closely spaced modes also occur in high-rise buildings, as is the case of the New Orleans tower.

Finally, the HPBW method can only be applied to stationary records. This means that all statistical properties are invariant with time. If only the mean values and the covariance functions are invariant with time, the random process is called weakly stationary. If all possible probability distributions are not dependent of time translations, the process is called strongly stationary. In case of a Gaussian process all possible probability distributions can be derived from the mean and covariance functions, therefore for this process weak stationarity is the same as strong stationarity (Bendat and Piersol, 2010).

In order to identify the mechanical admittance function, knowledge on the system input and the system output is required. For high-rise buildings under wind-excitation, the input would be the wind force spectrum and the output the acceleration spectrum. However, usually little information is available on the wind force spectrum and only the output spectrum is available. It is thought to be appropriate to apply the HPBW method to the output spectrum directly under the assumption that the input spectrum is a white-noise spectrum. This means that the shape of the output spectrum is defined by the mechanical admittance function, and not by the input spectrum. The spectrum of wind is not a white-noise spectrum, but since the width of the peak in the output and mechanical admittance functions is very narrow, the wind spectrum can be assumed to be white-noise for this narrow frequency band. Therefore, the HPBW method is commonly applied to the output spectrum for wind-excited high-rise buildings.

13.1.2. HPBW quality

Considering the prerequisites are met, the accuracy of the HPBW method is mostly dependent on the quality of the PSD. The PSD is obtained through:

1. Breaking up the data time series into N segments with length T
2. Applying the Fourier transform to all of these segments separately to generate N times a raw Fourier spectrum
3. All N spectra are averaged through the following equation, which yields the PSD:

$$\hat{S}_{qq}(f_q) = \frac{1}{NT} \sum_{h=1}^{N} \left| X_h(f_q) \right|^2 \tag{13.2}$$

Various factors affect the quality of the PSD, bringing along bias and variance errors:

- Spectral leakage
- The period length T
- The number of segments N

First of all, spectral leakage. When the Fast Fourier Transform (FFT) is used to obtain the frequency domain representation of a signal, the analysis is based on an infinite set of data; in reality it will always be based on a finite data set. The FFT sees the signal as a circular topology, meaning that the two endpoints are connected. This is a good assumption when the signal is a certain integer amount of periods, but usually the measured signal is not an integer number of periods. The sharp transitions at the endpoints are discontinuities that will show up in the FFT as high-frequency components. It appears as if energy from one frequency leaks into the other, and therefore this is called spectral leakage. This leakage can be decreased by applying a technique called windowing, which reduces the amplitude of the discontinuities at the edges. It makes the endpoints meet, and therefore the results are obtained without sharp transitions.

Then there is the segment length T and the number of segments N. In practice, the amount of data available is always limited and therefore a decision has to be made regarding the number of segments used N and the length of the segments T. Increasing N results in more segments to average and thus a decreased influence of variance errors. On the other hand, increasing T results in a larger frequency resolution which decreases the bias error. First, the relation between the required frequency resolution and the period length T is explained. The required minimum frequency resolution is given by:

$$\Delta f_{req} = \frac{2 f_n \zeta}{4} \tag{13.3}$$

When the required frequency resolution is known, the required number of FFT points, indicated by $NFFT_{req}$ is calculated based on the sampling frequency f_s through:

$$NFFT_{req} = \frac{1}{\Delta f_{req}} f_s \tag{13.4}$$

The required number of FFT points, $NFFT_{req}$ should be rounded up to the nearest power of two to obtain $NFFT$ in order to permit the use of the FFT. Using this, the required time length of the segments can be calculated:

$$T = \frac{NFFT}{f_s} \tag{13.5}$$

The discrete frequencies at which the Fourier Transform is calculated are the following:

$$f_q = \frac{x}{T} \tag{13.6}$$

in which x is given by:

$$x = 0, 1, .., \frac{NFFT}{2} - 1 \tag{13.7}$$

A required segment length, and thus a required frequency resolution Δf is specified to be able to accurately describe the narrow spectral peak at the natural frequency. Using a segment length that is too short, this peak cannot be accurately described and inevitably results in spectral bias. The bias implies that the spectral peak is underestimated and the width is too large, resulting in an overestimation of the damping (Kijewski-Correa, 2003). The magnitude of the bias error is proportional to the square of the frequency resolution (Bendat and Piersol, 2010). Therefore, increasing the frequency resolution is a very effective way to reduce the error (Tamura et al., 2002). Similar to Pirnia (Pirnia, 2009), Tamura (Tamura et al., 2002) also found that for a small frequency resolution the damping is overestimated, and as the resolution gets better the error decreases until it converges.

However, in case of limited available data, which is usually the case, specifying a required segment length T automatically affects the number of segments available N for averaging to minimise the variance error. This is the paradox in spectral analysis; when limited data is available, increasing the length of each segment reduces the bias errors, but this directly implies that there will be fewer segments available to minimise the variance (Kijewski-Correa, 2003). Therefore, the challenge is to obtain sufficient amounts of stationary data to minimise the competing errors. This problem has been highlighted by Jeary (Jeary, 1986) and Tamura (Yoshida and Tamura, 2003) before, but many papers continue to appear with unrealistically large damping values (Tamura, 2013).

Avoiding the spectral bias and variance errors may be done by using longer records. However, one of the prerequisites was using stationary data and using longer records is prone to the presence of nonstationarity. In case of stationary data, lengthening T will reduce the bias, and it will decrease the random errors in estimates of the statistical properties. However, in case of non-stationary signals, an increase in T will result in a smoothing of the actual time variations in the statistical properties of the signal.

Other attempts to improve the performance of the PSD for smaller amounts of data were made by averaging ensembles of the PSD or by increasing the resolution of the PSD through curve fitting.

As mentioned before, the bias due to the spectral approach yields a consistent overestimation of the damping. In addition to the errors due to the spectral analysis, there is the error due to application of the HPBW itself. The error associated with the HPBW itself is in the order of 3 % for damping and negligible for frequency (Pirnia, 2009). This only holds if the bias in the PSD is sufficiently small. According to Kijewski (Kijewski-Correa, 2003), under ideal conditions with stationary signals, the spectral analysis can produce an estimate of the damping which has no error or up to 10%.

In case of coupled modes, where energy exchange between the modes is present, spectral damping estimates can experience large inflation due to the widened spectral bandwidth (Pirnia, 2009). In addition, as was demonstrated in chapter 4, both the damping and frequency are amplitude dependent. In case the HPBW is applied to a signal with different amplitude conditions, widening of the spectral peak can occur, which will have an important effect on the damping identification in the frequency domain (Kijewski-Correa and Pirnia, 2007). This was also investigated by Pirnia (Pirnia, 2009), who found that the changing frequency with amplitude has an influence on the accuracy of the damping estimation. The spectral analysis alone cannot find nonlinear properties such as amplitude dependence, since it assumes a linear system. Therefore, not considering this fact introduces errors in the damping estimates, which will be an overestimation. The

greatest errors are found for systems with amplitude dependent frequency rather than amplitude dependent damping in (Pirnia, 2009). Caution should be taken when applying a spectral approach to a system that is nonlinear.

13.2. Application New Orleans tower

For application of the HPBW method to the New Orleans tower, a very large data set is required to avoid spectral bias and variance errors. A data set is available for which the wind direction is 240 degrees with the north, and the wind velocity is ranging from 4.5 m/s to 20.5 m/s. For each wind velocity, a certain number of samples of 10-minutes with a sampling frequency of 20 Hz is available. The total data set contains 3718 10-minute samples.

Applying eq. (13.3),eq. (13.4),eq. (13.5),eq. (13.6) and eq. (13.7), the following requirements are found for the application to measured data of the New Orleans tower:

		z-direction	y-direction
f_n	Hz	0.286	0.297
ζ	-	0.010	0.015
Δf_{req}	Hz	0.00143	0.00223
f_s	Hz	20	20
$NFFT_{req}$	-	13987	8979
$NFFT$	-	2^{14} = 16384	2^{14} = 16384
T_{req}	s	819.2	819.2
T_{max}	s	600	600
Δf_{max}		0.00167	0.00167

Table 13.1: Requirements for the application of the HPBW

This is based on an initial estimate of the values for the damping ratio ζ, which were obtained from a study on the New Orleans tower by TNO (Bronkhorst et al., 2018). In order to minimise the bias, the segments should have a length of 819.2 s and in order to create a smooth PSD which is not largely affected by variance errors, a sufficient amount of segments is required. The length of each record is 10 minutes or 600 s. This means that this is the maximum length that can be used for the segments of the HPBW method, and the maximum frequency resolution that may be reached is 0.00167 Hz.

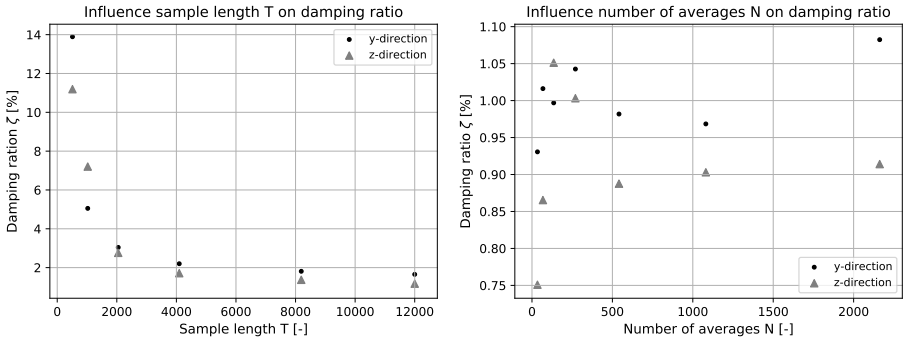

Figure 13.2: Influence of sample length T and number of averages N on damping ratio

In order to investigate whether this frequency resolution is close to convergence of the damping estimate from spectral bias, the damping ratio was calculated for this frequency resolution and smaller frequency resolutions in fig. 13.2. The length T varies from 512, 1024, 2048, 4096, 8192 to 12000 with frequency resolution of respectively 0.0391, 0.0195, 0.0098, 0.0049, 0.0024 and 0.0017 Hz.

According to previous calculations, the bias error would be avoided using a segment length of 819.2 s. The used segment length is slightly lower, and so it is expected that the resulting damping ratio is near convergence in terms of the bias error, although the bias error still exists. The convergence in terms of the bias error visualised in fig. 13.2 shows a similar result. Recall that the bias error is proportional to the square of the frequency resolution (Bendat and Piersol, 2010). The used frequency resolution is 0.00167, resulting in a bias error of 2.78×10^{-6}.

Figure 13.2 also shows the damping ratio depending on the amount of averages used. This study for the amount of averages was only performed for signals with wind velocity 4.5 m/s up to 8.0 m/s to avoid the effect of an inflated spectral peak due to amplitude dependence of the natural frequency. The maximum amount of averages is therefore 2162 and this number is decreased by removing segments. Since this is not a bias error, but rather a variance error with decreasing variance for larger numbers of averages, a large scatter is observed. The variance for smaller number of averages is larger due to the effect of the randomness in the averages. For z-direction it looks as though convergence occurs for a larger amount of segments. For y-direction this does not occur. This may be due to randomness in the signals used for the damping identification. It was the aim to reduce the amount of segments randomly, but this may not have been the case. Therefore, no requirement on the number of averages could be obtained from this figure. Similar to the requirement for the random decrement technique as will be explained in next section, it is assumed that at least 2000 averages are required.

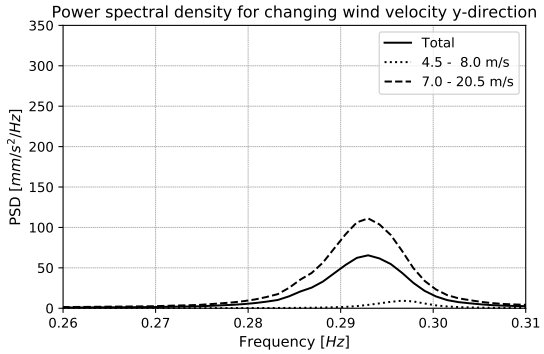

Figure 13.3: PSD total and wind velocity dependent in y-direction

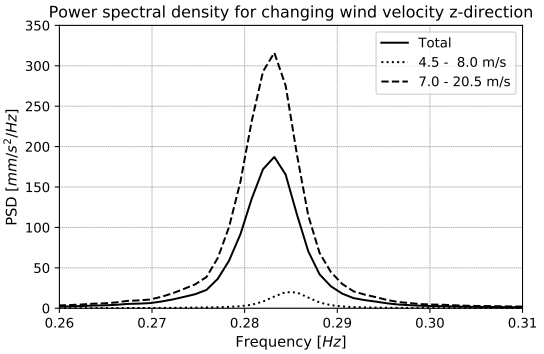

Figure 13.4: PSD total and wind velocity dependent in z-direction

After investigating the quality of the HPBW method, the damping ratios were calculated for sets of at least 2000 averages. In order consider amplitude dependence of these damping ratios, and in order to avoid spectral inflation, two sets were distinguished based on the wind velocity and therefore also on the amplitude of the response. The first set contains 2162 samples with wind velocity 4.5 up to 8.0 m/s, and the second set contains 2162 samples with wind velocity 7.0 up to 20.5 m/s. Due to limited data available, some overlap between the sets was necessary. The spectral plots of both sets and the total data set of 3718 segments are computed. These are visualised in fig. 13.3 for y-direction and in fig. 13.4 for z-direction. The amplitude dependent natural frequency and damping values are given in table 13.2.

	f_{ny} [Hz]	ζ_y [%]	f_{nz} [Hz]	ζ_z [%]
4.5 - 8.0 m/s	0.297	1.08	0.284	0.91
7.0 - 21.5 m/s	0.293	1.62	0.283	1.16
Total	0.293	1.65	0.283	1.17

Table 13.2: Amplitude-dependent natural frequency and damping ratio

From fig. 13.3, fig. 13.4, and table 13.2 it becomes apparent that the natural frequency decreases with increasing amplitude of vibration. The magnitude of the PSD also changes. This is due to the larger energy content of the set with larger amplitudes to average. This is the set with the highest average wind velocity. From table 13.2 it is clearly visible that the damping ratio increases with increasing amplitude of vibration. It should be noted that these values most likely provide an upper bound due to the fact that spectral bias could not entirely be eliminated and due to the fact that all sets contain a variety of amplitudes and therefore spectral inflation can be expected for all sets. This is also visible for the damping ratios obtained for the whole data set with 4.5 up to 20.5 m/s wind velocity. The obtained damping ratio is larger than any of the other two sets, while the data used is the same. This is expected to be a result of spectral inflation.

13.3. Summary

The half-power bandwidth method is a frequency domain method to obtain dynamic properties of a SDOF system. The method can be used for a stationary data set. Ideally the HPBW method should be applied to the

mechanical admittance function, but in case of white-noise input or a broad band spectral input function near the natural frequency, it is permitted to use the response spectrum directly. Using insufficient number of averages will result in a large variability of the damping estimates due to the influence of randomness in the signal. Spectral bias when obtaining the PSD is a major issue arising when the data set used does not provide sufficient frequency resolution. Due to spectral bias, overestimation of the damping ratio will be obtained, which has been observed in various studies. The amplitude dependence of the natural frequency and damping ratio can only be investigated by applying the HPBW method to data sets with different amplitudes. A data set that contains multiple amplitudes also results in larger damping estimates due to inflation of the spectrum width due to the variability in the frequencies involved. The effects of spectral bias for limited sample length, and variability for a limited number of averages have been observed when applying the HPBW method to data of the New Orleans tower. Also, amplitude dependence has been observed and the effect of spectral inflation with considering sets with multiple amplitudes has been recognised. Due to the fact that spectral bias could not be eliminated entirely and due to the fact that the data sets contain a range of amplitudes, the damping ratios provided in this chapter are most likely upper bound values. Besides, the New Orleans tower shows modal coupling, resulting in a MDOF system rather than a SDOF system.

14

Random Decrement Technique

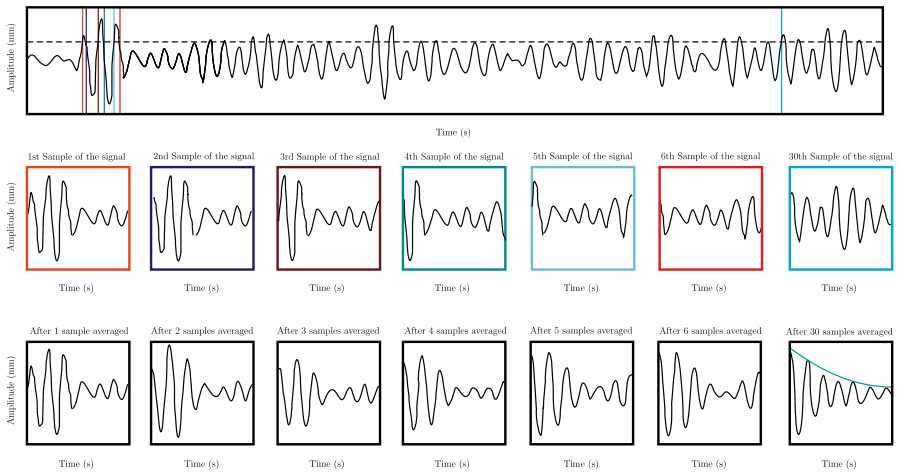

Figure 14.1: Application of the Random Decrement technique. Adapted from Seppänen (Seppänen, 2017)

14.1. Introduction

The issues with frequency resolution based on short length records in the spectral analysis explained in chapter 13 can be avoided using techniques in the time domain. A very commonly used time domain technique is the Random Decrement (RD) technique. In this technique a set of segments from the time domain response of the system is averaged; the resulting signature is called the Random Decrement Signature (RDS). This signature is supposed to resemble a free decay response, and dynamic properties can be identified from this signature using various methods such as a simple calculation from the peak values, fitting a logarithmic decrement function over the RDS envelope, or an analytical signal to fit the entire RDS (Pirnia, 2009).

Application of the RD technique is visualised in chapter 14. The segments used for the averaging to create the RDS are chosen based on a triggering condition. This triggering condition resembles an initial condition and the final signature is a free vibration from this initial displacement. It is possible to obtain a free decay response because the dynamic response of a linear system can be seen as a superposition of the response due to initial displacement, initial velocity and the forced vibration response (Kareem and Gurley, 1996):

$$x_t = x_{x_0} + x_{\dot{x}_0} + x_f \tag{14.1}$$

The samples should be averaged such that the initial velocity and the forced vibration response reduce to zero. This is possible in case the forced vibration response is a random process with stationary mean zero. If enough segments are averaged, the signature for the forced response will automatically become a decaying signal. Besides, if all segments begin at the same triggering level, with alternating positive and negative slope,

the response due to the initial velocity will also vanish. The response due to the triggering level will remain. The RDS obtained after averaging can be expressed as (Yang et al., 1983):

$$RDS(\tau) = \frac{1}{N}\sum_{i=1}^{N} x_i(t_i + \tau) \tag{14.2}$$

This equation essentially states that a signature of length of τ will be obtained by averaging N samples from their triggering time t_i with length of τ. The triggering value is given by $x_i(t_i)$.

14.1.1. System prerequisites

It is clear that this technique also does not require any information about the system input. It is good to mention that through this technique the auto-correlation function of the system is obtained. This is a function that describes the correlation between points separated by various time lags and is not generally proportional to the free decay of a linear system. Only for a SDOF system with a zero mean stationary Gaussian white noise input where the damped natural frequency is close to the undamped natural frequency, this auto-correlation function is analogous to the free decay response (Kareem and Gurley, 1996, Kijewski-Correa, 2003, Vandiver et al., 1982). However, this method is often used for cases where the input is not a white noise stationary Gaussian process.

Since the RD technique is based on a SDOF system, it is customary practice to use a bandpass filter around the mode of vibration of interest before applying the technique. Due to the fact that this technique is based on a SDOF system, it is not as reliable in a MDOF system with coupled modes. First of all, it is hard to filter out one particular mode, but second of all, the modes will exchange energy which will be captured through this technique in terms of damping. Therefore, a Multi-mode Random Decrement (MRD) technique was developed, which will be discussed in § 14.1.3.

14.1.2. RDS quality

Based on the system prerequisites and the decisions that have to be made when applying the RD technique, there are several factors that influence the quality of the RDS which have previously been investigated in literature. The quality of the RD technique is often explored using the variance of the obtained RDS.

Linearity

The effect of applying the RD technique to a nonlinear system was investigated (Kareem and Gurley, 1996). It was found that the result was comparable to the results obtained with the linear system. However, the results were not robust with respect to the chosen triggering level and the chosen cycles to obtain a damping value. These matters will be discussed later on in this chapter.

White noise assumption

As previously discussed, the technique is based on a white noise assumption of the input. However, in practice this assumption is often violated and the RDS cannot be equal to the free decay response. Fortunately, the errors made are marginal in case the input signal is sufficiently broad-band (Vandiver et al., 1982). Therefore, for wind load in the along wind direction the RD technique provides sufficiently accurate results. For vortex shedding wind loads in cross wind direction the identified damping values can differ from the known values, and were in fact found to be significantly lower (Kareem and Gurley, 1996).

Stationarity

The signal is assumed to be stationary, meaning that all statistical properties are invariant with time. In case of a Gaussian process all possible probability distributions can be derived from the mean and covariance functions (Bendat and Piersol, 2010). In practice it is commonly assumed that wind-induced response of structures is stationary, but examination of full-scale data has often demonstrated otherwise (Kijewski-Correa, 2003). Compared to the theoretically accepted stationary signals, the variance of the RDS for a nonstationary signal is significantly larger (Kijewski and Kareem, 2000).

Triggering condition and number of segments

The quality of the RDS is influenced by the triggering condition chosen and the number of segments used to average the response. These two are related, since the triggering level chosen influences the number of segments that can be included in the averaging process. Since sufficient number of segments have to be

included in the RD technique in order to obtain reliable results (Kareem and Gurley, 1996), one could argue that a lower triggering level is better. This is in fact not true, because the lower triggering levels tend to be more contaminated with noise (Brincker and Rodrigues, 2005). Therefore, a balance between the need to include sufficient segments and avoiding noise contamination has to be found. A good value for the triggering level can be expressed using the standard deviation σ. Brincker (Brincker and Rodrigues, 2005) found an optimum for the triggering level at $\sqrt{2}\sigma$ and Kijewski (Kijewski-Correa, 2003) mentioned that the triggering level should be between σ and 3σ. A triggering level below σ yielded inconsistent performance of the RD technique which could be either due to the aforementioned noise contamination, or because the segments are found to close to each other increasing the correlation of segments. It is worth mentioning that in case the same amount of segments can be found for a higher and a lower triggering level, the higher triggering level will yield more consistent performance even when no noise is present (Kijewski-Correa, 2003). This can be explained by the fact that the response after a high amplitude will already somewhat resemble a free decay response, and the response after a low amplitude will most certainly not. Therefore, for the same amount of averages, the higher amplitude triggering level will perform better. In other words, higher amplitude triggering levels will yield less segments, but also require less segments.

For a continuous response it is possible to describe the triggering level as a certain value, but for a discrete response, where the response is measured with a certain sampling rate, it is very unlikely that exactly the triggering value will be found. Therefore, the triggering condition can be expressed as the so called positive point condition. The triggering level is described in the order of a few percent and the data points within this triggering range will initiate a segment (Kijewski-Correa, 2003). By keeping this range in the order of a few percent, is should be avoided that multiple data points are found in the triggering level for one peak.

A larger range of triggering levels can be used to investigate the variability in the RDS and subsequently the damping estimates. A mean value and a coefficient of variation can be expressed for the identified damping estimates over this range and these properties can be allotted to the average triggering level.

In multiple studies, the amplitude dependence of a system is investigated by varying the triggering level. This means that the non-linearity of a system is investigated through a method that requires linearity. It is comparable to what has been done in the HPBW method to detect non-linearity; only those segments with a certain amplitude are considered. In case of the HPBW this was done by creating subsets depending on wind velocity. In this case it is done by varying the triggering level. Although it might be possible to investigate amplitude dependence using this technique, it is difficult to investigate the dependence of damping on amplitude for the high amplitude plateau as mentioned by Jeary (Jeary, 1996) and explained in chapter 4. This is because little data is available for these high amplitudes, and the RD technique requires a sufficient number of segments for averaging.

Therefore, when the triggering level is chosen for the RD technique, it is important to confirm whether sufficient segments are generated through this triggering level. Different number of segments were proposed in order to be able to remove the random component through averaging. Yang (Yang et al., 1983) proposed 400-500 segments, while Tamura proposed at least 2000 segments (Tamura et al., 1992). This difference can be explained by the dependence of the number of segments required on the randomness in the excitation (Kijewski-Correa, 2003) and the triggering level employed.

Segment correlation

The assumption that the averaged response of a random process with stationary mean zero value will yield a zero response is based on the fact that the segments that are averaged are independent. Therefore, the correlation of segments taken from the original response will have an influence on the reliability of the technique. The effects of correlation were found to be marginal (Kijewski and Kareem, 2000). This is advantageous, because by allowing overlap in the segments, more segments can be found for averaging.

Segment duration

Besides the triggering level, the number of segments and the segment correlation, the length or duration of the segments is also subjective. This is of interest, because the dynamic properties will be identified based on a certain number of cycles, which is usually in the order of several cycles. When the dynamic properties are identified through the logarithmic decrement, the peaks in the decay curve are used. The logarithmic decrement can be defined as follows (Kijewski-Correa, 2003):

$$\delta = \frac{1}{n} \ln\left(\frac{x(t)}{x(t+nT)}\right) \tag{14.3}$$

In this equation $x(t)$ is the amplitude of the first peak, while $x(t+nT)$ is the amplitude of the n-th peak. The damping ratio can then be found using this logarithmic decrement Δ:

$$\zeta = \frac{1}{\sqrt{1+\left(\frac{2\pi}{\Delta}\right)^2}} \tag{14.4}$$

For lightly damped structures, where the damping ratio is much smaller than 1 or 100% this may be simplified to:

$$\zeta \approx \frac{\Delta}{2\pi} = \frac{\frac{1}{n}\ln\left(\frac{x(t)}{x(t+nT)}\right)}{2\pi} \tag{14.5}$$

Another method to obtain the damping ratio and natural frequency of the system is using the entire RDS rather than the peak values. An analytical expression of the free decay of a SDOF system is used to fit to the RDS, yielding the damping ratio, natural frequency and phase using least squares estimates:

$$\begin{aligned} x(t) &= \frac{x_0}{\sqrt{1-\zeta^2}} e^{-\zeta\omega t}\cos\left(\sqrt{1-\zeta^2}\omega t - \phi_i\right) \\ RDS(t) &= x(t) \end{aligned} \tag{14.6}$$

The reliability of the damping estimates obtained from a single cycle is poor (Kijewski-Correa, 2003). The results are more stable when the damping is estimated based on the first few cycles. Since the variance in the damping estimate increases when more cycles are included (Kijewski-Correa, 2003), there is again a balance to be found. It is advised to use four cycles to obtain sufficient accuracy and to limit the variability (Kijewski-Correa, 2003). The same optimum for the amount of cycles included was found by (Pirnia, 2009). Besides, it was found that the damping estimates are better in case of higher damping and that the error in the frequency and damping obtained through the RD technique converge to a non-zero mean value, which is positive for the frequency and negative for the damping. This indicates a bias that overestimates the frequency and underestimates damping. The error found in the simulated damping when applying the logarithmic decrement after the RD technique was found to be around 20% and in case of a very low damping ratio of 0.5% the error was 50%. When subdividing the error it was found that 11% was due to the application of the logarithmic decrement, the remaining due to the derivation of the RDS. The large errors are most probably due to the sensitivity to noise; this problem is lessened when the damping values are obtained through the analytical fit rather than the logarithmic decrement (Pirnia, 2009). Applying the RD technique to coupled modes, the damping is generally overestimated (Kijewski-Correa and Pirnia, 2007, Pirnia, 2009). Therefore, a multi-mode approach of the RD technique was presented (Tamura et al., 2002).

14.1.3. Multi-mode Random Decrement technique

The RD technique is made for SDOF systems, but a Multi-mode RDT exists (Tamura, 2013). When applying the RD technique to a MDOF system rather than a SDOF system, the technique results in a MDOF autocorrelation function. This autocorrelation function is a superimposition of the free decays of several modes (Tamura et al., 2002). The RDS signal is then approximated by the superimposition of multiple SDOF systems with different dynamic properties, and the free decay can be given as follows:

$$\begin{aligned} x_i(t) &= \frac{x_{0_i}}{\sqrt{1-\zeta_i^2}} e^{-\zeta_i\omega_i t}\cos\left(\sqrt{1-\zeta_i^2}\omega_i t - \phi_i\right) \\ RDS(t) &= \sum_{i=1}^{n} x_i(t) + m \end{aligned} \tag{14.7}$$

In this equation $RDS(t)$ is the RDS signature that has to be matched with the one found through the RD technique. $RDS_i(t)$ is the i-th mode component, x_{0_i} is the initial value of the i-th mode component, ζ_i is the i-th mode damping ratio, ω_i is the i-th mode circular frequency, t is the time, ϕ_i is the phase shift and m is the mean value correction for the RDS. An approximation of the dynamic properties can be made by the least-square method. This approach was investigated by Tamura (Tamura et al., 2002), and the results were satisfactory.

14.2. Application New Orleans tower

In chapter 13 it was specified that a data set is available for which the wind direction is 240 degrees with the north and in which the wind velocity is ranging from 4.5 m/s to 20.5 m/s. For each of these wind velocities, a certain number of 10-minute samples with a sampling frequency of 20 Hz is available. The total set contains 3718 10-minute samples. As previously discussed, for the random decrement method around 400-2000 averages are required. In addition, the damping estimate should be obtained from the first few cycles, and it is recommended to use the first four cycles. For this building, this means that the segments should have a length of 4 times the period. The period is approximately 3.5 s, so this means that a segment length will be 17.5 s. Therefore, there is sufficient data available to perform the RD technique with a sufficient amount of averages. The amplitude dependence of a system can be investigated in the RD technique by using all the data available and by changing the trigger value. As mentioned before, it is interesting that a nonlinear system is investigated through a method based on a linear system. Besides, by using all data available, the requirement of stationarity most certainly is not met, since the standard deviation will be much higher for data recorded under higher wind velocity. Since there sufficient data available for this technique, two approaches of investigating the amplitude dependence were performed:

1. The entire data set of 3718 10-minute samples with wind velocity from 4.5 to 20.5 m/s will be used. The trigger value is varied from 0.2 mm/s^2 to 10.0 mm/s^2. The damping ratio and natural frequency will be obtained based on the trigger value, which is the amplitude at the onset of the free decay. This results in a plot for the amplitude dependence of both damping and frequency.

2. To meet the requirement of stationarity, the data set is divided into subsets based on the wind velocity. For each of these sets, the RD technique is performed for one trigger value. This is chosen to be $\sqrt{2}\sigma$, as is recommended in the literature. The number of averages for each subset was kept similar, around 2000 averages. The amplitude dependence of damping is obtained by comparison of the damping ratio obtained for each subset.

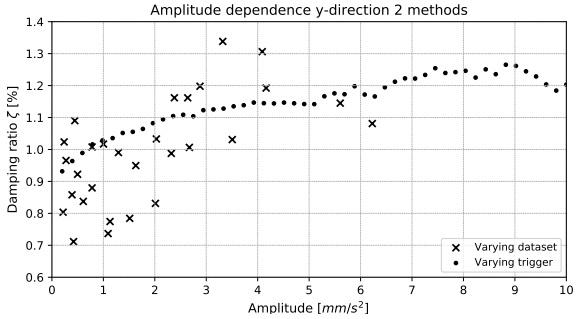

Figure 14.2: Amplitude dependence damping ratio y-direction 2 methods

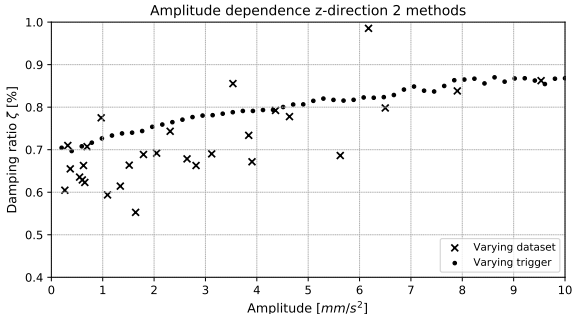

Figure 14.3: Amplitude dependence damping ratio z-direction 2 methods

The first method is represented in fig. 14.2 and fig. 14.3 by the black dots, while the second method is represented by the crosses. It becomes apparent that the second method results in a large scatter in the damping ratios, while the first method provides a neat line. Only for the lower amplitude levels, the number of averages used for the second method is lower than the number of averages used for the first. A possible explanation could be that the second method only contains values for lower amplitudes. Figure 14.2 and fig. 14.3 also show the increasing trend for the damping with amplitude. The higher plateau from fig. 4.4 is not directly visible, although in y-direction the damping seems to decrease for higher amplitudes, in z-direction the damping is rather flat for higher amplitudes. The amplitude dependence of the natural frequency was also investigated through the first method, and the result is presented in fig. 14.4. A clear decrease in natural frequency with increasing amplitude is visible. It appears that the natural frequency decreases faster for smaller amplitudes compared to larger amplitudes. Since the RD technique is based on a SDOF system, it might not be directly applicable to the New Orleans tower. Positive is the fact that mainly one frequency is observed in the principal directions, but from the varying amplitudes it appears that energy is being transferred. Therefore, the MRD technique is applied to investigate the effect of the MDOF approach to the damping ratios. This is shown in fig. 14.5. For smaller amplitudes, the MDOF approach appears to provide smaller damping ratios than the

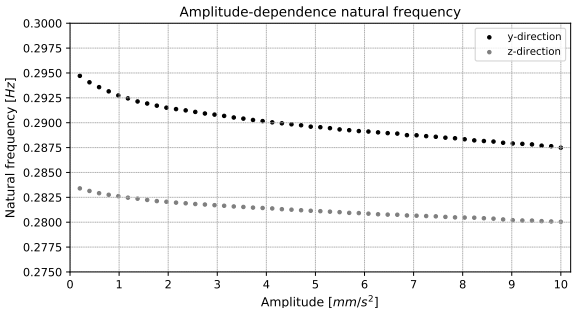

Figure 14.4: Amplitude dependence natural frequency

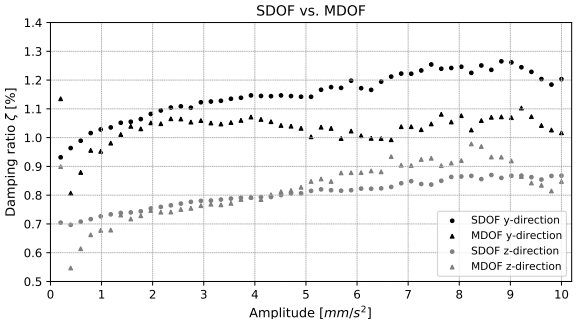

Figure 14.5: SDOF vs. MDOF random decrement technique

SDOF approach. However, for the larger amplitudes in z-direction this does no longer hold. For larger amplitudes it appears that the damping ratios for both directions are more similar than for the SDOF approach, leading to smaller damping ratios in y-direction and larger damping ratios in z-direction. It should be noted that a bias error was found when applying the RD technique (Pirnia, 2009), which overestimates the natural frequency and underestimates the damping ratio.

14.3. Summary

Application of the random decrement technique provides damping ratios for both directions of vibration. When investigating the amplitude dependence by varying the triggering level, a more or less smooth plot was obtained in which the damping increases for increasing amplitudes. For the natural frequency, as expected, a decreasing trend was observed for larger amplitudes. It should be noted that due to a bias error (Pirnia, 2009), the natural frequency is most likely overestimated, while the damping ratio is underestimated. This application did not directly meet the stationarity conditions, and the random decrement technique is a technique for SDOF systems, which the New Orleans tower is not. Therefore, a comparison was made with the multi-mode random decrement technique. It demonstrates that for smaller amplitudes the damping ratios are generally smaller than the ones obtained from the SDOF approach, while for larger amplitudes the damping ratios seem to be more similar, the damping ratios in z-direction are larger and the damping ratios in y-direction are smaller.

15

Comparison identification techniques

In this chapter three different techniques to identify damping in high-rise structures are compared. The commonly used Half-power Bandwith (HPBW) method and Random Decrement (RD) technique are compared to the novel Energy Flux Analysis (EFA). All three techniques have been applied to the New Orleans tower, and the application and results were discussed in chapter 13 and chapter 14 for the HPBW method and RD technique respectively. An extensive sensitivity study of the EFA has been performed in this report, of which the results are given in chapter 9, chapter 10, and chapter 12. Due to the fact that no reliable results have been obtained with the EFA, this comparison is rather qualitative and is made based on the following aspects:

- **Applicability**: The applicability of the techniques focuses on the assumptions on which the techniques are based. These assumptions results in prerequisites for applying the identification technique.
- **Workability**: The aspect of workability focuses on the amount of effort required to apply the techniques. In this case effort means both computational effort, required measurements and required knowledge of the user.
- **Outcome**: The outcome section concentrates on the results that can be obtained with the technique and how these can be interpreted.

15.1. Applicability

Degrees of freedom

First, the prerequisites regarding the amount of degrees of freedom is discussed. The HPBW method is strictly only applicable under the assumption that the measured building motion concerns a SDOF system. This assumption applies to high-rise building when the separate modes are far apart and can therefore be distinguished. This means that the HPBW method is not applicable in case of closely spaced modes. In this case, the spectral analysis will determine the damping based on a coupled, more energetic response, and this will result in an overestimation of the damping ratio (Kijewski-Correa, 2003). The same holds for the RD technique. However, by means of superimposition the method can be applied to a MDOF system. The resulting Random Decrement Signature (RDS) will be representing multiple modes, of which the damping will be found by means of a least squares fit. Results of the MDOF RD technique presented in literature (Tamura et al., 2002) are promising.

The EFA approaches the damping identification through an energy description. Energy is a scalar quantity, it does not depend on the direction. Therefore, when applied to a SDOF system, the energy dissipation found is the energy dissipation for that particular mode. When applied to a MDOF system the resulting energy dissipation is a combination of the energy dissipation of multiple modes. This makes the EFA more widely applicable.

Lightly damped structures

The HPBW method and the RD technique can only applied to lightly damped structures. This is due to the fact that damping affects the natural frequency of a system. However, for lightly damped structures where the damping ratio is below 0.1 or 10%, this effect can be neglected. For the EFA, the system does not necessarily

have to be lightly damped. Energy dissipation can be computed through this technique irrespective of the amount of damping, and the result will be the amount of energy dissipated.

The application of these technique to high-rise structures directly satisfies the prerequisite of a lightly damped structure is met. This means that this prerequisite will not affect its application to high-rise structures, which makes them equally suitable.

Stationarity
The requirement of stationarity means that all statistical properties are invariant with time. This is important for both the HPBW method as well as the RD technique, because it is the randomness in the data that influences the quality of the Power Spectral Density used in the HPBW method and the Random Decrement Signature used in the RD technique (Kijewski-Correa, 2003). Both techniques must average out the effects of randomness, and therefore their performance is dependent on the amount of averages used. The fact that the input motion signal has a zero mean Gaussian distribution is the basis for the RD technique assumption that the effect of the initial velocity and forced vibration response will reduce to 0 for sufficient amount of averages. In case the stationarity requirement is not met, the RDS will contain large variability.

The EFA measures the system input and is not based on any statistical assumptions. Therefore, stationarity of the signals used is not a prerequisite. However, one could argue that the use of non-stationary measurements does not consider any non-linearity occurring in the measurements. The analysis of non-linearity is discussed in § 15.3.

White-noise input
Both the HPBW method and the RD technique require the input of the system to have a white-noise spectrum at the frequencies of interest. When applying these techniques in the along wind direction, the spectrum is sufficiently broad band such that the errors made due to the violation of this assumption are marginal (Vandiver et al., 1982). However, in cross wind direction, due to the effect of vortex shedding and possible lock-in effects, the white-noise assumption may violated to a larger extent, making the errors of importance. The identified damping values for the RD technique in case of cross wind measurements were found to be significantly lower (Kareem and Gurley, 1996).

15.2. Workability

Measurements
All three methods require in situ measurements on the high-rise structure under investigation. The HPBW method and RD technique only require measurements of the building motion, the input is assumed to be white-noise. When designing the measurements campaign it is important to consider the possibility to distinguish different modes in the measurements.

The EFA, however, requires additional measurements. Information on the wind force is required and due to the importance of the fluctuations of this wind load, and the phase between both measurements, is not sufficient to use a theoretical wind spectrum. This could be seen as a major drawback of this method, since pressure measurements are not straightforward and affect the practical and economical feasibility of application of this technique. Besides, the requirement of time synchronised measurements requires attention and the importance of the phase of the measurements requires attention. This thesis shed light on the fact that the Energy Flux Analysis is extremely sensitive to any deviations in the phase, which significantly complicates its workability.

Measurement time
Due to the statistical basis of the HPBW method and the RD technique, sufficient mount of segments are required for averaging. For the HPBW method the segment length should be sufficiently large to ensure the required frequency resolution. For the application to the New Orleans tower with a sampling frequency of 20 Hz, each segments should be at least 819.2 s when additionally, although not specified in literature but based on the same assumption of the RD technique, at 2000 segments are required. This means that the measurement length should at least be 1,638,400 s, which is at least 19 days of measuring. Clearly, such long measurement lengths affect the condition of stationarity and the measurements will contain responses of varying amplitude. This means that the result of the HPBW method are affected by non-stationary and non-linearity for the method assuming stationarity and linearity. Avoiding this would require much more than 19 days of measuring, to be able to categorise the measurements based on statistical properties and amplitude of vibration. In case this limited measurement time for the HPBW method is not respected, spectral bias

will inevitably occur due to limited frequency resolution. This spectral bias results in an overestimation of the damping (Kijewski-Correa, 2003). This is the reason that it is often argued in literature that time domain techniques are more representative than spectral methods (Smith and Willford, 2008).

For the RD technique, it is also assumed that at least 2000 segments are required. The important difference is the fact that these segments allow overlap, which means that one measurement can supply many segments. The segment length for the RD technique should at least provide approximately four cycles of vibration in the resulting RDS. For the New Orleans tower, this means that the segment length should at least be 14 s. When the allowance of overlap is not considered, the required measurement time is 28,000 s or 8 hours. Similar to the HPBW method, to be able to guarantee stationarity in these measurements used, it is advisable to increase this measurement length such that the measurements can be categorised based on statistical properties.

In case of the EFA, no statistical assumptions were made. This means that even when measuring a single cycle of vibration, it should be possible to find the dissipated energy in the system. This means that theoretically a measurement length of 3.5 s would be sufficient. However, filtering may affect the beginning and end of a signal and using such limited measurement time results in a large dependency of the result on the estimation of the total wind load magnitude and building vibration. Therefore, it is wise to use larger measurement times.

Computational effort

When many analyses will be performed, the computational effort of the techniques becomes important. Rough estimates of the computation time were found by applying the methods to the New Orleans tower in two directions using a simple laptop. The RD technique and the HPBW method take less than 5 minutes, the EFA takes around 10 minutes. However, the comparison is not exactly fair. The HPBW method uses a readily available package of Python to find the power spectrum, while the RD technique and the EFA use self-made scripts. Due to the limited programming skills of the author, the efficiency of the latter two can most likely be improved.

User knowledge

The user of the HPBW method does not require any specific knowledge on the background of the methods for certain decisions to be made in the application. The user should only be aware of the fact that sufficient, stationary data should be used and that non-linearity can affect these results and should be considered. For application of the RD technique, this knowledge is also required. Additionally the user should be aware of the effects of the triggering level chosen. Through this triggering level, non-linearity can be considered. However, for a too low triggering level the results will be affected by noise.

For the EFA a little more knowledge is required in order to interpret the resulting energy dissipation and to be able to translate this to a desired damping representation such as a damping value or damping ratio. Many different approaches may be used. Besides, an important difference with the other techniques, is the fact that knowledge on the structural properties is required. Chapter 12 showed that the EFA is sensitive to the structural properties assigned to the structure.

15.3. Outcome

The first important difference in the output of the techniques to consider is the fact that the HPBW method and RD technique directly provide a damping value or ratio, whereas the EFA provides the energy dissipation. This means that when objective is to obtain a damping value, which usually is the objective, the dissipated energy still requires translation.

Although this may be seen as a drawback of the EFA, it actually is an advantage. Obtaining the dissipated energy rather than a value straight away, allows for interpreting the results and acquiring knowledge on the behaviour of the structure. The user is free to decide as to whether the dissipated energy should be modelled as viscous damping, Coulomb damping, or any other damping model. Another major importance is the fact that the EFA allows for identifying damping of a part of a system, while the HPBW method and RD technique only allow for total damping identification. This latter advantage is one of the major motivations of developing this method. Overall, the EFA can contribute to the understanding of damping in structures, while the other techniques will only provide a value that may be used for modelling structures and comparison reasons.

The RD technique allows for simple investigation of non-linearity in terms of amplitude and frequency dependence of damping by varying the triggering level. The spectral approach of the HPBW method is said to only provide an averaged sense of the dynamic properties of the system in time (Kijewski-Correa, 2003).

This also holds for the EFA. However, when sufficient measurements are available, and the measurements can be categorised based on amplitude of vibration, the HPBW method and EFA may also be used to detect non-linearity.

15.4. Conclusions

The HPBW method and RD technique can only be applied to find the total damping in a system of which the input spectrum for the wind load can e assumed white-noise for the frequencies of interest, which is only justifiable for the along wind direction. Besides, measurements should provide stationary data. For the HPBW method an additional limitation is the fact that it can only be applied to systems with well separated, uncoupled modes. No such prerequisites apply to the Energy Flux Analysis. All three methods allow for investigation of the non-linearity of damping, although this is most straightforward for the RD technique.

Additional to structure motion measurements, the Energy Flux Analysis requires wind pressure measurements, which affect its practical and economical feasibility. Besides, the Energy Flux Analysis was found to be extremely sensitive to any delay in terms of phase. This makes application of the Energy Flux Analysis challenging. The Energy Flux Analysis also requires more knowledge of the user than the other two techniques. This is because the result is damping expressed as dissipated energy rather than a damping value or damping ratio. The user should choose a method to obtain a damping value or ratio if desired. Besides, the Energy Flux Analysis requires input of the structural properties, which can only be estimated with limited accuracy, and this estimation requires understanding of the structural behaviour.

On the contrary, the Energy Flux Analysis also provides the user with more knowledge on the structural behaviour. A major advantage of the Energy Flux Analysis technique is the fact that it can also identify damping in components of a system. This opportunity is in demand because many researchers are focusing on the contribution of, for instance, the soil-structure interaction on the total damping of a structure.

V

CONCLUSIONS AND RECOMMENDATIONS

16

Conclusions

The novel Energy Flux Analysis is a promising damping identification technique that should aid in acquiring further knowledge of damping behaviour in structures. Damping identification techniques already exist to date, and the two most commonly used techniques are the Half-power Bandwidth method and the Random Decrement technique. However, these techniques are only reliable in case of extensive measurements in terms of time and if their application meets specific requirements. The methods require the structure to be lightly damped, require extensive stationary motion measurements, and an input spectrum that has a white-noise shape for the frequencies of interest. The requirement of using extensive stationary motion measurements has often been violated in literature resulting unreliable damping values, and the requirement of the input having a white-noise spectrum means that application in cross wind direction may not be allowed. Besides, the Half-power Bandwidth method is only applicable to structures with well separated modes. The Energy Flux Analysis does not have any of these requirements, making it more widely applicable. Another major benefit of the Energy Flux Analysis is its ability to identify not only the total damping of a structure, but also the damping contribution of components of a structure. This is a very significant difference, as this will strongly contribute to the understanding of damping behaviour in structures. However, where the other techniques only require structure motion measurements at one location, the Energy Flux Analysis applied to find total or superstructure damping requires information on structure motion and wind load over the full structure height, and it requires information on internal forces at the boundary of components. The Energy Flux Analysis has been verified using lab structures, but when applied to high-rise structures, little is known about its performance. The aim of this thesis was to investigate the sensitivity of the Energy Flux Analysis to the uncertainties imposed when applying it to a high-rise structure to identify the total, superstructure and soil-structure interaction damping using spatially limited in situ measurements and to additionally formulate its prerequisites of use.

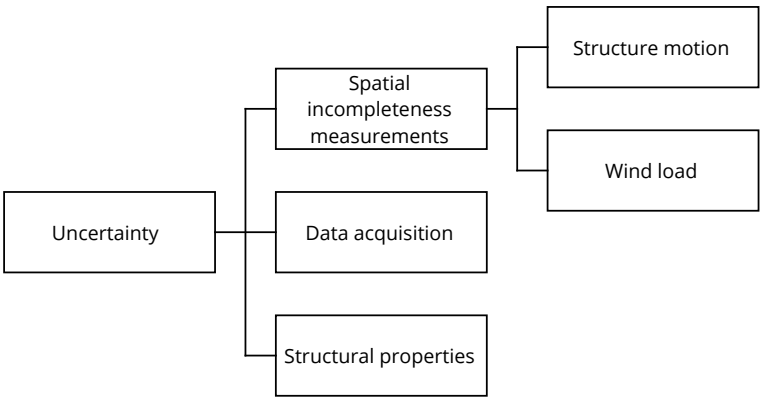

Figure 16.1: Uncertainties introduced to the Energy Flux Analysis when applied to high-rise structures excited by wind using in situ measurements

Using spatially limited measurements imposes uncertainty on the structure motion and wind load input of the Energy Flux Analysis. Both have to be specified along the full building height, but due to practical and

economical reasons both will only be measured at limited locations. Besides, the data acquisition, which refers to measurement instrument and set-up, data collection and data processing, introduces further uncertainties. Finally, the Energy Flux Analysis requires specification of the building mass, building stiffness, and foundation stiffness. Accuracy of the estimates of these properties is limited.

Sensitivity of the Energy Flux Analysis to the aforementioned four sources of uncertainty, presented in fig. 16.1, has been investigated through application of the Energy Flux Analysis to the New Orleans tower in Rotterdam. Acceleration and wind pressure measurements are available at 114 m height of the 155 m tall building. This thesis revealed that the Energy Flux Analysis is most sensitive to uncertainties in the structure motion and wind load. More specifically, sensitivity to the magnitude of the structure motion and wind load is limited, but it is highly sensitive to the phase of the signals. The signal phase is assumed to be known at the measurement location, but extrapolation of the measured structure motion and wind load does not allow for accurate knowledge of the phase of structure motion and wind load at other locations along the building height. Besides, even at the measurement location data acquisition may affect the phase of signals, which means that the Energy Flux Analysis is also sensitive to uncertainties introduced by data acquisition. Sensitivity of the Energy Flux Analysis to the specified structural properties proved to be limited.

The specific investigation into the sensitivity of the Energy Flux Analysis to the four possible sources of uncertainty led to new insights, the formulation of prerequisites of application, and important considerations for future research. Therefore, the findings of all four will now be discussed in slightly more detail.

Structure motion

The sensitivity of the Energy Flux Analysis to limited structure motion measurements was investigated by comparison with a FEM model of the New Orleans tower of which limited information on structural motion was extracted. To find the total or superstructure damping, it is advised to avoid uncertainty in the deformed shape of vibration of the structure by performing multiple acceleration measurements over the structure height. The assumed shape has a significant effect on the Energy Flux Analysis results and it may deviate from the assumed Euler-Bernoulli beam when bending is not dominant or when discontinuities of the building stiffness over the structure height occur.

When a distinction between superstructure and soil-structure interaction has to be made, the energy flux over the boundary is computed by multiplication of the internal forces with the structure motion. This multiplication is highly sensitive to any phase difference present as a result of damping. Highly sensitive means that a phase difference as small as 0.0023 s resulted in an error in the dissipated energy of 70%. In the model used, a phase difference between stress and strain occurred as a result of material damping and local dampers resulted in a delay of the motion close to the damper. This means that measuring at one location along the building height, which is not at the bottom, will not allow for accurate computation of the energy flux at the boundary. The phase effects were a result of modelled damping, and although a brief investigation was done as to whether this may be expected in true structures, this investigation was limited and requires further attention. Besides, in a true structure many damping mechanisms will occur that may show different behaviour in terms of phase. This could, for instance, mean that the influence of material damping may not be as relevant as it was in this model, or that effects as a result of different damping mechanisms should be considered. To limit the uncertainty in the energy flux at the boundary, it is advised to measure all required components at the boundary directly rather than through extrapolation. This is not straightforward, and therefore the recommendations will pay special attention to this.

Wind load and data acquisition

Similar to motion measurements, wind load will also be measured at limited locations along the building height. As a result, it is crucial to model the wind load at other heights, which is not straightforward due to the random nature of wind. The sensitivity to modelled wind load was investigated by comparing the Energy Flux Analysis results of different approaches of modelling the wind load to a reference approach. The mean wind load is not significant, it is the part of the fluctuating wind load at the natural frequency of the building that is most relevant. Sensitivity in the modelled wind load was mostly found in the phase of this fluctuating signal, rather than the magnitude. Based on the coherence, the phase of the fluctuating wind load will vary over the building height, but when measured at one location little is known about the phase at other heights. This results in a very large uncertainty in the applied wind load, to which the Energy Flux Analysis is highly sensitive.

This investigation also showed that the Energy Flux Analysis is not repeatable to signals with the same assumptions under similar wind conditions. The resulting dissipated energy for these signals did not continuously increase in time, it varied from having an increasing, a decreasing, or a constant trend throughout

the measurements. This resulted in nonphysical damping ratios. This dissipated energy is a function of the external introduced by wind, which is found as a multiplication of wind load with structure velocity. The reason for the varying trend of the dissipated energy was found to be the phase difference between the structure velocity and the wind load. This phase difference was also found to vary over the measurement time. Physical causes for this varying phase difference were sought for in terms of signal amplitude and wind direction, but could not be visually detected. Mode coupling was proposed as another cause, together with the wind pressures not being representative for the global wind load. Data processing was ruled out as a cause in this research, although measurement noise is a possibility. Future application should pay special attention to the time synchronisation in data collection and the effect of the tubing system for pressure measurements on the phase of the measured pressure. This latter effect has been considered by TNO through corrections for the tubing system. However, this research proved the sensitivity of the Energy Flux Analysis to extremely small phase differences. The measurement set-up was designed for a different purpose, meaning that the accuracy of corrections and measurements might not be sufficient.

Structural properties
The required structural properties as input for the Energy Flux Analysis are building mass, building stiffness, and foundation stiffness. A range of possible values for each property was formulated, and only those combinations that satisfied the measured natural frequency of the building were allowed. The sensitivity study was performed by computing the Energy Flux Analysis with the same measurement input, but using many different combinations of structural properties. Only the building stiffness was found to affect the results. An error in the building mass of 30% could result in an error in the damping found of 20-45%.

This thesis shed light on the high sensitivity of the Energy Flux Analysis to the phase of the required input signals for structure motion, internal forces and wind load. However, the application of the Energy Flux Analysis can be chosen such that these sensitivities are limited. For instance, computing the soil-structure interaction damping does not require wind load information. The Energy Flux Analysis still knows many advantages as opposed to commonly damping identification techniques, and it is therefore profitable to continue investigation into its application to structures. The next chapter will formulate recommendations on required future research into the Energy Flux Analysis for its application to high-rise structures.

17

Recommendations

The aim of this thesis was to discover the sensitivities of the Energy Flux Analysis when applied to a high-rise building using in situ measurements to find total, superstructure and soil-structure interaction damping. The research shed light on aspects that had not been considered before and aspects that require further attention. These recommendations will first treat the most pressing matters that require attention upon further application of the Energy Flux Analysis to high-rise structures. These are divided in the following sections:

1. Structure motion measurements and damping mechanisms
2. Phase difference structure velocity and wind load
3. Wind load
4. Measurement accuracy

The recommendations in the first point regarding structure motion measurements are relevant when one is interested in finding the superstructure or soil-structure interaction damping separately. The second two points are relevant when computing damping of the superstructure or for the total structure, as this requires including the external energy as a result of wind load. Finally, the latter point is relevant in general, but more specifically when two signals need to be multiplied. This is the case when computing the external energy or the energy flux over the boundary. This chapter will finish with some more generally formulated recommendations that are relevant once sufficient knowledge on the previous points has been obtained.

17.1. Structure motion measurements and damping mechanisms

17.1.1. Structure motion measurements

One major finding of this research is the importance of considering the phase difference occurring between internal forces and structure motion when computing the energy flux at the boundary of the chosen system. In itself it is not surprising that damping affects the signal phase, but its relevance at the system boundary for the Energy Flux Analysis and its dependence on the damping mechanisms occurring is an interesting finding that needs to be considered more thoroughly. In this research, two damping mechanisms were applied to the FEM model; material damping, and local damping through a translation and rotation dashpot. Material damping resulted in a delay between stress and strain, which is the same at any location along the model height. The local dampers were responsible for a delay in the response at foundation level compared to that at a higher location. The phase difference compared to the foundation motion increases with distance from the foundation level.

A brief investigation as to whether this phase difference may be expected in real structures showed that the relation between stress and strain due to material damping is indeed affected for viscoelastic materials. However, this investigation was limited and it is therefore recommended to further examine the behaviour of true materials and structures through experiments. This section will illustrate the first thoughts of the author on how to perform such an experiment. A proposed set-up is visualised in fig. 17.1.

Set-up 1 in fig. 17.1 consists of a cantilever beam with a fixed and a flexible end. For translation of the results to high-rise structures, concrete and steel are most relevant for the beam material. The mass of the

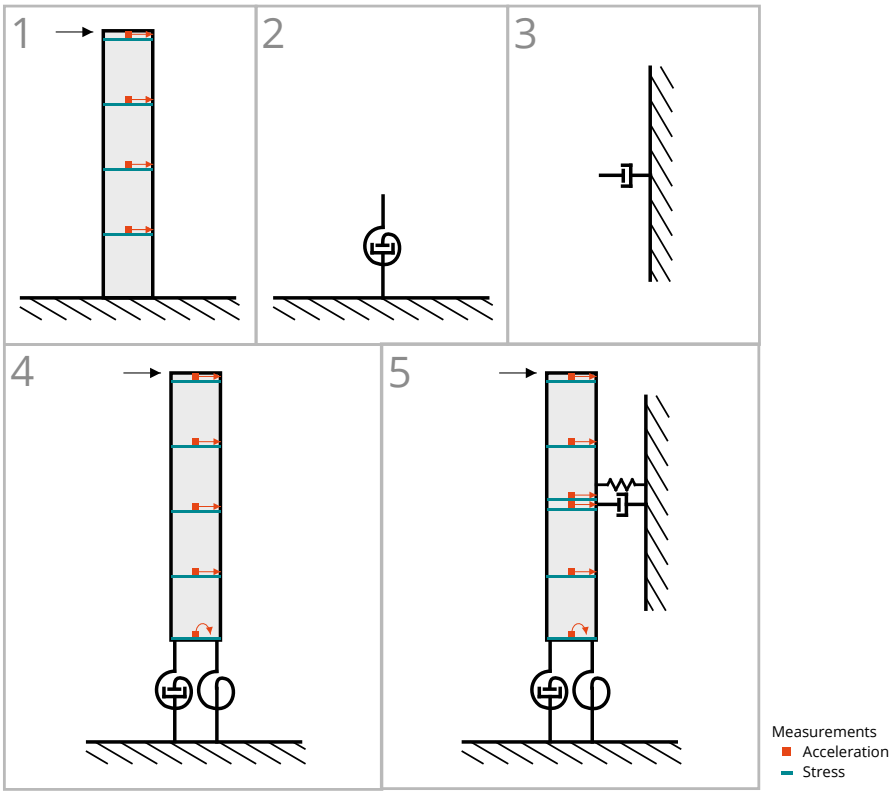

Figure 17.1: Lab experiment structure measurements and combined damping mechanisms

beam can be measured, and the beam stiffness can be identified through an experiment similarly as performed by Gómez (Gómez, 2019). Material damping is the only expected mechanism of damping to occur in this set-up, and the damping can therefore be identified through either a free-decay motion or by applying a known force at different frequencies and amplitudes. Since the beam is fixed at the bottom, no motion will occur, and thus no energy flux to the fixation will occur. The effect of material damping on the relation between stress and strain could be investigated by measuring both on different locations along the specimen. The author is aware that this is not straightforward, as stress is commonly measured using strain gauges. It is therefore recommended to explore measurement campaigns that allow for stress measurements through, for instance, pressure sensors. Once this measurement campaign has been designed, this set-up will contribute to the knowledge on the impact of material damping on constitutive relations. Besides, the measurement campaign designed to account for the effect of material damping in this measurement set-up will also allow for accounting for this effect when designing the measurement campaign for the high-rise structure itself.

To find the phase difference effects as a result of local damping, the fixed support can be replaced with a rotational spring and a rotational damper to allow for rotation and energy dissipation at the bottom of the beam. This is visualised in the fourth set-up in fig. 17.1. Using such a viscous dashpot means that the damping model imposed is a viscous model to represent soil-structure interaction, while in the true structure this may not be the case. Therefore, to better represent the true soil-structure interaction damping, which is a combination of radiation damping and material damping of the soil, a scale model of the foundation including soil may be attached to the bending beam. Using accelerometers over the beam height allows for investigating the delay caused by local damping at the bottom. Alternatively, the motion of the complete beam can be measured using visual devices such as a digital camera.

So far, the experiment has provided knowledge on the impact of material damping and localised damping representing damping due to soil-structure interaction. However, previous studies have found a significant contribution to the total damping by damping mechanisms that have not yet been considered in this experiment such as friction damping in joints of structural elements or friction with non-structural elements. The fifth set-up presented in fig. 17.1 aims at including this additional damping mechanisms through viscous dampers. These were chosen as they will aid in the experiment described in the next section, but it is to be considered if the viscous dampers are in any way representative of friction damping. Alternatively, friction

damping can be applied by placing the bending beam between two surfaces, which will introduce friction. The differences observed in the measurements compared to the fourth set-up may then be owed to friction damping. Considering additional damping mechanisms is important, as the damping in a high-rise structure is expected to be a combination of many different damping mechanisms. The influence of phase difference as a result of material damping is now considered important, but if damping in high-rise structures is mainly owed to friction damping, the effect due to friction damping will be more relevant.

17.1.2. Combined damping mechanisms

The set-up presented in fig. 17.1 has another purpose. First, the separate damping characteristics of the damping devices in set-up 1, 2, and 3 can be considered for forces of varying amplitude and frequency. Adding the rotational damper in the fourth set-up, measuring the response for varying force amplitude and frequency, and application of the Energy Flux Analysis for these different forces will provide knowledge about the combined effect of different damping mechanisms. While currently the combined effect is considered as a summation in the codes, there is little insight into this combined behaviour. This can be repeated by adding more damping devices and performing response measurements at the border of different damping mechanisms.

17.1.3. Measurement to internal forces

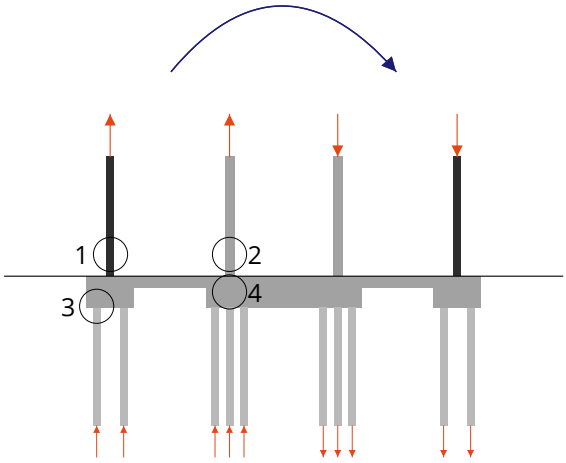

Figure 17.2: Measuring internal forces at foundation level; 1 = Column, 2 = Core wall, 3 = Foundation pile, 4 = Pile cap

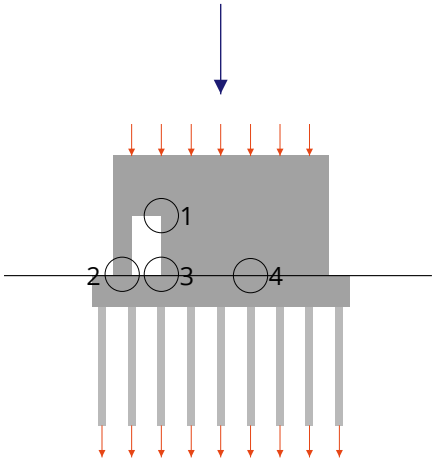

Figure 17.3: Measuring internal forces in a stability core wall; 1 = Above opening, 2,3 = Next to opening, 4 = In continuous section

For computation of the internal forces, § 17.1.1 discusses the use of, for instance, strain gauges or pressure sensors. In a solid bending beam, local measurements may not be globally representative due to material heterogeneity but at least the geometry will allow for translation of locally identified internal forces to global internal forces. However, translation of the measurements at the foundation of a high-rise structure to global internal moments is not as straightforward. This should be considered upon performing these measurements for the purpose of avoiding the use of non-representative measurements due to material heterogeneity and local effects. Therefore, it is advised to perform multiple measurements at different locations. Figure 17.2 presents some possible measurement locations, which naturally lead to different stress levels. Based on hand calculations, or an extensive FEM model, these measurements may be translated to a global force. Local effects such as the influence of the presence of an opening as presented in fig. 17.3 should be considered. Besides, when measuring stress, t is important to realise that static stress may also be measured. It is of interest to investigate which measurement location is least prone to local effects or of which it is straightforward to cope with these effects, while the measurement location is also practically and economically feasible.

17.2. Phase difference wind load and building motion

When applying the Energy Flux Analysis to a high-rise building, this work encountered difficulties in providing repeatable results due to the importance of the phase difference between structure velocity and wind force. This thesis mainly put effort in finding possible solutions, but did not manage isolate the source or to provide a solution. Further investigation is required to find the source and an experiment is proposed in

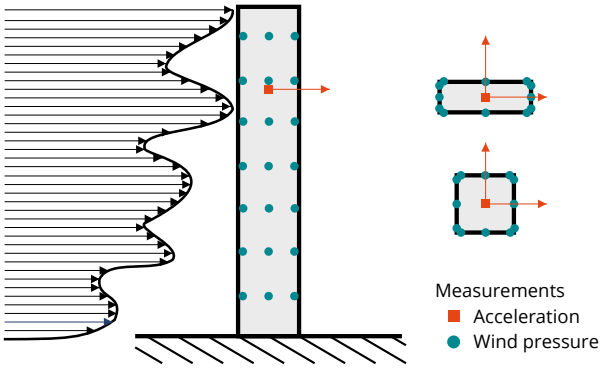

Figure 17.4: Experiment to find source of phase difference

this section. The experiment is designed such that it can rule out and ideally point at the explanation(s). The explanations formulated in this thesis are roughly the following:

1. Data processing
2. Data collection
3. Measurement noise
4. Tube length effect in pressure measurements
5. Local effects pressure measurements
6. Changing wind conditions
7. Structural coupling

The first point was ruled out as a cause in this thesis, and data processing in the experiment such also be performed such that it has no effect on the signal phase or it should correct for this phase difference. Additionally, it is important te be aware of the effects of data collection upon performing the experiments. By performing a lab experiment in a wind tunnel using a cross section with largely varying natural frequencies in two orthogonal directions, as is the case for the top cross section in fig. 17.4, the last three points are be ruled out. This means that if a varying phase difference between structure velocity and wind load resulting in non-repeatable results is found, the cause can be sought for in points three and four. Changing the wind conditions in the experiment allows for identifying its consequences. And finally, designing the cross section such that the bending beam experiences structural coupling, can investigate the influence of structural coupling.

The occurrence of such phase difference can also be investigated by going through databases of experiments that performed both wind force and structural response measurements. To the author's best knowledge, the effect has not been considered in literature yet.

17.3. Modelling wind load

17.3.1. Wind sensitivity

This thesis has shown that the Energy Flux Analysis is sensitive to the fluctuating wind load, mainly in terms of its phase. While measurement of the fluctuating wind load at one location may contain its own uncertainties in terms of measurement accuracy and uncertainty, further uncertainty is introduced by translating this measured wind load to a wind load over the complete structure height. This section will discuss some thoughts on obtaining further understanding of the sensitivity of the Energy Flux Analysis to the chosen wind load modelling, and it will discuss a possible further investigation on how to cope with this. It should be noted that this wind load input is not relevant when one is interested in damping from soil-structure interaction only.

First of all, a further investigation of the sensitivity of the Energy Flux Analysis may be done by continuing with the work done by Talib (Talib, 2019). This means that a numerical model of the structure is used, and a wind load based on wind tunnel measurements is applied to the model. The Energy Flux Analysis can be performed using all required information from the numerical model, and then repeated assuming one or several measurement locations for the wind load only and extrapolating measured wind as was done in this thesis. The benefit of using a numerical model is the fact that the true wind load is known, as this is prescribed

to the numerical model. However, this sensitivity study may also be performed through a lab experiment using pressure sensors distributed over the test specimen as is commonly done in wind tunnel tests.

It would be interesting to investigate the sensitivity of the structure response to the specifics of the wind load applied. One way of doing this would be by using a numerical model of the high-rise structure. A wind load based on the measured wind pressures would then be applied to this numerical model and the response of the model could be compared to the measured response of the true high-rise structure. The issue with this approach is the fact that the response of the numerical model also depends on the structural properties assigned to it, such as stiffness, mass and damping. Therefore, a deviation in the response cannot directly be assigned to the wind load. To overcome this, this approach can be applied to the same cantilever beam as used in the previous sections, or to a scale model of a high-rise structure, of which these properties can be experimentally identified.

17.3.2. Measurement campaign based on coherence

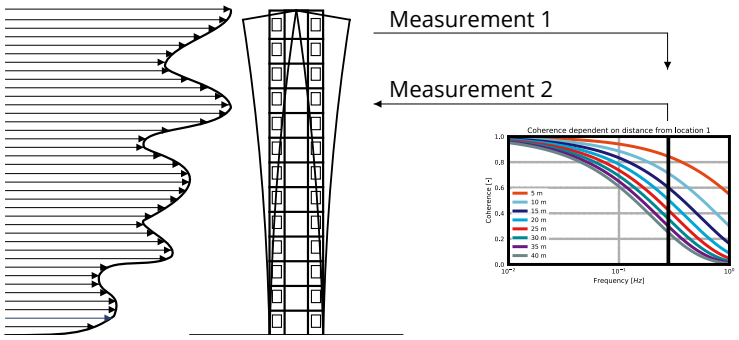

Figure 17.5: Designing measurement campaign based on coherence locations

The fact that there is theory available on coherence of wind velocity at different locations might provide a solution. Based on the coherence between different points, research could focus on designing a measurement campaign such that the uncertainty in terms of phase of the fluctuating wind load is limited to an acceptable level. The economical feasibility of this measurement campaign should be considered as well, as this would result in performing wind pressure measurements at multiple locations along the building height. The fact that the wind load at higher locations contributes more to the external energy flux due to an increased structure velocity should be used in the design of this measurement campaign.

17.4. Measurement accuracy

Measurement accuracy and measurement uncertainty have been discussed previously. While measurement accuracy is most likely not the cause for the largely varying phase difference between structure velocity and wind force, it is certainly relevant due to the extreme sensitivity of the Energy Flux Analysis to deviations in the phase. Allowable phase deviations should be formulated, and based on this a certain measurement accuracy should be guaranteed by the measurement device and the chosen sampling frequency. It should be noted that reducing the measurement accuracy to limits well below a possible measurement uncertainty is fruitless.

17.5. Further recommendations

This section provides some further recommendations to be considered for future research.

- Torsion has not been considered in this thesis, as it was not relevant for the New Orleans tower. Including torsion may introduce new considerations that could not have been foreseen in this study.
- The result of the Energy Flux Analysis is the dissipated energy of the system, rather than a damping ratio. The translation from dissipated energy to damping ratio requires further attention, as this translation forces the user to assume a certain damping model. Based on the model used, information might be lost. An alternative method for comparing dissipated energy in different buildings could be developed.
- Further recommendations in terms of structural properties are the following:

  - The sensitivity study has been performed for finding the total damping in the structure, as no measurements were available to distinguish between superstructure and soil-structure interaction damping for the case study used. The sensitivity to the structural properties is expected to differ when considering soil-structure interaction damping only. In this case, the results depend on the building stiffness, as this is used to compute the internal forces at foundation level, and the soil stiffness. The building mass is not directly involved. However, it is still advised to match natural frequency as a result of the chosen properties with the measured natural frequency. This is where the building mass becomes relevant again.
  - The structural properties building mass and stiffness have been assumed continuous over the structure height. For the specific application to the New Orleans tower this is justifiable. When the Energy Flux Analysis is applied to a structure with a substantially varying geometry, this should be considered in the description of the mode shape and natural frequency, and when computing the energies.
  - The sensitivity of the Energy Flux Analysis to structural properties presented here might change when the structural properties have significantly different magnitudes or ratios. This could be the case for buildings with very different natural frequencies or, for instance, much taller buildings.
  - The sensitivity study has been performed considering the response in along wind direction only. The sensitivity of the Energy Flux Analysis to the structural properties when considering both lateral directions with different properties for the building and the soil is yet to be investigated. For some buildings it is also of interest to consider torsional motion and properties.
  - In this thesis the cross term EI_{yz} responsible for coupling the two directions did not affect the results. However, for buildings with a different geometry and a more substantial coupling term, the sensitivity study might be affected.

- This thesis provided a comparison between the Energy Flux Analysis and the commonly used Half-power Bandwidth method and Random Decrement technique. Although all techniques were applied to the New Orleans tower, it was not possible to make a quantitative comparison of the results and their scatter due to uncertainty. This can only be done when the Energy Flux Analysis produces repeatable results. Once this has been achieved, it is interesting to make the comparison.

VI

APPENDICES

A

Basic dynamics

This appendix explains the basic general structural dynamic principles which will be used as a starting point of this thesis and which will be referred to quite frequently. More specific application of these principles to high-rise buildings under wind-induced dynamic loading is discussed in the main report in chapter 3.

A.1. Single degree-of-freedom systems

A single degree of freedom (SDOF) system has one degree of freedom and can be described by a single mass, stiffness and damping constant only. The system can be subdivided into an undamped system in which no damping is present, and a damped system. Both will be discussed.

A.1.1. Undamped systems

An undamped single degree of freedom system is described by its mass m and an ideal massless stiffness k, and the single degree of freedom $x(t)$ its representation is shown in fig. A.1. Newton's second law is used to formulate the equation of motion:

$$m\ddot{x}(t) + kx(t) = f(t) \tag{A.1}$$

The response of the system to the force $f(t)$ applied to the system can be subdivided in a homogeneous and a particular solution. The particular solution is the response due to the applied force, the homogeneous solution is the response of the system in case of free vibration when no force is applied:

$$m\ddot{x}(t) + kx(t) = 0 \tag{A.2}$$

The trivial solution to this differential equation is $x(t) = 0$. However, this is not the solution of interest since this represent a static state when displacements take place, The general form of the non-trivial solution to the differential equation in eq. (A.2) has the following form:

$$x(t) = \hat{x}e^{i\omega t} \tag{A.3}$$

In this equation. $\hat{x}$ is the amplitude of the displacement and ω is the frequency of vibration. Through substitution in eq. (A.2), an expression for the natural frequency ω_n is found:

$$\omega_n = \sqrt{\frac{k}{m}} \tag{A.4}$$

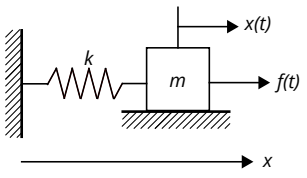

Figure A.1: Undamped single degree of freedom system

This frequency in radians is related to the commonly used frequency in Hz through:

$$\omega_n = 2\pi f_n \tag{A.5}$$

The system will vibrate in this frequency once it has been set into motion. However, usually in dynamic systems, the system is excited by an external force. This external force can have different characteristics, but in case of an harmonic force it can be described using:

$$f(t) = \hat{f} e^{i\omega t} \tag{A.6}$$

The amplitude of the force is given by $\hat{f}$. Often, the behaviour of a dynamic system is studied through the Frequency Response Function (FRF). This function relates the output of the system, for instance the acceleration, to the input of the system which is the excitation force. The relation is described in the frequency domain. For an undamped system excited by a harmonic force as described here, it may be found through the ratio of the amplitude of the force and the response in the frequency domain:

$$-m\hat{x}\omega^2 e^{i\omega t} + k\hat{x}e^{i\omega t} = \hat{f}e^{i\omega t} \tag{A.7}$$

$$h(\omega) = \frac{\hat{x}}{\hat{f}} = \frac{1}{k - \omega^2 m} \tag{A.8}$$

A.1.2. Viscously damped systems

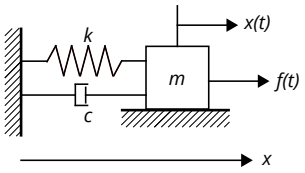

Damped single degree of freedom system

Almost any real system contains some form of damping. Many damping mechanisms exists, as was discussed in chapter 4, but for structures damping is often well described through viscous damping. In viscous damping, damping is related to the velocity and modelled using an ideal massless dashpot with a constant damping coefficient c as is shown in appendix A.1.2. The equation of motion for a viscously damped system is similar to the equation of motion of the undamped system, but in this case the damping force term is added:

$$m\ddot{x}(t) + c\dot{x}(t) + kx(t) = f(t) \tag{A.9}$$

Also for the damped case, the solution is subdivided in a particular solution and a solution for the free vibration system. The solution to the free vibration problem has the following shape:

$$x(t) = \hat{x}e^{st} \tag{A.10}$$

In this solution, the factor s is yet to be determined. Substitution of eq. (A.10) into the equation of motion of free vibration yields:

$$ms^2 + cs + k = 0 \tag{A.11}$$

The roots of this equation give the values of s for the solution:

$$s_{1,2} = -\frac{c}{2m} \pm \sqrt{\left(\frac{c}{2m}\right)^2 - \frac{k}{m}} \tag{A.12}$$

When the term inside the square root is zero the system is critically damped, which means that it will just return to its equilibrium position without vibrating even once. The damping coefficient that satisfies this requirement is called the critical damping coefficient c_{cr} and is defined as:

$$c_{cr} = 2\sqrt{km} = 2\omega_n m \tag{A.13}$$

Often, damping is expressed as a damping ratio. This ratio is defined as the ratio of the damping present in the system over the critical damping ratio of the system. A damping ratio of 1 indicates that the system is critically damped, a damping ratio larger than 1 indicates an over-damped system and a system with a damping ratio smaller than 1 is an under-damped system. It is also common to express the damping ratio in terms of percentages.

The roots s can also be expressed using the damping ratio and natural frequency rather than the damping coefficient, mass and stiffness by substituting the expression for the natural frequency and damping ratio into the equation of motion:

$$\ddot{x}(t) + 2\zeta\omega_n\dot{x}(t) + \omega_n^2 x(t) = 0 \tag{A.14}$$

In this case the roots for the general solution are given by:

$$s_{1,2} = -\omega_n\zeta \pm i\omega_n\sqrt{\zeta^2 - 1} \tag{A.15}$$

An overdamped system does not vibrate whatsoever, but an underdamped system will vibrate at a frequency which is lower than the natural frequency called the damped natural frequency ω_d.

$$\omega_d = \omega_n\sqrt{1-\zeta^2} \tag{A.16}$$

For systems with a very low damping ratio, this damped natural frequency will approximate the undamped natural frequency.

Similarly to the undamped system, the FRF for a damped system undergoing an excitation force $f(t)$ can be defined when the response is expected to have the same shape as the excitation force:

$$\hat{x}(k + i\omega c - m\omega^2) = \hat{f} \tag{A.17}$$

$$h(\omega) = \frac{1}{k + i\omega c - m\omega^2} \tag{A.18}$$

As opposed to an undamped system, for a damped system this is a complex quantity. It is usually presented using two figures of which one represents the magnitude and the other represents the phase angle of $h(\omega)$ over the frequency This phase angle is defined as: magnitude

$$\phi = \tan^{-1}\left(\frac{\Im(h(\omega))}{\Re(h(\omega)}\right) \tag{A.19}$$

In this the imaginary part of the Frequency Response function is given by $\Im$ and the real part is given by $\Re$. Both the magnitude as well as the phase angle depend on the amount of damping. Figure A.2 shows both for an undamped case and for increasing damping. In case of an increasingly damped system, the peak in the magnitude of the FRF decreases. In case of no damping and an excitation force which the same frequency as the natural frequency, resonance will occur: the magnitude at the natural frequency becomes infinite. Fortunately, in real structures some damping is always present and the response will not go to infinity. However, resonance should always be avoided. For the theoretical undamped case the phase shift of the response occurs instantaneously at the natural frequency from $0°$ to $-180°$, but this shift becomes gradual when damping is present and a value for the phase at the natural frequency of $-90°$ is found.

A.2. Multi degree-of-freedom systems

Usually, representing a structure using a SDOF system is too simplistic. More commonly, a real structure with infinitely many degrees of freedom is modelled using a finite number of elements, each which their own degree(s) of freedom. Such a system would be called a multi degree-of-freedom system (MDOF). It represented by multiple masses that are connected through springs and dampers as is shown in fig. A.3 for the undamped case.

A.2.1. Undamped systems

A simple example of undamped multi degree of freedom system is a system of three masses, each with one degree of freedom indicated by x_1, x_2 and x_3 shown in fig. A.3. The three degrees of freedom result in three coupled equations of motion:

$$\begin{aligned} m_1\ddot{x}_1(t) + (k_1 + k_2)x_1(t) - k_2x_2(t) &= 0 \\ m_2\ddot{x}(t) - k_2x_1(t) + (k_2 + k_3)x_2(t) - k_3x_3(t) &= 0 \\ m_3\ddot{x}_3(t) - k_3x_2(t) + k_3x_3(t) &= f(t) \end{aligned} \tag{A.20}$$

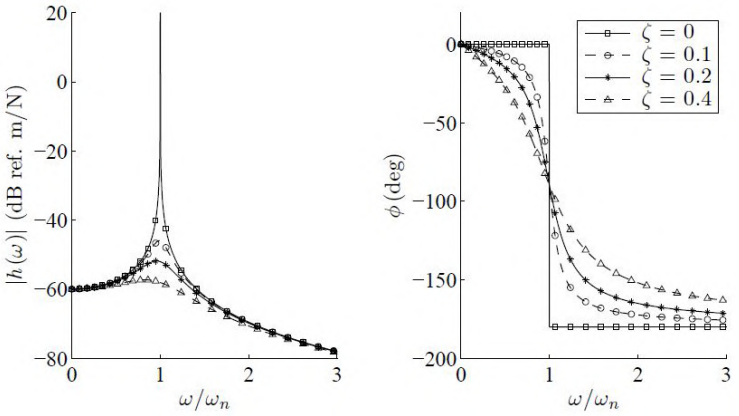

Figure A.2: Example of a magnitude and phase angle plot of the FRF (Prandina, 2010)

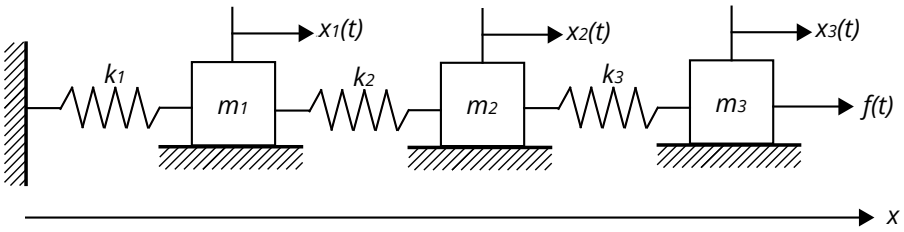

Figure A.3: Undamped multi degree of freedom system

This system of coupled equations can be written in matrix form:

$$\mathbf{M}\underline{\ddot{x}}(t) + \mathbf{K}\underline{x}(t) = \underline{f}(t) \tag{A.21}$$

The mass matrix **M** and stiffness matrix **K** are symmetric and positive definite. The free vibration solution to this system of equations is the same as the one presented for the SDOF system. Filling in the solution into the matrix representation of the equations of motion, the following expression is obtained:

$$(\mathbf{K} - \omega^2\mathbf{M})\underline{\hat{x}} = \underline{0} \tag{A.22}$$

This is a homogeneous set of n algebraic equations and is called the "generalised eigenvalue problem". The number of equations n is the same as the amount of degrees of freedom of the system. In the equation ω^2 is the eigenvalue and the square root of this gives the natural frequency. The eigenvector is given by $\underline{\hat{x}}$. In this case, the non-trivial solution for the eigenvalues and eigenvectors that satisfies all equations can be found using:

$$\det\left(\mathbf{K} - \omega^2\mathbf{M}\right) = 0 \tag{A.23}$$

From this equation the characteristic equation can be obtained, and using this equation the roots, or natural frequencies, can be found. For systems of over 2 degrees of freedom this is not possible without numerical methods. The solutions to the characteristic equation gives the same amount of solutions as the number of degrees of freedom n in the system. Using each natural frequency that was found, an eigenvector can be obtained. These eigenvectors represent the mode shapes of the dynamic vibrating system, it describes how the structure vibrates for each natural frequency. The magnitude of these eigenvectors should not be used, since it describes the shape of the mode shape and the relation between different degrees of freedom, not the physical magnitude of the response. The summation of all n solutions naturally also satisfies the homogeneous set of linear differential equations. Thus, the free vibration is the sum of all possible modes and this solution to the homogeneous problem is written as follows:

$$\underline{x}(t) = \sum_{i=1}^{n} \underline{\hat{x}_i} u_i(t) \tag{A.24}$$

The time functions $u_i(t)$ are derived from a set of uncoupled homogeneous differential equations similar to the SDOF problem:

$$\ddot{u}_i(t) + \omega_i^2 u_i(t) = 0 \tag{A.25}$$

Equation (A.24) is often written in the following representation:

$$\underline{x}(t) = \mathbf{E}\underline{u}(t) \tag{A.26}$$

In this equation the nxn matrix $\mathbf{E}$ is called the eigenmatrix containing the eigenvectors as columns. This matrix is also important when solving the inhomogeneous problem of the forced vibration problem of a multi degree of freedom system. Orthogonality conditions will be used in order to decouple the set of equations, to ultimately find the solution to the coupled problem.

Orthogonality The orthogonality conditions will be explained and applied in order to obtain the modal mass and modal stiffness matrices which yield a decoupled set of equations. Consider two different solutions $(\omega_r^2, \underline{\hat{x}}_r)$ and $(\omega_s^2, \underline{\hat{x}}_s)$ of the eigenvalue problem in eq. (A.22):

$$\begin{aligned} \omega_r^2 \mathbf{M}\underline{\hat{x}}_r &= \mathbf{K}\underline{\hat{x}}_r \\ \omega_s^2 \mathbf{M}\underline{\hat{x}}_s &= \mathbf{K}\underline{\hat{x}}_s \end{aligned} \tag{A.27}$$

The top expression is pre-multiplied with the vector $\underline{\hat{x}}_s^T$ and the bottom expression is pre-multiplied with $\underline{\hat{x}}_r^T$:

$$\begin{aligned} \omega_r^2 \underline{\hat{x}}_s^T \mathbf{M}\underline{\hat{x}}_r &= \underline{\hat{x}}_s^T \mathbf{K}\underline{\hat{x}}_r \\ \omega_s^2 \underline{\hat{x}}_r^T \mathbf{M}\underline{\hat{x}}_s &= \underline{\hat{x}}_r^T \mathbf{K}\underline{\hat{x}}_s \end{aligned} \tag{A.28}$$

Since the mass matrix and the stiffness matrix are both symmetrical, it is allowed to interchange pre- and post-multiplication. When this is done for the bottom equation only, it yields:

$$\begin{aligned} \omega_r^2 \underline{\hat{x}}_s^T \mathbf{M}\underline{\hat{x}}_r &= \underline{\hat{x}}_s^T \mathbf{K}\underline{\hat{x}}_r \\ \omega_s^2 \underline{\hat{x}}_s^T \mathbf{M}\underline{\hat{x}}_r &= \underline{\hat{x}}_s^T \mathbf{K}\underline{\hat{x}}_r \end{aligned} \tag{A.29}$$

Now both expressions have the same right-hand-side and can be subtracted from one another:

$$(\omega_r^2 - \omega_s^2)\underline{\hat{x}}_s^T \mathbf{M}\underline{\hat{x}}_r = 0 \tag{A.30}$$

Under the condition that the natural frequencies are not equal, the following condition can be stated, which is the orthogonality condition with respect to the mass matrix:

$$\underline{\hat{x}}_s^T \mathbf{M}\underline{\hat{x}}_r = 0 \tag{A.31}$$

Substitution of this equation into the previous equations shows that also an orthogonality condition applies with respect to the stiffness matrix:

$$\underline{\hat{x}}_s^T \mathbf{K}\underline{\hat{x}}_r = 0 \tag{A.32}$$

As mentioned before, but stressed again here, the condition only holds for two different eigenvectors: $\underline{\hat{x}}_s \neq \underline{\hat{x}}_r$. This means that if the vector is multiplied with the same eigenvectors, the result is non-zero. Using this condition, the mass matrix and stiffness matrix can be made diagonal using the eigenvectors:

$$\begin{aligned} \mathbf{M}^* &= \mathbf{E}^T \mathbf{M}\mathbf{E} \\ \mathbf{K}^* &= \mathbf{E}^T \mathbf{K}\mathbf{E} \end{aligned} \tag{A.33}$$

These matrices are called the modal mass matrix and the modal stiffness matrix. By filling in these matrices in the eq. (A.22) it turns out these matrices hold the following condition:

$$\Omega^2 \mathbf{M}^* = \mathbf{K}^* \tag{A.34}$$

The matrix Ω^2 is a diagonal matrix with the eigenvalues ω_i^2 as diagonal elements. This condition and the orthogonality condition are used to solve the undamped forced vibration system. The aim is to obtain uncoupled equations for each mode of which a simple solution can be found. The total solution is the sum of

these modal solutions as was shown in eq. (A.24) or eq. (A.26). This approach is often referred to as "Modal Analysis". Substitution into the inhomogeneous set of differential equations gives:

$$\mathbf{ME}\underline{\ddot{u}}(t) + \mathbf{KE}\underline{u}(t) = \underline{f}(t) \tag{A.35}$$

Similar to what was previously done, pre-multiplication is applied:

$$\mathbf{E}^T\mathbf{ME}\underline{\ddot{u}}(t) + \mathbf{E}^T\mathbf{KE}\underline{u}(t) = \mathbf{E}^T\underline{f}(t) \tag{A.36}$$

Considering eq. (A.33) and eq. (A.34) this expression can be written into:

$$\mathbf{M}^*\underline{\ddot{u}}(t) + \mathbf{M}^*\Omega^2\underline{u}(t) = \mathbf{E}^T\underline{f}(t) \tag{A.37}$$

Since the matrices $\mathbf{M}^*$ and Ω^* are both diagonal, this expression leads to a set of decoupled differential equations for the variable $\underline{u}(t)$. For every mode, the uncoupled expressions are:

$$m^*_{ii}\ddot{u}_i + m^*_{ii}\omega_i^2 u_i = \underline{\hat{x}}_i^T\underline{f}(t) \tag{A.38}$$

$$\ddot{u}_i + \omega_i^2 u_i = \frac{\underline{\hat{x}}_i^T\underline{f}(t)}{m^*_{ii}} \tag{A.39}$$

The solution of these decoupled differential equations is the same as the solution to the differential equation of the single degree-of-freedom system. Using the modal degrees of freedom $u_i(t)$ and the eigenvector, the solution is found through eq. (A.26). Depending on the force applied, the total solution can be found as a summation of the homogeneous and particular solutions. Parameters of the homogeneous solution depend on the initial conditions and the particular solution depends on the force applied. The undamped response to a harmonic load will be analysed. The load is described by:

$$\underline{f}(t) = \underline{\hat{f}}\sin(\omega t) \tag{A.40}$$

The particular solution assumed will have the same shape as this harmonic load, but the amplitude is not yet known:

$$u_i(t) = \hat{u}_i\sin(\omega t) \tag{A.41}$$

This amplitude can be found by substituting this relation into eq. (A.39), which yields:

$$\hat{u}_i = \frac{1}{\omega_i^2 - \omega^2}\frac{\underline{\hat{x}}_i^T\underline{\hat{f}}(t)}{\underline{\hat{x}}_i^T m_{ii}\underline{\hat{x}}_i} \tag{A.42}$$

In case there is only one harmonic load active, the expression changes to:

$$\hat{u}_i = \frac{1}{1-\left(\frac{\omega}{\omega_i}\right)^2}\frac{1}{\omega_i^2}\frac{\hat{x}_{pi}\hat{f}_p}{\underline{\hat{x}}_i^T\mathbf{M}\underline{\hat{x}}_i} \tag{A.43}$$

Again, the Frequency Response Function can be found by dividing the amplitude of the response by the amplitude of the force:

$$H_{u_i f_p}(\omega) = \frac{\hat{u}_i}{\hat{f}_p} = \frac{1}{1-\left(\frac{\omega}{\omega_i}\right)^2}\frac{1}{\omega_i^2}\frac{\hat{x}_{pi}}{\underline{\hat{x}}_i^T\mathbf{M}\underline{\hat{x}}_i} \tag{A.44}$$

The values of both i and p can range from 1 to n, so nxn different FRF's are defined, which are collected in a non-symmetrical Frequency Response Matrix. This method was now shown in case there was only one load active, but can also be used when a synchronous load is applied, meaning that all loads vary according to the same harmonic function. Also then, the response will follow this harmonic motion of the force.

$$u_i(t) = \hat{u}_i\sin(\omega t) = H_{u_i f_p}(\omega)\hat{f}_p\sin(\omega t) \tag{A.45}$$

And for the response formulated in the physical degrees of freedom:

$$\begin{aligned}\underline{x}(t) &= \sum_{i=1}^{n}\underline{\hat{x}}_i H_{u_i f_p}(\omega)\hat{f}_p\sin(\omega t)\\ &= \sum_{i=1}^{n}\underline{\hat{x}}_i\frac{1}{1-\left(\frac{\omega}{\omega_i}\right)^2}\frac{1}{\omega_i^2}\frac{\hat{x}_{pi}\hat{f}_p}{\underline{\hat{x}}_i^T\mathbf{M}\underline{\hat{x}}_i}\sin(\omega t)\end{aligned} \tag{A.46}$$

This concerns the steady-state response when the transient motion has died out and it describes the harmonic motion of the whole structure, of all the degrees of freedom. The response of a specific degree of freedom can also be found using this expression. Now, the Frequency Response of a physical degree of freedom x_q is written as follows:

$$H_{x_q f_p}(\omega) = \frac{\hat{x}_q}{\hat{f}_p} = \sum_{i=1}^{n} \frac{1}{1-\left(\frac{\omega}{\omega_i}\right)^2} \frac{1}{\omega_i^2} \frac{\hat{x}_{qi}\hat{x}_{pi}}{\underline{\hat{x}}_i^T \mathbf{M} \underline{\hat{x}}_i} \tag{A.47}$$

This FRF has vertical asymptotes at the postitions of the natural frequencies. Following Maxwell's reciprocal theorem, the following holds:

$$H_{x_q f_p}(\omega) = H_{x_p f_q}(\omega) \tag{A.48}$$

In the case of synchronous harmonic load, the response can be written as:

$$\underline{x}(t) = \mathbf{EH}_{u_i F_p}(\omega) \underline{f}(t) \tag{A.49}$$

A.2.2. Viscously damped systems

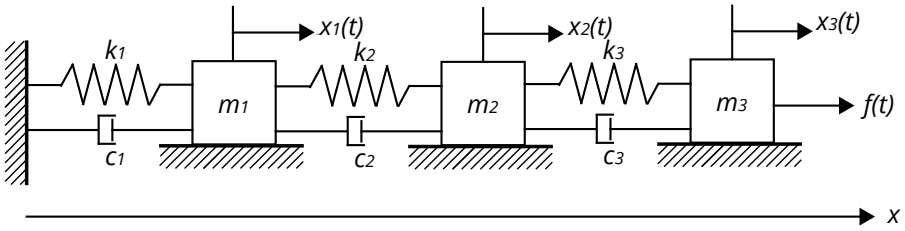

Figure A.4: Damped multi degree of freedom system

A similar system to previous system is considered, but this time there are viscous dampers present between the masses and the boundary as is shown in fig. A.4. Therefore, the system of equations of motion becomes:

$$\begin{aligned} m_1\ddot{x}_1 + (k_1+k_2)x_1 + (c_1+c_2)\dot{x}_1 - k_2x_2 - c_2\dot{x}_2 &= 0 \\ m_2\ddot{x}_2 - k_2x_1 - c_2\dot{x}_1 + (k_2+k_3)x_2 + (c_2+c_3)\dot{x}_2 - k_3x_3 - c_3\dot{x}_3 &= 0 \\ m_3\ddot{x}_3 - k_3x_2 - c_3\dot{x}_2 + k_3x_3 + c_3\dot{x}_3 &= f \end{aligned} \tag{A.50}$$

Which is written in the matrix form as

$$\mathbf{M}\ddot{\underline{x}}(t) + \mathbf{C}\dot{\underline{x}}(t) + \mathbf{K}\underline{x}(t) = \underline{f}(t) \tag{A.51}$$

This is a coupled inhomogeneous system of equations with an nxn damping matrix $\mathbf{C}$, this matrix multiplied with the velocity vector $\dot{\underline{x}}(t)$ represents the viscous damping forces. Also in this case the Modal Analysis can be adapted to obtain:

$$\mathbf{M}^*\ddot{\underline{u}}(t) + \mathbf{C}^*\dot{\underline{u}}(t) + \mathbf{K}^*\underline{u} = \mathbf{E}^T\underline{f}(t) \tag{A.52}$$

In this equation, matrix $\mathbf{C}^*$ is the so called modal damping matrix given by:

$$\mathbf{C}^* = \mathbf{E}^T\mathbf{CE} \tag{A.53}$$

Unfortunately, generally the eigenvectors are not orthogonal to the damping matrix $\mathbf{C}$ and therefore the modal damping matrix is not a diagonal matrix. Therefore, through this modal damping matrix damping coupling is present and the system cannot be uncoupled. The result is that the relatively simple solution method presented before cannot be applied for damped systems. However, methods exist that assume a non-synchronous motion rather than synchronous motion which results in a description using complex numbers. This approach is therefore known as "Complex Modal Analysis". For special cases it is also possible to force the modal damping matrix to be diagonal. Using the expression $\mathbf{K}^* = \mathbf{M}^*\Omega^2$ and pre-multiplying each term with $\mathbf{M}^{*-1}$, eq. (A.52) is written as:

$$\mathbf{I}\ddot{\underline{u}}(t) + \mathbf{M}^{*-1}\mathbf{C}^*\dot{\underline{u}}(t) + \Omega^2\underline{u}(t) = \mathbf{M}^{*-1}\mathbf{E}^T\underline{f}(t) \tag{A.54}$$

The decoupled system gets the following form:

$$\ddot{u}_i(t) + 2\zeta_i\omega_i\dot{u}_i + \omega_i^2 u_i = \frac{\hat{x}_i^T \underline{F}(t)}{\underline{\hat{x}_i^T \mathbf{M} \hat{x}_i^T}} \tag{A.55}$$

This equation is written using the modal damping ratio using the following expression:

$$2\zeta_i\omega_i = \frac{\underline{\hat{x}}_i^T \underline{f}(t)}{\underline{\hat{x}}_i^T \mathbf{M} \underline{\hat{x}}_i} \tag{A.56}$$

In practice the damping matrix cannot be quantified because of a lack of fundamental models (Spijkers et al., 2005). The modal damping ratio is therefore estimated based on insight and experience using damping ratios:

$$\begin{aligned} \mathbf{C}^* &= \mathbf{M}^* [2\zeta_i\omega_i] \\ \mathbf{E}^T\mathbf{C}\mathbf{E} &= \mathbf{E}^T\mathbf{M}\mathbf{E} [2\zeta_i\omega_i] \\ \mathbf{C}\mathbf{E} &= \mathbf{M}\mathbf{E} [2\zeta_i\omega_i] \\ \mathbf{C} &= \mathbf{M}\mathbf{E} [2\zeta_i\omega_i] \mathbf{E}^{-1} \end{aligned} \tag{A.57}$$

It is inconvenient that to compute the damping matrix the inverse matrix $\mathbf{E}^{-1}$ is required. A way was found to avoid this expression:

$$\begin{aligned} \mathbf{I} &= \mathbf{M}^{*-1}\mathbf{M}^* = \mathbf{M}^{*-1}\mathbf{E}^T\mathbf{M}\mathbf{E} \\ \mathbf{E}^{-1} &= \mathbf{M}^{*-1}\mathbf{E}^T\mathbf{M} \end{aligned} \tag{A.58}$$

This results in the following expression for the damping matrix, based on estimated damping ratios:

$$\mathbf{C} = \mathbf{M}\mathbf{E} [2\zeta_i\omega_i] \mathbf{M}^{*-1}\mathbf{E}^T\mathbf{M} \tag{A.59}$$

After numerical evaluation it will become clear whether the terms of this damping matrix are still realistic or if the damping decoupling has been too big of an assumption. It turns out that for structures where the damping is reasonably uniformly distributed in the whole structure and where the damping is not too large, damping uncoupling will deliver reasonably accurate results (Spijkers et al., 2005).

Rayleigh Damping Another way to define a diagonal damping matrix is to express the damping matrix proportionally to the (modal) mass and stiffness matrices. This is therefore often called proportional damping or Rayleigh damping. The matrix is defined as follows:

$$\mathbf{C}^* = \alpha\mathbf{M}^* + \beta\mathbf{K}^* \tag{A.60}$$

The coefficients α and β can be found using the following expression:

$$\zeta_i = \frac{\alpha}{2\omega_i} + \frac{\beta}{2}\omega_i \tag{A.61}$$

To find the coefficients, the modal damping ratio ζ_i of two modes should be known:

$$\begin{aligned} \alpha &= \frac{2\omega_1\omega_2(\zeta_1\omega_2 - \zeta_2\omega_1)}{\omega_2^2 - \omega_1^2} \\ \beta &= \frac{2(\zeta_2\omega_2 - \zeta_1\omega_1)}{\omega_2^2 - \omega_1^2} \end{aligned} \tag{A.62}$$

Three cases can be distinguished based on the natural frequencies and damping ratios:
Case A $\left(\frac{\omega_1}{\omega_2} < \frac{\zeta_2}{\zeta_1} < \frac{\omega_2}{\omega 1}\right)$:
There will be no problems for this case. All values of the modal damping ratios will be positive as long as the damping ratios used to compute the coefficients are smaller than 1.
Case B $\left(\frac{\zeta_2}{\zeta_1} \leq \frac{\omega_1}{\omega_2}\right)$:

For the higher natural frequencies this case may cause problems, because the damping values can become negative for natural frequencies that are larger than $\sqrt{\alpha/-\beta}$. Negative damping ratios are physically not acceptable.
Case C $\left(\frac{\zeta_2}{\zeta_1} \geq \frac{\omega_2}{\omega_1}\right)$:
The case can cause problems for frequencies lower than $\sqrt{-\alpha/\beta}$, which is usually not acceptable.

The response to the same harmonic load as for the undamped case will be analysed. Again, the response is assumed to be a harmonic time function with the same frequency as the load, but this time with a phase shift:

$$u_i(t) = \hat{u}_i \sin(\omega t - \phi_i) \tag{A.63}$$

The amplitude $\hat{u}_i$ and the phase shift ϕ_i can be deduced in the same manner as for the single degree of freedom system:

$$\begin{aligned} \hat{u}_i &= \frac{1}{\sqrt{\left(1-(\omega/\omega_i)^2\right)^2 + (2\zeta_i\omega/\omega_i)^2}} \frac{1}{\omega_i^2} \frac{\underline{\hat{x}}_i^T \underline{\hat{f}}}{\underline{\hat{x}}_i^T \mathbf{M} \underline{\hat{x}}_i} \\ \tan\phi_i &= \frac{2\zeta_i\omega/\omega_i}{1-(\omega/\omega_i)^2} \end{aligned} \tag{A.64}$$

When, just like for the undamped case, one looks at a loading case with a harmonic load acting on one degree of freedom only, the response amplitude will be:

$$\hat{u}_i = \frac{1}{\sqrt{\left(1-(\omega/\omega_i)^2\right)^2 + (2\zeta_i\omega/\omega_i)^2}} \frac{1}{\omega_i^2} \frac{\hat{x}_{pi}\hat{f}_p}{\underline{\hat{x}}_i^T \mathbf{M} \underline{\hat{x}}_i} \tag{A.65}$$

Also for the damped system the FRF can be found. It differs slightly from the undamped system, but this small difference is essential:

$$H_{u_i f_p}(\omega) = \frac{\hat{u}_i}{\hat{f}_p} = \frac{1}{\sqrt{\left(1-(\omega/\omega_i)^2\right)^2 + (2\zeta_i\omega/\omega_i)^2}} \frac{1}{\omega_i^2} \frac{\hat{x}_{pi}}{\underline{\hat{x}}_i^T \mathbf{M} \underline{\hat{x}}_i} \tag{A.66}$$

Due to the presence of damping, a phase difference occurs between the applied force and the response, therefore the following is not true in this case:

$$H_{u_i f_p}(\omega) = \frac{\hat{u}_i}{\hat{f}_p} \neq \frac{u_i(t)}{f_p} \tag{A.67}$$

In this case the FRF matrix $\mathbf{H}_{u_i f_p}$ is a non-symmetrical matrix, the response of the system can be found using these terms:

$$u_i(t) = \hat{u}_i \sin(\omega t - \phi_i) = H_{u_i f_p}(\omega)\hat{f}_p \sin(\omega t - \phi_i) \tag{A.68}$$

The response in the physical degrees of freedom is:

$$\underline{x}(t) = \sum_{i=1}^{n} \underline{\hat{x}}_i \frac{1}{\sqrt{\left(1-(\omega/\omega_i)^2\right)^2 + (2\zeta_i\omega/\omega_i)^2}} \frac{1}{\omega_i^2} \frac{\hat{x}_{pi}\hat{f}_p}{\underline{\hat{x}}_i^T \mathbf{M} \underline{\hat{x}}_i} \sin(\omega t - \phi_i) \tag{A.69}$$

After some substitutions and adjustments (Spijkers et al., 2005), eventually the expression for the FRF between the force and the physical response of a system is expressed using the FRF for the response $\underline{u}(t)$ and the phase shift ϕ_i:

$$H_{x_q f_p}(\omega) = \frac{\hat{x}_q}{\hat{f}_p} = \sqrt{\left(\sum_{i=1}^{n} \hat{x}_{qi} H_{u_i f_p}(\omega)\cos\phi_i\right)^2 + \left(\sum_{i=1}^{n} \hat{x}_{qi} H_{u_i f_p}(\omega)\sin\phi_i\right)^2} \tag{A.70}$$

If the frequency of the load is known, then the amplitude of the physical response can be obtained from:

$$\hat{x}_q = H_{x_q f_p}(\omega)\hat{f}_p \tag{A.71}$$

And the response of degree of freedom q is:

$$x_q(t) = \hat{x}_q \sin(\omega t - \theta_q) = H_{x_q f_p}(\omega)\hat{f}_p \sin(\omega t - \theta_q) \tag{A.72}$$

with

$$\tan\theta_q = \frac{\sum_{i=1}^{n} \hat{x}_{qi} H_{u_i f_p}(\omega)\sin\phi_i}{\sum_{i=1}^{n} \hat{x}_{qi} H_{u_i f_p}(\omega)\cos\phi_i} \tag{A.73}$$

It should be stressed again that the Modal Analysis as presented here is only applicable to linear elastic systems and cases in which all forces applied contain the same variation in time.

A.3. Continuous systems

Opposed to the discrete or lumped mass systems discussed before, this section focuses on systems where the mass is continuously distributed along the system. These systems are described by partial differential equations. The bending beam, which is the relevant system for this thesis, is described using a fourth order partial differential equation. Another interesting continuous system is the elastic half-space used to describe a three dimensional structure, often used for foundation and soil problems. The differential equations for the Euler-Bernoulli bending beam will be derived here using the sign convention of the internal forces given in fig. 5.3.The beam has a flexural stiffness EI in Nm^2, a cross-sectional area A in m^2 and a mass density ρ in kg/m^3. To derive the differential equations, the displacement method is applied to an infinitesimal element δx of the beam.

Kinematic relations Using the kinematic relations, the deformations are related to the degree of freedom. The deformations can be expressed as the strain ϵ, the curvature κ and the rotation ϕ. The degree of freedom is positive downwards in fig. 5.3 and is dependent on both location along the beam axis and time: $w(x,t)$.

$$\begin{aligned} \phi(x,t) &= -\frac{\partial w(x,t)}{\partial x} \\ \kappa(x,t) &= \frac{\partial \phi}{\partial x} = -\frac{\partial^2 w(x,t)}{\partial x^2} \\ \epsilon(x,z,t) &= z\kappa = -z\frac{\partial^2 w(x,t)}{\partial x^2} \end{aligned} \tag{A.74}$$

The top equation is based on the assumption that no shear deformations occur, meaning that the cross-section remains perpendicular to the neutral line of the beam. The third equation assumes that plane cross-sections remain plane.

Constitutive relation The constitutive relation relates the deformation as expressed through the strain with the stress using material behaviour as defined in Hooke's law:

$$\sigma(x,z,t) = \epsilon(x,z,t)E = zE\kappa(x,t) \tag{A.75}$$

Using the definition of the bending moment this can be expressed as follows:

$$M(x,t) = \int z\sigma(z,x,t)\mathrm{d}A = E\kappa(x,t)\int z^2 \mathrm{d}A \tag{A.76}$$

Using the expression for the second moment of area, the bending moment can ultimately be written as:

$$M = EI\kappa(x,t) = -EI\frac{\partial^2 w(x,t)}{\partial x^2} \tag{A.77}$$

Newton's second law To write the differential equations Newton's second law is used, which relates the acceleration to the internal forces and external forces on an object.

$$ma = \sum F \tag{A.78}$$

For the object in fig. 5.3 in lateral direction it can be filled in as follows:

$$\begin{aligned} \rho A \Delta x \frac{\partial^2 w(x,t)}{\partial t^2} &= -Q(x,t) + Q(x,t) + \Delta Q(x,t) + q(x,t)\Delta x \\ \rho A \frac{\partial^2 w(x,t)}{\partial t^2} &= \frac{\partial Q(x,t)}{\partial x} + q(x,t) \end{aligned} \tag{A.79}$$

The second row of eq. (A.79) is obtained applying Taylor expansion and dividing by Δx. Also, the moment equilibrium has to be used to describe the beam motion. Neglecting the effect of rotational inertia and the contribution of the distributed force q and thus considering a static case, after Taylor expansion and again dividing by Δx, the moment equilibrium reads:

$$\begin{aligned} &- M(x,t) + M(x,t) + \Delta M(x,t) - Q(x,t)\Delta x = 0 \\ Q(x,t) &= \frac{\partial M(x,t)}{\partial x} = -EI \frac{\partial^3 w(x,t)}{\partial x^3} \end{aligned} \tag{A.80}$$

Inserting the expression found in eq. (A.80) into eq. (A.79) yields the final equation of motion:

$$\rho A \frac{\partial^2 w(x,t)}{\partial t^2} + EI \frac{\partial^4 w(x,t)}{\partial x^4} = q(x,t) \tag{A.81}$$

In this expression the assumption is made that the Young's modulus E and the moment of inertia I are independent of the x-coordinate. In case of free vibration, the equation of motion is given by:

$$\rho A \frac{\partial^2 w(x,t)}{\partial t^2} + EI \frac{\partial^4 w(x,t)}{\partial x^4} = 0 \tag{A.82}$$

Using separation of variables, this differential equation can be rewritten to a time-dependent equation and a space-dependent equation:

$$\begin{aligned} w(x,t) &= W(x)\Psi(t) \\ W(x)\frac{\mathrm{d}^2\Psi(t)}{\mathrm{d}t^2} &+ \frac{EI}{\rho A}\frac{\mathrm{d}^4 W(x)}{\mathrm{d}x^4}\Psi(t) = 0 \end{aligned} \tag{A.83}$$

Division by $W(x)\Psi(t)$ leads to the following expression, which can only be satisfied if the space-dependent part and the time-dependent part are constant.

$$\frac{1}{\Psi t}\frac{\mathrm{d}^2\Psi(t)}{\mathrm{d}t^2} + \frac{EI}{\rho A}\frac{1}{U(x)}\frac{\mathrm{d}^4 U(x)}{\mathrm{d}x^4} = 0 \tag{A.84}$$

This constant is introduced as follows:

$$\begin{aligned} \frac{1}{\Psi t}\frac{\mathrm{d}^2\Psi(t)}{\mathrm{d}t^2} &= -\omega^2 \\ \frac{EI}{\rho A}\frac{1}{W(x)}\frac{\mathrm{d}^4 W(x)}{\mathrm{d}x^4} &= \omega^2 \end{aligned} \tag{A.85}$$

In eq. (A.85) ω is the natural frequency of the system. From now on the focus will be on solving the second, space-dependent, solution to the equation of motion. The general form of the solution to this differential equation is given in eq. (A.86).

$$\begin{aligned} W(x) &= A_1\cosh(\beta x) + A_2\sinh(\beta x) + A_3\cos(\beta x) + A_4\sin(\beta x) \\ \beta^4 &= \omega^2\frac{\rho A}{EI} \end{aligned} \tag{A.86}$$

The coefficients given in this equation are dependent on the boundary conditions of the beam. The coefficients will be derived for the four models. To find the coefficients, the derivatives of the mode shape to space are required.

$$\begin{aligned} \frac{\mathrm{d}W(x)}{\mathrm{d}x} &= \beta\left(A_1\sinh(\beta x) + A_2\cosh(\beta x) - A_3\sin(\beta x) + A_4\cos(\beta x)\right) \\ \frac{\mathrm{d}^2 W(x)}{\mathrm{d}x^2} &= \beta^2\left(A_1\cosh(\beta x) + A_2\sinh(\beta x) - A_3\cos(\beta x) - A_4\sin(\beta x)\right) \\ \frac{\mathrm{d}^3 W(x)}{\mathrm{d}x^3} &= \beta^3\left(A_1\sinh(\beta x) + A_2\cosh(\beta x) + A_3\sin(\beta x) - A_4\cos(\beta x)\right) \end{aligned} \tag{A.87}$$

The mode shape will be used in this thesis to extrapolate the measured motion at one location of the structure to the remaining part of the structure, depending on the choice of boundary conditions. The mode shape will be derived for the following boundary conditions:

1. Fixed - free beam
2. Flexible - free beam with rotational spring
3. Flexible - free beam with rotational and translational spring
4. Flexible - free beam with rotational and translational spring with an added mass for the foundation

Fixed-free beam To find the description of the coefficients in eq. (A.86), the boundary conditions are required. Since the differential equation is of order 4, 4 are required of which 2 at each side of the beam. For the fixed-free beam the conditions at the fixed end, $x = 0$, and free end, $x = L$, are as follows:

$$W(x) = 0 \quad \text{for } x = 0 \tag{A.88}$$
$$\frac{\mathrm{d}W(x)}{\mathrm{d}x} = 0 \quad \text{for } x = 0 \tag{A.89}$$
$$\frac{\mathrm{d}^2W(x)}{\mathrm{d}x^2} = 0 \quad \text{for } x = L \tag{A.90}$$
$$\frac{\mathrm{d}^3W(x)}{\mathrm{d}x^3} = 0 \quad \text{for } x = L \tag{A.91}$$

Which results in the following coefficient matrix:

$$M = \begin{bmatrix} 1 & 0 & 1 & 0 \\ 0 & 1 & 0 & 1 \\ \cosh(\beta L) & \sinh(\beta L) & -\cos(\beta L) & -\sin(\beta L) \\ \sinh(\beta L) & \cosh(\beta L) & \sin(\beta L) & -\cos(\beta L) \end{bmatrix} \tag{A.92}$$

The determinant of this matrix will provide the frequency equation, with which the natural frequencies of the system can be found.

$$2 + 2\cosh(\beta L)\cos(\beta L) = 0 \tag{A.93}$$

The first solution to this equation can be found in the form $\beta L = 0$, but is trivial. The first non-trivial solution is found for $\beta L = 1.875104069$. This leads to the following first natural frequency of the beam:

$$\omega_1 = \sqrt{\frac{EI}{\rho A}}\frac{(\beta L)^2}{L^2} = \sqrt{\frac{EI}{\rho A}}\frac{(1.875104069)^2}{L^2} \tag{A.94}$$

The coefficients of the beam deflection description $W(x)$ are as follows:

$$\begin{aligned} A_1 &= \frac{\sin(\beta L) + \sinh(\beta L)}{\cos(\beta L) + \cosh(\beta L)} \\ A_2 &= -1 \\ A_3 &= \frac{-\sin(\beta L) - \sinh(\beta L)}{\cos(\beta L) + \cosh(\beta L)} \\ A_4 &= 1 \end{aligned} \tag{A.95}$$

Flexible rotational - Free beam To find the description of the coefficients in eq. (A.86), the boundary conditions for the flexible-free beam with rotational spring are required.

$$EI\frac{\mathrm{d}^2W(x)}{\mathrm{d}x^2} - K_\theta\frac{\mathrm{d}W(x)}{\mathrm{d}x} = 0 \quad \text{for } x = 0 \tag{A.96}$$
$$W(x) = 0 \quad \text{for } x = 0 \tag{A.97}$$
$$\frac{\mathrm{d}^2W(x)}{\mathrm{d}x^2} = 0 \quad \text{for } x = L \tag{A.98}$$
$$\frac{\mathrm{d}^3W(x)}{\mathrm{d}x^3} = 0 \quad \text{for } x = L \tag{A.99}$$

These are analogous to the boundary conditions found using Lagrangian mechanics. The difference is that Lagrangian mechanics considered both directions. Which results in the following coefficient matrix:

$$M = \begin{bmatrix} -EI\beta^2 & K_\theta\beta & EI\beta^2 & K_\theta\beta \\ 1 & 0 & 1 & 0 \\ \cosh(\beta L) & \sinh(\beta L) & -\cos(\beta L) & -\sin(\beta L) \\ \sinh(\beta L) & \cosh(\beta L) & \sin(\beta L) & -\cos(\beta L) \end{bmatrix} \tag{A.100}$$

The determinant of this matrix will give the frequency equation. Using this equation, the natural frequency of the system can be found.

$$-2\beta\left(\left(-EI\beta\sin(\beta L) + K_\theta\cos(\beta L)\right)\cosh(\beta L) + EI\sinh(\beta L)\cos(\beta L)\beta + K_\theta\right)\beta = 0 \tag{A.101}$$

Unfortunately, an analytical expression for the natural frequencies cannot be found, to solve the frequency equation, the parameters have to be filled in. The coefficients of the beam deflection description $W(x)$ are as follows:

$$\begin{aligned} A_1 &= \frac{K_\theta\left(\sinh(\beta L) + \sin(\beta L)\right)}{2EI\sinh(\beta L)\beta + K_\theta\left(\cos(\beta L) + \cosh(\beta L)\right)} \\ A_2 &= \frac{2EI\beta\sin(\beta L) - K_\theta\cosh(\beta L) - K_\theta\cos(\beta L)}{2EI\sinh(\beta L)\beta + K_\theta\cosh(\beta L) + K_\theta\cos(\beta L)} \\ A_3 &= -\frac{K_\theta\left(\sinh(\beta L) + \sin(\beta L)\right)}{2EI\sinh(\beta L)\beta + K_\theta\left(\cos(\beta L) + \cosh(\beta L)\right)} \\ A_4 &= 1 \end{aligned} \tag{A.102}$$

Flexible rotational and translational - Free beam To find the description of the coefficients in eq. (A.86), the boundary conditions for the flexible-free beam with rotational spring are required.

$$EI\frac{\mathrm{d}^2W(x)}{\mathrm{d}x^2} - K_\theta\frac{\mathrm{d}W(x)}{\mathrm{d}x} = 0 \quad \text{for } x = 0 \tag{A.103}$$

$$EI\frac{\mathrm{d}^3W(x)}{\mathrm{d}x^3} + K_tW(x) = 0 \quad \text{for } x = 0 \tag{A.104}$$

$$\frac{\mathrm{d}^2W(x)}{\mathrm{d}x^2} = 0 \quad \text{for } x = L \tag{A.105}$$

$$\frac{\mathrm{d}^3W(x)}{\mathrm{d}x^3} = 0 \quad \text{for } x = L \tag{A.106}$$

This results in the following coefficient matrix:

$$M = \begin{bmatrix} -EI\beta^2 & K_\theta\beta & EI\beta^2 & K_\theta\beta \\ K_t & EI\beta^3 & K_t & -EI\beta^3 \\ \cosh(\beta L) & \sinh(\beta L) & -\cos(\beta L) & -\sin(\beta L) \\ \sinh(\beta L) & \cosh(\beta L) & \sin(\beta L) & -\cos(\beta L) \end{bmatrix} \tag{A.107}$$

The determinant of this matrix will give the frequency equation. Using this equation, the natural frequencies of the system can be found.

$$\begin{aligned} &2\left(\left(\left(EI^2\beta^4 - K_\theta K_t\right)\cos(\beta L) + EI\beta\sin(\beta L)\left(K_\theta\beta^2 + K_t\right)\right)\cosh(\beta L)\right)\beta \\ &+2\left(EI\beta\sinh(\beta L)\left(K_\theta\beta^2 - K_t\right)\cos(\beta L) - EI^2\beta^4 - K_\theta K_t\right)\beta = 0 \end{aligned} \tag{A.108}$$

To find the natural frequencies which are the solution to this equation, the parameters have to be filled in. The coefficients of the beam deflection description $W(x)$ are as follows:

$$\begin{aligned} A_1 &= \frac{\left(EI^2\beta^4 + K_\theta K_t\right)\sinh(\beta L) + 2EIK_\theta\cos(\beta L)\beta^3 - \left(EI^2\beta^4 - K_\theta K_t\right)\sin(\beta L)}{2EIK_t\sinh(\beta L)\beta + \left(EI^2\beta^4 + K_\theta K_t\right)\cos(\beta L) - \left(EI^2\beta^4 - K_\theta K_t\right)\cosh(\beta L)} \\ A_2 &= \frac{EI^2\cosh(\beta L)\beta^4 - EI^2\cos(\beta L)\beta^4 - 2EIK_t\sin(\beta L)\beta + K_\theta K_t\cosh(\beta L) + K_\theta K_t\cos(\beta L)}{EI^2\cosh(\beta L)\beta^4 - EI^2\cos(\beta L)\beta^4 - 2EIK_t\sinh(\beta L)\beta - K_\theta K_t\cosh(\beta L) - K_\theta K_t\cos(\beta L)} \\ A_3 &= \frac{2EIK_\theta\cosh(\beta L)\beta^3 + \left(EI^2\beta^4 - K_\theta K_t\right)\sinh(\beta L) - \left(EI^2\beta^4 + K_\theta K_t\right)\sin(\beta L)}{\left(-EI^2\beta^4 + K_\theta K_t\right)\cosh(\beta L) + \left(EI^2\beta^4 + K_\theta K_t\right)\cos(\beta L) + 2EIK_t\sinh(\beta L)\beta} \\ A_4 &= 1 \end{aligned} \tag{A.109}$$

Flexible - Free beam with added foundation mass To find the description of the coefficients in eq. (A.86), the boundary conditions for the flexible-free beam with added foundation mass are required.

$$EI\frac{\mathrm{d}^2W(x)}{\mathrm{d}x^2} - K_\theta\frac{\mathrm{d}W(x)}{\mathrm{d}x} + I\omega^2\frac{\mathrm{d}W(x)}{\mathrm{d}x} = 0 \quad \text{for } x = 0 \tag{A.110}$$

$$EI\frac{\mathrm{d}^3W(x)}{\mathrm{d}x^3} + K_tW(x) - M\omega^2W(x) = 0 \quad \text{for } x = 0 \tag{A.111}$$

$$\frac{\mathrm{d}^2W(x)}{\mathrm{d}x^2} = 0 \quad \text{for } x = L \tag{A.112}$$

$$\frac{\mathrm{d}^3W(x)}{\mathrm{d}x^3} = 0 \quad \text{for } x = L \tag{A.113}$$

$$\tag{A.114}$$

This results in the following coefficient matrix:

$$M = \begin{bmatrix} -EI\beta^2 & -\left(I\omega^2 - K_\theta\right)\beta & EI\beta^2 & -\left(I\omega^2 - K_\theta\right)\beta \\ \omega^2M - K_t & -EI\beta^3 & \omega^2M - K_t & EI\beta^3 \\ \cosh(\beta L) & \sinh(\beta L) & -\cos(\beta L) & -\sin(\beta L) \\ \sinh(\beta L) & \cosh(\beta L) & \sin(\beta L) & -\cos(\beta L) \end{bmatrix} \tag{A.115}$$

The determinant of this matrix will give the frequency equation. Using this equation, the natural frequencies of the system can be found.

$$\begin{aligned} &2\beta\left(\left(\left(-EI^2\beta^4 - \left(-\omega^2M + K_t\right)\left(I\omega^2 - K_\theta\right)\right)\cos(\beta L) + EI\beta\left(\left(I\omega^2 - K_\theta\right)\beta^2 + \omega^2M - K_\theta\right)\sin(\beta L)\right)\right)\cosh(\beta L) \\ &+ 2\beta\left(EI\left(\left(I\omega^2 - K_\theta\right)\beta^2 - \omega^2M + K_t\right)\beta\sin(\beta L)\cos(\beta L) + EI^2\beta^4 - \left(-\omega^2M + K_t\right)\left(I\omega^2 - K_\theta\right)\right) = 0 \end{aligned} \tag{A.116}$$

Unfortunately, an analytical expression for the natural frequencies cannot be found, to solve the frequency equation, the parameters have to be filled in. The coefficients of the beam deflection description $W(x)$ are as follows:

$$\begin{aligned} A_1 &= \frac{\left(-IM\omega^4 + (IK_t + K_\theta M)\omega^2 - EI^2\beta^4 - K_\theta K_t\right)\sinh(\beta L) + 2EI\beta^3\left(I\omega^2 - K_\theta\right)\cos(\beta L)}{-2EI\beta\left(-\omega^2M + K_t\right)\sinh(\beta L) + \left(-IM\omega^4 + (IK_t + K_\theta M)\omega^2 - EI^2\beta^4 - K_\theta K_t\right)\cos(\beta L)} \\ &\frac{+\left(-IM\omega^4 + (IK_t + K_\theta M)\omega^2 + EI^2\beta^4 - K_\theta K_t\right)\sin(\beta L)}{+\left(-IM\omega^4 + (IK_t + K_\theta M)\omega^2 + EI^2\beta^4 - K_\theta K_t\right)\cosh(\beta L)} \\ A_2 &= \frac{\left(IM\omega^4 + (-IK_t - K_\theta M)\omega^2 + EI^2\beta^4 + K_\theta K_t\right)\cosh(\beta L)}{-2EI\beta\left(-\omega^2M + K_t\right)\sinh(\beta L) + \left(-IM\omega^4 + (IK_t + K_\theta M)\omega^2 - EI^2\beta^4 - K_\theta K_t\right)\cos(\beta L)} \\ &\frac{+\left(IM\omega^4 + (-IK_t - K_\theta M)\omega^2 - EI^2\beta^4 + K_\theta K_t\right)\cos(\beta L) - 2\sin(\beta L)EI\beta\left(-\omega^2M + K_t\right)}{+\left(-IM\omega^4 + (IK_t + K_\theta M)\omega^2 + EI^2\beta^4 - K_\theta K_t\right)\cosh(\beta L)} \\ A_3 &= \frac{2EI\beta^3\left(I\omega^2 - K_\theta\right)\cosh(\beta L) + \left(IM\omega^4 + (-IK_t - K_\theta M)\omega^2 - EI^2\beta^4 + K_\theta K_t\right)\sinh(\beta L)}{\left(-IM\omega^4 + (IK_t + K_\theta M)\omega^2 + EI^2\beta^4 - K_\theta K_t\right)\cosh(\beta L) - 2EI\beta\left(-\omega^2M + K_t\right)\sinh(\beta L)} \\ &\frac{+\left(IM\omega^4 + (-IK_t - K_\theta M)\omega^2 + EI^2\beta^4 + K_\theta K_t\right)\sin(\beta L)}{-\cos(\beta L)\left(IM\omega^4 + (-IK_t - K_\theta M)\omega^2 + EI^2\beta^4 + K_\theta K_t\right)} \\ A_4 &= 1 \end{aligned} \tag{A.117}$$

A.4. Equivalent mass

A multi degree of freedom system, or a continuous system, may be translated to a single degree of freedom system through the "equivalent mass", "equivalent spring stiffness" and "equivalent force". This equivalences should be found for each mode separately, since of course the single degree of freedom system can only represent one mode. The equivalences of a multi degree of freedom system with j masses, s springs and n modes are found to be (Biggs, 1964):

$$\begin{aligned} \sum_{r=1}^{j} m_r\mathbf{E}_{rn}^2 &= \text{equivalent mass} \\ \sum_{g=1}^{s} k_g\mathbf{E}_{gn}^2 &= \text{equivalent spring constant} \\ \sum_{r=1}^{j} f_r\mathbf{E}_{rn} &= \text{equivalent force} \end{aligned} \tag{A.118}$$

Of course, the amount of modes n is the same as the amount of degrees of freedom in the system. Of the eigenmatrix $\mathbf{E}$ containing the mode shapes, the column corresponding to mode n is taken and the element in the row corresponding to the mass or stiffness under consideration. The equivalent mass, stiffness and force can be found for any mode n. It is also possible to translate these equivalences for the discrete system to the equivalences for a continuous system:

$$\begin{aligned} \int_0^l \rho A(x)\phi(x)^2 \,\mathrm{d}x &= \text{equivalent mass} \\ \int_0^l k(x)\phi(x)^2 \,\mathrm{d}x &= \text{equivalent stiffness} \\ \int_0^l q(x)\phi(x) \,\mathrm{d}x &= \text{equivalent force} \end{aligned} \tag{A.119}$$

Note that $\phi(x)$ is the mode shape of the continuous system, which was discussed in appendix A.3 and presented as $W(x)$.

B

Rigid body translation

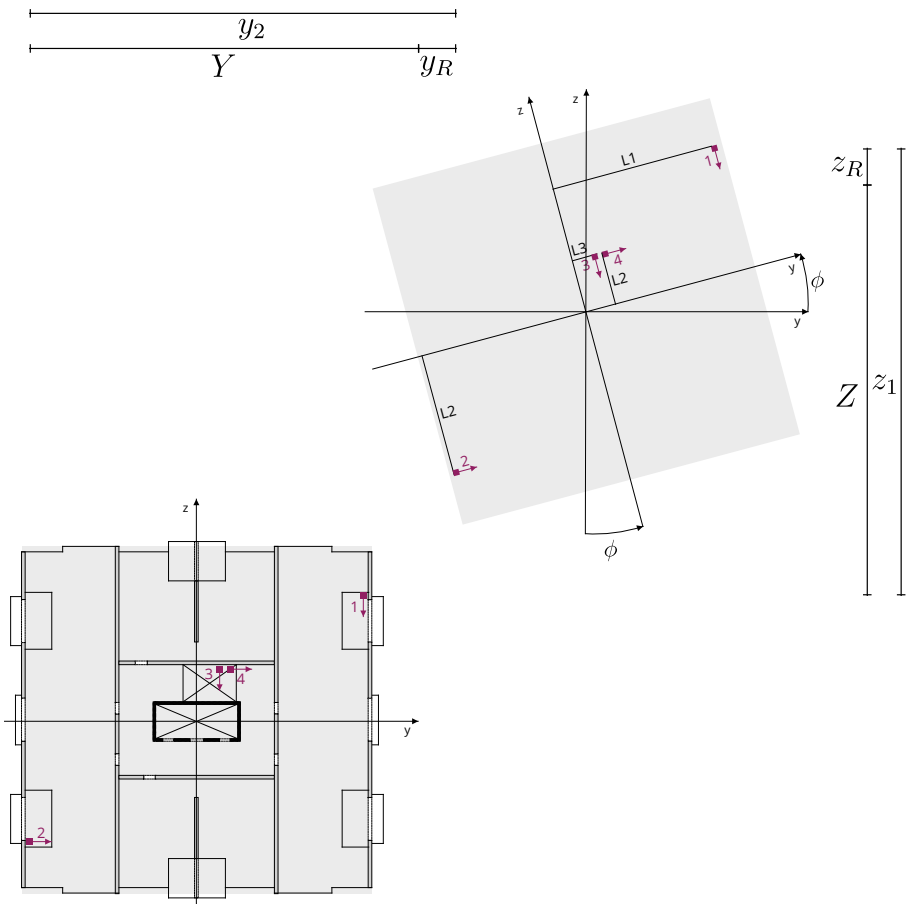

Figure B.1: Rigidly translated and rotated building

The acceleration in the coordinate directions cannot be obtained simply from one accelerometer in the relevant direction. The coordinate system might not be in line with the principal axis of translation of the building and the accelometer might register rotation of the building. For the New Orleans tower, TNO found that the coordinate axes of the building system are in line with the principal axes of the building. Therefore, acceleration in each translational direction can be obtained from the measured acceleration and the measured rotation around the origin.

The relevant translational acceleration in z-direction and y-direction are indicated by Z and Y respectively. However, the measured accelerations, z_1 and y_2, did not only measure this pure translation, but also an addi-

tional translation due to rotation, z_{R1} and y_{R2}.This is visualised in fig. B.1. Measured accelerations z_1, z_3, y_2 and y_4 can be decomposed of their translational and rotational components:

$$\begin{aligned} z_1 &= -Z - z_{R1} \\ z_3 &= -Z - z_{R3} \\ y_2 &= +Y + y_{R2} \\ y_4 &= +Y - y_{R4} \end{aligned} \tag{B.1}$$

This is shown in more detail in fig. B.2. The minus signs in the top two equations of eq. (B.1) is due to the fact that sensor 1 and 3 measure in negative z-direction. The principal accelerations Y and Z can be obtained from these equations and trigonometry which is shown in fig. B.2. First for the z-direction:

$$\begin{aligned} Z = -z_1 - z_{R1} = -z_1 - \tan(\phi_z) L_1 \\ \tan(\phi_z) = \frac{z_{R1} - z_{R3}}{L_1 - L_3} = \frac{-z_1 + z_3}{L_1 - L_3} \end{aligned} \tag{B.2}$$

This yields:

$$Z = -z_1 - L_1 \frac{-z_1 + z_3}{L_1 - L_3} = \frac{-z_1 L_1 + z_1 L_3 + z_1 L_1 - z_3 L_1}{L_1 - L_3} = \frac{z_1 L_3 - z_3 L_1}{L_1 - L_3} \tag{B.3}$$

And for the y-direction:

$$\begin{aligned} Y = y_2 - y_{R2} = y_2 - \tan(\phi_y) L_2 \\ tan(\phi_y) = \frac{y_{R2} + y_{R4}}{L_2 + L_4} = \frac{y_2 - y_4}{L_2 + L_4} \end{aligned} \tag{B.4}$$

Which finally yields:

$$Y = y_2 - L_2 \frac{y_2 - y_4}{L_2 + L_4} = \frac{y_2 L_2 + y_2 L_4 - y_2 L_2 + y_4 L_2}{L_2 + L_4} = \frac{y_2 L_4 + y_4 L_2}{L_2 + L_4} \tag{B.5}$$

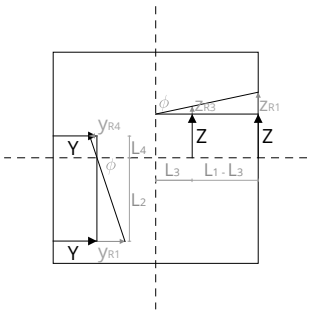

Figure B.2: Geometry to calculate principal accelerations

C

Mesh convergence

Upon performing the sensitivity study, a short mesh convergence study for the mode shape description is performed. This is necessary because the mode shapes have to be modelled with a certain mesh size and it is undesirable that this mesh size influences the results of the Energy Flux Analysis. The results of this mesh convergence study are visualised in fig. C.1. These graph clearly show convergence of the kinetic and potential energies found with decreasing mesh size. From around 100 elements the mesh size will not influence the results. Since the modelled structure is 155 m tall, the mesh size used in this research will be 1 m with 155 elements.

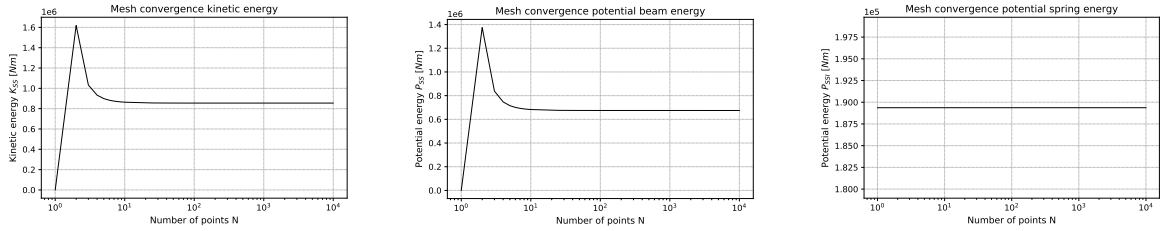

Figure C.1: Mesh convergence mean kinetic energy, mean potential energy, and mean potential spring energy

The peak in the mesh convergence can be explained by the overestimation of the energies in case of one element only. This is presented using the blue line in fig. C.2, which shows that both the deformation and the curvature are too large for any point along the beam height.

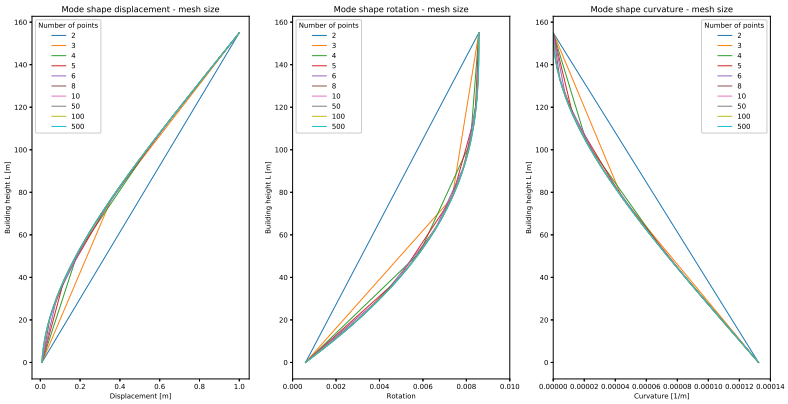

Figure C.2: Overestimation in case of limited points for extrapolation mode shape

D

FEM material damping

This appendix will present the modelled material damping in a FEM model in Abaqus, and its influence on the stress. Looking at the method to integrate material damping into the FEM model, the following relation between stress and strain in given:

$$\sigma = E\epsilon + E\beta_R\dot{\epsilon} \tag{D.1}$$

In this relation σ is the stress, ϵ is the strain, β_R is the stiffness proportional factor for Rayleigh damping used as input for the FEM model, and $\dot{\epsilon}$ is the first derivative in time of the strain.

The strain as a result of harmonic motion can be described using a sine function, in vibration mechanics this is a generally accepted description. Therefore the strain and its derivative are given as:

$$\begin{aligned} \epsilon &= A_1 \sin(\omega t) \\ \dot{\epsilon} &= A_1 \omega \cos(\omega t) \end{aligned} \tag{D.2}$$

$A1$ represents some amplitude coefficient. Inserting these expressions in eq. (D.1), the following expression for the stress is obtained:

$$\sigma = EA_1 \sin(\omega t) + E\beta_R A_1 \omega \cos(\omega t) \tag{D.3}$$

To find the phase shift of this function compared to the static stress without damping, which is the first term of eq. (D.2), the following rule from trigonometry is applied:

$$\begin{aligned} &a_1 \sin(Bt) + a_2 \cos(Bt) = A\sin(Bt) \\ &A = \sqrt{a_1^2 + a_2^2} \\ &\tan\phi = \frac{a_2}{a_1} \end{aligned} \tag{D.4}$$

This results in the final expression of the stress:

$$\sigma = \sqrt{(EA_1)^2 + \left(EA_1\omega\beta_R\right)^2}\sin(\omega(t+\beta_R)) \tag{D.5}$$

In this equation β_R represents the phase shift compared to the original static function as is given in eq. (D.2). This is exactly the stiffness proportional factor used as input for Rayleigh material damping.

E

Vertical wind profile sensitivity

This appendix provides the exact description of the mean wind profiles used in § 10.3 to study the sensitivity of the Energy Flux Analysis to the mean wind profile used. The profiles used are shown in appendix E and were chosen to represent some extreme, not necessarily realistic, cases. All profiles are normalised to 114 m to be able to multiply with the measured wind force. Wind fluctuations have magnitude proportional to the fluctuations in the wind force measured and the mean wind force at the specific height. Therefore, the fluctuations at all heights move synchronous in time.

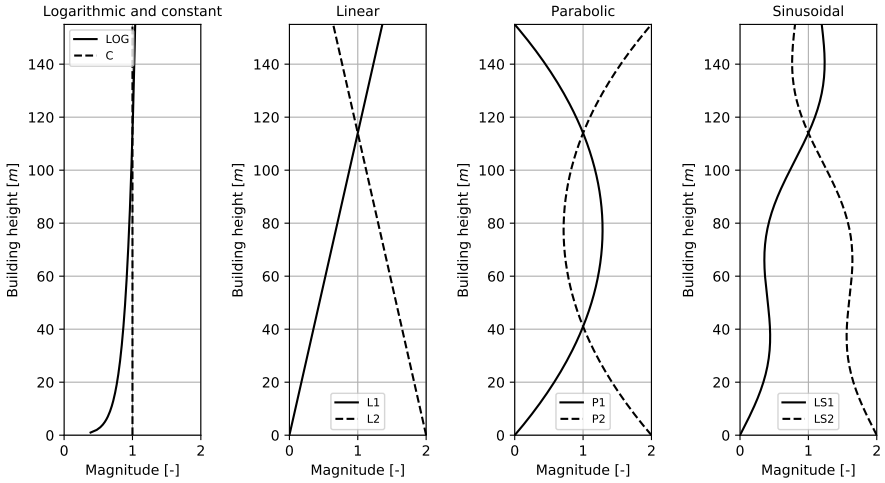

Figure E.1: Mean wind profiles used for sensitivity study

- **LOG**: This is a logarithmic profile, which is commonly used for mean wind velocities. The parameter z_0 depends on the terrain characteristics and is chosen to be .. in this case. The parameter κ is taken as 0.4, which is a commonly used value. The value of u_* can normally be found by filling in the measured wind velocity at a specific height z. However, in this case it is specified such that the logarithmic profile has a value of 1 at z = 114 m. For z_0 = 0.05 m, u_* is found to be 0.052. The mathematical description of the profile is given in eq. (E.1).

$$y(x) = \frac{u^*}{\kappa} \log\left(\frac{x}{z_0}\right) \tag{E.1}$$

- **C**: In this case the vertical profile is constant, it has a value of 1 for all heights.

$$y(x) = 1 \tag{E.2}$$

- **L1**: The first linear profile has a value of 0 at x = 0 m, so at the bottom of the building, and increases

with height. At x = 114 m the value of this wind profiles is again 1.

$$y(x) = \frac{1}{114}x \tag{E.3}$$

- **L2**: The second linear profile has a value of 0 at x = 155 m and is increasing towards the bottom of the building. Also this profile has a value of 1 at x = 114 m. This results in a different area under the wind profile than for L1.

$$y(x) = -\frac{1}{114}x + 2 \tag{E.4}$$

- **P1**: The first parabolic profile has a value of 0 at both x = 0 m and x = 155 m and has its maximum value at the middle of the tower. The profile has a value of 1 for x = 114 m and therefore the value halfway the tower height is larger than 1.

$$y(x) = -\frac{1}{4674}x^2 + \frac{155}{4674}x \tag{E.5}$$

- **P2**: The second parabolic profile has a value of 2 at both x = 0 m and x = 155 m and has its minimum value at the middle of the tower. The profile has a value of 1 for x = 114 m and therefore the value halfway the tower height is smaller than 1. Similar to the linear wind profiles, the area underneath the two parabolic profiles is not the same.

$$y(x) = \frac{1}{4674}x^2 - \frac{155}{4674}x + 2 \tag{E.6}$$

- **LS1**: The sinusoidal profile, or rather linear sinusoidal profile, is a linear profile similar to L1, but with a sinusoidal function moving around the linear line. For LS1, this creates even larger values at the top and bottom of the tower, and a smaller value halfway the tower height. This profile also satisfies the required value of 1 at x = 114 m.

$$y(x) = \frac{1 - 0.2\sin\left(\frac{3\pi}{155}114\right)}{114}x + 0.2\sin\left(\frac{3\pi}{155}x\right) \tag{E.7}$$

- **LS2**: This sinusoidal profile consists of a linear profile similar to L2, but with a sinusoidal function moving around the linear line. For LS2, this creates smaller values at the top and bottom and a slightly larger value halfway the tower height. The area under the LS2 profile is much larger than the area under the LS1 profile. The aim is not to compare these profiles, but to compare some extreme wind profiles and therefore this is not seen as a problem.

$$y(x) = -\frac{1 - 0.2\sin\left(\frac{3\pi}{155}114\right)}{114}x - 0.2\sin\left(\frac{3\pi}{155}x\right) + 2 \tag{E.8}$$

F

Generating wind fluctuations

This appendix demonstrates the procedure to generate wind pressure fluctuations along the building height, based on the wind pressure spectra along the building height and the coherence between these points. The relevant relations from chapter 2 are repeated here.

First of all, the wind pressure spectrum at every height has to be created. The approach was previously explained in § 2.2.3 and requires the use of the wind velocity spectrum. The spectrum developed by Simiu and Scanlan (Simiu and Scanlan, 1996) has been adopted:

$$S_{uu}(n) = \frac{u_*^2}{n} \frac{200f}{(1+50f)^{5/3}} \tag{F.1}$$

with

$$f = \frac{nz}{\bar{U}(z)} \tag{F.2}$$

Then, the pressure spectrum has been derived from the wind velocity spectrum through:

$$S_{pp}(n) = \left|\chi_{p,u}(n)\right|^2 (C_{pm}\rho_a \bar{U})^2 S_{uu}(n) \tag{F.3}$$

In this equation $\chi_{p,u}$ is the aerodynamic admittance, for an area-averages pressure it may be found using:

$$\left|\chi_{p,A}\right|^2 = \left((1+80f^2)\left(1+20\left(\frac{n\sqrt{A}}{\bar{U}}\right)^2\right)\right)^{-5/12} \tag{F.4}$$

The area-averaged mean pressure coefficient was calculated through:

$$C_{pm} = \frac{\bar{p}}{\frac{1}{2}\rho_a \bar{U}^2} \tag{F.5}$$

These theoretical spectra have previously been compared to the measured spectra in chapter 7, and the pressure spectra show agreement. The coherence between different locations along the building height has to be prescribed, the coherence used here is the coherence of the wind velocity rather than the wind pressure. The wind pressure is larger than the wind velocity pressure (Geurts, 1997). The coherence used for windward side, which is used for along wind, is given by:

$$coh_{uu}(n) = e^{-F} \tag{F.6}$$

with

$$F = n\frac{\sqrt{((z_1 - z_2)c_z)^2}}{\frac{1}{2}(\bar{U}(z_1) + \bar{U}(z_2)} \tag{F.7}$$

Finally, using the wind pressure spectrum it is possible to define an amplitude of vibration for each frequency at each location along the building height. This amplitude factor is indicated with c, and may be found through:

$$c = \sqrt{2S_{pp}(z_i, n)\mathrm{d}n} \tag{F.8}$$

The wind pressure fluctuations can now be generated, the procedure shown here has to be repeated for every time moment t_i. First, a unity amplitude sine function is created for every location z_j and every frequency f_k, with a randomly generated phase ϕ:

$$p_s(t_i, f_k, z_j) = \sin(2\pi f_i t_i + \phi(f_k, z_j)) \tag{F.9}$$

The following is repeated for every frequency f_k, and for every location taken as reference z_j:

$$p_{cor,j}(f_k) = \sum_{m=0}^{H} coh(z_j, z_m, f_k) p_s(t_i, f_k, z_j) \tag{F.10}$$

The result should be a p_{cor} for every location along the building height z_j. Finally, the fluctuating signal at each building height is found for every frequency through:

$$p'_j(t_i) = \sum_{k=0}^{f} c(f_k) p_{cor,j}(f_k) \tag{F.11}$$

A random fluctuating pressure has now been generated along the total building height. The fluctuations satisfy the theoretical pressure spectrum and coherence between locations based on the wind velocity coherence. The total area-averaged wind pressure may now be found, simply by adding the mean wind pressure using the logarithmic-squared profile. The force is then found by multiplication with the area A.

G

Single phase shift correction

This appendix shows the feasibility of obtaining an increasing external energy by applying a signal phase shift correction to all signals. This single phase shift correction would be useful in case the phase difference was caused by the measurement technique where the measured signals are stored one by one.

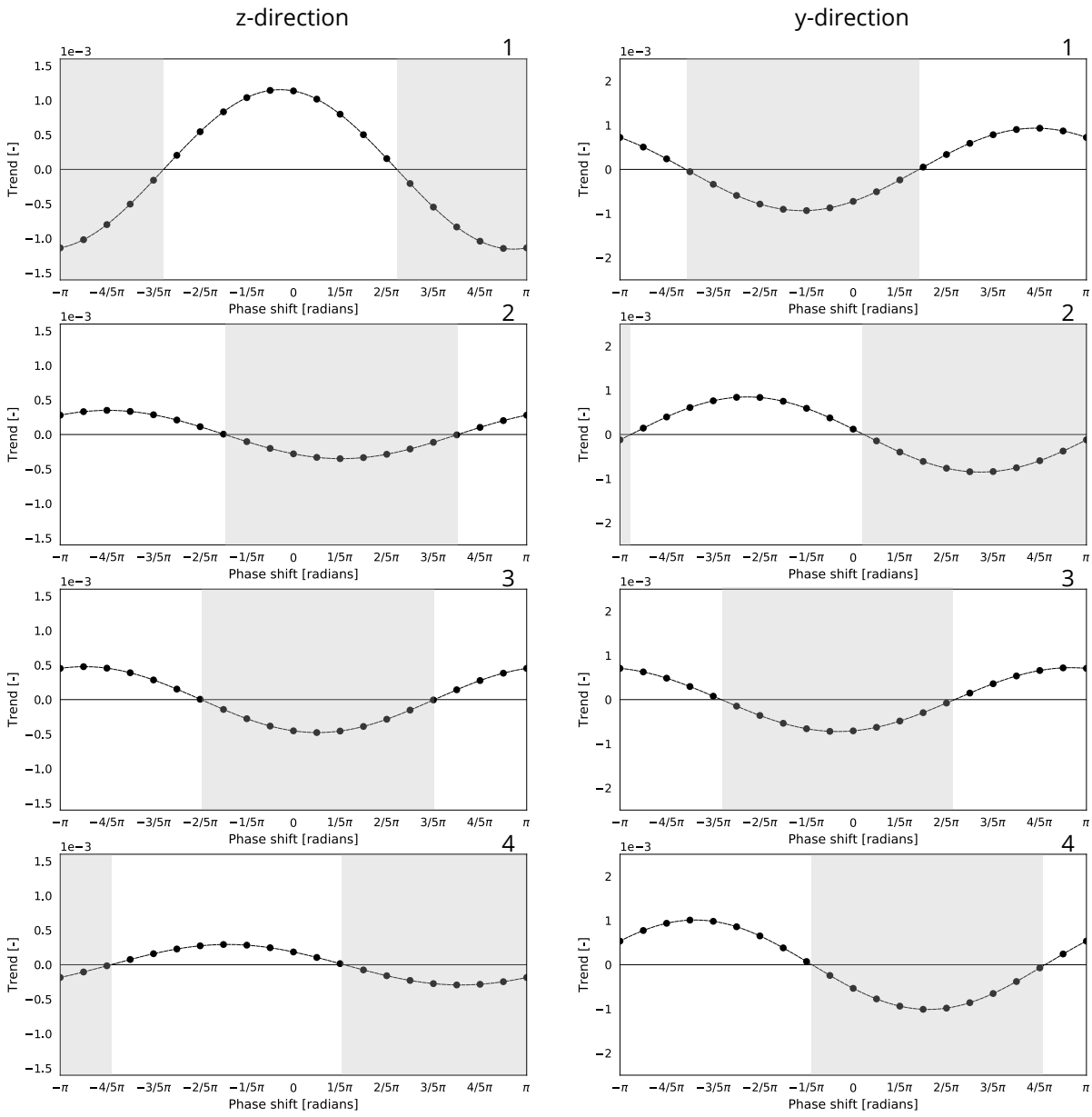

Required shift for signal 1-4

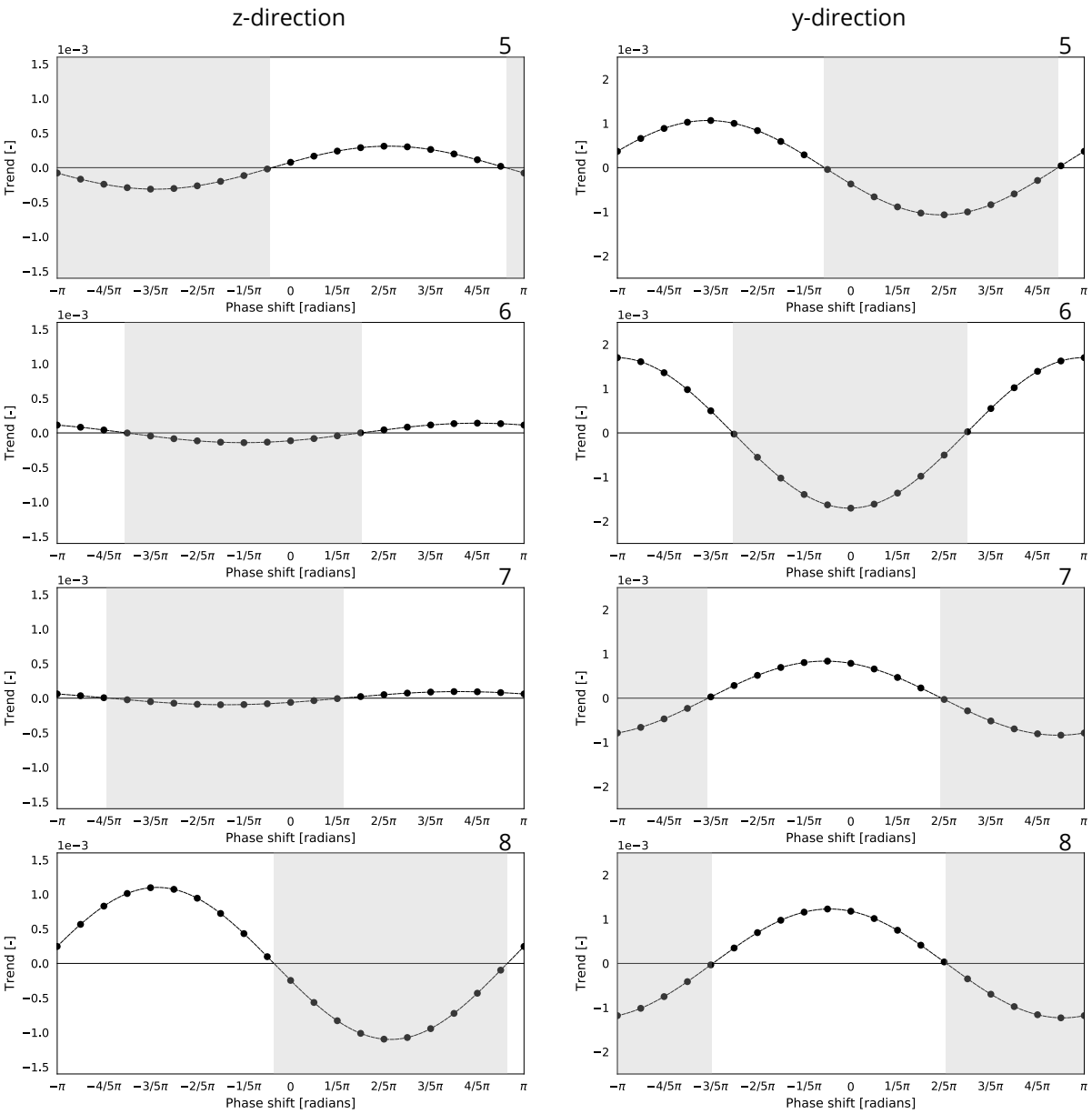

Required shift for signal 5-8

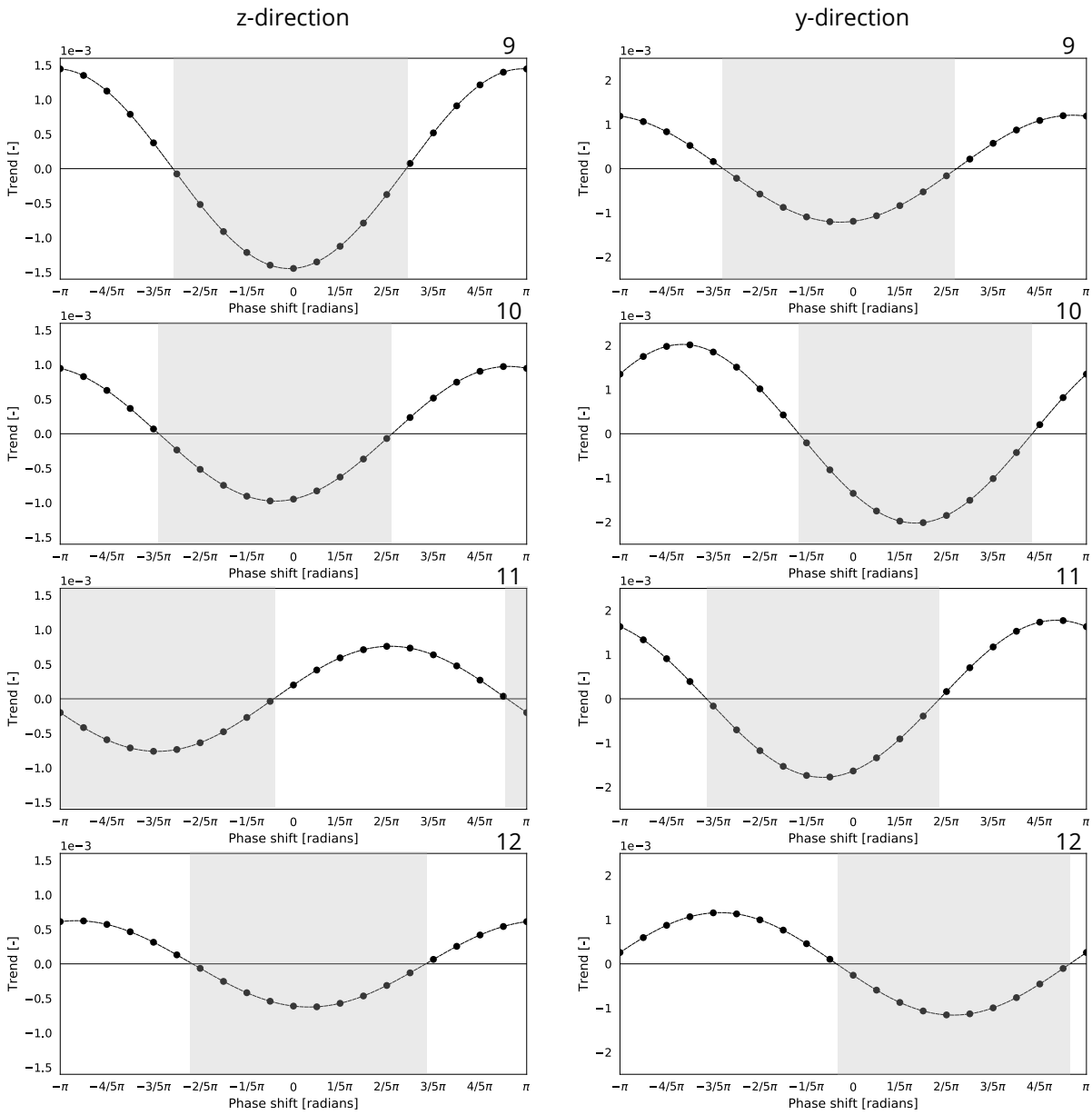

Required shift for signal 9-12

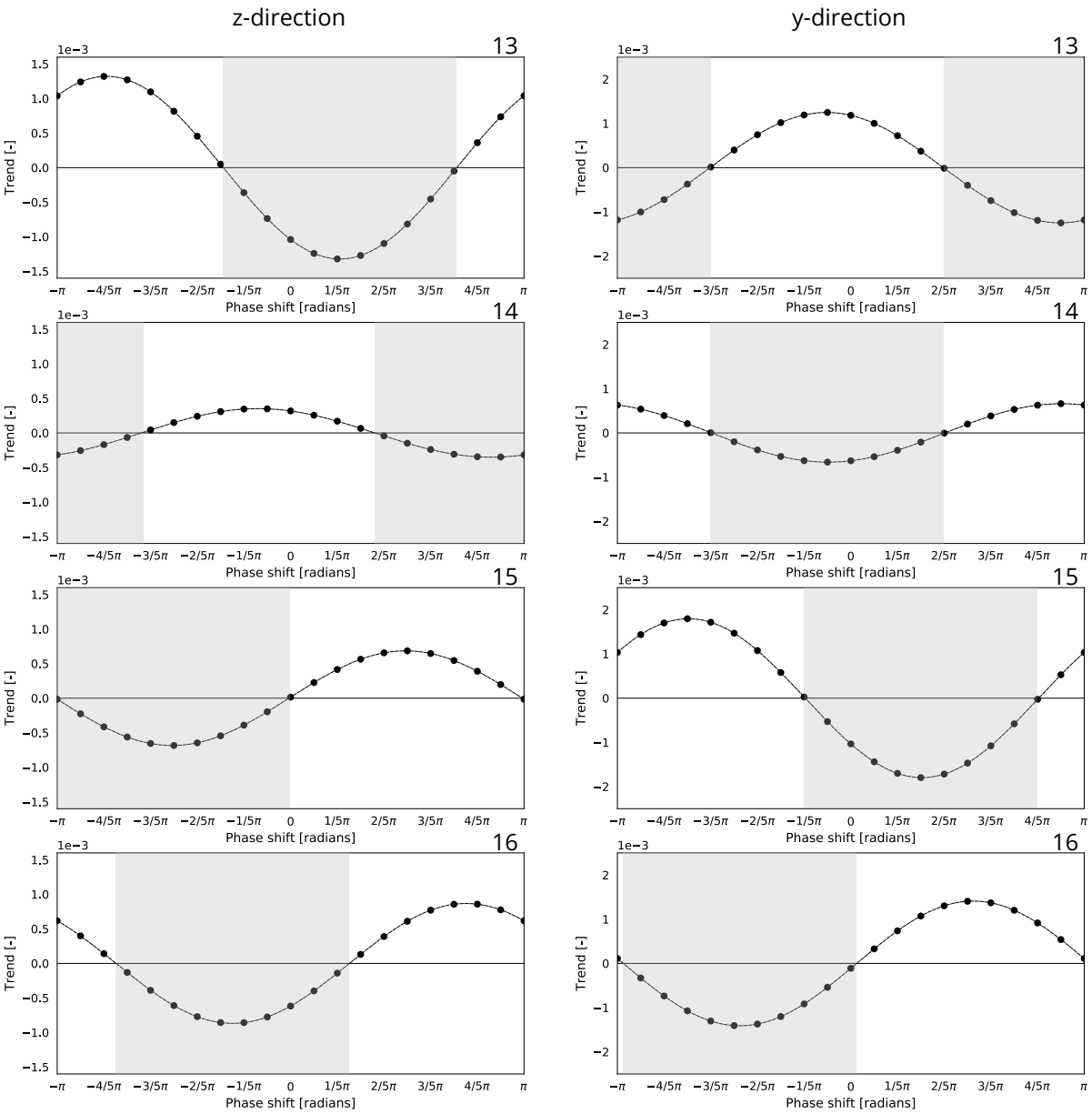

Required shift for signal 13-16

H

Phase observations

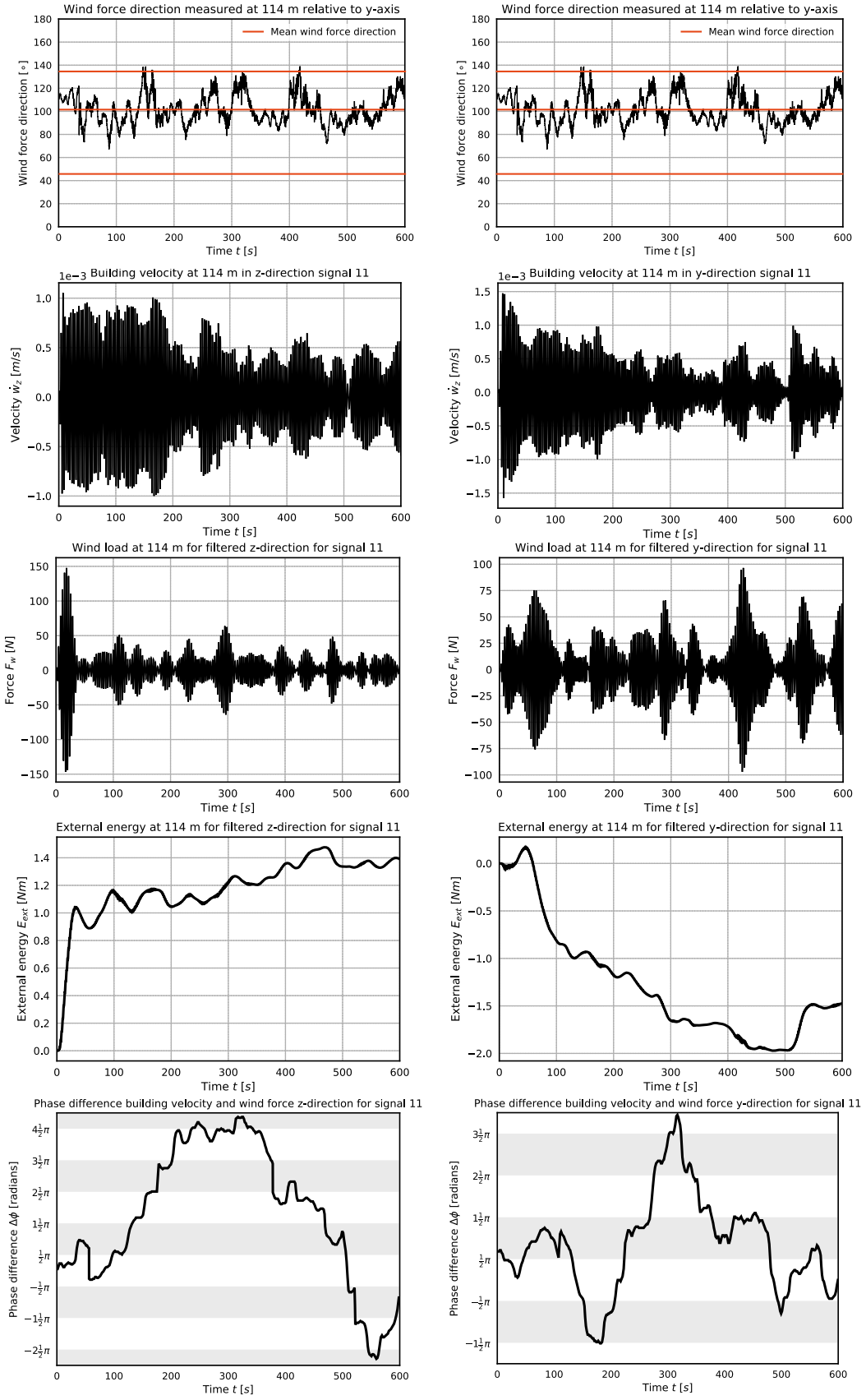

Figure H.1: Comparing the wind force direction, building velocity, wind force magnitude, and external energy with the phase difference between building velocity and wind force

Cross correlation function for time delay

The correlation function of two stationary random processes is found through:

$$\begin{aligned} R_{xx}(\tau) &= E[x(t)x(t+\tau)] \\ R_{yy}(\tau) &= E[y(t)y(t+\tau)] \\ R_{xy}(\tau) &= E[x(t)y(t+\tau)] \end{aligned} \tag{I.1}$$

R_{xx} and R_{yy} are the autocorrelation functions and R_{xy} is the cross correlation function. Now consider two signals of which signal $x(t)$ is transmitted to signal $y(t)$ through:

$$y(t) = \alpha x(t-\tau_0) + n(t) \tag{I.2}$$

Both $x(t)$ and $y(t)$ are zero mean value random stationary signals. In eq. (I.2), α is a constant attenuation factor, which changes the amplitude. The constant time delay is represented by τ_0 and n(t) represents uncorrelated zero mean value noise. The cross correlation for these signals is given by (Bendat and Piersol, 2010):

$$\begin{aligned} R_{xy}(\tau) &= E[x(t)y(t+\tau)] \\ &= E[x(t)\left(\alpha x(t+\tau-\tau_0) + n(t+\tau)\right)] \\ &= \alpha E[x(t)x(t+\tau-\tau_0)] \\ &= \alpha R_{xx}(\tau-\tau_0) \end{aligned} \tag{I.3}$$

The cross correlation function R_{xy} is the autocorrelation function R_{xx} displaced by the time delay τ_0 and scaled through the attenuation factor α. The peak of this cross correlation function occurs at τ_0. By finding the location fo the peak of the cross correlation function, it is possible to find the time delay between the two signals. The peak value of the cross correlation function is given by:

$$R_{xy}(\tau_0) = \alpha R_{xx}(0) = \alpha\sigma_x^2 \tag{I.4}$$

J

Dynamic response of pressure measuring systems

Berg and Tijdeman (Berg and Tijdeman, 1965) introduced a method to correct for the deviating pressure measurements, which is very commonly used and is further discussed in appendix J. In this method, the magnitude ratio is expressed as follows:

$$\frac{P_L(\omega)}{P_0(\omega)} = \frac{1}{\cosh\left[\omega\Gamma_p(L/c)\right] + V\left(\omega\Gamma_p/A_c c\right)\sinh\left[\omega\Gamma_p(L/c)\right]} \tag{J.1}$$

It depends on the tube length L, the velocity of sound c, the wave propagation factor Γ_p, the cross-sectional area of the tubes A_c, and naturally the frequency ω.

The time lag was expressed first by Lamb (Lamb, 1957), and then by Whitmore and Fox (Whitmore and Fox, 2009) using eq. (J.2). The equation depends on the polytropic exponent ξ, which is explained in the work of Whitmore (Whitmore and Fox, 2009). This polytropic exponent can be taken as 1.0 when no temperature change is expected, and when an expression of the polytropic exponent independent of time is used, it is equal to the ratio of specific heats γ (Whitmore and Fox, 2009). Aside from the polytropic exponent, the time lag depends on the dynamic viscosity of the fluid μ, the tube diameter D, the incoming pressure P_0, the volume of the pressure transducer V, the length of the tube L, and the cross-sectional area of the tube A_c.

$$\tau = \frac{128}{\xi}\frac{\mu L}{\pi D^4 P_0}\left(V + \frac{L\cdot A_c}{2}\right) \tag{J.2}$$

Most of the parameters in this expression are independent of time, and through the polytropic exponent ξ this expression is dependent on frequency. However, the expression is dependent on P_0, which is the incoming pressure. This indicates that the time lag does not only depend on the pressure frequency, but also on the pressure magnitude.

K

New Orleans building mass

This appendix shows the loads as assumed in the design of the New Orleans tower. These loads are used in the report to provide a best estimate for the building mass density, a lower bound and an upper bound.

K.1. Floors

In total, the New Orleans tower has 47 floor. Two of these are below the ground floor and offer parking place, floor 0 is the ground floor. Above the ground floor the 1st floor offers storage space for bikes and a shop, the 2nd floor functions as an installation floor and the 3rd floor offers further storage space. Above this, floors 4 to 44 have a residential function and the 45th floor is the roof of the tower. Based on the functionality of each floor, a different flooring system, and different variable loads are assumed. Besides this, a combination factor ψ_0 is provided. This factor is used when considering the total vertical load of the tower, it takes into account the fact that the maximum variable load will never take place on all floors at the same time. It is customary to use a psi-factor of 0.4 for residential buildings. When combining multiple floors, at least one floor variable load should be applied without combination factor. This should be the most heavily loaded floor in terms of variable load.

Floors 4 to 45: Residential

By far the largest number of floors of the tower have a residential function. These floors are made of 300 mm thick in situ poured concrete, the resulting structural load and additional permanent and variable loads are shown in table K.1. The combination factor for these floors is $\psi_0 = 0.4$.

	Structural	Permanent	Variable
In situ poured concrete floor (d=300mm)	7.5		
Suspended screed floor (d=20-60 mm)		1.2	
Non-structural walls		1.2	
Variable			1.75

Table K.1: Structural, permanent and variable residential floor loads in kN/m^2 used in the design

Floor 3: Storage

The third floors offers storage spaces for the building residents, which results in larger variable loads and additional ceiling and tubing. The loads assumed for this floor are given in table K.2 and the combination factor for this floor is given as $\psi_0 = 0.25$.

	Structural	Permanent	Variable
In situ poured concrete floor (d=300mm)	7.5		
Suspended screed floor (d=20-60 mm)		1.2	
Non-structural walls		1.2	
Ceiling and tubing		0.5	
Variable			5.0

Table K.2: Structural, permanent and variable storage floor loads in kN/m^2 used in the design

Floor 2: Installations

The 2nd floor of the New Orleans tower is the installation floor. Besides the larger variable load for the installations, the structural floor is 350 mm thick instead of 300 mm thick. The loads are given in table K.3, the combination factor for this floor is $\psi_0 = 1.00$.

	Structural	Permanent	Variable
In situ poured concrete floor (d=350mm)	8.8		
Suspended screed floor (d=60 mm)		1.2	
Variable			5.0

Table K.3: Structural, permanent and variable installation floor loads in kN/m^2 used in the design

Floor 1: Storage

The 1st floor of the New Orleans tower has a shop and storage for bikes, again resulting in a different loading scheme as is shown in table K.4. The combination factor for this floor is the same as for the 3rd floor storage, namely $\psi_0 = 0.25$.

	Structural	Permanent	Variable
Concrete hollow core slabs (d=260mm)	3.8		
Floor finishing		1.2	
Ceiling and tubing		0.5	
Concrete topping (d=70 mm)		1.75	
Variable			5.0

Table K.4: Structural, permanent and variable bike storage floor loads in kN/m^2 used in the design

Floor 0: Entrance

The ground floor is the entrance floor and a much larger variable load was assumed for this floor as is shown in table K.5. The combination factor is given by $\psi_0 = 0.25$.

	Structural	Permanent	Variable
In situ poured concrete floor (d=450mm)	11.25		
Suspended foamed concrete floor (d=370mm)		4.44	
Concrete topping (d=50 mm)		1.00	
Tubing		0.5	
Variable			10.0

Table K.5: Structural, permanent and variable ground floor loads in kN/m^2 used in the design

Floor -1 to -2: Parking

Below the ground floor, two levels of parking floors are present. The loading for these floors are given in table K.6. Below the bottom parking floor, the foundation blocks to introduce the column loads to the foundation piles are present. The combination factors for these floors is $\psi_0 = 0.70$.

	Structural load	Permanent load	Variable load
In situ poured concrete floor (d=310mm)	7.75		
Tubing		0.5	
Variable			2.0

Table K.6: Structural, permanent and variable parking floor loads in kN/m^2 used in the design

K.2. Walls

The structural walls present in the New Orleans tower are presented in fig. L.1. The walls are numbered from 1 to 10, the core walls are given in purple, while the frame/outrigger walls are given in orange. For the walls the concrete B65 or C53/65 was used which, according to the design, has a mass density of 2,500 kg/m^3.

	b $[m]$	h $[m]$	A $[m^2]$	N	Distributed mass $[kg/m]$
1	0.300	27.860	8.358	2	41,790
2	0.300	9.530	2.859	4	28,590
3	0.300	5.155	1.547	2	7,735
4	0.300	3.495	1.049	2	5,245
5	0.300	3.195	0.959	2	4,795
6	0.300	1.095	0.329	2	1,645
7	1.295	0.300	0.389	1	973
8	10.595	0.300	3.179	1	7,948
9	1.995	0.300	0.599	1	1,498
10	9.895	0.300	2.969	1	7,423
Total					107,642

Table K.7: Structural wall load used in the design

K.3. Facade

Besides the floors, finishing and structural walls, the facade will contribute to the building mass. The facade is made up of roughly two elements, on the inside concrete blocks are placed and these are separated by a cavity from natural stone cladding on the outside of the building.

	Permanent $[kN/m^2]$	Permanent $[kg/m^2]$	l $[m]$	N	Distributed mass $[kg/m]$
Concrete block (d=150 mm)	3.0	305.8	29	4	35,474
Natural stone cladding (d= 40mm)	1.1	112.1	29	4	13,007
Total					48,481

Table K.8: Permanent facade load in kN/m^2 used in the design

L

New Orleans building stiffness

This appendix discusses the building stiffness due to the structural system which will be used in this report. The building stiffness is either gathered directly from the design calculations, or calculated manually based on the building second moment of area and the elastic modulus.

L.1. Design stiffness

In the design, the stiffness of the building was found using the deformations of the FEM model and knowledge on the load acting on the model. The static stiffness was estimated to be $2.43 \times 10^{13}\ Nm^2$ and the estimate of the dynamic stiffness from the dynamic design calculations is $1.89 \times 10^{13}\ Nm^2$.

L.2. Second moment of area

The structural elements which may be used to calculate the second moment of area of the floor plan of the New Orleans tower are shown in fig. L.1. Indicated in purple are the elements that are part of the stability core, and indicated in orange are the walls that act as outrigger in one direction and frame action in the other direction. The second moment of area will be computed for the core and the walls separately.The black rectangle inside the stability core is assumed not to contribute to the building stiffness, since this is a prefab concrete elevator shaft, which is closer to the axes and has a smaller thickness than the outer core.

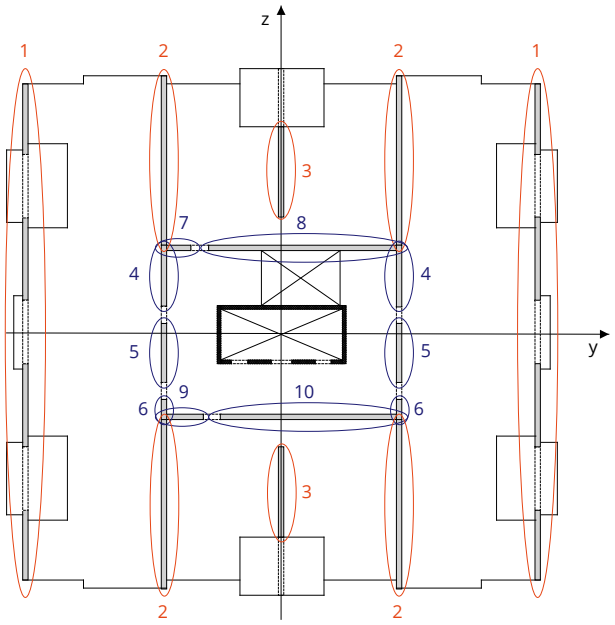

Figure L.1: Cross section New Orleans and numbered structural walls

L.2.1. Core

When computing the second moment of area of the core in fig. L.1, the openings in the core are assumed to be present over the entire building height. Therefore, any contribution of the lintels is omitted. The core is subdivided in walls 4-10. For these walls the stiffness in y- and z-direction can be simply calculated using $1/12bh^3$ and the Steiner rule.

$$I = \frac{1}{12}bh^3 + bhd^2 \tag{L.1}$$

First, the second moment of area around the y-axis is calculated in table L.1, this second moment of area is referred to as $I_{yy,core}$.

	N	b $[m]$	h $[m]$	d_z $[m]$	$\frac{1}{12}bh^3$ $[m^4]$	bhd^2 $[m^4]$	$I_{yy,core}$ $[m^4]$
Wall 4	2	0.300	3.495	3.153	1.067	10.420	22.975
Wall 5	2	0.300	3.195	-1.198	0.815	1.374	4.380
Wall 6	2	0.300	1.095	-4.353	0.033	6.223	12.512
Wall 7	1	1.295	0.300	4.750	0.003	8.766	8.768
Wall 8	1	10.595	0.300	4.750	0.024	71.715	71.739
Wall 9	1	1.995	0.300	-4.750	0.004	13.504	13.508
Wall 10	1	9.895	0.300	-4.750	0.022	66.977	66.999
Total							200.881

Table L.1: Second moment of area in y-direction for the stability core

For the same walls the second moment of area around the z-axis is calculated in table L.2. This is referred to as $I_{zz,core}$.

	N	b $[m]$	h $[m]$	d_y $[m]$	$\frac{1}{12}bh^3$ $[m^4]$	bhd^2 $[m^4]$	$I_{zz,core}$ $[m^4]$
Wall 4	2	3.495	0.300	+/- 6.600	0.008	45.673	91.361
Wall 5	2	3.195	0.300	+/- 6.600	0.007	41.752	83.519
Wall 6	2	1.095	0.300	+/- 6.600	0.002	14.309	28.624
Wall 7	1	0.300	1.295	-5.803	0.054	13.080	13.135
Wall 8	1	0.300	10.595	1.453	29.733	6.706	36.439
Wall 9	1	0.300	1.995	-5.453	0.199	17.793	17.992
Wall 10	1	0.300	9.895	1.803	24.221	9.645	33.865
Total							304.935

Table L.2: Second moment of area in z-direction for the stability core

The cross section of a building might also have a cross moment of area I_{yz}.A cross moment of area only exists if the area in the positive quadrants (quadrant I and III) is not the same as the area in the negative quadrants (quadrant II and IV). When considering the openings in the core, which is the approach here, this results in a cross moment of area for the New Orleans tower.

	N	b $[m]$	h $[m]$	d_y $[m]$	d_z $[m]$	bhd_yd_z $[m^4]$	I_{yz} $[m^4]$
Wall 4	2	0.300	3.495	3.153	+/- 6.600	+/-21.816	0.000
Wall 5	2	0.300	3.195	-1.198	+/- 6.600	+/-7.576	0.000
Wall 6	2	0.300	1.095	-4.353	+/- 6.600	+/-9.437	0.000
Wall 7	1	0.300	1.295	4.750	-5.803	-10.708	-10.708
Wall 8	1	0.300	10.595	4.750	1.453	21.930	21.930
Wall 9	1	0.300	1.995	-4.750	-5.453	15.501	15.501
Wall 10	1	0.300	9.895	-4.750	1.803	-25.416	-25.416
Total							1.307

Table L.3: Cross moment of area for the stability core

L.2.2. Walls

Besides the core, the walls in the structure provide stiffness. Also for these walls it is possible to compute the second moment of area in y- and z-direction using eq. (L.1). Due to the symmetry of these walls and their openings, they will not provide any cross second moment of area. For these walls the openings are assumed closed over the entire building height. The second moment of area in z-direction, indicated as I_{yy} is presented in table L.4,

	N	b $[m]$	h $[m]$	d_z $[m]$	$\frac{1}{12}bh^3$ $[m^4]$	bhd^2 $[m^4]$	I_{yy} $[m^4]$
Wall 1	2	0.300	27.860	0.000	540.609	0.000	1081.218
Wall 2	4	0.300	9.530	9.515	21.638	258.840	1121.913
Wall 3	2	0.300	5.155	9.003	3.425	125.336	257.522
Total							2460.653

Table L.4: Second moment of area in y-direction

The second moment of area in y-direction, indicated as I_{zz} is presented in table L.5.

	N	b $[m]$	h $[m]$	d_y $[m]$	$\frac{1}{12}bh^3$ $[m^4]$	bhd^2 $[m^4]$	I_{zz} $[m^4]$
Wall 1	2	27.860	0.300	14.400	0.063	1733.115	3466.355
Wall 2	4	9.530	0.300	6.600	0.021	124.538	498.238
Wall 3	2	5.155	0.300	0.000	0.012	0.000	0.023
Total							3964.616

Table L.5: Second moment of area in z-direction

L.3. Elastic modulus

The elastic modulus is a material property, it describes the relation between stress and strain. The material used for the elements that contribute to the building stiffness, the walls, is concrete B65. This is an old concrete label and corresponds to the current label of C53/65. It is a high-strength or high-performance concrete. The elastic moduli applied in the design for the New Orleans tower are shown in table L.6, not only for the walls but for all structural elements. The moduli presented here from the design are based on the internal forces, but in the model more conservative moduli are applied.

	Calculated E_{ULS} $[N/mm^2]$	Conservative E_{ULS} $[N/mm^2]$	Calculated $E_{SLS-short}$ $[N/mm^2]$	Conservative $E_{SLS-short}$ $[N/mm^2]$
Lintels	22,000	13,000	37,000	37,000
Core lintels	22,000	15,000	34,000	34,000
Floors	15,000	12,000	38,000	38,000
Walls	21,000	19,000	37,000	37,000
Core walls	21,000	21,000	37,000	37,000
Steel columns	210,000	210,000	210,000	210,000
Foundation blocks (d=2500mm)	8,500	8,500	13,000	13,000
Foundation blocks (d=600mm)	8,000	6,000	10,000	10,000

Table L.6: Elastic moduli used in the design of the New Orleans tower

M

Cone model

This chapter will explain the cone model. This model is one of the methods used to find the SSI rotational and translational stiffness. The intelligible explanation of the application of this model of TNO (Bronkhorst et al., 2018) was used to write this chapter. In the Cone model, the foundation is modelled as a flat disk on a semi-infinite elastic body, also called a half-space. This elastic body has certain properties such as mass density ρ_s, elastic modulus E, shear modulus G and Poisson's ratio ν. The elastic modulus and shear modulus are often used to compute another property, the shear wave speed V_s and the compression wave speed V_p as shown in eq. (M.1). These wave speeds provide information about the propagation of waves in the elastic half-space.

$$\begin{aligned} V_s &= \sqrt{\frac{G}{\rho_s}} \\ V_p &= \sqrt{\frac{E}{\rho_s}} \end{aligned} \tag{M.1}$$

Since the elastic modulus E and the shear modulus G can be related to one another through the Poisson's ratio, the two wave speeds can also be related to one another using the Poisson's ratio using eq. (M.2).

$$V_p = V_s \sqrt{\frac{2(1-\nu)}{(1-2\nu)}} \tag{M.2}$$

Since the foundation is modelled as a flat disk, it is first of importance to translate the usual rectangular foundation shape to an equivalent radius as shown in fig. M.1:

$$r_0 = \sqrt{\frac{BL}{\pi}} \tag{M.3}$$

In this equation B is the dimension of the foundation in one direction and L is the dimension of the foundation in the perpendicular direction. The presence of piles for the foundation is not considered in this model. The moment of inertia for the foundation can be found using eq. (M.4).

$$I_0 = \frac{\pi r_0^4}{4} \tag{M.4}$$

The opening angle of the cone depends on the dimension of the foundation disk r_0 and the Poisson's ratio ν of the soil. This opening angle is expressed using an apex height of the cone above the flat disk as shown in fig. M.1. The apex height is different depending on whether one is interested in translational soil stiffness and soil damping or the rotational, or rocking, soil stiffness and soil damping. The apex heights are given in eq. (M.5) and respectively eq. (M.6).

$$z_{0,t} = \frac{1}{32} \frac{7-8\nu}{1-\nu} \pi r_0 \tag{M.5}$$

$$z_{0,\theta} = \frac{9}{128} \frac{3-4\nu}{1-\nu} \frac{2(1-\nu)}{1-2\nu} \pi r_0 \tag{M.6}$$

Finally, the translational and rotational soil stiffness is given through:

$$K_t = \frac{2\rho_s V_s^2 \pi r_0^2}{z_{0,t}} \tag{M.7}$$

$$K_\theta = \frac{2 \cdot 3\rho_s V_p^2 I_0}{z_{0,\theta}} \tag{M.8}$$

The damping values can also be found using the same soil properties as shown in eq. (M.9) and eq. (M.9). However, this model does not account for material damping in the soil, it considers radiation damping only.

$$C_t = \rho_s V_s \pi r_0^2 \tag{M.9}$$

$$C_\theta = \rho_s V_p I_0 \tag{M.10}$$

If one is interested in the soil damping ratio rather than damping values, it is necessary to know the flexible base radial natural frequency $\tilde{\omega_n}$. The damping ratios can then be found using:

$$\zeta_t = \frac{\tilde{\omega} C_t}{2K_t} \tag{M.11}$$

$$\zeta_\theta = \frac{\tilde{\omega} C_\theta}{2K_\theta} \tag{M.12}$$

This model is based on a disk on an elastic half-space. As mentioned before, it does not consider piles in case of a pile foundation. In case of a pile foundation, the soil under the foundation plate is often layered soil with different properties, while the Cone model as explained here only considers one type of soil. In the research of TNO, only the bottom soil layer was considered for the calculation of the soil stiffness and damping properties (Bronkhorst et al., 2018). This can be justified by the fact that the piles reach to this deepest soil layer exactly to obtain the bearing strength from this layer. The soft layer in between could result in slightly larger stiffness and damping values.

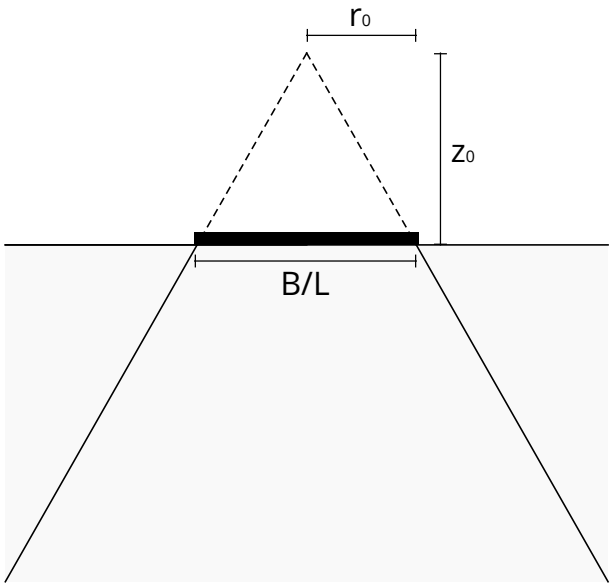

Figure M.1: Cone model

N

Shear wave velocity

In order to apply the cone model from appendix M, it is required to know the shear wave speed or the shear modulus of the soil. The first, the shear wave speed V_S can be derived from data obtained from a Cone Penetration Test (CPT). These tests are often performed before construction of a new structure and the data is freely available at DINOloket for the whole Netherlands. To find the shear wave speed, the equations by Robertson (Amoroso, 2013, Bronkhorst et al., 2018, Robertson, 1990) can be used. The required information for these equations are the cone resistance q_c, the sleeve friction f_s, soil density ρ_s and their corresponding depth d. If available, the water stress is can also be used. If not available, this property is derived from:

$$\sigma_w = 9.81 \rho_w d \tag{N.1}$$

In this equation ρ_w is the mass density of water, which at a temperature between 0 and 15 degC is approximately 1000 kg/m^3. Similarly, the soil stress is found using the soil density:

$$\sigma_{vo} = 9.81 \rho_s d \tag{N.2}$$

The effective vertical stress is given as the difference between the water and soil vertical stress:

$$\sigma'_{vo} = \sigma_{vo} - \sigma_w \tag{N.3}$$

Following the following path, the shear wave speed is obtained. First, the normalised cone resistance, Q_t is computed:

$$Q_t = \frac{q_c - \sigma_{vo}}{\sigma'_{vo}} \tag{N.4}$$

Then the normalised friction ratio F_r is computed:

$$F_r = \frac{f_s}{q_c - \sigma_{vo}} \cdot 100\% \tag{N.5}$$

Together, the normalised cone resistance Q_t and the normalised friction ratio F_r give the so called soil type index I_c:

$$I_c = \sqrt{\left(3.47 - \log(Q_t)\right)^2 + \left(\log(F_r) + 1.22\right)^2} \tag{N.6}$$

Finally, the shear wave velocity is found using eq. (N.7).

$$V_s = \sqrt{\sigma_{vs} \frac{q_c - \sigma_{vo}}{p_a}} \tag{N.7}$$

In this equation p_a is the atmospheric pressure, which is approximately 1×10^5 Pa. The factor σ_{vs} can be obtained using the soil type index I_c:

$$\sigma_{vs} = 10^{0.55 I_c + 1.68} \tag{N.8}$$

The shear wave speed is now given over the entire depth of the CPT.

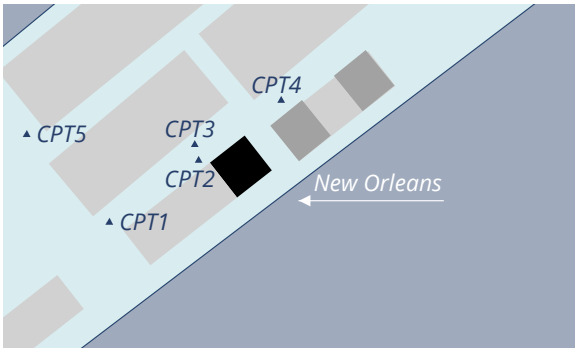

Figure N.1: Location of the CPTs

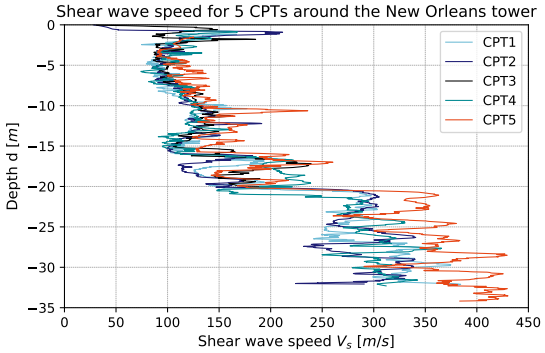

Figure N.2: Shear wave speed obtained from CPTs in fig. N.1

Figure N.1 shows the locations around the New Orleans tower where Cone Penetration Tests were performed. Using the information of these tests, the shear wave velocity of the soil was computed and is shown in fig. N.2. Quite a clear distinction can be made between two different soil layers, the first layer reaching from 0 to approximately -21 m containing clay and some silt and the second layer starting from -21 m down which consists of sand. For each layer and all the tests, the minimum, mean and maximum value of the shear wave velocity is given in table N.1.The deviations at the top are not taken into account.

	Layer 1 V_s $[m/s]$			Layer 2 V_s $[m/s]$		
	minimum	mean	maximum	minimum	mean	maximum
CPT1	74.75	122.50	196.09	241.61	302.53	384.30
CPT2	85.28	120.42	191.42	224.10	293.36	340.81
CPT3	86.23	136.81	239.34			
CPT4	74.12	134.90	238.84	249.80	300.19	365.73
CPT5	89.29	146.55	260.46	260.46	364.88	430.25

Table N.1: Shear wave velocity found for 5 CPTs

O

New Orleans foundation stiffness

This appendix provides the foundation stifness properties computed in three distinct ways; first the point support stiffness and the pile configuration from the design is used, second the values obtained by TNO from Dynapile (Bronkhorst et al., 2018) are presented, and finally stiffness properties are computed using the analytical cone model.

O.1. Design configuration

The design of the New Orleans tower considers the foundation stiffness through modelling the foundation piles as spring supports. The spring stiffness values are provided by a third party named Geomat. Both a vertical and a horizontal dynamic stiffness are provided and shown in table O.1. The vertical support stiffness is the stiffness in the longitudinal direction of the pile and the horizontal stiffness is the stiffness of the pile in lateral direction of the pile. Using the pile plan of the tower, a rotational soil stiffness may be computed. Using the total number of piles it is also possible to find the translational soil stiffness.

	Vertical	Horizontal
Pile stiffness [N/m]	196×10^6	5×10^6

Table O.1: Support dynamic stiffness from the design of the New Orleans tower

The rotational stiffness is found using the vertical stiffness of the piles and their distance to the centre of rotation of the foundation. From this distance the relative deflection per pile can be computed and the total moment due to the forces of these piles. The rotational stiffness follows from this moment and the assumed angle through eq. (O.1).

$$K_\theta = \frac{M}{\phi} \tag{O.1}$$

This calculation is done for the two directions separately and these are also subdivided in two, since it became clear that the foundation is not exactly symmetric. The differences, however, turned out to be very small.

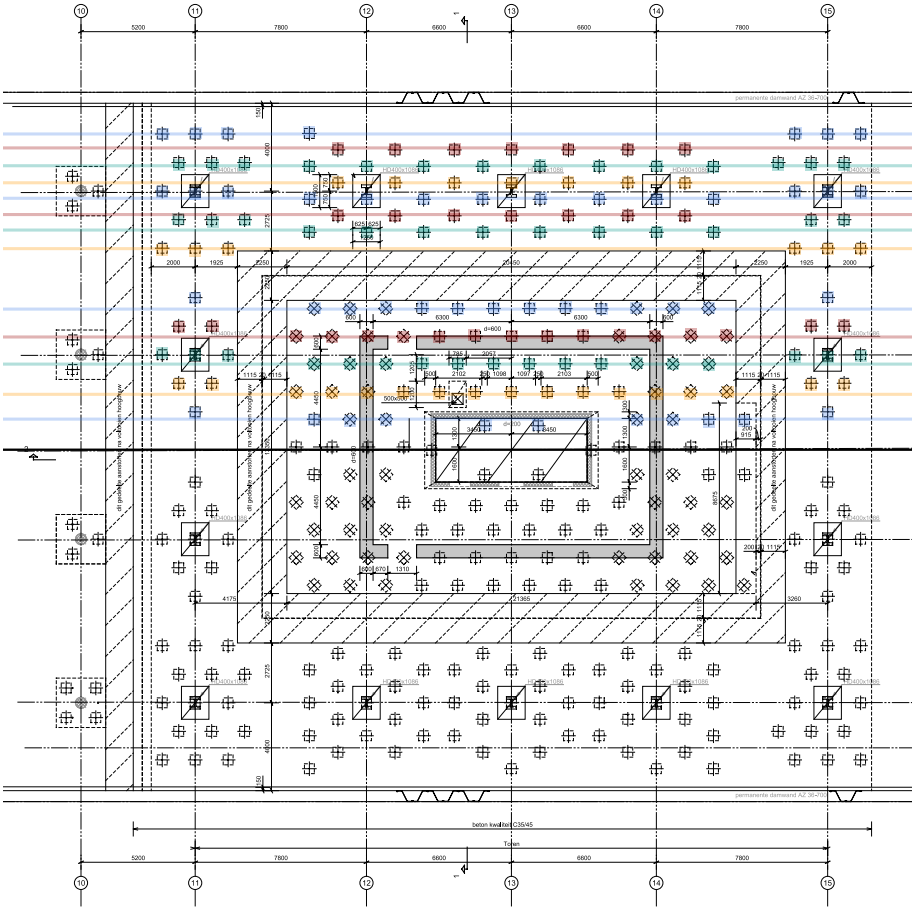

Figure O.1: Contribution positive side rotation stiffness around y-axis

Axis	N	Distance d [m]	Displacement u [m]	Force F [N]	Bending moment M [Nm]
0	10	0.00	0.00	0.00	0.00
1	11	1.42	0.10	2.11×10^{8}	3.00×10^{8}
2	17	2.60	0.18	5.95×10^{8}	1.54×10^{9}
3	18	4.02	0.28	9.75×10^{8}	3.92×10^{9}
4	17	5.19	0.36	1.19×10^{9}	6.17×10^{9}
5	14	6.51	0.45	1.23×10^{9}	7.99×10^{9}
6	6	9.21	0.63	7.45×10^{8}	6.86×10^{9}
7	14	10.10	0.69	1.91×10^{9}	1.92×10^{10}
8	7	10.84	0.75	1.02×10^{9}	1.11×10^{10}
9	14	11.56	0.79	2.18×10^{9}	2.52×10^{10}
10	7	12.30	0.85	1.16×10^{9}	1.43×10^{10}
11	14	13.05	0.90	2.46×10^{9}	3.21×10^{10}
12	7	13.90	0.96	1.31×10^{9}	1.82×10^{10}
13	7	14.54	1.00	1.37×10^{9}	2.00×10^{10}
Total					1.67×10^{11}

Table O.2: Contribution positive side rotation stiffness around y-axis

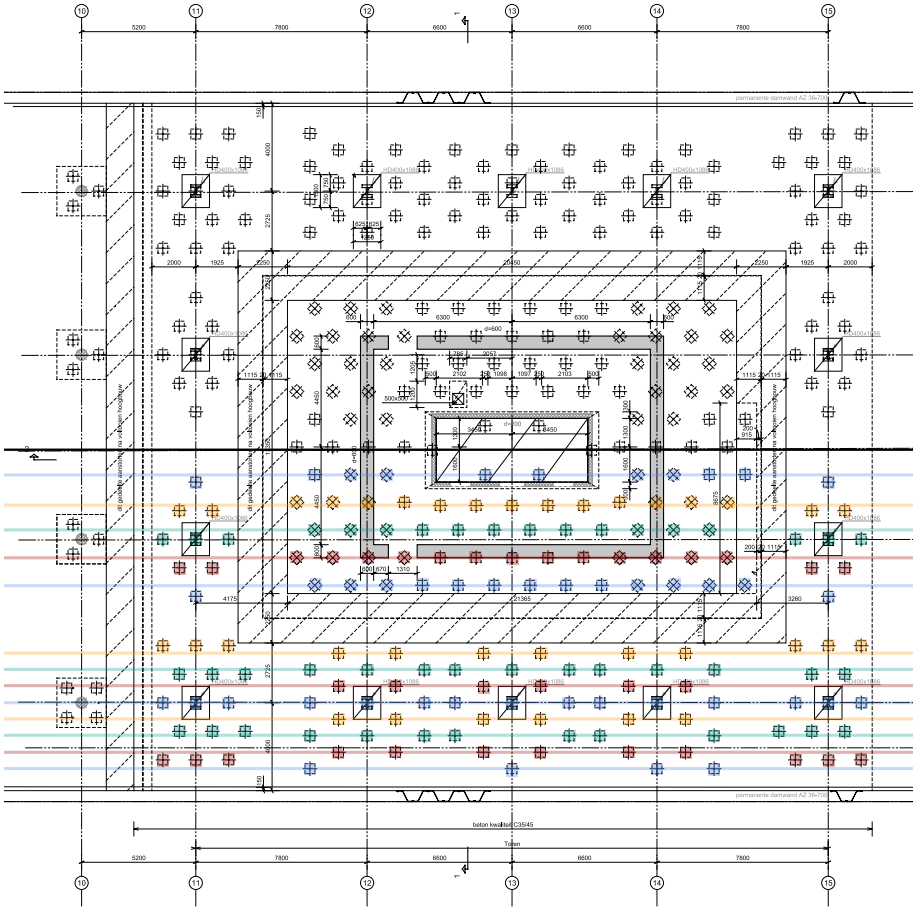

Figure O.2: Contribution negative side rotation stiffness around y-axis

Axis	N	Distance d [m]	Displacement u [m]	Force F [N]	Bending moment M [Nm]
0	0	0.00	0.00	0.00	0.00
1	11	1.14	0.08	1.67×10^{8}	1.91×10^{8}
2	17	2.52	0.17	5.74×10^{8}	1.45×10^{9}
3	18	3.68	0.25	8.86×10^{8}	3.26×10^{9}
4	17	4.98	0.34	1.13×10^{9}	5.64×10^{9}
5	15	6.22	0.42	1.25×10^{9}	7.77×10^{9}
6	12	9.33	0.64	1.50×10^{9}	1.40×10^{10}
7	14	10.13	0.69	1.90×10^{9}	1.92×10^{10}
8	6	10.88	0.74	8.73×10^{8}	9.50×10^{9}
9	15	11.63	0.79	2.33×10^{9}	2.71×10^{10}
10	6	12.37	0.84	9.93×10^{8}	1.23×10^{10}
11	13	13.16	0.90	2.29×10^{9}	3.01×10^{10}
12	12	13.94	0.95	2.24×10^{9}	3.12×10^{10}
13	4	14.65	1.00	7.84×10^{8}	1.15×10^{10}
Total					1.73×10^{11}

Table O.3: Contribution negative side rotation stiffness around y-axis

For the foundation rotational stiffness in z-direction and around the y-axis this results in the following stiffness:

$$K_{\theta_z} = \frac{1.67 \times 10^{11}}{1/14.54} + \frac{1.73 \times 10^{11}}{1/14.65} = 4.96 \times 10^{12} \text{ Nm/rad} \tag{O.2}$$

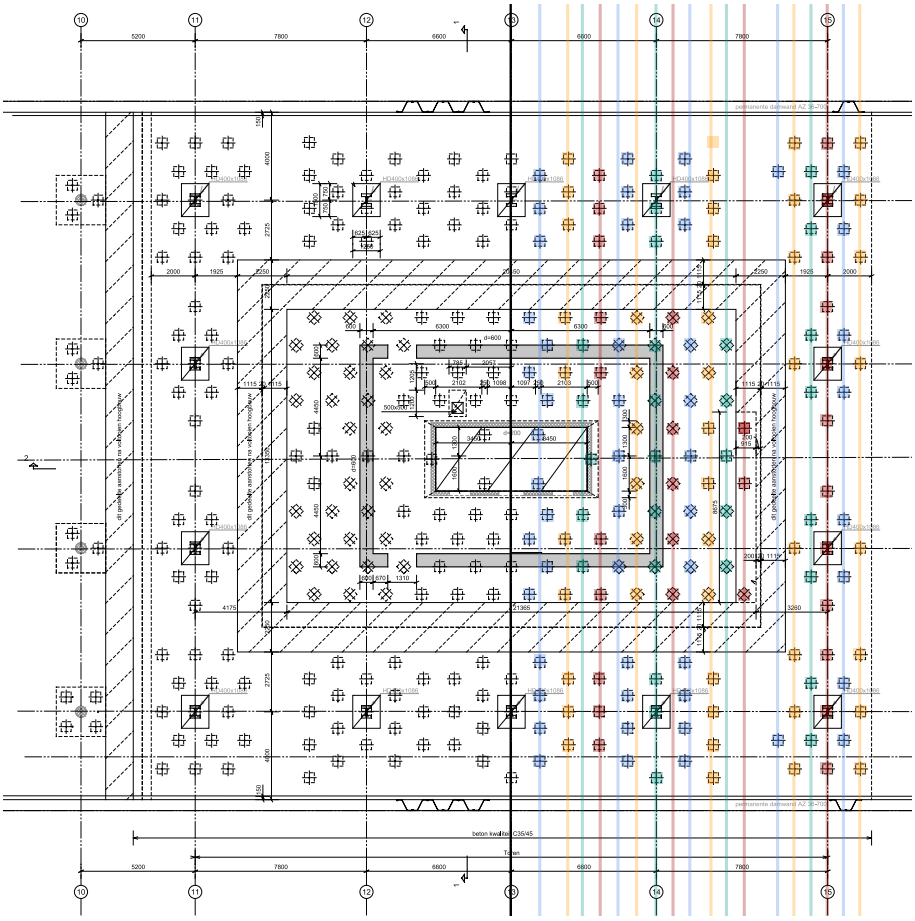

Figure O.3: Contribution positive side rotation stiffness around z-axis

Axis	N	Distance d [m]	Displacement u [m]	Force F [N]	Bending moment M [Nm]
0	10	0.00	0.00	0.00	0.00
1	17	1.32	0.08	2.75×10^{8}	3.64×10^{8}
2	10	2.61	0.16	3.20×10^{8}	8.36×10^{8}
3	5	3.29	0.21	2.01×10^{8}	6.62×10^{8}
4	10	4.11	0.26	5.03×10^{8}	2.06×10^{9}
5	12	4.92	0.31	7.23×10^{8}	3.56×10^{9}
6	6	5.78	0.36	4.24×10^{8}	2.45×10^{9}
7	11	6.67	0.42	8.97×10^{8}	5.98×10^{9}
8	6	7.45	0.47	5.47×10^{8}	4.07×10^{9}
9	12	8.24	0.51	1.21×10^{9}	9.97×10^{9}
10	14	9.19	0.57	1.57×10^{9}	1.45×10^{10}
11	5	9.20	0.62	6.06×10^{8}	6.00×10^{9}
12	3	10.72	0.67	3.94×10^{8}	4.22×10^{9}
13	2	12.25	0.76	3.00×10^{8}	3.67×10^{9}
14	8	13.00	0.81	1.27×10^{9}	1.65×10^{10}
15	8	13.78	0.86	1.35×10^{9}	1.86×10^{10}
16	12	14.52	0.91	2.13×10^{9}	3.10×10^{10}
17	8	15.27	0.95	1.49×10^{9}	2.28×10^{10}
18	8	16.02	1.00	1.57×10^{9}	2.51×10^{10}
Total					1.72×10^{11}

Table O.4: Contribution positive side rotation stiffness around z-axis

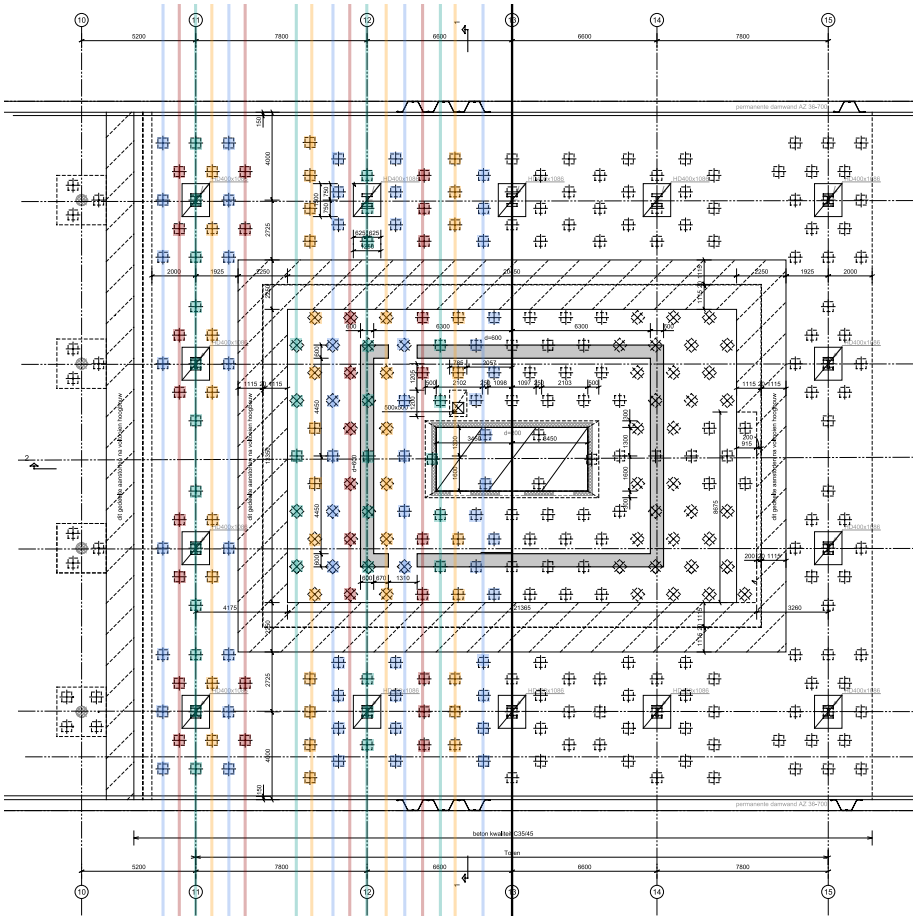

Figure O.4: Contribution negative side rotation stiffness around z-axis

Axis	N	Distance d [m]	Displacement u [m]	Force F [N]	Bending moment M [Nm]
0	0	0.00	0.00	0.00	0.00
1	17	1.32	0.08	2.75×10^{8}	3.64×10^{8}
2	10	2.61	0.16	3.20×10^{8}	8.36×10^{8}
3	5	3.29	0.21	2.01×10^{8}	6.62×10^{8}
4	10	4.11	0.26	5.03×10^{8}	2.06×10^{9}
5	12	4.92	0.31	7.23×10^{8}	3.56×10^{9}
6	6	5.78	0.36	4.24×10^{8}	2.45×10^{9}
7	11	6.67	0.42	8.97×10^{8}	5.98×10^{9}
8	6	7.45	0.47	5.47×10^{8}	4.07×10^{9}
9	12	8.24	0.51	1.21×10^{9}	9.97×10^{9}
10	14	9.19	0.57	1.57×10^{9}	1.45×10^{10}
11	5	9.90	0.62	6.06×10^{8}	6.00×10^{9}
12	4	12.25	0.76	6.00×10^{8}	7.34×10^{9}
13	8	13.00	0.81	1.27×10^{9}	1.65×10^{10}
14	8	13.78	0.86	1.35×10^{9}	1.86×10^{10}
15	12	14.52	0.91	2.13×10^{9}	3.10×10^{10}
16	8	15.27	0.95	1.49×10^{9}	2.28×10^{10}
17	8	16.02	1.00	1.57×10^{9}	2.51×10^{10}
Total					1.72×10^{11}

Table O.5: Contribution positive side rotation stiffness around z-axis

For the foundation rotational stiffness in y-direction and around the z-axis this results in the following

stiffness:

$$K_{\theta_y} = \frac{1.72 \times 10^{11}}{1/16.02} + \frac{1.72 \times 10^{11}}{1/16.02} = 5.51 \times 10^{12} \text{ Nm/rad} \tag{O.3}$$

The translation stiffness is found by multiplying the lateral stiffness of each pile with the number of piles present in the foundation under the tower:

$$K_y = K_z = 323 \cdot 5 \times 10^6 = 1.62 \times 10^9 \text{ N/m} \tag{O.4}$$

O.2. Dynapile

The work of TNO (Bronkhorst et al., 2018) also presents a calculation of the foundation properties using Dynapile. This is a software package that considers the configuration of the foundation piles and the soil properties. In the calculation by TNO two values are given for each property. The first is calculated without soil material damping and is indicated as Dynapile 0%. This means that in this model only soil radiation damping is included. The second is indicated as Dynapile 3% and includes 3% soil material damping. This only affects the damping values found.

	$K_{\theta_y} = K_{\theta_z}$ [Nm/rad]	$C_{\theta_y} = C_{\theta_z}$ [Nms/rad]	$K_y = K_z$ [N/m]	$C_y = C_z$ [Ns/m]
Dynapile 0%	5.33×10^{12}	2.59×10^{10}	3.65×10^9	8.41×10^5
Dynapile 3%	5.33×10^{12}	1.77×10^{11}	3.65×10^9	2.07×10^8

Table O.6: Summary of soil-structure stiffness from Dynapile 0% and Dynapile 3% (Bronkhorst et al., 2018)

O.3. Cone model

Another way to find the stiffness is by using the cone model (Wolf and Deeks, 2004). The model does not consider the pile configuration, but calculated the stiffness of the foundation based on a rigid disk on an elastic half-space. Required input are the foundation dimensions and the soil density, Poisson's ratio and shear wave velocity. The cone model is explained in appendix M and the shear wave velocity for the soil at the location in the New Orleans tower is given in appendix N. For each of the shear wave velocities found in table N.1 the stiffness can be computed.

For the second soil layer, which is made of sand, the Poisson's ratio of can take a value between 0.3 and 0.4 (Sharma et al., 1990) and the density of dense, saturated sand can be expected to be between 19.5 and 24 kN/m^3 according to JCSS (Baker and Calle, 2006) and between 17 and 23 kN/m^3 according to Bowles (Bowles, 1996). This results in an expectation of the density to be between 17 and 24 kN/m^3, which corresponds to a mass density between 1733 kg/m^3 and 2446 kg/m^3. The mass density of the soil layer measured with the CPT is 1955 kg/m^3. Based on these ranges of values for the shear wave velocity, Poisson's ratio and mass density, it is possible to calculate the largest, smallest and best estimate of the stiffness using the cone model:

	$K_{\theta_y} = K_{\theta_z}$ [Nm/rad]	K_y=K_z [N/m]
minimum	3.53×10^{12}	1.40×10^{10}
best estimate	8.18×10^{12}	3.25×10^{10}
maximum	2.99×10^{13}	7.85×10^{10}

Table O.7: Summary of soil-structure stiffness from the cone model for the second soil layer

The first soil layer, which is most likely not affecting the stiffness as much, is made of clay and silt. The Poisson's ratio for this layer can be between 0.3 and 0.5 (Sharma et al., 1990) and the density of saturated clay may be between around 18 and 24 kN/m^3 (Baker and Calle, 2006). This equal to a mass density between 1835 and 2446 kg/m^3. Together with the shear wave speed in appendix N, a similar table is constructed for the first soil layer:

	$K_{\theta_y} = K_{\theta_z}$ [Nm/rad]	K_y=K_z [N/m]
minimum	4.23×10^{11}	1.68×10^{9}
best estimate	1.74×10^{12}	6.50×10^{9}
maximum	8.78×10^{12}	3.01×10^{10}

Table O.8: Summary of soil-structure stiffness from the cone model for the first soil layer

Bibliography

S. Amoroso. Prediction of the shear wave velocity from cpt and dmt. *Advances in Soil Mechanics and Geotechnical Engineering*, 2(Proceedings of the 5th International Young Geotechnical Engineers' Conference):473–476, 2013. ISSN 2212-781X. doi: 10.3233/978-1-61499-297-4-473.

J. Baker and E. Calle. *JCSS Probabilistic Model Code, Section 3.7: Soil Properties*, 2006.

J. W. Baron Rayleigh Strutt. *The theory of sound*, volume II. Macmillan, second edition, 1896.

C. F. Beards. The damping of structural vibration by controlled interfacial slip in joints. *Journal of Vibration and Acoustics*, 105(3):369–373, jul 1983. doi: 10.1115/1.3269115.

J. S. Bendat and A. G. Piersol. *Random Data*. John Wiley & Sons, 4 edition, 2010. ISBN 978-0-470-24877-5.

H. Berg and H. Tijdeman. Theoretical and experimental results for the dynamic response of pressure measuring systems. *NLR report E238, Nat*, 1 1965.

R. E. Berg and T. S. Marshall. Wilberforce pendulum oscillations and normal modes. *American Journal of Physics*, 59(1):32–38, jan 1991. doi: 10.1119/1.16702.

J. M. Biggs. *Introduction to Structural Dynamics*. McGraw-Hill Book Company, 1964. ISBN 07-005255-7.

K. Y. Billah and R. H. Scanlan. Resonance, tacoma narrows bridge failure, and undergraduate physics textbooks. *American Journal of Physics*, 59(2):118–124, feb 1991. doi: 10.1119/1.16590.

R. D. Blevins. *Formulas for natural frequency and mode shape*. Krieger Pub Co, 1979. ISBN 9781575241845.

L. E. Bowles. *Foundation Analysis and Design*. McGrawl-hill, 1996.

G. Breeze. Wind tunnel investigation upon the coherence of pressure measurements taken around a tall building in open site terrain. *Journal of Wind Engineering and Industrial Aerodynamics*, 42(1-3):1151–1161, 1992.

R. Brincker and J. Rodrigues. Application of the random decrement technique in operational modal analysis. In *Proceedings of the 1st International Operational Modal Analysis Conference (IOMAC)*, page 22, 2005.

A. J. Bronkhorst, C. A. van Bentum, and S. S. Gómez. Wind-induced vibrations and damping in highrise buildings. Report R10644, TNO, 2018.

S. Butterworth. On the theory of filter amplifiers. *Experimental Wireless and the Wireless Engineer*, 7:536–541, 1930.

A. Campbell, J. Hanania, J. Jenden, and J. Donev. Law of conservation of energy, 2020. URL `https://energyeducation.ca/encyclopedia/Law_of_conservation_of_energy`.

X. Chen and A. Kareem. Coupled dynamic analysis and equivalent static wind loads on buildings with three-dimensional modes. *Journal of Structural Engineering*, 131(7):1071–1082, jul 2005. doi: 10.1061/(asce)0733-9445(2005)131:7(1071).

A. K. Chopra. *Dynamics of Structures*. Pearson, 3 edition, 2007. ISBN 0-13-156174-X.

C. Collette, S. Janssens, P. Fernandez-Carmona, K. Artoos, M. Guinchard, C. Hauviller, and A. Preumont. Review: Inertial sensors for low-frequency seismic vibration measurement. *Bulletin of the Seismological Society of America*, 102(4):1289–1300, aug 2012. doi: 10.1785/0120110223.

J. Counehan. Wind tunnel determination of the roughness length as a function of the fetch and the roughness density of three-dimensional roughness elements. *Atmospheric Environment (1967)*, 5(8):637–642, aug 1971. doi: 10.1016/0004-6981(71)90120-x.

A. G. Davenport. Th application of statistical concepts to the wind loading of structures. *Proceedings of the Institution of Civil Engineers*, 19(4):449–472, aug 1961. doi: 10.1680/iicep.1961.11304.

A.G. Davenport and P. Hill-Carroll. Damping in tall buildings: its variability and treatment in design. In *Building motion in wind*, pages 42–57. ASCE, 1986.

C. Dyrbye and S. O. Hansen. *Wind Loads on Structures*. Wiley, 1997. ISBN 978-0471956518.

B. R. Ellis. *An assessment of the accuracy of predicting the fundamental natural frequencies of buildings and the implications concerning the dynamic analysis of structures*, volume 69, pages 763–776. Institution of Civil Engineers, 1980. ISBN 1753-7789. doi: 10.1680/iicep.1980.2376.

B. R. Ellis. The significance of dynamic soil-structure interaction in tall buildings. *Proceedings of the Institution of Civil Engineers*, 81(2):221–242, jun 1986. doi: 10.1680/iicep.1986.601.

B. R. Ellis and A. J. Bougard. Dynamic testing and stiffness evaluation of a six-storey timber framed building during construction. *Engineering Structures*, 23(10):1232–1242, oct 2001. doi: 10.1016/s0141-0296(01)00033-5.

B. R. Ellis, R. A. Evans, A. P. Jeary, and B. E. Lee. The wind induced vibration of a tall building. In *Proceedings of the IAHR/IUTAM Symposium on Practical Experiences with Flow Induced Vibrations*, 1980.

B.R. Ellis. Full-scale measurements of the dynamic characteristics of buildings in the uk. *Journal of Wind Engineering and Industrial Aerodynamics*, 59(2-3):365–382, mar 1996. doi: 10.1016/0167-6105(96)00017-7.

S. Erwin, T. Kijewski-Correa, and S. W. Yoon. Full-scale verification of dynamic properties from short duration records. In *New Horizons and Better Practices*. American Society of Civil Engineers, oct 2007. doi: 10.1061/40946(248)39.

L. F. Fan, L. N. Y. Wong, and G. W. Ma. Experimental investigation and modeling of viscoelastic behavior of concrete. *Construction and Building Materials*, 48:814–821, 2013. doi: 10.1016/j.conbuildmat.2013.07.010.

C. P. W. Geurts. Wind-induced pressure fluctuations on building facades, 1997.

S. E. Gryning, E. Batchvarova, M. Quante, and V. Matthias. Evaluation of vertical profiles in mesoscale meteorological models based on observations. In Douw G. Steyn and Silvia Trini Castelli, editors, *Air Pollution Modeling and its Application XXI*, pages 499–503, Dordrecht, 2012. Springer Netherlands. ISBN 978-94-007-1359-8.

S. S. Gómez. *Energy flux method for identification of damping in high-rise buildings subject to wind*. Report, Delft University of Technology, 2019.

S. S. Gómez and A. V. Metrikine. The energy flow analysis as a tool for identification of damping in tall buildings subjected to wind: Contributions of the foundation and the building structure. *Journal of Vibration and Acoustics*, 141(1), 2019. ISSN 1048-9002 1528-8927. doi: 10.1115/1.4040975.

S. S. Gómez, C. P. W. Geurts, and A. V. Metrikine. On the importance of soil damping for tall buildings loaded by wind. *Engineering Structures*, 163:426–435, 2018. ISSN 01410296. doi: 10.1016/j.engstruct.2017.11.029.

R. I. Harris and D. M. Deaves. The structure of strong winds. In *Proc. CIRIA Conf. on Wind Engineering in the Eighties*, 1981.

N. A. Heckert, J. J. Filliben, C. M. Croarkin, B. Hembree, W. F. Guthrie, P. Tobias, and J. Prinz. *Handbook 151: NIST/SEMATECH e-Handbook of Statistical Methods*. 2002. doi: https://doi.org/10.18434/M32189A. URL `https://www.itl.nist.gov/div898/handbook/index.htm`.

J. Holmes. *Wind Loading of Structures*. Spon Press, jul 2001. doi: 10.4324/9780203301647.

U. Högström, H. Bergström, and H. Alexandersson. Turbulence characteristics in a near neutrally stratified urban atmosphere. *Boundary-Layer Meteorology*, 23(4):449–472, aug 1982. doi: 10.1007/bf00116272.

H. P. A. H. Irwin, K. R. Cooper, and R. Girard. Correction of distortion effects caused by tubing systems in measurements of fluctuating pressures. *Journal of Wind Engineering and Industrial Aerodynamics*, 5(1-2):93–107, oct 1979. doi: 10.1016/0167-6105(79)90026-6.

H. Ishizaki and N. Hatakeyama. Experimental and numerical studies on vibrations of buildings. *Proceedings of the second world conference on earthquake engineering*, 2:1263–1284, 1960.

A. P. Jeary. Damping in tall buildings - a mechanism and a predictor. *Earthquake Engineering & Structural Dynamics*, 14(5):733–750, 1986. doi: 10.1002/eqe.4290140505.

A. P. Jeary. The damping parameter as a descriptor of energy release in structures. In *Proceedings CD-ROM TI93-4, Structural Engineers World Congress*, 1998.

A. P. Jeary and B. R. Ellis, editors. *A study of the measured and predicted behaviour of a 46-storey building*, 1979.

Alan P. Jeary. The description and measurement of nonlinear damping in structures. *Journal of Wind Engineering and Industrial Aerodynamics*, 59(2-3):103–114, mar 1996. doi: 10.1016/0167-6105(96)00002-5.

J. C. Kaimal and J. J. Finnigan. *Atmospheric Boundary Layer Flows: Their Structure and Measurement*. Oxford University Press, 1994. ISBN 0195062396.

J. C. Kaimal, J. C. J. Wyngaard, Y. Izumi, and O. R. Coté. Spectral analysis of surface-layer turbulence. *Quarterly Journal of the Royal Meteorological Society*, 98(417):563–589, 1972.

A. Kareem. Aerodynamic response of structures with parametric uncertainties. *Structural Safety*, 5(3):205–225, sep 1988. doi: 10.1016/0167-4730(88)90010-0.

A. Kareem and X. Chen. Recent advances in coupled dynamic analysis of wind-induced structures. In *Asia-Pacific Conference on Wind Engineering VI (APCWE-VI)*, pages 114–149, 2005.

A. Kareem and K. Gurley. Damping in structures: its evaluation and treatment of uncertainty. *Journal of Wind Engineering and Industrial Aerodynamics*, 59(2-3):131–157, mar 1996. doi: 10.1016/0167-6105(96)00004-9.

H. Kawai, J. Katsura, and H. Ishizaki. Characteristics of pressure fluctuations on the windward wall of a tall building. In *Wind Engineering*, pages 519–528. Elsevier, 1980. doi: 10.1016/b978-1-4832-8367-8.50053-x.

K. Kayvani. Design of high-rise buildings: past, present and future. In editor, editor, *23rd Australasian Conference on the Mechanics of Structures and Materials (ACMSM23)*, 2014.

C. W. Kent, C. S. B. Grimmond, D. Gatey, and J. F. Barlow. Assessing methods to extrapolate the vertical wind-speed profile from surface observations in a city centre during strong winds. *Journal of Wind Engineering and Industrial Aerodynamics*, 173:100–111, feb 2018. doi: 10.1016/j.jweia.2017.09.007.

A. C. Khanduri, T. Stathopoulos, and C. Bédard. Wind-induced interference effects on buildings — a review of the state-of-the-art. *Engineering Structures*, 20(7):617–630, jul 1998. doi: 10.1016/s0141-0296(97)00066-7.

T. Kijewski and A. Kareem. Reliability of random decrement technique for estimates of structural damping. In *8th ASCE Speciality Conference on Probabilistic Mechanics and Structural Reliability*, pages 294–299, 2000.

T. Kijewski-Correa and J. D. Pirnia. Dynamic behavior of tall buildings under wind: insights from full-scale monitoring. *The Structural Design of Tall and Special Buildings*, 16(4):471–486, 2007. doi: 10.1002/tal.415.

T. Kijewski-Correa, J. Kilpatrick, A. Kareem, D. K. Kwon, R. Bashor, M. Kochly, B. S. Young, A. Abdelrazaq, J. Galsworthy, N. Isyumov, D. Morrish, R. C. Sinn, and W. F. Baker. Validating wind-induced response of tall buildings: Synopsis of the chicago full-scale monitoring program. *Journal of Structural Engineering*, 132 (10):1509–1523, oct 2006. doi: 10.1061/(asce)0733-9445(2006)132:10(1509).

T. L. Kijewski-Correa. *Full-scale Measurements and System Identification: A Time-Frequency Perspective*. PhD thesis, University of Notre Dame, 2003.

D. H. Kim and J. Y. Kim. Assessment on natural frequencies of structures using field measurement and fe analysis. *International Journal of High-Rise Buildings*, 3:305–310, 2014. doi: 10.21022/IJHRB.2014.3.4.305.

K. C. S. Kwok. Aerodynamics of tall buildings. In *Ninth International Conference on Wind Engineering*, volume 1, pages 180–205, 1995.

K. C. S. Kwok, K. T. Tse, and S. Campbell. Field measurements of dynamic properties of high-rise buildings. *Advances in Structural Engineering*, 14(6):1107–1128, dec 2011. doi: 10.1260/1369-4332.14.6.1107.

S. Lagomarsino. Forecast models for damping and vibration periods of buildings. *Journal of Wind Engineering and Industrial Aerodynamics*, 48(2-3):221–239, oct 1993. doi: 10.1016/0167-6105(93)90138-e.

J. P. Lamb. The influence of geometry parameters upon lag error in airborne pressure measuring systems. Technical report, Wright Air Development Center Wright-Patterson, 1957.

T. V. Lawson. The design of cladding. *Building and Environment*, 11(1):37–38, 1976. doi: 10.1016/0360-1323(76)90017-2.

H. Lettau. Note on aerodynamic roughness-parameter estimation on the basis of roughness-element description. *Journal of Applied Meteorology*, 8(5):828–832, 1969.

R. W. Macdonald, R. F. Griffiths, and D. J. Hall. An improved method for the estimation of surface roughness of obstacle arrays. *Atmospheric Environment*, 32(11):1857–1864, jun 1998. doi: 10.1016/s1352-2310(97)00403-2.

F. Matichard and M. Evans. Review: Tilt-free low-noise seismometry. *Bulletin of the Seismological Society of America*, 105(2A):497–510, mar 2015. doi: 10.1785/0120140200.

M. Meyers and K. Chawla. *Mechanical Behavior of Materials*. Cambridge University Press, 2008. ISBN 9780511810947. doi: https://doi.org/10.1017/CBO9780511810947.

NEN. Nen-en 1991-1-4. Technical report, NEN, Brussels, 2005.

NEN. Nen-en 1990+a1+a1/c2/nb. techreport, NEN, 2011.

M. Novak. Effect of soil on structural response to wind and earthquake. *Earthquake Engineering & Structural Dynamics*, 3(1):79–96, 1974a. doi: 10.1002/eqe.4290030107.

M. Novak. Dynamic stiffness and damping of piles. *Canadian Geotechnical Journal*, 11(4):574–598, nov 1974b. doi: 10.1139/t74-059.

M. Novak and L. El Hifnawy. Damping of structures due to soil-structure interaction. *Journal of Wind Engineering and Industrial Aerodynamics*, 11(1-3):295–306, may 1983. doi: 10.1016/0167-6105(83)90108-3.

M. Novak and L. El Hifnawy. Structural response to wind with soil-structure interaction. *Journal of Wind Engineering and Industrial Aerodynamics*, 28(1-3):329–338, aug 1988. doi: 10.1016/0167-6105(88)90129-8.

H. A. Panofsky and J. A. Dutton. *Atmospheric turbulence: models and methods for engineering applications*. Wiley, 1984. ISBN 0471057142, 9780471057147.

J. D. Pirnia. Full-scale characteristics of tall buildings and impacts on occupant comfort. Master's thesis, University of Notre Dame, 2009.

M. Prandina. *Spatial Damping Identification*. PhD thesis, University of Liverpool, 2010.

P. K. Robertson. Soil classification using the cone penetration test. *Canadian Geotechnical Journal*, 27(1):151–158, feb 1990. doi: 10.1139/t90-014.

J. Seppänen. *Methods for Monitoring Electromechanical Oscillations in Power Systems*. PhD thesis, Aalto University, 2017.

H. D. Sharma, M. T. Dukes, and D. M. Olsen. Field measurements of dynamic moduli and poisson's ratios of refuse and underlying soils at a landfill site. In *Geotechnics of Waste Fills: Theory and Practice*, page 69. International, 1990. doi: 10.1520/stp25299s.

R. N. Sharma. *The influence of internal pressure on wind loading under tropical cyclone conditions*. PhD thesis, University of Auckland, 1996.

E. Simiu and R. H. Scanlan. *Wind effects on structures: Fundamentals and Applications to Design*. Wiley, third edition edition, 1996. ISBN 9780471121572.

R. Smith and M. Willford. Damping in tall buildings - uncertainties and solutions. *IABSE Congress Report*, 17 (28):66–67, jan 2008. doi: 10.2749/222137908796225618.

G. Solari. Turbulence modeling for gust loading. *Journal of Structural Engineering*, 113(7):1550–1569, jul 1987. doi: 10.1061/(asce)0733-9445(1987)113:7(1550).

J. M. J. Spijkers, A. W. C. M. Vrouwenvelder, and E. C. Klaver. *Structural Dynamics CT4140*. Delft University of Technology, 2005.

G. G. Stokes. On the effect of the internal friction of fluids on the motion of pendulums. *Transactions of the Cambridge Philosophical Society*, IX(II):106, 1951.

I. Talib. Verification of the energy flow analysis method as identification tool for damping in high-rise buildings. Report, Eindhoven University of Technology, 2019.

Y. Tamura. Application of damping devices to suppress wind-induced responses of buildings. *Journal of Wind Engineering and Industrial Aerodynamics*, 74-76:49–72, apr 1998. doi: 10.1016/s0167-6105(98)00006-3.

Y. Tamura. Damping in buildings, 2008. URL `http://www.wind.arch.t-kougei.ac.jp/info_center/ITcontent/tamura/10.pdf`.

Y. Tamura. *Damping in Buildings and Estimation Techniques*, book section 13, pages 347 – 374. Springer, Tokyo, 2013. ISBN 978-4-431-54337-4. doi: 10.1007/978-4-431-54337-4_13.

Y. Tamura, A. Sasaki, T. Sato, and R. Kousaka. Evaluation of damping ratios of buildings during gusty wind using the random decrement technique. In *12th Wind Engineering Symposium*, 1992.

Y. Tamura, M. Yamada, and H. Yokota. Estimation of structural damping of buildings. In *Structures Congress XII*, pages 1012–1017. ASCE, 1994.

Y. Tamura, L. Zhang, A. Yoshida, S. Nakata, and T. Itoh. Ambient vibration tests and modal identification of structures by fdd and 2dof-rd technique. In *Structural Engineers World Congress*, 2002.

J. Thijssen. *Notes on Classical and Quantum Mechanics*. Delft University of Technology, 2008.

E. E. Ungar. The status of engineering knowledge concerning the damping of built-up structures. *Journal of Sound and Vibration*, 26(1):141–154, jan 1973. doi: 10.1016/s0022-460x(73)80210-x.

J. K. Vandiver, A. B. Dunwoody, R. B. Campbell, and M. F. Cook. A mathematical basis for the random decrement vibration signature analysis technique. *Journal of Mechanical Design*, 104(2):307–313, apr 1982. doi: 10.1115/1.3256341.

J. Vellozzi and E. Cohen. Gust response factors. *Journal of the Structural Division*, 1968.

S. A. Whitmore and B. Fox. Improved accuracy, second-order response model for pressure sensing systems. *Journal of Aircraft*, 46(2):491–500, mar 2009. doi: 10.2514/1.36262.

J. P. Wolf and A. J. Deeks. Cones to model foundation vibrations: incompressible soil and axi-symmetric embedment of arbitrary shape. *Soil Dynamics and Earthquake Engineering*, 24(12):963–978, dec 2004. doi: 10.1016/j.soildyn.2004.06.016.

J. C. S. Yang, N. G. Dagalakis, G. C. Everstine, and Y. F. Wang. Measurement of structural damping using the random decrement technique. *Shock and Vibration Bulletin*, 53(4):63–71, 1983.

A. Yoshida and Y. Tamura. Modal identification of structures by fdd and 2dof-rd technique. *The Proceedings of the Symposium on the Motion and Vibration Control*, 2003.8(0):601–604, 2003. doi: 10.1299/jsmemovic.2003.8.601.